Investigation of micro- and macro-phenomena in densely packed granular media using the discrete element method

Chong Zhou

School of Engineering

The University of Edinburgh

A dissertation submitted for the degree of

Doctor of Philosophy

January 2011

Declaration

I declare that this thesis was composed by myself, that the work contained herein is my own except where explicitly stated otherwise in the text, and that this work has not been submitted for any other degree or professional qualification except as specified.

Chong Zhou

January 2011

Acknowledgements

This dissertation owes its existence to the encouragement of my supervisor, Professor Jin Ooi, who gave me tremendous inspiration and confidence both to tackle what others said would be an impossible problem and to carry it through to fruition. I have learned and benefited much from his guidance, which made the past four years I spent at the University of Edinburgh the most remarkable and rewarding time in my life. I very much appreciate the invaluable cross-training opportunities and transferable skills I have gained through my studentship with Professor Ooi. The privilege to study under his esteemed supervision is a gift that I will always treasure and one which I will never take lightly. The great support in believing in me and what we could accomplish together will never be forgotten.

I have been fortunate in having the opportunity to work with a group of energetic people in silo and granular solids group at the University of Edinburgh. The whole group provided an ideal working environment, giving me liberties to shape my own research. I have enjoyed every moment that we have worked together including all those late night office activities. I appreciate the friendship and collective encouragement from all former and present group members to complete this dissertation: to Dr. Johannes Haertl, for a lifetime friendship, technical wisdom, and for always being there when there were bumps in the road; to Dr. Jun Ai, for an encyclopedia of knowledge about

Itasca PFC; to Prof. Michael Rotter, for constant sources of keen insight and sharing his tremendous knowledge in silo structures; to Dr. Zhijun Zhong, for the generous assistance in my laboratory tests; to Dr. Jian-Fei Chen, for interesting technical discussion and moral support. I would also like to thank Hamish Cullens and Ruaridh Evans, for their hard work in completing the footing experiments as the last part of my PhD project.

There are a few my longstanding and treasured friends who deserve a special mention, without whom my life in Edinburgh would have been bare and empty: Rick Lee, Tang Tang, Bian Zhuang, Yangyang Chen, Yaorong Wang, Daniel Tam, Li Li, Yin Wang, Xiaoqin Li, Yi Tao, Shiqing Li, Mical Johnstone, Finn Donaldson, Meng Xu, Vickie Gao and Sam Wong. Their good spirits and care made my PhD journey productive, memorable and enjoyable.

I am extremely grateful to the full financial support from Dorothy Hodgkin Postgraduate Awards (DHPA), without which this dissertation would not have been possible. This distinguished fellowship is sponsored by British Engineering and Physical Sciences Research Council (EPSRC) and Shell UK Ltd.

I deeply thank Prof. David Muir Wood, my thesis external examiner, for his insightful and integral examination. The proposed corrections contribute to a indispensable portion to the multiscale study and significantly strengthen the research quality of the thesis.

Finally and most importantly, I'm deeply blessed that my family, particularly Mom and Dad, who took turns calling on Sunday nights to listen to my latest snag and to help establish a rhythm for beginning the work week. Particularly, my mum came to Edinburgh to take very

good care of me in the last few months of my PhD. I owe an untold amount to my grandparents. Without their patience and wonderful value of education, I wonder whether my curiosity for engineering learning would ever have emerged.

To all of you, thank you.

To my dedicated parents and grandparents.

Our deepest fear is not that we are inadequate.

Our deepest fear is that we are powerful beyond measure.

It is our light , not our darkness, that most frightens us.

— Marianne Williamson

Abstract

Granular materials are in abundance in nature and are estimated to constitute over 75% of all raw materials passing through the industry. Granular or particulate solids are thus of considerable interest to many industrial sectors and research communities, where many unsolved challenges still remain.

This thesis investigates the micro- and macro-phenomena in densely packed particulate systems by means of the Discrete Element Method (DEM), which is a numerical tool for analysing the internal complexities of granular material as the mechanical interactions are considered at the grain scale. It presents an alternative approach to phenomenological continuum approaches when studying localisation problems and finite deformation problems in granular materials.

In order to develop a comprehensive theoretical understanding of particulate matter and to form a sound base to improve industrial processes, it is desirable to study the mechanical behaviour of granular solids subject to a variety of loading conditions. In this thesis, three loading actions were explored in detail, which are biaxial compression, rigid object penetration and progressive formation of granular piles. The roles of particle shape and contact friction in each of these loading scenarios were investigated. The resulting packing structures were compared and studied to provide a micromechanical insight into the

development of contact force network which governs the collective response. The interparticle contact forces and displacements were then used to evaluate the equivalent continuum stress and strain components thus providing the link between micro- and macroscopic descriptions. The information collected from the evolution of strong contact network illustrates the underlying mechanism of force transmission and propagation.

DEM simulations presented in this thesis demonstrate strong capability in predicting the bulk behaviour as well as capturing local phenomenon occurring in the system. The research first simulates a testing environment of biaxial compression in DEM, in which the phenomenon of strain localisation was investigated, with special attention given to the interpretation of underlying failure mechanism. Several key micromechanical quantities of interest were extracted to understand the bifurcation instability, such as force chains, contact orientation, particle rotation and void ratio. In the simulation of progressive formation of granular piles, a counterintuitive pressure profile with a significant pressure dip under the apex was predicted for three models under certain conditions. Both particle shape and preparation history were shown to be important in the resulting pressure distribution. During the rigid body penetration into a granular sample, the contact forces were used to evaluate the equivalent continuum stress components. Significant stress concentration was developed around the punch base which further led to successive collapse and reformation of force chains. Taking the advantage of micromechanical analysis at particle scale, two distinct bearing failure mechanisms were identified as the penetration proceeded.

To further quantify the nature of strain mobilisation leading to failure, Particle Image Velocimetry (PIV) was employed to measure the deformation over small strain interval in association with shear band propagation in the biaxial test and deformation pattern in the footing test. The captured images from DEM simulation and laboratory experiments were evaluated through PIV correlation. This optical measuring technique is able to yield a significant improvement in the accuracy and spatial resolution of the displacement field over highly strained and localised regions. Finally, a series of equivalent DEM simulations were also conducted and compared with the physical footing experiments, with the objective of evaluating the capability of DEM in producing satisfactory predictions.

Contents

List of Figures

List of Tables

Chapter 1

Introduction

1.1 General background

Granular materials are in abundance in nature and constitute over 75% of all raw materials passing through industry (Nedderman, 1992). They are normally composed of discrete contacting particles, and voids filled with fluid and/or air. Granular solids can show multiple phase behaviour, e.g. behave like a solid, a fluid or a solid-fluid mixture. Particle systems present many challenges for innovation and fundamental science, to solve problems in areas as diverse as natural disasters and unsolved industrial material handling issues which incur extensive economic losses. The study of granular materials can thus improve the understanding in controlling a wide range of industrial processes and fundamental science such as: pneumatic conveying of mineral ores and agricultural products (Singer, 2003); segregation and mixing of granular materials (Ottino and Khakhar, 2000); design of silo structures (Rotter et al., 1998); soil mechanics (Cheng et al., 2003); particulate multiphase hydrodynamics (Gao and Herbst, 2009); wellbore stability and drilling operation in hydrocarbon exploration (Galindo Torres and Muñoz Castaño, 2007); and nanoparticle science (Wang et al., 2007).

In the past decades, the knowledge of bulk response of granular materials was mostly obtained from observations in the field and laboratory tests, which has provided much macro-scale information. Alongside these experiments, significant insights have been gained through the use of constitutive models. However, such continuum based models cannot always be successful as the discontinuous and inhomogeneous nature of granular materials cannot be fully incorporated. It further leads to the difficulty in capturing the complex mechanical behaviour such as avalanching in granular slopes, large deformation problems and failure caused by strain localisation. The macroscopic behaviour is governed by the interactions between individual particles. Therefore, investigating the microscopic mechanism in terms of these interactions at the grain scale is important for a comprehensive understanding of particulate matter. Over the last three decades, a promising numerical tool: the Discrete Element Method (DEM) which follows in detail the motion and interaction of particle assemblies, has increasingly proved as an invaluable technique to study granular materials. This dissertation concerns the application of DEM to investigate the response of densely packed granular solids at both micro- and macro-scale.

1.2 Objectives and scope of this research

One of the distinctive features of granular materials is that they are dramatically inhomogeneous and anisotropic. Mobilised friction, packing density, stress and strain, etc. can easily vary from one place to another. These variations could be introduced when the granular assembly is initially formed or packed. Alternatively, they can develop when the assembly undergoes different loading conditions. Therefore, the influence of the resulting packing structure on the micro- and macroscopic behaviour subject to a variety of loading scenarios is of prime importance to many industries, and has been identified as one of the few

core research areas in particulate science and technology.

In this study only densely packed granular media composed of cohesionless particles is considered. The research will first use the discrete element method to explore the role of particle shape and contact friction in a variety of loading actions on granular systems, including biaxial compression, rigid body penetration and formation of granular piles. The resulting packing structure will be studied in detail to provide particle scale probing of the contact force network that controls the collective mechanical behaviour of a particulate assembly. In order to measure the progressive deformation of granular solids, Particle Image Velocimetry (PIV) is applied in carefully conducted physical experiments of footing penetration. Furthermore, a verification example is given to shed further light on how to improve the capability of DEM simulation in producing quantitative predictions.

As the relatively inexpensive hardware of high performance is rapidly becoming available, it is anticipated that DEM will be more widely and frequently used as a research and design tool for bulk solids handling in the near future. This thesis deploys relevant analytical techniques to explore several particulate solid applications using DEM. Given the fast ongoing improvements on DEM methodology, it is therefore hoped that the thesis will also provide stimulus for further research and development.

1.3 Structure of the dissertation

The dissertation is divided into eight chapters. A brief introduction for each chapter is described below. It should be noted that previous research endeavours made towards granular mechanics comes from a broad range of sources, due to the multidisciplinary nature of particulate science and technology. As the current research involves a diverse range of topics, literature review for each loading investigation is given at the beginning of the respective chapter.

Chapter 1 presents the background, objectives and scope of this research. The layout of the dissertation is also outlined.

Chapter 2 gives a brief review of the DEM methodology. An overview of the numerical principle and implementation of DEM is provided. Several key issues which are important to achieve satisfactory predictions are discussed. It also considers the relevant issues relating to the fundamental concepts of mathematics and mechanics in granular solids. A number of numerical interpretive techniques to characterise the system's micromechanical variations which are used throughout the whole thesis are outlined.

Chapter 3 simulates a testing environment of biaxial compression in DEM. Special attention is placed on the shear band formation, voidage development and force chain buckling. The way in which all these aspects of the phenomena are influenced by variables such as particle shape and contact friction, is discussed. Additionally, both stress and strain are evaluated from particle scale information, thus providing the link between microscopic and macroscopic description. This chapter also addresses the measurement of progressive deformation in granular solids using Particle image velocimetry (PIV).

Chapter 4 explores the dynamics of granular piles made up from spherical and non-spherical particles. The elusive "stress dip" under a granular sandpile placed on a rough rigid base was carefully investigated. There are three numerical models considered, which are single layer, wedge-shaped and conical piles.

Chapter 5 includes the DEM simulation of rigid body penetration test. A rigid punch is driven into the granular samples with different particle shapes and gravity fields. Improved interpretations of the progressive penetration mechanism are obtained with the aid of homogenised stress analysis and microstructure of contact network. Another primary focus lies in the experimental study of footing penetration test, in which displacements fields and strain components are evaluated from PIV measurement to access the underlying deformation mechanism. A

series of DEM simulations to compare against the footing experiments were also carried out to examine the validity of DEM predictions.

Chapter 6 summarises general conclusions drawn from this study. Some recommendations for further research and potential applications are discussed.

Chapter 2

Brief review of granular material and discrete element method

2.1 Introduction

The study of fundamental mathematics and mechanics of granular materials has long been a subject of considerable importance. Historically, it can date back to the pioneering work of Charles-Augustin de Coulomb in 1776, when the failure condition in granular materials were firstly postulated. Since then, particle science and technology has been a rapidly developing interdisciplinary research area. Previous studies are carried out largely at a macroscopic scale by studying the constitutive relationship, which connects the applied stresses to strains or deformations. The resulting bulk response within a representative volume element (RVE) is helpful as a design tool and in developing a general understanding of particulate processes and handling. More recently, attempts have been made toward microscopic approaches that consider a granular material as an assembly of individual grains interacting with each other at a particle scale. Mathematicians, physicists and engineers have devoted a large mount of effort in advancing

the knowledge in bridging the gap between micro- and macroscopic modelling of granular material, which is widely encountered but poorly understood. Researchers have well recognised the critical importance of mathematically correct and mechanically admissible theories to describe the complex behaviour of granular solids.

In general, attempts made towards the modelling of granular materials can be divided into two different branches, either from macroscopic or from microscopic considerations. From macroscopic view, the domains of most engineering materials can be ideally modelled as a continuous mass in the analysis of the kinematics and the mechanical behaviour. On the basis of the continuum assumption, numerical solution techniques such as finite element, finite difference and boundary element methods have been established and widely employed in solving many engineering problems. However, the continuum mechanics approaches are phenomenological and are primarily concerned with mathematical formulations of the observed phenomenon without much detailed attention to the fundamental physics. Granular materials such as soil, rock and aggregate, are largely discontinuous and inhomogeneous in nature, which make the constitutive relationship rather complex and cannot be easily formulated. Difficulties thus arise in numerical modelling such as large deformation and bifurcation problems.

In materials dominated by particulate behaviour, it is advantageous to treat the sample as an assemblage of particles rather than as a continuum, as it permits the exploration of actual mechanisms involved. The most popular approach among alternatives to the continuum model is the discrete element method (DEM). The DEM discretises a granular material using rigid element that interact with its neighbouring elements according to certain contact laws. These rigid elements can have a variety of shapes, although most often they are circular or spherical due to the simplicity and efficiency in contact detection. The particles deform locally at the contact points by means of an overlap, known as the soft

contact method. This overlap is not a real phenomenon but instead intends to model the deformation of the interacting bodies in an indirect way.

This chapter is devoted to a brief review of both granular material and discrete element method. It commences with an introduction of mathematics and mechanics of granular solids relevant for this thesis, including packing structure and force transmission. Then the homogenisation averaging method that correlate the bulk behaviour and microscopic quantities is concerned. Another key element of the chapter lies in the general discussion and demonstration of Particle Image Velocimetry (PIV), which is an optical measurement technique and will be largely used in the current thesis. Finally power spectral analysis of DEM output and single layer model used in the current DEM simulations are described.

2.2 Mechanical descriptors of packing structure

Forming a granular packing is a complex and dynamic process in which a large number of factors will come into play together. The packing arrangement can be characterised quantitatively through some measurement within the granular sample, such as the coordination number, void ratio, contact orientation and particle orientation. In this section, the concept of these mechanical descriptors are introduced and discussed.

2.2.1 Coordination number

An important statistical measurement of contact density in a particulate assembly is the coordination number. The average coordination number is defined as the number of contacts per particle:

$$Z_a = \frac{2C}{N} \tag{2.1}$$

where C is the number of contacts and N is the number of particles. The coordination number characterises the packing density of granular materials. The higher coordination number usually corresponds to higher packing density or lower void ratio (e). It has been frequently used in the evaluation of mechanical properties related to the connectivity between particles, such as force transmission and bulk strength. O'Sullivan et al. (2002) found out that the material strength and stiffness are both proportional to specimen coordination number in the absence of any particle crushing.

2.2.2 Void ratio

It is well accepted that voidage in granular specimen plays an important role in the mechanical response subject to loadings such as compression and direct shear. The void ratio e is defined as the volume of voids in a particulate mixture divided by the volume of solids:

$$e = \frac{V - V_s}{V_s} \tag{2.2}$$

where V is the total volume of the sample and V_s is the solid part. Considering an assembly composed of mono-spherical particles, the maximum and minimum void ratios can be associated with two reference packing structures. In the least efficient packing form, face-centered cubic packing (FCC), the solids fill 52% of the total volume. In the most efficient packing arrangement, hexagonal close packing (HCP), solids fill 74% of the total sample volume. Thus for the FCC case, void ratio can be calculated as e=0.48/0.52=0.92; whereas for the HCP case, e=0.26/0.74=0.35. Noticeably, it is worth mentioning that these are theoretical upper and lower limits which are not realistic to be achieved in actual granular samples. Therefore, the above values should not be applied to any industrial bulk solids handling, because particles encountered in reality consist of a wide range of shapes and size distributions.

2.2.3 Contact and particle orientation

The anisotropy of granular materials can be developed during the packing forming process or induced through external loading. A convenient way to characterise the anisotropy within the sample is by plotting the polar distribution of normal contact vectors, where the possible bias in contact direction can be evaluated. A unit circle is partitioned into a series of orientation groups to accommodate the contacts that fall in the respective range. In the current study, an interval of 5° is used to divide the unit circle ranging from 0° to 360° into 72 bands. Since each contact always appears in pair, there exists a 180° rotational symmetry. A polar histogram is then constructed by interrogating each contact vector to find out which inclination band it belongs to. Nouguier-Lehon et al. (2005) investigated the distribution of contact orientations for samples with grains having different aspect ratio, as shown in Figure 2.1. In the sample composed of circular particles (R_a=1), the distribution of contact orientation presents the two usual preferential directions around ±60°, where the rest samples with elongated particles exhibit a single vertical preferential direction instead.

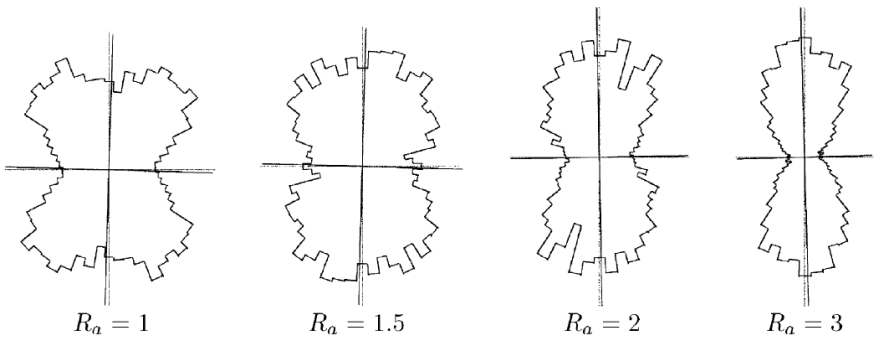

Figure 2.1: Distribution of contact orientations at the end of pluviation process with different particle aspect ratios R_a (Nouguier-Lehon et al., 2005)

Similar to contact orientation, particle orientation is referred to the direction of the major axes of the particles and only applies to non-spherical particles.

Figure 2.2 compares the definitions of contact and particle orientation for non-spherical particles (aspect ratio=1.5), in which the contact orientation is defined as the contact angle made by the constituent spheres of the two particles in contact.

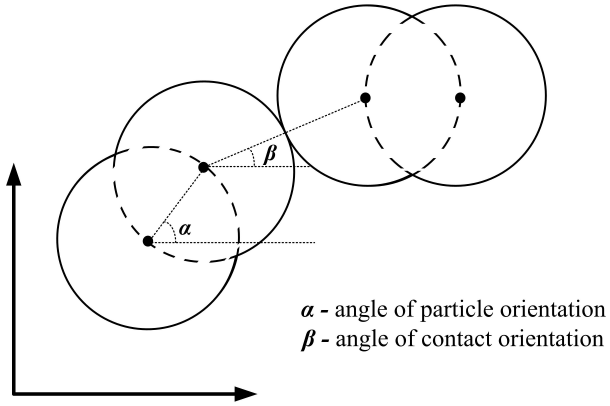

Figure 2.2: Contact orientation and particle orientation for non-spherical particles in contact

2.3 Force transmissions in granular solids

The macroscopic behaviour of granular material is governed by the micromechanics acting at the interparticle scale. Of special importance and interest is the relation between the stresses imposed at the boundary and the interparticle contact forces. When subject to external loadings, the force propagation in granular media can only be achieved via the interparticle contacts in order to establish a continuous and stable path. However, propagation of forces along such discrete paths can be rather ramified in granular systems. Extensive experimental and theoretical effort has been devoted to the study of force network in dense granular materials, suggesting that forces in granular solids are transmitted along

chain-like particle groups called "force chain". This section aims to review some experimental findings and analytical theories with regard to the structure and evolution of the force transmissions.

The concept of "force chain" was firstly proposed through the observation from photoelastic experiments (Figure 2.3), which makes the force network within a deforming granular assembly visible and investigatable. When visualised through force induced birefringence within an assembly of photoelastic disks, it is apparent that the manner of contact network is highly ramified and undergoes rapid changes as deformation proceeds.

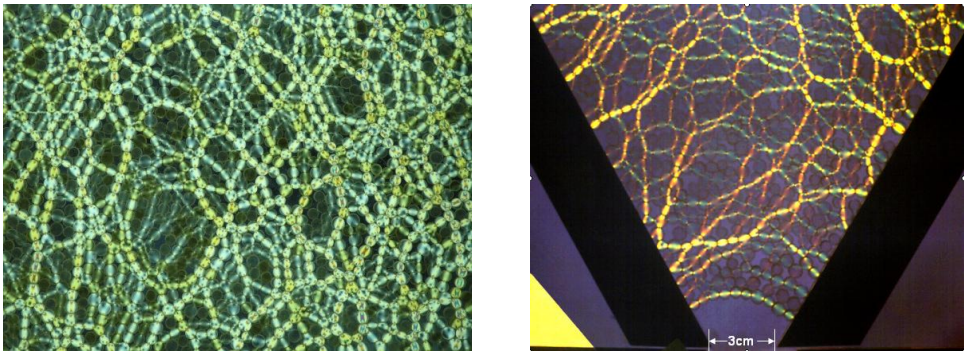

(a) Force chains under vertical confinement (Howell et al., 1999)

(b) Force chains near the silo outlet (Tang et al., 2009)

Figure 2.3: Image showing photoelastic particles in optical experiment

Although the term "force chain" has been widely used in numerous published literature, admittedly, its specific definition is still rather vague. Over the past few decades, a number of attempts have been made toward the quantitative characterisation of this force network. Radjai et al. (1998) suggested that the contact network can be decomposed into two subnetworks with complementary mechanical properties: a load-bearing percolating network of contacts carrying forces larger than the average force, and a dissipative network of contacts (typically greater than 60%) carrying forces smaller than the average force. Experimentally, measurements of contact forces inside three-dimensional piles of frictionless

liquid droplets (Zhou et al., 2006) have revealed long-range chainlike correlations of large forces, whose length was approximately ten particle diameters and the magnitude followed an exponential distribution. Peters et al. (2005) proposed a technique by which force chains in a two-dimensional granular assembly could be identified quantitatively from contact force data. In this technique, the identification of force chains proceeds in two steps: first, a force chain is defined to be a quasilinear arrangement of three or more particles where stress is concentrated; second, along the chain, stress concentration within each grain is characterised by the vector delineating the most compressive principal stress. This algorithm was further utilised by Muthuswamy and Tordesillas (2006a) to compile force chain statistics using data derived from DEM simulations, in which a two-dimensional granular assembly subject to indentation by a rigid flat punch. During the course of deformation, the results indicate that macroscopically stronger systems showed more branching in their force chain network and were in favour of shorter chains.

2.4 Homogenisation method

Particle displacement and interparticle force are the two fundamental quantities at particle contact. However, continuum quantities (e.g. stress and strain) are more often considered in engineering practice and are still dominant in the numerical modelling. Therefore it is necessary and important to link the data obtained from these two length scales. In discrete systems, the conventional continuum parameters can be obtained by performing statistical averaging over sufficiently large spatial or temporal scale. The techniques used to calculate stress and strain from contact forces and particle displacement, respectively, are called homogenisation methods.

The theory of averaging stress tensors from interparticle contact forces within a domain of granular materials has been well established (Bardet, 1998). Its

general form can be expressed as:

$$\bar{\sigma}_{ij} = \frac{1}{V} \sum_{c=1}^{N_c} l_i^c f_j^c \tag{2.3}$$

where N_c is the number of contacts within the domain of interest, V is the volume of the domain, f_j^c is the contact force vector at contact c, l_i^c is the branch vector connecting two contacting particles.

Strain is a fundamental kinematical state variable in continuum mechanics, adequately describing the gradient of displacement fields. Similar to the average stress tensor (Equation 2.3), strain can be calculated according to the displacement gradients $u_{i,j}$ (Muir Wood, 2004):

$$\bar{u}_{i,j} \approx \sum_{c=1}^{N_c} \Delta u_i^c d_j^c \tag{2.4}$$

where Δu_i is the relative translation of the centres of two particles and d_j is an area vector which assigns an area and a direction to each contact on the boundary. Therefore, the macroscopic average strain can be expressed as:

$$\bar{\epsilon}_{ij} = \frac{\bar{u}_{i,j} - \bar{u}_{j,i}}{2} \tag{2.5}$$

While the homogeneous averaging method for stress in granular materials has been well developed, there is no general agreement on the strain calculation. The main reason behind this is due to the fact that it is not easy to define an initial reference state to calculate the strain. Nevertheless, several studies have attempted to establish numerical formulations of strain in discrete systems. Generally, strain components in these methods are calculated as average displacement gradients within a collection of particles (Bagi and Bojtar, 2001; Cambou et al., 2000; Dedecker et al., 2000; Kuhn, 1999). The whole deformation body is

reconstructed into small elements by using triangulation or voronoi tessellation. Similar to the shape function in finite element method, strain within each element is deemed to be constant and calculated through local interpolation in association with the particle displacement and contact position. O'Sullivan et al. (2003) proposed a kinematic approach of strain calculation in particulate media, in which the particle rotation was incorporated as illustrated in Figure 2.4. This method is capable of smoothing the erratic displacements in zones of highly localised strain and capturing particle rotation for problems involving both two and three dimensions. However, these methods only consider spherical particles, and to date there is no rigorous strain formulation can be applied to non-spherical particles. This thesis aims to achieve a better understanding of micro-deformation mechanism in granular materials, which requires the knowledge of local strain measurement with increasing precision and is still lacking. In the current study, image analysis techniques will be used to study the incremental strain field and is discussed in the subsequent section.

2.5 Introduction of Particle Image Velocimetry (PIV)

Measurement of soil deformation with high accuracy is fundamental to the success of geotechnical modelling. Since the deformation process in a particulate system is rather progressive, conventional measurements carried out at the sample boundary may not be able to reflect the internal variations which govern the bulk response. This procedure is inadequate in the study of strain localisation problems where deformation at the boundary can sometimes show no significant changes. In recognition of the importance of achieving deformation measurement at high level of accuracy, a diverse range of measuring devices have been developed in the last decade. Among these available approaches, optical measuring technique such as Particle Image Velocimetry (PIV), is finding increasing use as

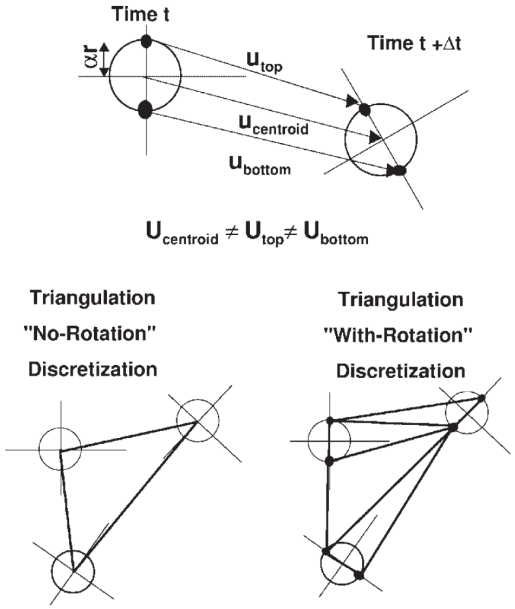

Figure 2.4: Schematic diagram of discretisation approach to capture the effects of particle rotation in strain calculation (O'Sullivan et al., 2003).

a research and design tool. PIV is a non-intrusive and indirect optical method originally used for the measurement of two-dimensional flow velocity in fluids. It captures the instantaneous in-plane displacement, and has demonstrated strong capability in yielding a significant increase in the measurement accuracy within a section of deformation field. Therefore, PIV technique is utilised to overcome the abovementioned deficiencies in conventional experimental measurement in granular materials and to investigate the deformation leading to failure at high spatial resolution.

In the current thesis, PIV measurement will be used in two loading scenarios to evaluate its performance in processing successive digital images containing flowing grains, including biaxial compression (Chapter 3) and model footing experiment (Chapter 5). This section begins with a brief introduction of PIV, including image recording technique, correlation algorithm and data post-processing. Then

a literature review of its recent application in geomechanics is provided. Finally, a calibration test is carried out to measure the Poisson's ratio of an aluminum sample by using PIV.

2.5.1 Basics and principles

PIV is originally developed in the field of experimental fluid dynamics (Adrian, 1991), where the velocity vectors are measured simultaneously over a seeded flow area. A typical PIV system for flow measurement (Figure 2.5) consists of a laser light sheet (for illumination), fluid flow with seeding particles, an image recording system (camera) and a computer for image processing.

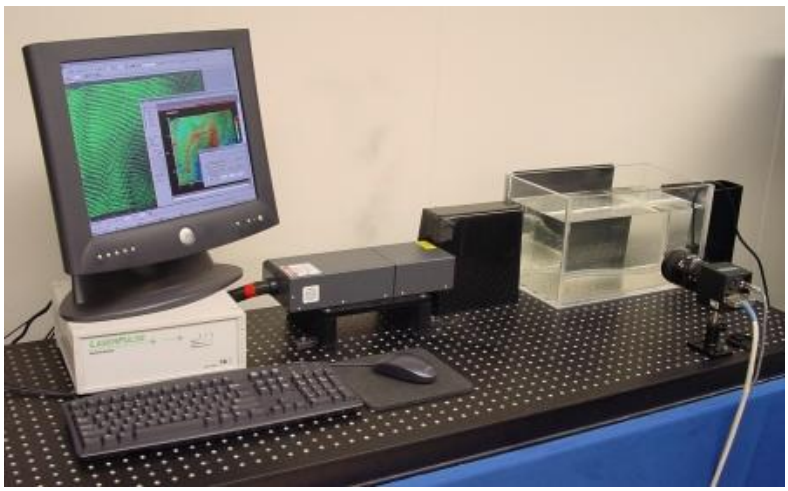

Figure 2.5: A PIV system used in fluid mechanics (http://www.aem.umn.edu/people/students/troolin/tutorial_piv_principle.html)

Basically, PIV determines particle displacement over the time exposure between two images. Therefore, the essential idea of PIV in its early application is to identify particles within an image from the background, and track them along their trajectories throughout an image sequence. The image is divided into a series of subregion (interrogation window), and the best match for each of these

testing subregions in the second image was found by means of correlation method, which averages the displacement of all the particles in the interrogation window.

2.5.2 PIV software

As a consequence of the rapid growth of PIV application in the past decades, a number of commercial packages (e.g. LaVision and TSI) and open-source codes (e.g. MPIV, MatPIV and OpenPIV) have been developed. These programs have many adaptabilities for users with different requirements and provide satisfied suitability for both industrial practice and academic research. Among them, MPIV (Mori and Chang, 2003) performs as a MatLab toolbox and offers a flexible platform to modify for use in specific area for both engineers and scientists. Therefore MPIV was chosen for use in the current PIV analysis. The following sections deals with the discussion on those aspects that are important to the numerical implementation of MPIV, such as image evaluation method and data post-processing.

2.5.3 Image evaluation method

In a standard PIV approach, two subsequent recording frames are first partitioned into a set of interrogation windows, and then an image evaluation method is applied to calculate the pixel differences between the searching windows. Statistically, PIV assumes all the particles in an interrogation window to move a similar distance and direction. The processing algorithm then computes the mean displacement vector for the particles in each interrogation window. MPIV offers cross-correlation algorithm and minimum quadratic difference (MQD) algorithm as the image evaluation methods. A brief description of the mathematical concepts for each method is presented next.

2.5.3.1 Cross-correlation algorithm

The cross-correlation algorithm is the most conventional method to calculate displacement vectors. The formula for two-dimensional cross correlation of image f_1 and f_2 can be expressed as:

$$C(\Delta X, \Delta Y) = \frac{\sum_{i=1}^{N}\sum_{j=1}^{N}\left[f_1(X_i, Y_j) - \overline{f}_1\right]\left[f_2(X_i + \Delta X, Y_j + \Delta Y) - \overline{f}_2\right]}{\sqrt{\sum_{i=1}^{N}\sum_{j=1}^{N}\left[f_1(X_i, Y_j) - \overline{f}_1\right]^2}\sqrt{\left[f_2(X_i + \Delta X, Y_j + \Delta Y) - \overline{f}_2\right]^2}} \tag{2.6}$$

where f_1 and f_2 are the small windows from each image in the image pair, N is the window size and the overbar denotes the mean quantity. The location of the maximum value (peak) in C is used as the mean particle displacement of this small area. In the MPIV program, the calculated displacement is retained as valid only if the ratio of the highest peak to the second highest peak exceeds a preset threshold value, and the ratio of the values of the highest peak to the root-mean-square noise also exceeds a preset threshold value (determine by trial and error).

2.5.3.2 Minimum quadratic difference algorithm

The minimum quadratic difference (MQD) technique is a least-squares algorithm that determines the degree of similarity of two matrices. The MQD function for two interrogation areas of frame f_1 and f_2 is defined by:

$$C(\Delta X, \Delta Y) = \sum_{i=1}^{N}\sum_{j=1}^{N}\left|f_1(X_i, Y_j) - f_2(X_i + \Delta X, Y_j + \Delta Y)\right| \tag{2.7}$$

The location of the minimum value in C is used as the particle displacement. Note that MQD is sometimes referred as "gray level difference accumulation".

The criteria to retain the calculated vectors is similar to that in the correlation algorithm, i.e. by checking the ratio of the two highest peaks and the signal to noise ratio of the highest peak. The MQD algorithm may be more robust than the cross-correlation algorithm in certain situations. For example, the correlation algorithm does not work well for images containing no particles such as speckle images. Gui and Merzkirch (2000) concluded that MQD generally gave better results in terms of statistical and principal errors. Hence MQD is the technique of choice in the current study. It should be noted that the MQD algorithm is in general more computationally demanding than the cross-correlation algorithm.

2.5.4 Error correction of PIV data

After the image correlation, a certain amount of incorrectly determined velocity vectors can be identified simply by visual inspection of the data plotted. In most cases, their magnitudes and directions differ considerably from the surrounding vectors. Based on the hypothesis that the flow paths should be smooth in general, apparent discontinuities within the displacement field should not be present and thus be eliminated. In order to detect these spurious vectors, the original data needs to be validated according to certain outlier criteria. Some methods, such as global mean filtering, are not used in this study, as the deformation in granular materials can sometimes be mainly characterised by local regions with high strain gradient. Shinneeb et al. (2004) suggested that local median threshold is more suitable to high gradient flows, as spurious vectors in the windows do not affect the median. Therefore, in this study the local median value was used in vector filtering, which is a one of post-processing routines available in MPIV. This technique validates each vector against its neighbours by comparing its magnitude with the median of all the members in a selected area (3×3 vectors). More detail of this technique are summarised by Westerweel (1994). Once completing the

identification of spurious vectors, it is possible to fill the removed error vectors using an interpolation scheme. MPIV uses Kriging method to assign a value for each spurious vectors, which serves the purposes of data reconstruction and spatial enhancement. Although post-interrogation error correction is extremely useful and has been widely applied, it should bear in mind that these errors can only be replaced by artificially interpolated values.

2.5.5 Vector plotting of PIV data

Displacement vectors are the major output from PIV analysis. When plotting these vectors, it is intuitive and convenient to draw arrows such that the direction in which the arrow points is the direction of the vector and the length of the arrow represents its magnitude. Such plots have been very popular in fluid mechanics in either two or three space dimensions. However, there are several distinct disadvantages of this method. First of all, vectors of small magnitude will be depicted as dots. As a result, direction information is lost at these points, which also makes it extremely difficult to represent a wide range of magnitudes. Additionally, in the areas with high density of vectors, a large amount of overlap between adjacent arrows can easily dissolve the plot into a mass of confusing line segments.

In the current study, an improved vector plotting scheme is proposed to provide a better visual inspection of the entire displacement field, which has becoming prevalent in earth system analysis as illustrated in Figure 2.6. This function includes the ability to plot colour vectors, all of equal length but colour coded according to their magnitudes. Colour is an important dimension in data visualisation. A well chosen colour map can make features embedded in a series of data become easily observed and analysed. In this case, a colour bar is provided to indicate the mapping of data value with axis labels.

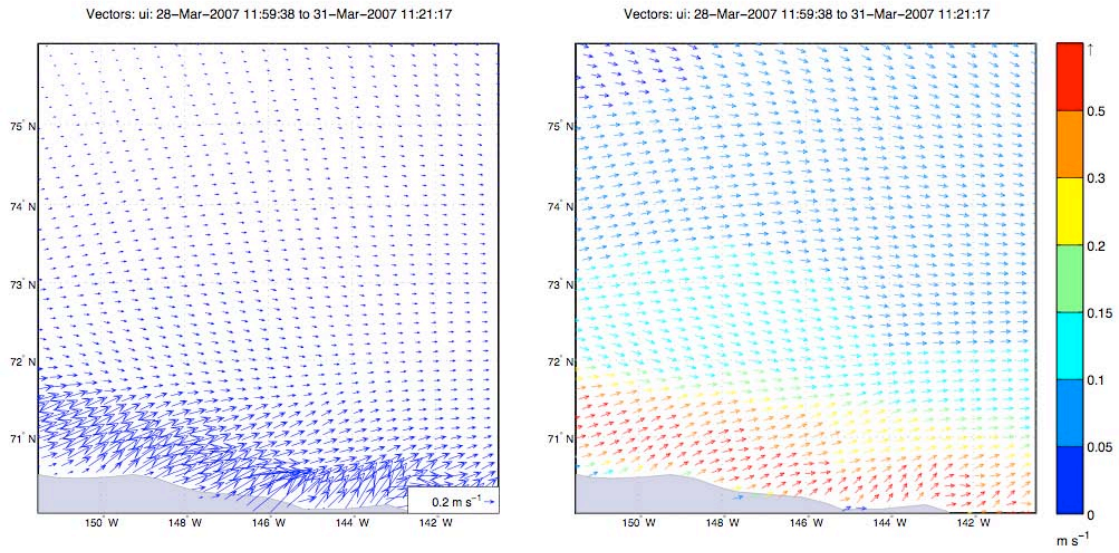

Figure 2.6: Vector plotting technique: (left) conventional length scaled vectors; (right) proposed colour scaled vectors (Roberts, 2007).

2.5.6 Literature review

The development of PIV in the past decades is characterised by the improvements in both digital image recording and numerical evaluation techniques. This methodology is now applied with confidence in a wide range of disciplines, yielding data not possible before. Although relatively new, recently PIV has been introduced and used to measure the dynamics of granular solids. In this section, the applications of PIV in particulate systems are briefly reviewed.

Lueptow et al. (2000) adapted PIV for use in measuring particle movement in granular flows. The application was demonstrated by measuring convection rolls of spherical glass beads in a vertically oscillating box. Similar to the application in fluid mechanics, light and dark particles were selected as seedings in order to provide distinctions in pixel characterisation. The PIV measured displacement was consistent with the displacement of a marked layer of particles. White et al. (2003) explored the application of PIV in the study of installing a displacement

pile in Dog's bay carbonate sand and Leighton Buzzard silica sand. The displacement fields and strain paths during the pile indentation were found to be relatively independent of sand type. The measured strain paths were similar to the analytical solutions made by the strain path method. Sielamowicz et al. (2005) evaluated the performance of PIV in the analysis of flow pattern during the discharge of granular material from planar hoppers. The plug flow evolution as a function of time was quantitatively determined using the velocity profiles predicted by PIV. It also provided the possibility to reveal the boundaries between flowing and stagnant zones based on the calculated velocity gradients. Rechenmacher (2006) used a similar technique called digital image correlation (DIC) to study the shear band initiation and propagation in sand specimens during biaxial and triaxial compression. It was reported that the accuracy in displacement measurement was better than $0.01mm$ by using the commercial program VIC-2D. Incremental displacement fields and strain components obtained from DIC were used to interpret the spatial nonlinearity and provide a better understanding of the local failure mechanisms. Hall et al. (2010) performed a 2D laboratory test of a granular material subject to deviatoric loading along different strain paths. By using DIC, the strains and patterns of strain localisation were characterised. The evolving internal structures of deformation which consisted of bands of localised deformation and cells of low deformation between the bands were revealed.

2.5.7 Calibration test of PIV measurement in physical experiments

Before applying PIV technique to a series of experimental measurement, a simple calibration test was conducted to access its performance and accuracy. To serve this purpose, a calibration test to determine the Poisson's ratio of aluminum was designed. In this test, a strip aluminum cutting was placed into the Instron

machine and subject to a uniaxial extension. PIV was used to track the sample deformation by working out the lateral and axial displacement.

PIV evaluation not only requires successive images of the deformation body to be captured, but also relies on the image quality to perform correlation. In order to introduce sufficient pixel information during PIV operation, the sample surface was sprayed with randomly distributed paint spots. A digital high-speed camera (CASIO Exlim F1, 12 megapixel) was used to record images at an interval of 15 frames/second. Figure 2.7 shows the testing aluminum test sample and the experimental setup.

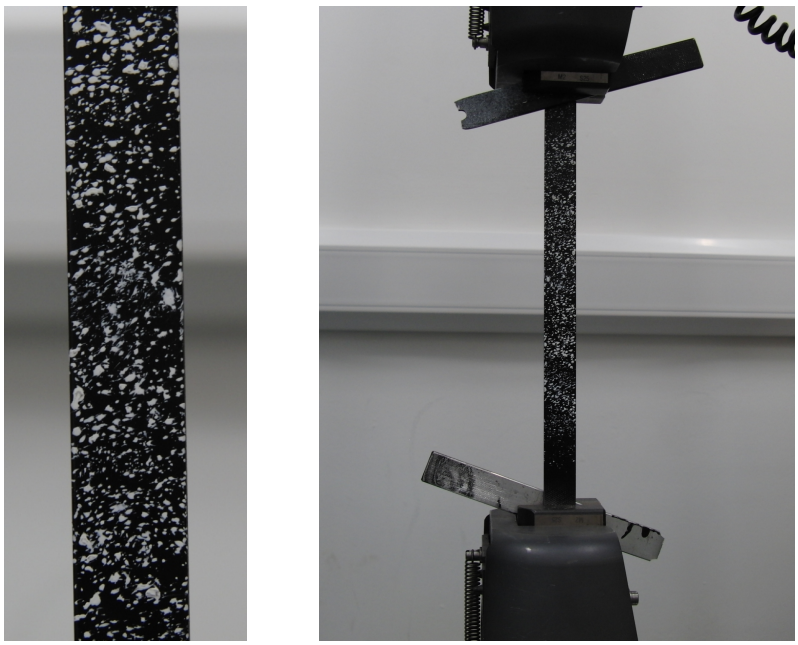

Figure 2.7: Aluminium sample and loading setup

The dimension of the testing sample is $30 \times 200mm$ and the interrogation size was chosen as 64×64 pixels, which can be converted into physical length of 5.2×5.2mm. The yielded displacement vectors were plotted in Figure 2.8, in which most of the vectors were aligned in vertical direction with the magnitudes increased linearly from bottom to top of the specimen where the tensile loading

was applied. Overall, the displacement field produced from PIV image evaluation was rather smooth, with only a few error vectors outside the primary deformation zone. Figure 2.9 shows the magnitude of v_x and v_y output from a horizontal and a vertical layer of the interrogation window that cross the sample centre, respectively. As square interrogation window was used in the PIV evaluation, the Poisson's ratio can be easily calculated by working out the ratio of average increment in lateral direction over axial direction, according to Figure 2.9. The predicted value of Poisson's ratio for the current aluminum test sample is 0.30, whereas typical value obtained from specific physical tests lies between 0.32 and 0.34. The smaller value estimated from the current PIV analysis can be attributed to the fact that the two ends of the sample were fully clamped during the loading, and therefore the horizontal contraction was restrained to some extent. Also, some numerical errors can be also resulted from the least squares fitting of the average horizontal displacement.

This example demonstrates the capability of PIV technique in measuring the material properties. The result shows satisfactory agreement with other physical measurements. Normally in material experiments, Poisson's ratio is determined from the changes of strain gages in both lateral and longitudinal directions. Comparing to the conventional approaches, PIV presents not only simplicity in both experimental and numerical operations, but also reasonable accuracy and stability.

2.6 Strength of granular materials

Granular materials exhibit a large and often poorly understood set of failure modes, where particle frictional properties play an important role. As far as strength is concerned, such a behaviour can be mathematically described by the classical Mohr-Coulomb or Drucker-Prager failure criteria. The Mohr-Coulomb

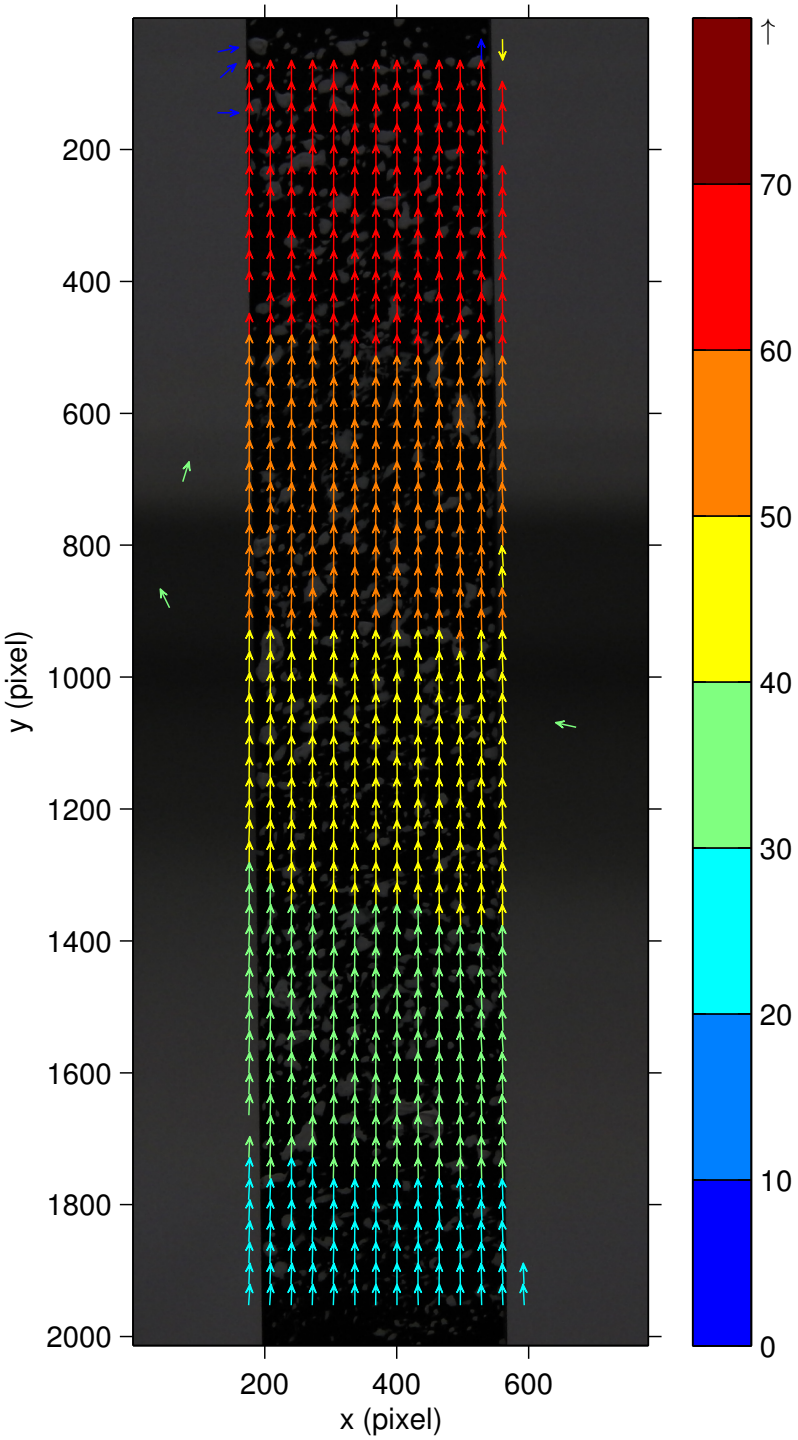

Figure 2.8: Displacement vectors from PIV

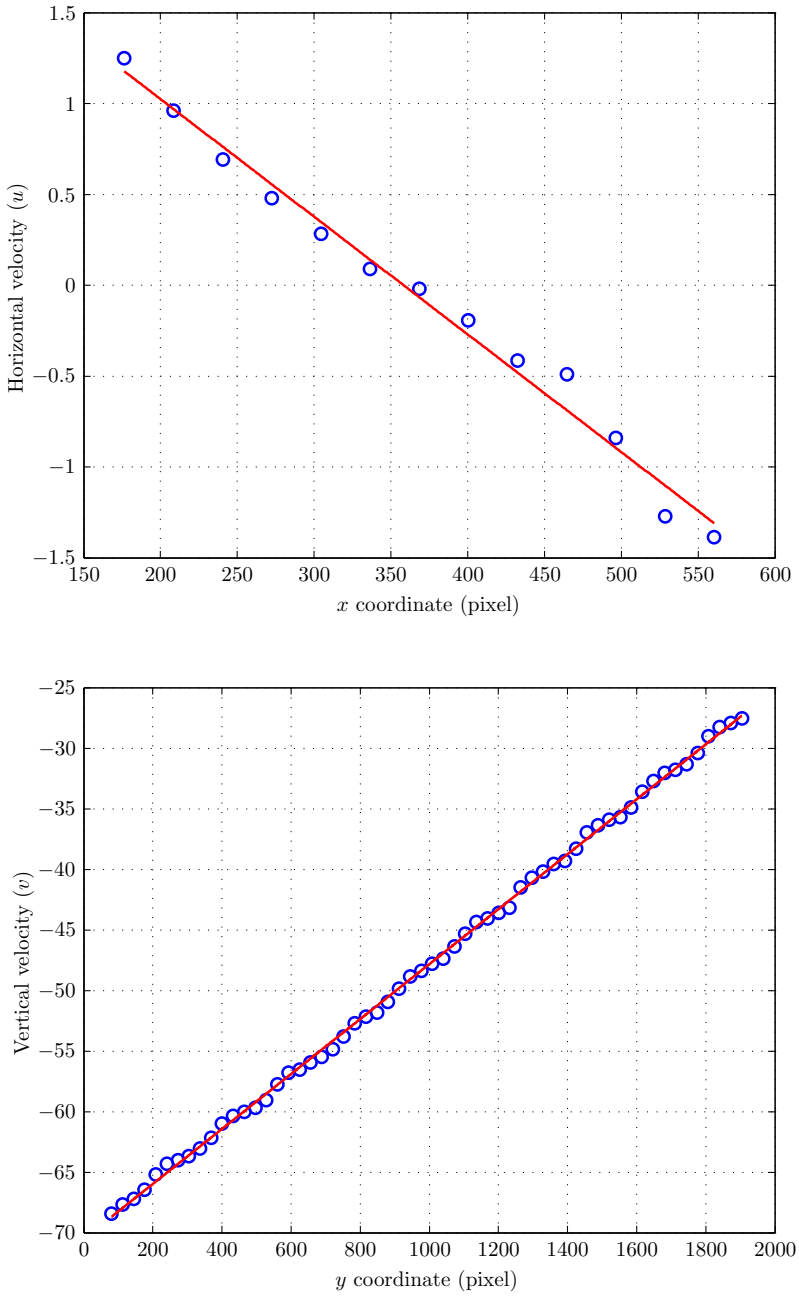

Figure 2.9: Velocity components in horizontal and vertical direction

failure criterion says that failure of a soil mass will occur if the resolved shear stress τ on any plane in that soil mass reaches a critical value. It can be written as:

$$\tau = c + \sigma \tan \varphi \tag{2.8}$$

where c is the coefficient of cohesion and φ is often called the internal friction angle. The coefficients of friction normally encountered vary from about 0.3 for smooth spherical particles to about 1.5 for angular particles. Equation 2.8 can be rewritten in terms of principal stresses, σ_1 and σ_2:

$$q = p \sin \varphi + c \cos \varphi \tag{2.9}$$

where $p = (\sigma_1 + \sigma_2)/2$ and $q = (\sigma_1 - \sigma_2)/2$ are the pressure and deviatoric stress, respectively. Equation 2.9 is illustrated and used in conjunction with the classic Mohr-Coulomb circle (Figure 2.10), assuming the general shear failure occurs along the plane where the stress ratio τ/σ is a maximum.

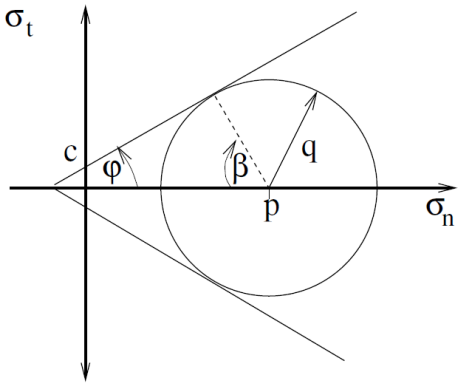

Figure 2.10: Mohr-Coulomb circle

For cohesionless sample where c is equal to zero, the strength solely relies on the internal friction angle. However, a number of experiments and simulations

have proved that the friction angle is strongly dependent on a number of factors which affect the mechanical state at any given time and on the frame of reference, in particular the packing fabric, void ratio, dilatancy and loading condition etc. This suggests that considering granular assembly as a frictional material is not adequate, and therefore there is no concrete definition of "shear strength" for granular materials.

The Drucker-Prager yield criterion is a pressure-dependent model for determining whether a material has failed or undergone plastic yielding. The criterion was introduced to deal with the plastic deformation of soils. It and its many variants have been applied to rock, concrete, polymers, foams, and other pressure-dependent materials in finite element analysis. The Drucker-Prager yield criterion has the form:

$$\sqrt{J_2} = A + BI_1 \tag{2.10}$$

where I_1 is the first invariant of the Cauchy stress and J_2 is the second invariant of the deviatoric part of the Cauchy stress. The constants A, B are determined from experiments. The Drucker-Prager yield surface is a smooth approximation of the Mohr-Coulomb yield surface.

2.7 Discrete element method

Developed in 1970s, DEM has proved to be able to analyse multiple interacting deformable continuous, discontinuous or fracturing bodies, undergoing large translations and rotations. The primary merits of this method lie in its ability to handle a wide range of material constitutive behaviour, interaction laws and arbitrary geometries. Several numerical issues in DEM implementation are described in this section.

2.7.1 Contact Models

When a contact takes place between two particles, they mutually affect each other's movement. The relative displacement and interactive forces can be represented by associating a contact model with each contact. To describe various particle to particle and particle to boundary interactions, contact models acting at a particular contact include several elements, such as stiffness and slip formulations. The principal theories of three contact models used in the current DEM simulations are briefly outlined.

2.7.1.1 Linear contact model

The linear contact model provides an elastic relation between the contact force and relative displacement, as defined by the normal and shear stiffnesses of the two contacting bodies (between two particles or between a particle and a boundary), which is shown schematically in Figure 2.11. The normal contact force is linearly proportional to the magnitude of the overlap at the contact, while the tangential contact force is linearly proportional to the cumulative tangential displacement at that contact point. The normal K_n and shear contact stiffness K_s for the linear contact model are given by:

$$K_n = \frac{k_n^{[A]} k_n^{[B]}}{k_n^{[A]} + k_n^{[B]}} \tag{2.11}$$

$$K_s = \frac{k_s^{[A]} k_s^{[B]}}{k_s^{[A]} + k_s^{[B]}} \tag{2.12}$$

where the superscripts $[A]$ and $[B]$ denote the two particles in contact.

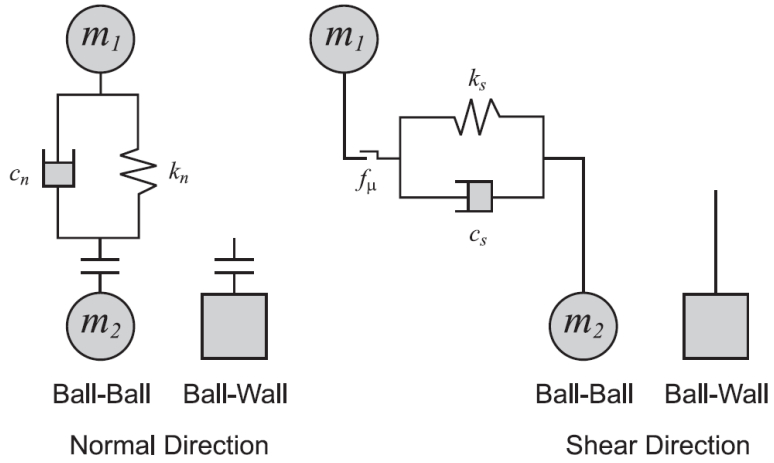

Figure 2.11: Linear contact model in PFC3D (Itasca Consulting Group Inc, 2003)

2.7.1.2 Hertz-Mindlin with no slip contact model

Hertz-Mindlin no-slip contact model, with damping and a frictional slider in the tangential direction (Tsuji et al., 1992), is a set of non-linear contact formulations as illustrated in Figure 2.12. This contact model has been largely adopted in both academic codes and commercial packages. The normal and shear contact stiffnesses are given by:

$$K_n = \left(\frac{2 \langle G \rangle \sqrt{2\widetilde{R}}}{3(1 - \langle \nu \rangle)} \right) \sqrt{U^n} \tag{2.13}$$

$$K_s = \left(\frac{2 \left(\langle G \rangle^2 3(1 - \langle \nu \rangle) \widetilde{R} \right)^{1/3}}{2 - \langle \nu \rangle} \right) |F_i^n|^{1/3} \tag{2.14}$$

where U_n is the sphere overlap and $|F_i^n|$ is the magnitude of the normal contact force. For a particle to particle contact, the coefficients $\widetilde{R}$, $\langle G \rangle$ and $\langle \nu \rangle$ are given

by

$$\widetilde{R} = \frac{2R^{[A]}R^{[B]}}{R^{[A]} + R^{[B]}} \tag{2.15}$$

$$\langle G \rangle = (G^{[A]} + G^{[B]})/2 \tag{2.16}$$

$$\langle \nu \rangle = (\nu^{[A]} + \nu^{[B]})/2 \tag{2.17}$$

and for a particle to wall contact, the coefficients are given by:

$$\widetilde{R} = R^{particle} \tag{2.18}$$

$$\langle G \rangle = G^{particle} \tag{2.19}$$

$$\langle \nu \rangle = \nu^{particle} \tag{2.20}$$

where G is the elastic shear modulus, ν is Poisson's ratio and R is particle radius.

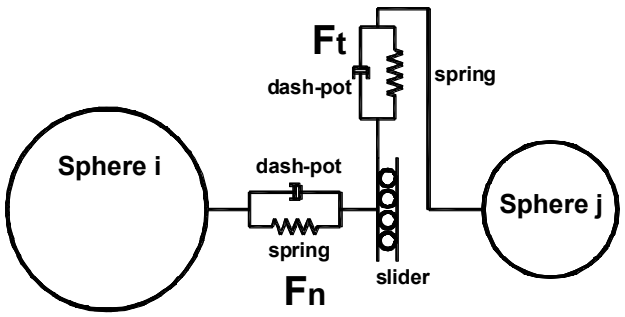

Figure 2.12: Spring dashpot contact model

2.7.1.3 Bonding model

Interparticle bonding is one of the key features in most geotechnical materials. To date, limited experimental work has been reported regarding the bonding phenomena in soil mechanics. This is mainly due to the lack of quantitative measurement within the sample. DEM provides an effective and convenient approach

to explore the bonding effect at particle level. The bonds can be envisioned as a glue joining the two particles. Numerically, bonding failure occurs if the tension or shear resistance at a contact reaches to its critical value. PFC^{3D} allows particles to be bonded together at contacts, where two bonding models are supported: a contact-bond model and a parallel-bond model. A full numerical implementation of these models are covered in the user's manual of PFC^{3D} (Itasca Consulting Group Inc, 2003).

2.7.2 Numerical implementation

The analytical procedure in DEM simulation consists of three major computational steps: internal force evaluation, in which contact forces are calculated; integration of equations of motion, in which element displacements are computed; and contact detection, where new contacts are identified and broken contacts are removed. These particle interaction is treated as a dynamic process which requires cyclic calculations. The step-by-step integration procedure is typically as follows:

1. The positions and velocities of all particles are known at time t_{n-1}. The normal force and displacement for each contact are given and the tangential force and displacement for each contact are also given at time t_{n-1};

2. The updated normal and tangential displacements at time t_n are calculated over a small time step. The updated normal and tangential forces at time t_n can then be evaluated according to the force-displacement contact model;

3. The forces and moments that act on each particle at time t_n are summed;

4. The positions and velocities of all particles at time t_n are calculated by integrating the equations of motion of particles numerically.

The above operations are repeated for each time step so that the motion of each particle can be determined and updated. In this procedure there are several important aspects including the contact force model, the representation of non-spherical particles, critical time step, contact detection, etc. The aim of this chapter is not to describe the DEM general methodology in details as this has been described many times before in the literature, but to discuss the key issues which are important in producing satisfactory numerical simulations.

2.7.3 Computational time step

DEM simulates granular assembly at particle scale, in which the position, translational and rotational velocity, forces and torques acting on each individual particle are calculated by explicit integration of Newton's equation of motion over a certain time step. Although this explicit numerical scheme is more computationally efficient than the implicit numerical scheme, there is a limitation that it is only conditionally stable, so small time steps must be used. If the adopted time step is greater than a critical time step, the scheme is unstable and the simulation outcomes are unreliable. Therefore, the determination of the computational time step is crucial for numerical stability and for keeping computing effort to a manageable level.

In an assembly of particles, the force transmission between individual particles is through the Rayleigh wave that travels around the surface of elastic bodies. The criterion to determine a time step for DEM simulations is that the time step for calculating the incremental forces and displacements must be less than the time it takes for the wave to transverse the minimum size particle in the assembly. The Rayleigh wave velocity of force transmission is given by (Johnson, 1985):

$$V_R = (0.1631\nu + 0.8766)\sqrt{\frac{G}{\rho}} \tag{2.21}$$

where where G is the shear modulus, ρ is particle density and ν is Poisson's ratio. Provided that the properties of all constituent particles are the same, the critical time step Δt_c is therefore given by

$$\Delta t_c = \frac{\pi r_{min}}{0.1631\nu + 0.8766}\sqrt{\frac{\rho}{G}} \tag{2.22}$$

where r_{min} is the radius of the minimum size particle in the assembly. For an assembly consisting of different material type particles, the critical time step should be the smallest among those determined by different material properties. It should be noted that Equation 2.22 is the simplified formula for estimating the critical time step. The actual computation time step used in DEM simulations is normally chosen by multiplying the critical time step with a fraction. Itasca Consulting Group Inc (2003) suggested that the critical time increment should be multiplied by a safety factor with a default value of 0.8. In the present study, a multiplier for critical time step was set as 0.2 for all DEM simulations reported. This value was chosen to balance computational accuracy with computational speed. Choosing a multiplier that is larger than 20% speeds up the calculation but may lead to increasing numerical inaccuracy.

2.7.4 Rolling friction

Particle level parameters in a contact law, such as friction coefficient are important in accurate simulation of granular media. Conventional DEM models use springs and dampers in the normal and tangential directions to describe particle to particle and particle to boundary interactions. According to Coulomb theory, sliding friction occurs at a contact when

$$|F_s| > \mu F_n \tag{2.23}$$

where μ is the coefficient of sliding friction. However, this does not account for the rotation of particles. Extensive research in physical experiments (Calvetti et al., 1997; Oda et al., 1982) and numerical studies (Bardet, 1994; Iwashita and Oda, 1998), has suggested that circular or spherical particles have little resistance to shear or frictional forces. Without incorporating a torque in the rotational direction to account for the rolling resistance, these forces cause the particle microstructure to yield prematurely.

Ai et al. (2008) extensively reviewed a number of existing rolling friction models in the literature, and the robustness of these models in reproducing rolling resistance effects arising from several physical conditions was assessed through several testing cases. Furthermore, a new rolling friction model which is more general and suitable for modelling problems ranging from both dynamic and pseudo-static regimes was proposed. There were two key components in this innovative model: a mechanical spring torque (dependent on the relative rotation between the two contacting entities) and a viscous damping torque.

In the current DEM implementation, rolling friction is not thoroughly implemented in the contact laws unless specified. Instead, particle shape (non-sphericity in 3D or non-circularity in 2D) is introduced to account for the effects of rolling resistance, which has been widely adopted in previous DEM simulations (Bagi and Kuhn, 2004; Lin and Ng, 1997; Morgan, 2004).

2.7.5 General representation of granular materials

The accuracy of DEM model largely depends on the input parameters. These parameters include the physical properties (mass, density and geometric shape parameters) and mechanical properties (Young's modulus, Poisson's ratio, friction coefficient, coefficient of restitution) of the grains. The input parameters used in DEM simulations were often simply given without any explanation as to

where they came from, and seldom measured in laboratory tests, so the influence of the input parameters on the prediction outcomes can be rather obscure. In order to acquire meaningful results, it is essential that the parameters involved in the model are either carefully determined, or the effect of assuming certain values for these parameters is carefully explored. Chung (2006) carried out a comprehensive study in developing methodologies and experimental apparatuses to measure physical and mechanical properties of several particles, including corn, wheat and glass beads. This work provides a database of measurement which can be used for a wide range of granular dynamics.

One essential aspect in the representation of granular materials is particle shape. Traditional approaches in DEM have modelled particulate sample as an assembly of 2D discs or 3D spheres. Due to the higher tendency to rotate of circular or spherical particles, the resulting angle of internal shearing resistance is much less than that of actual particle, which can easily lead to a rather weak packing structure. Additionally, most particles in industrial applications are not spheres at all. The inclusion of non-spherical particles into DEM models is therefore crucial for an accurate simulation of real particle behaviour, with implications for contact detection algorithm and method for calculating contact forces, which in turn influence the computational efforts required for simulations.

The effect of particle shape has been investigated by many researchers. Currently, there are two-dimensional models available with particles as circular discs, ellipses and polygons and three-dimensional models with particles as spheres, blocks/bricks, and ellipsoids. Figure 2.13 illustrates various shapes used in previous DEM simulations. Cleary and Sawley (2002) studied the effect of particle shape on hopper discharge. In their DEM study, circular particles were found to always lead to mass flow, whereas elongated particles were shown to increase resistance to flow and produce much lower flow rates. Furthermore, complex microstructure fabric was generated within the sample of non-spherical particles,

which essentially developed funnel flow pattern. Guo and Morgan (2004) carried out DEM simulations of granular materials under shear using irregularly shaped grains. It was shown that significant grain interlocking contributed to a higher system dilation and frictional strength. The results also suggested an inverse power law relationship between normal stress and maximum sliding friction, in which both the coefficient and exponent were dependent on particle angularity.

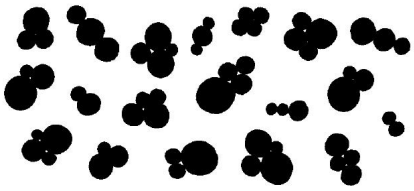

(a) 2D disk clusters (Thomas and Bray, 1999)

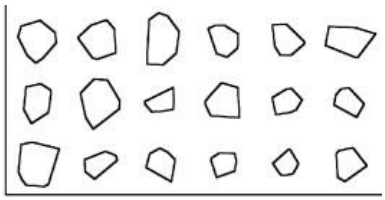

(b) 2D polygons (Nouguier-Lehon et al., 2005)

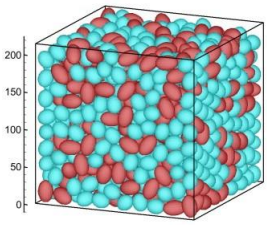

(c) 3D ellipsoids (Ng, 2004)

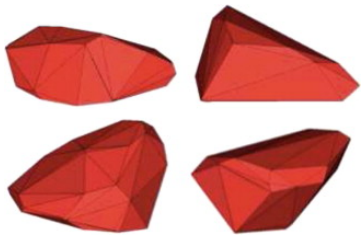

(d) 3D polyhedra (Azéma et al., 2009)

Figure 2.13: Non-spherical particles used in DEM simulations

Among all the algorithms of particle shape representation, the multiple sphere method using a set of rigidly linked and inscribed element spheres is the most prevalent method to simulate non-spherical particles. These spheres may be of different diameters and may overlap to any extent. The number, radii and positions of the spheres used to represent the particle govern the degree of approximation to the actual particle surface contour. The number of overlapping spheres depends on:

- the degree of non-uniformity and angularity in the original particle shape;
- the desired level of geometric accuracy;
- the computational time and resource limitation.

In the multiple sphere method, contact detection between particles is sphere-based and any optimisation procedures developed for resolving sphere-sphere contact in DEM are completely applicable. The normal and tangential contact forces can then be calculated using standard discrete element formulation for spherical system. Contacts between these spheres inside the particle are skipped during the calculation cycle, resulting in a saving of computer time compared to a similar calculation in which all contacts are active. Figure 2.14 shows an application of multiple sphere method in the representation of corn shape. It can be clearly observed that increasing the number of spheres in a particle will produce a more accurate physical representation, which indeed meanwhile increases the computation time.

Throughout all the DEM simulations in the current study, non-spherical particle was created by overlapping two uniform spheres together to give an aspect ratio of 1.5 (Figure 2.15). This shape representation does not dramatically increase the consumption of computational resource, while being able to introduce sufficient "angularity" to distinguish from spherical particles.

2.7.6 DEM codes

Since the first application of DEM to simulate the dynamic behaviour of granular solids in the 70-ies, there has been a large number of codes developed by research institutes and some of them have been launched as commercial softwares.

1. Commericial package:

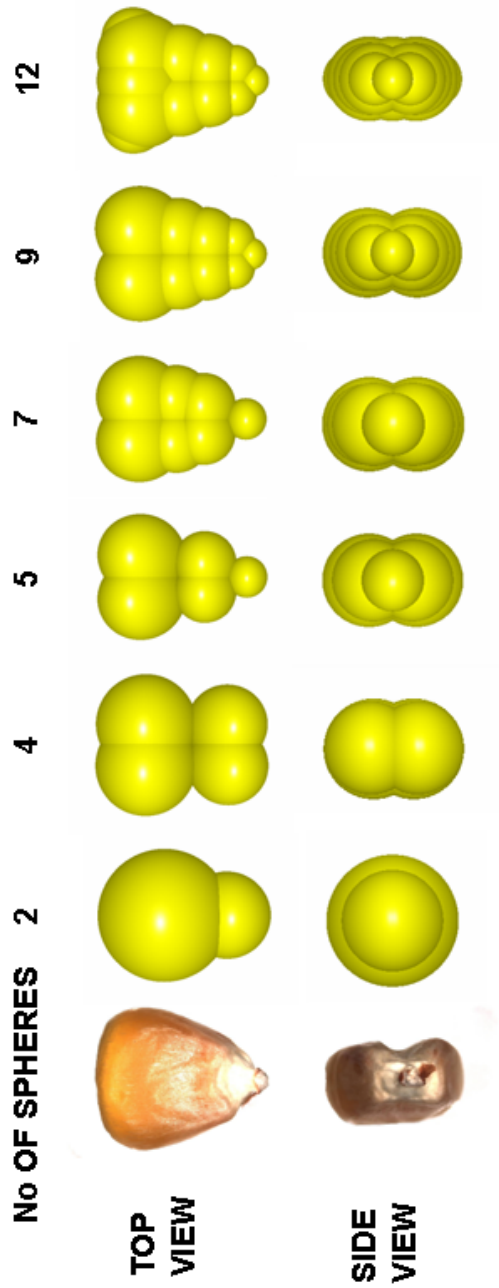

Figure 2.14: Multiple sphere method in representation of corn shape

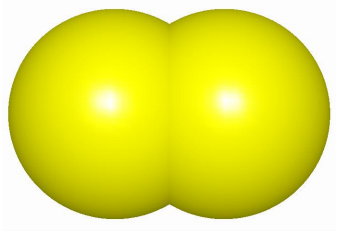

Figure 2.15: Non-spherical particles (aspect ratio=1.5) used in the current DEM simulations

- Itasca PFC$^{2D/3D}$ (Particle Flow Code in two/three Dimensions) are the most prevalent DEM codes to date. PFC^{2D} uses BALL codebase, whereas PFC^{3D} adopts TRUBAL codebase.
- EDEM was firstly launched by DEM Solutions Ltd in 2001. EDEM is a general-purpose DEM programme with CAD import of particle and machine geometry, GUI-based model set-up, extensive post-processing tools, programmable API, couples with CFD, FEA and MBD software.
- Chute Maven (Hustrulid Technologies Inc.) simulates granular system using spherical particles in three dimensions. It can directly reads in AutoCad dxf files and interfaces with SolidWorks.

2. Open source and academic codes:

- ESyS-Particle is a high-performance computing implementation of the DEM released under the Open Software License. Its major applications to date include granular flow, rock breakage and earthquake nucleation. The DEM computing engine is written in C++ and parallelised using MPI, permitting simulations of more than one million particles.
- BALL & TRUBAL are DEM codes written in Fortran, originally developed by Peter Cundall and currently maintained by Colin Thornton at University of Birmingham.

- ELLIPSE3D code developed by Lin and Ng (1997) has a high capability to simulate ellipsoidal particles.

Among all these available DEM codes, Itasca PFC^{3D} was chosen in the current thesis. Rather than codes built in black boxes, it is an open software with flexible platform to suit a wide range of multiphysical problems. The user can access to almost all internal variables via the powerful *FISH* programming language. In the results reported below, unless specifically mentioned, all the simulations are performed in PFC^{3D}.

2.7.7 Limitations of DEM

A major drawback of DEM is its intensive computational requirement, which limits either the length of a simulation or the number of particles. Also, to date, there is no satisfactory solution to incorporate complex particle shape, pore pressure and crushing mechanism. Additionally, the main output from DEM is the local contact information (e.g. displacement and inperparticle force), which may not be easily considered in engineering practice. Provided this scale separation holds, averaging techniques need to be developed to derive homogenised quantities (e.g. stress and strain) characterising the continuum behaviour of the assembly. Notwithstanding the limitations abovementioned, DEM is still an effective approach to advance the knowledge and provide complementary insight into the physics and mechanics of granular solids.

2.8 Measurement spheres in Itasca PFC^{3D}

A number of quantities in a PFC^{3D} model can be defined with respect to a specified measurement volume, such as stress, strain rate, coordination number and porosity etc. This homogenisation algorithm is numerically implemented

within a spherical measurement volume, referred as a "measurement sphere".

Considering stress, which cannot be defined at each point in a particle assembly, is calculated in terms of an average stress tensor. In a PFC^{3D} model, only the particles with centroids that are contained within the measurement sphere are considered in the computation of the average stress tensor. In order to account for the additional volume of particles that is being neglected, a correction factor, based on the porosity, is applied to the computed value of stress. The final expression of Equation 2.3 used in PFC^{3D} to compute the average stress tensor within a measurement sphere is:

$$\bar{\sigma}_{ij} = \frac{n-1}{\sum_{N_p} V^{(p)}} \sum_{N_p} \sum_{N_c} \left| x_i^{(c)} - x_i^{(p)} \right| n_i^{(c,p)} F_j^{(c)} \tag{2.24}$$

where the summations are taken over the N_p balls within the centroids contained within the measurement sphere and N_c contacts of these balls;

n	is the porosity within the measurement sphere;
$V^{(p)}$	is the volume of particle (p);
$x_i^{(p)}$, $x_i^{(c)}$	are the locations of a particle centroid and its contact, respectively;
$n_i^{(c,p)}$	is the unit normal vector directed from a particle centroid to its contact location; and
$F_j^{(c)}$	is the force acting at contact (c) arising from both particle contact and parallel bonds.

The algorithm of "measurement sphere" in PFC^{3D} is implemented and illustrated in a DEM simulation of confined compression test. In many engineering applications, the constrained response of granular materials under loading is most important. Snapshots of a particulate system containing 8000 non-spherical particles before and during the confined compression are shown in Figure 2.16.

It is clear that particles are confined in a quasi-static configuration, therefore

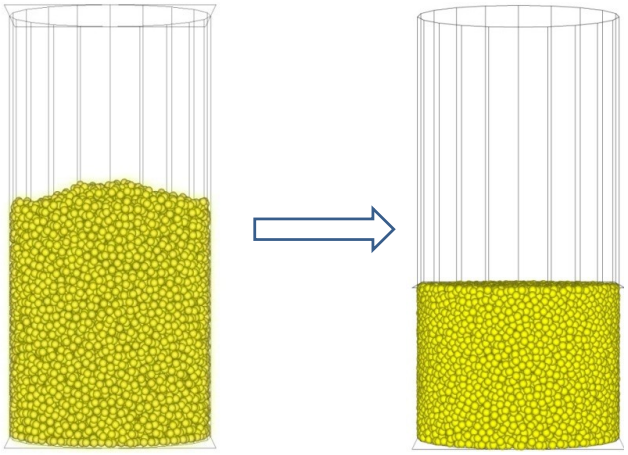

Figure 2.16: Example snapshots of confined compression test

the measurement spheres can be used to derive some continuum results to describe the mechanical state in a quantitative manner. A single layer of measurement sphere was placed along the central plane of the assembly as shown in Figure 2.17. The diameter of the measurement sphere was set as five times larger than the one of particle itself, to ensure the averaging is performed over a representative volume. The measured quantities include the stress and strain rate in vertical z direction, as well as the porosity. Figure 2.18 shows the contour plots of the three quantities obtained from measurement spheres. As the external loading was applied by moving the top platen downwards with a constant velocity, therefore there is a strong concentration of vertical stress observed beneath the surface of top loading platen. However, the distributions of strain rate and porosity showed no clear pattern, which reiterate the inhomogeneous nature of the deformation in granular media.

The measurement sphere does provides a useful averaging procedure to make the step from the micro-scale to a continuum. There is however no information given on how large the measurement volume in relation to the particle diameter

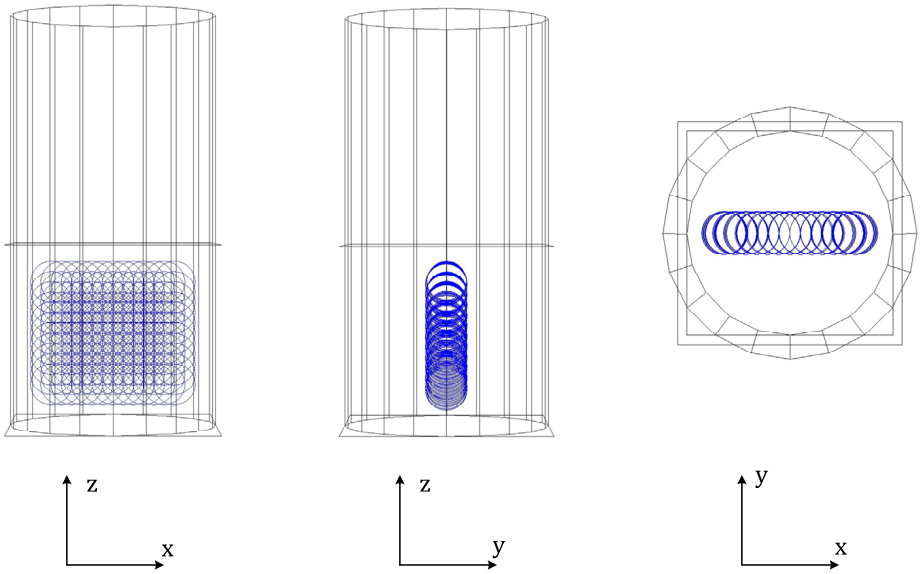

Figure 2.17: Placement of measurement spheres

should be to obtain meaningful and representative results. Haertl (2008) explored the effect of averaging volume in obtaining representative results. As shown in Figure 2.19, an enclosed cube was filled with 1,000 spherical particles using the radius expansion filling method. After an initial isotropic sample was achieved, it was slowly compressed from all sides by moving each side wall towards the cube centre. Measurement spheres with sizes ranging from 1 to 9 particle diameters (d_p) were placed in the centre of the cube to calculate the stress value.

The calculated vertical stress using different sizes of measurement spheres are shown in Figure 2.19 at three loading stages. It clearly suggests that a measurement sphere with radius of 3 particle diameter is sufficient to reach a steady value of vertical stress, and no significant changes were observed beyond this averaging volume. Muir Wood (2004) pointed out that stress is only relevant at a scale considerably larger than the individual particles and the force chains. The influence of averaging length scale will be further investigated in the rest of the thesis.

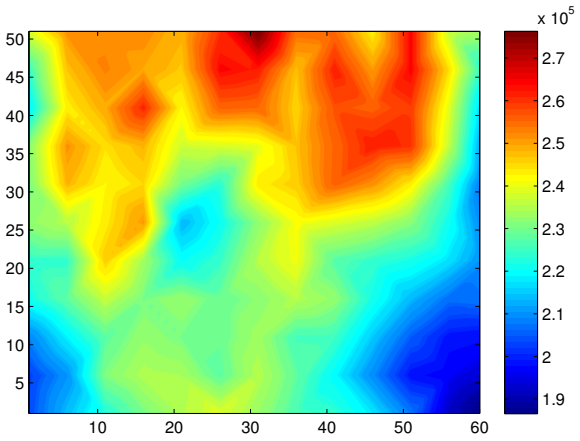

(a) Stress σ_z

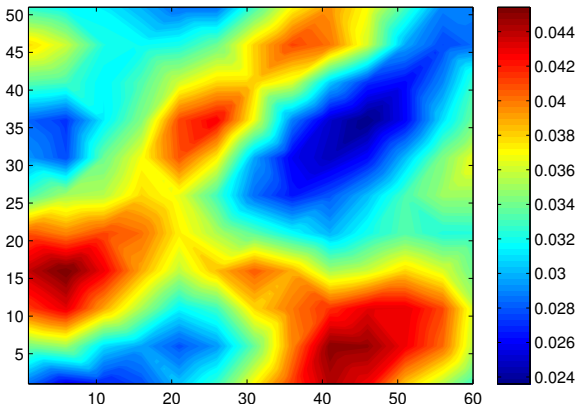

(b) Strain rate $\dot{\epsilon}_z$

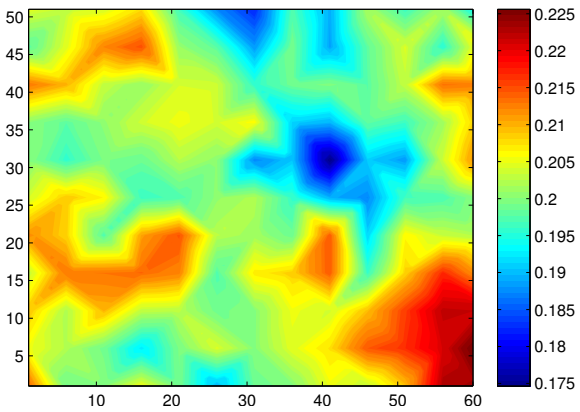

(c) Porosity

Figure 2.18: Contours of quantities calculated within measurement spheres

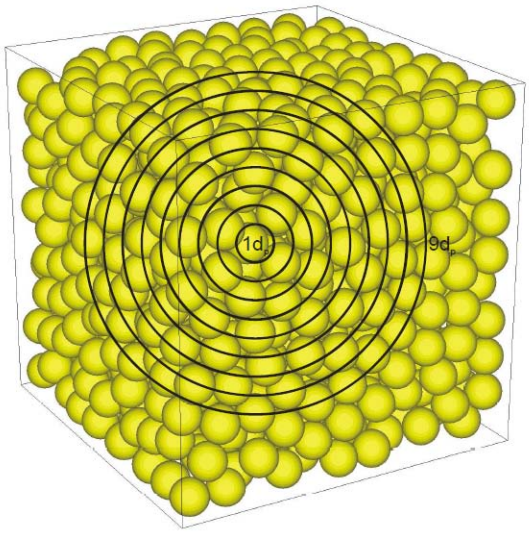

(a) Placement of measurement spheres in the cube

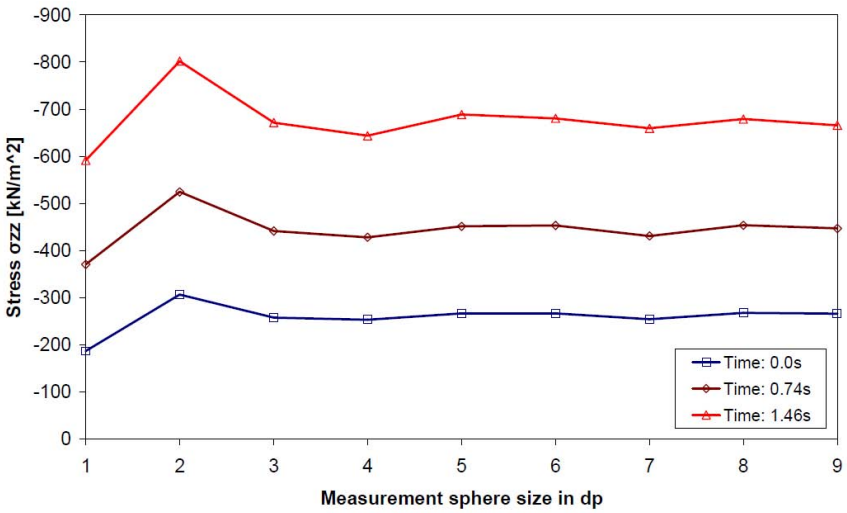

(b) Measured vertical stress measurement spheres with different radius

Figure 2.19: Measurement spheres in a uniformly compressed cube (Haertl, 2008)

2.9 Power spectral analysis of DEM output

Since DEM simulations can easily employ up to hundreds of thousands of particles, two significant issues arise in tackling with the DEM results. First of all, as it is impractical to output all the quantities at every computational time step, the time interval (frequency) to output the desired data becomes critical; Secondly, the abundance of time-series data from DEM simulations poses challenges in developing numerical processing tools to extract the key information of special interest. Smith et al. (2001) utilised Fast Fourier Transforms (FFT) to investigate periodicity throughout the formation of 2D granular piles at different feeding rates. Tuzun et al. (2004) applied wavelet analyses to capture the variations in periodicity and the relative sequence of evolution of the stress and voidage states in avalanching granular heaps and hopper flows. These studies highlight the potential to investigate the temporal evolution of DEM output and to identify interesting phenomena based on the filtered data.

In this section, a preliminary application of power spectral analysis is carried out to investigate the frequential characteristics of DEM output data. The power spectral density (PSD), describes how the variance of an analog signal is distributed with frequency. Mathematically, it is defined as the Fourier Transform of the autocorrelation sequence of the time series. An equivalent definition of PSD is the squared modulus of the Fourier Transform of the time series, scaled by a proper constant term. Two examples are presented to demonstrate the application of power spectral analysis of DEM results, including the wall pressure development in a silo and the base resistance in penetration test.

- The data used in the first example comes from the DEM study of flow pattern and wall pressure in silos, carried out by Haertl (2008). Significant fluctuations in the measured wall pressure during silo filling and discharge have been widely reported from both experiments (Zhong et al., 2001) and

numerical simulations (Holst et al., 1999). In Figure 2.20, the silo geometry and the time series of normal pressure on each wall segment throughout the whole filling and discharge courses are shown, in which the DEM data was output at a frequency of 200Hz. It can be observed that the wall pressure development is far more from smooth. Zhong et al. (2001) pointed out that the extent of the scatter indicates the extent of asymmetry in the silo's response to the pressures, but a high peak value does not necessarily correlate precisely with the change in pressure.

- The data used in the second example comes from the DEM simulation of penetration tests (Figure 5.2), which is part of the current thesis and will be explored in much more detail in Chapter 5. The loading-displacement curve (Figure 2.22a) shows an initial linear increase, followed by a more gradual and moderate increase after the bearing capacity was reached. The frequency of the numerical output in this DEM simulation was 1000Hz.

DEM results from both examples exhibit significant numerical fluctuation, which are well suited to the power spectral analysis, giving the answer that whether a periodicity exists in the DEM outcome. Figure 2.21 and 2.22 show the range of continuous data used for power spectral analysis in the raw DEM output, in conjunction with the plots of power spectral density in its frequency domain. Results from both examples are quite similar, with only one estimated peak occurring at zero frequency and suggesting no periodicity embedded in the DEM time-series data. To gain further insight into the inherent nonlinearity and discontinuity of granular materials, the underlying mechanism leading to the spatial inhomogeneities and temporal fluctuations needs to be elucidated. Meanwhile, it also highlights the importance of appropriate averaging schemes (e.g. spatial and temporal smoothing operator) in post-processing the DEM results, which will be discussed later in this thesis.

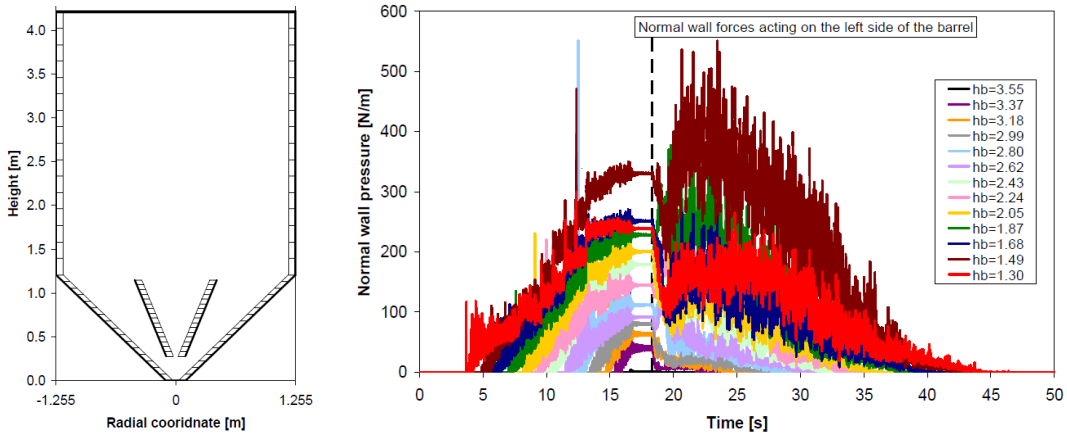

Figure 2.20: Silo geometry and normal wall pressure (Haertl, 2008)

2.10 Single layer model

Plane strain problems occur frequently in geotechnical engineering. Long structures like embankments, retaining walls and strip footings, with loading in the plane of the cross-section, are frequently approximated to be in plane strain conditions. To simulate these problems and to reduce the number of particles in the numerical model, a representative single layer of the physical assembly will be implemented in the current PFC^{3D} simulation. All particles were generated to fall randomly with particle centres aligned in a vertical plane. The non-spherical particles were generated with random orientation of the particle longitudinal axis in the prescribed plane. It thus represents a pseudo 3D model where particle movements only occur in the vertical x-z plane. Figure 2.23 shows an example of this single layer model in three-dimensional DEM simulation, viewing from two perspective angles. It should however be noted that this is only an illustrative representation of all the physical models, since particle interaction is indeed three dimensional in nature. Nevertheless, this single layer model is sufficiently simple to produce certain amount of information within reasonable computational resources, and it does provide useful insights into the behaviour of granular solids

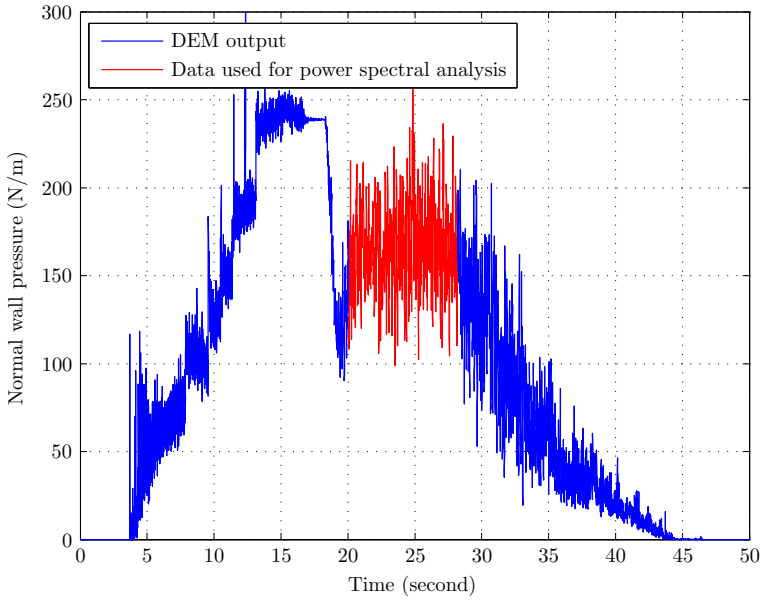

(a) Development of normal wall pressure during filling and discharge

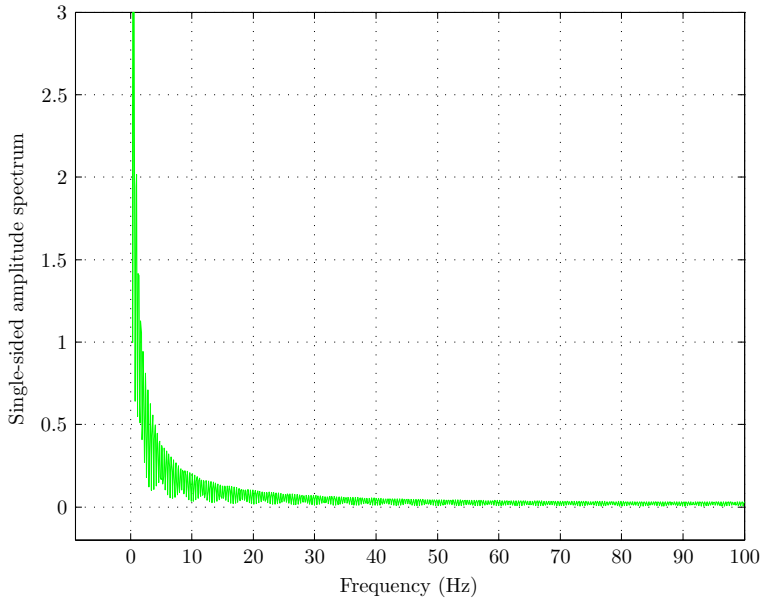

(b) Power spectral density

Figure 2.21: Power spectral analysis of DEM results from silo simulation

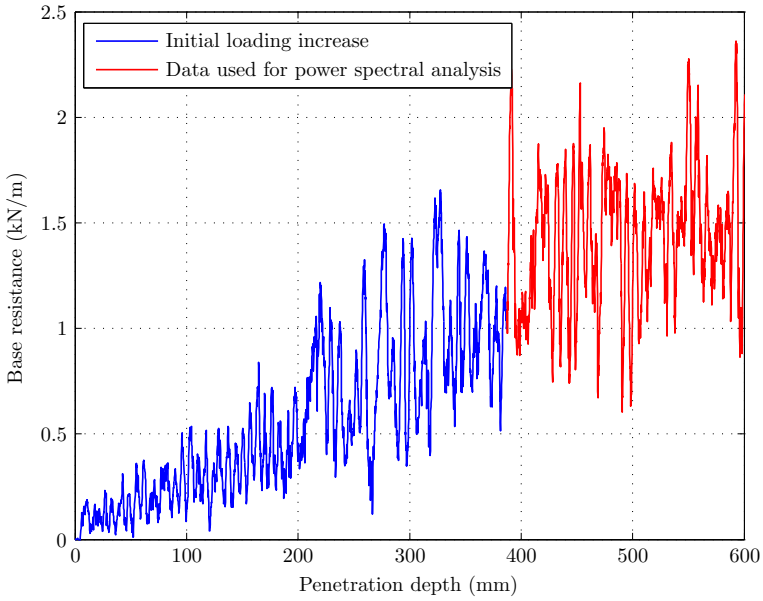

(a) Loading-displacement curve during penetration

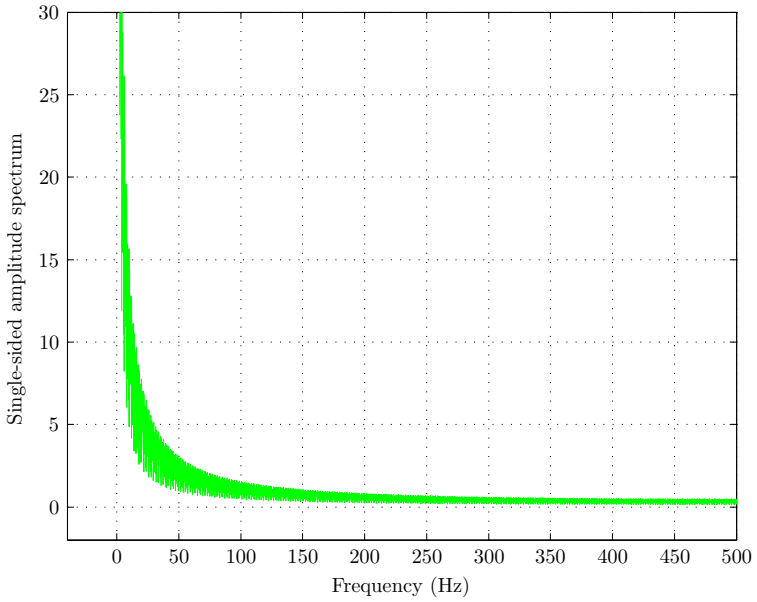

(b) Power spectral density

Figure 2.22: Power spectral analysis of DEM penetration results

under various loading conditions. Therefore, unless else specified throughout the whole thesis, all the DEM simulations will be performed by employing this single layer modelling technique.

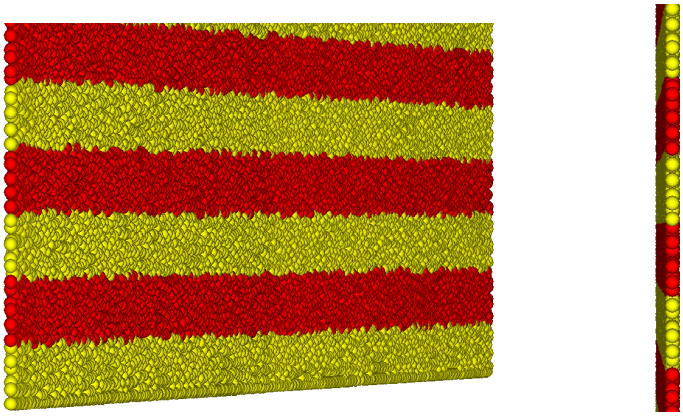

Figure 2.23: Single layer model in three-dimensional DEM code

2.11 Summary

In this chapter, a wide range of issues relating to the mathematics and mechanics of granular solids were briefly discussed. Description of several analytical techniques to characterise the micromechanical variations during loading and deformation, as well as the key references have been presented. Special attention was given to particle packing structure, homogenisation scheme and force propagation within granular systems. Meanwhile, Particle Image Velocimetry, which is an optical tool to measure the deformation of particulate solids, is carefully introduced and demonstrated. These numerical interpretive techniques will be used throughout the whole thesis. A brief review of DEM was also presented in this chapter. Several key issues that are important for achieving satisfactory DEM predictions have been discussed. Itasca PFC^{3D} is selected to perform DEM simulations in the current thesis. To speed up the simulation, a multiplier for critical

time step is set as 0.2. A number of contact laws which will be employed were outlined. In the representation of non-spherical particles, two uniform spheres were overlapped together giving an aspect ratio of 1.5.

Chapter 3

DEM simulations of granular materials under biaxial compression

3.1 Introduction

Prior to the development of computational simulations, researchers have conducted extensive physical tests to advance the understanding of soil response. Various types of test can be carried out, including monotonic strain controlled test, isotropic and anisotropic consolidation test, dynamic shear strength test, loading path test, cyclic loading test etc. Among these experimental approaches, biaxial test is a common method to measure the mechanical properties of granular solids and powders, such as sand, clay, and other industrial powders. Due to the relative simplicity, versatility, and the degree of controlled deformation which it allows, the biaxial test is one of the most useful in situ tools for characterising the stress-strain-dilation behaviour of granular materials in the past several decades.

Noticeably, significant strain localisation can be observed in biaxial compression test. In soil mechanics, strain localisation refers to the failure of a soil specimen along a well-defined plane of highly localised shear strain, which is mostly

observed as the form of shear bands spanning over several grain diameters in width. The phenomenon of shear band is an important element in understanding the failure mechanism of granular solids, which has been extensively studied theoretically and experimentally. However, it remains technically challenging to capture the micro-processes taking place inside shear bands through experimental measurement, while classical continuum approaches fail to account for the dimension of the shear band due to the absence of an intrinsic lengthscale. Therefore, in spite of the abundant research reported in the literature, the micro-deformation mechanism leading to the development of shear bands is still not yet clearly understood. In this chapter, DEM is adopted to examine the influence of several factors on the phenomenon of strain localisation in dense granular packings subject to biaxial compression. This study seeks to understand the failure mechanism at particle scale by investigating the evolution of the sample microstructure before, during and after the strain localisation event.

The chapter is organised as follows. Firstly, a brief literature review is presented. The basic elements of DEM deployed are then outlined, followed by the presentation and discussion of the simulation results from biaxial compression with different particle shape and contact frictions. Furthermore, the underlying failure mechanisms regarding the bifurcation instability are interpreted by extracting key micromechanical quantities of interest, such as void ratio, particle rotation, contact orientation and force chains. Finally, in order to bridge a link between particle scale information and constitutive response, both stress and strain within the granular sample are derived from particle displacement and contact forces at increasing strain levels.

3.2 Literature review

Strain localisations in granular materials have been extensively investigated using laboratory tests, analytical methods and numerical simulations. In this section, the primary findings in the literature are presented and summarised.

3.2.1 Experimental study

The biaxial and triaxial tests are the most commonly used apparatuses in soil mechanics to determine soil characteristics. Figure 3.1 shows a typical apparatus of biaxial test, where the boundary displacements and stresses are measured by load cells and linear voltage displacement transducers (LVDT). Proper experimental evaluation of shear band evolution plays an important role in the formulation of instability theory and validation of numerical calculation. The majority of previous experiments of soils under plane strain compression have mostly relied on boundary measurement only. More recently, a variety of non-intrusive measurement have been developed for granular systems, which includes particle tracking, diffusive wave spectroscopy and X-ray imaging etc. These techniques offer powerful capability to capture grain-scale processes and significantly advance the knowledge in granular mechanics. Several representative experimental work in this scope will be outlined below.

Oda and Kazama (1998) examined the microstructure of shear bands in Toyoura and Ticino sands by means of X-ray and optical measurements. Their results revealed that particle orientation changes significantly near the boundaries of shear band, which explained the fact that a high gradient of particle rotation developed within a narrow zone during the shear band formation. Additionally, images containing two-dimensional assembly of photoelastic oval rods showed column-like structures started to buckle at peak stress and tended to take place mainly within shear bands. Desrues and Viggiani (2004) summarised a large

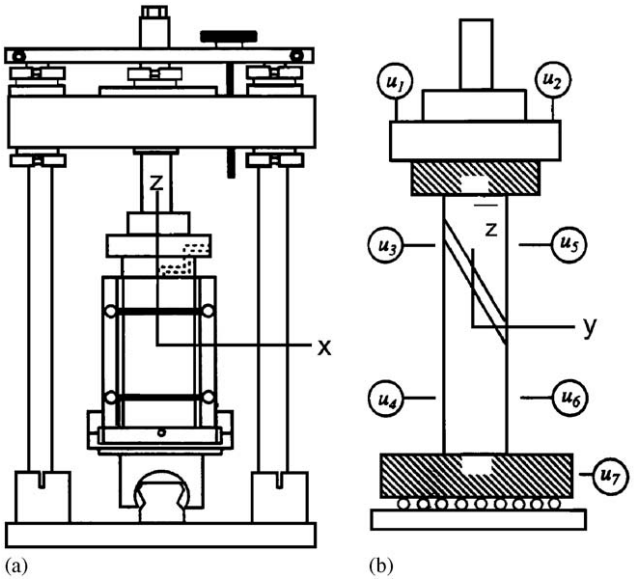

Figure 3.1: Schematic of plane strain testing apparatus (Harris et al., 1995a): (a) out of plane view: axial rod support frame, specimen, platens, base sled, and sidewalls; (b) in plane view and LVDT positions(u_i).

amount of experimental research in drained plane strain compression tests on loose and dense Hostun sand. Stereophotogrammetry was utilised to quantitatively and to interpret the findings concerning the occurrence and progression of strain localisation. A thorough and critical discussion of the influence of some key variables, such as initial specimen size and slenderness, mechanical state of the sample (effective stress and relative density), as well as grain size and distribution, was presented. This rather comprehensive study well documented a large body of experimental data with regard to temporary and persistent strain localisation. More details reported from this work will be discussed later and compared with the current DEM predictions in the subsequent sections.

3.2.2 Analytical theory and constitutive modelling

Rice (1975) first proposed the bifurcation theory to explain the strain localisation phenomenon, i.e. the deformations migrate from a continuous mode to both continuous and discontinuous modes, where a unique mathematical description of material behaviour cannot be obtained. Vardoulakis and Sulem (1995) reviewed the experimental and theoretical aspects of bifurcation analysis in geomechanics. The book covered the principles of continuum mechanics of bifurcation and stability analyses applied to layered geological media and granular materials, and theories for generalised continua as applied to materials with microstructure and in relation to strain localisation phenomena. Indeed, the simulation results from constitutive modelling strongly depend on the constitutive relation employed and the quantity of the constitutive parameters involved. Anand and Gu (2000) implemented a "double-shearing" constitutive model to predict the formation of shear bands in plane strain compression and plane strain expansion of a cylindrical cavity. The model provided a physically-based flow rule to capture the typical dilatant and hardening/softening response observed in granular materials. The values of the material parameters in the constitutive model were adjusted using a trial-and-error method to match the experimental data. A weak element was assigned in the centre of the specimen, serving as a nucleation site for the shear band. The numerical calculations were shown to be in good quantitative agreement with the corresponding experiments on localisation in a dry Ottawa sand under low pressure conditions.

3.2.3 DEM simulation

Whilst considerable amount of information about the soil response has been achieved using advanced measuring techniques from experiments, the measurement of certain quantities such as interparticle forces remains rather challenging.

DEM has proved to be a powerful numerical method for granular materials that explicitly models the interaction of individual particles. Consequently, a large number of DEM simulations have been performed in the past decades aiming to understand the micromechanism associated with strain localisation. Iwashita and Oda (1998) emphasised the role of rolling resistance in DEM simulation of biaxial test. Considering the rolling component in DEM contact model made it possible to reproduce some shear band features observed in experiments, such as large voids and high gradient of particle rotation inside the shear region. Antony and Kuhn (2004) carried out DEM simulations of triaxial compression by employing spherical, oblate and prolate particles. To study the sensitivity of distribution of contact forces to the local particle arrangements, a fabric tensor describing the contacts with normal forces greater than the mean was proposed. Mathematically, it was revealed that more than 50% of the lightly loaded contacts contributed little to the deviatoric stress, and the load was mainly transmitted by a sparse network of strong contacts. Pena et al. (2008) investigated the effect of the initial sample density and the interparticle friction on the bulk behaviour of a packing of polygonal particles under biaxial compression. The results showed that at large strains the samples reached a critical state regardless of the initial packing density, in terms of constant void ratio, volume and coordination number.

3.3 Numerical implementation of DEM model

3.3.1 Sample preparation

The granular assembly in the current study is composed of 8000 particles (for both spherical and non-spherical shape). Table 3.1 lists the material parameters used in this study. The sample was prepared by charging the particles into a plane section with a dimension of $400 \times 950mm$ under gravity. In order to make

the DEM simulations comparable between spherical and non-spherical samples, apart from the same particle number and initial undeformed sample dimension, it is also desired to achieve an equivalent level of effective consolidation stress. To meet this requirement, once the particles were generated and placed, the radius expansion method described in PFC^{3D} was used to obtain the target effective consolidation stress. In this dynamic approach, a population of particles with smaller radii than the target value are firstly generated randomly within a given volume, then the radii of all particles are expanded by the same factor until the expected mechanical phase is achieved. Overlaps between particles are consequently induced and then a number of DEM computational cycles are performed to bring the system into equilibrium. This radius expansion approach has been commonly used in many DEM simulations and confirmed that it was a valid approach to obtain an isotropic consolidation (Nguyen et al., 2009; Powrie et al., 2005; Yan et al., 2009). Here, all the particles were expanded until the target value of stress $\sigma_x = \sigma_z = 5 \times 10^3 N/m$ was reached, at which an isotropic force network can be observed (Figure 3.2). This confirmed that the radius expansion method is a computationally efficient technique of sample preparation, which allows the generation of a relatively homogeneous contact force network within a specified volume. After the expansion, the radius of constituent spheres in non-spherical particles is $3.1mm$. For spherical particles, to avoid the formation of crystalline structure in monosized spherical system, the particle size followed a linear size distribution, with radius of $3.5 \pm 1mm$ after expansion (Figure 3.3). The resulting initial void ratio in the sample with spherical and non-spherical particles is $e_s = 0.189$ and $e_{ns} = 0.160$, respectively. As reported from experimental work (Park et al., 2008) and numerical simulation (Pena et al., 2008), it can be expected that the lower initial void ratio generated in the non-spherical sample may exhibit a larger volumetric expansion due to stronger dilation, if compared to a spherical sample.

Table 3.1: Values of the DEM parameters used

Name of the variable	Symbol	Value
Particle density (kg/m^3)	ρ	3000
Normal stiffness of particle and wall (N/m^2)	K_n	$5e+06$
Tangential stiffness of particle and wall (N/m^2)	K_s	$5e+05$
Damping coefficient	B	0.8
Sliding friction between particle and particle	f_p	0.3, 0.9
Sliding friction between particle and base	f_w	0.1, 0.3

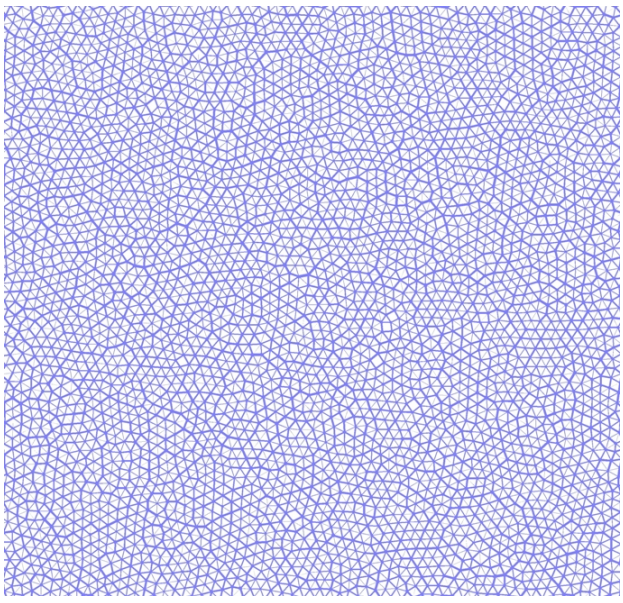

Figure 3.2: Force network after particle radius expansion

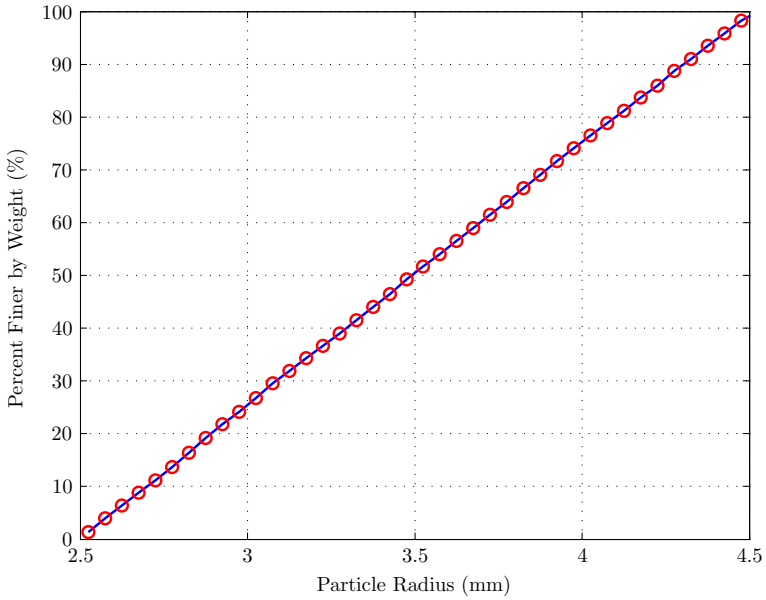

Figure 3.3: Grain size distribution of spherical particles

3.3.2 Boundary condition

The top and bottom loading platens were modelled as rigid walls, and the axial stress was applied by moving these two walls towards to each other with a constant velocity. In the horizontal direction, it is important to set up the side boundary condition properly in biaxial test, as it will significantly influence the bulk deformation and loading response. There are several types of boundary conditions popularly employed in the literature. Rigid boundaries (Thornton and Zhang, 2006) and periodic boundaries (Cundall, 1989) can be easily implemented in DEM, but they can restrain the development of shear band by restricting both particle motions and the natural nucleation of shear band tips. Force controlled boundaries can result in numerical difficulties when a small perturbation caused by particle reorientations, which makes the equilibrium difficult to maintain. In the current study, in order to mimic the experimental setup, the latex

membrane surrounding the granular sample was modelled by using strings of velocity-controlled bonded particles (Evans, 2005). To allow the membrane to deform around the particle assembly, bonding contact model in PFC^{3D} was used to assemble the membrane particle chains. Figure 3.4 shows a magnified view of a particle membrane conforming to the sample as deformation proceeds. The complexity associated with using a chain of particles to simulate a membrane arises from the fact that the length of the membrane will change (i.e., "stretch") over the course of a simulation. To overcome this problem, membrane endpoints (top and bottom) were closely monitored throughout the simulation. Once loading began, the endpoint locations relative to the positions of the loading platens is checked at every time step. If a membrane end particle is more than 1.5 particle diameters away from the platen (measured normal to the platen), then a new ball is added to the end of the membrane to decrease the gap between the membrane and the platen. Similarly, if a membrane endpoint is less than 0.5 particle diameter away from a platen (measured normal to the platen) then a ball is removed from the membrane end. In this manner, the membrane length is constantly adjusted to prevent particles from escaping the assembly and to prevent "bunching" of the membrane adjacent to a platen. It should be noted that with bonded particles being used to mimic the membrane, a linear contact model was required as PFC^{3D} only supports linear contacts in simulations with bonded particles.

3.3.3 Confining stress

Alshibli and Sture (2000) conducted plain strain compression tests on several silica sand samples with different grain sizes and shapes, under low (15kPa) and high (100kPa) confining pressure conditions. The results showed that a more pronounced peak stress was developed under high confining pressure. Considering the relatively small scale DEM model in the current study, a more distinct and

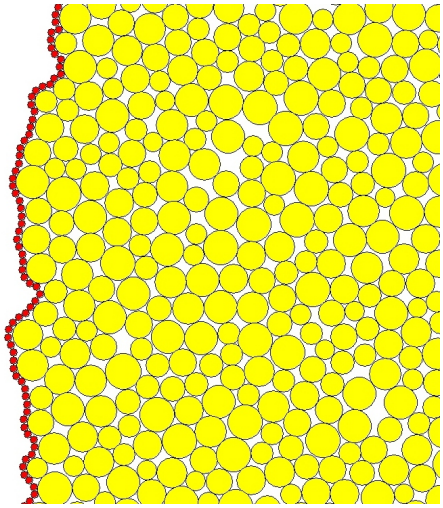

Figure 3.4: Membrane boundary used in DEM simulation

clearly defined stress drop will facilitate the characterisation of critical points associated with the triggering of bifurcation instability. Therefore, a high constant confining stress was applied as $\sigma_x = 1.5 \times 10^4 N/m$ in the current model, after the initial isotropic consolidation state $\sigma_x = \sigma_z = 5 \times 10^3 N/m$ was achieved under particle radius expansion scheme. The top and bottom rigid walls moved downwards and upwards respectively at the same time with a constant velocity of $1mm/s$, while the velocity of the lateral membrane boundaries were adjusted to maintain the specified confining pressure.

3.4 Results and discussion

In an attempt to explore the sensitivity of system response to contact friction, a number of simulations with various coefficients of particle-particle friction and particle-boundary friction were first performed. Then more comprehensive investigation into the local void ratio, particle rotation and force network were carried out to probe the underlying failure mechanism.

3.4.1 Influence of end friction of loading platens

The influence of friction of the loading platens on the observed loading response of a soil specimen has been widely documented (Bishop and Green, 1965; Lee, 1978; Lee and Seed, 1964; Rowe and Barden, 1964; Ueng et al., 1988). When a specimen is compressed between two end platens, frictional forces arise at the ends so as to prevent lateral expansion. Reduction of this end friction by lubrication in physical experiments is thought to bring the state of strain within the sample to a more homogeneous one. In the study, DEM simulation was used as an attractive approach to study different hypothetical conditions that are not feasible to perform in physical experiments, for example, frictionless end platens.

The first set of simulations was performed to investigate the influence of end friction (f_w) on specimen response, where three simulations were performed by assigning different friction coefficients to the loading platens. The predicted sample responses to biaxial compression are presented in Figure 3.5, where the stress ratio and volumetric strain ϵ_v were plotted against vertical strain ϵ_y. The stress ratio K is calculated as σ_y/σ_x, in which the vertical stress σ_y is determined by adding the contact forces on the upper platen and dividing the total resultant vertical force by the horizontal length of platen. The vertical strain is considered from the relative displacements between the top and bottom platens divided by the initial sample height, while the volumetric strain ϵ_v is equal to the area changes divided by the initial sample area.

All simulations exhibit typical stress-strain behaviour under biaxial loading, i.e. an initial strain hardening behaviour accompanied by a dilatancy phase. For both spherical and non-spherical systems without end friction, the stress ratio decreased rapidly towards an ultimate failure after reaching its peak value, and this was associated with the dramatic sample expansion due to the lack of lateral restraints. The mode of failure developed in the samples with frictionless ends

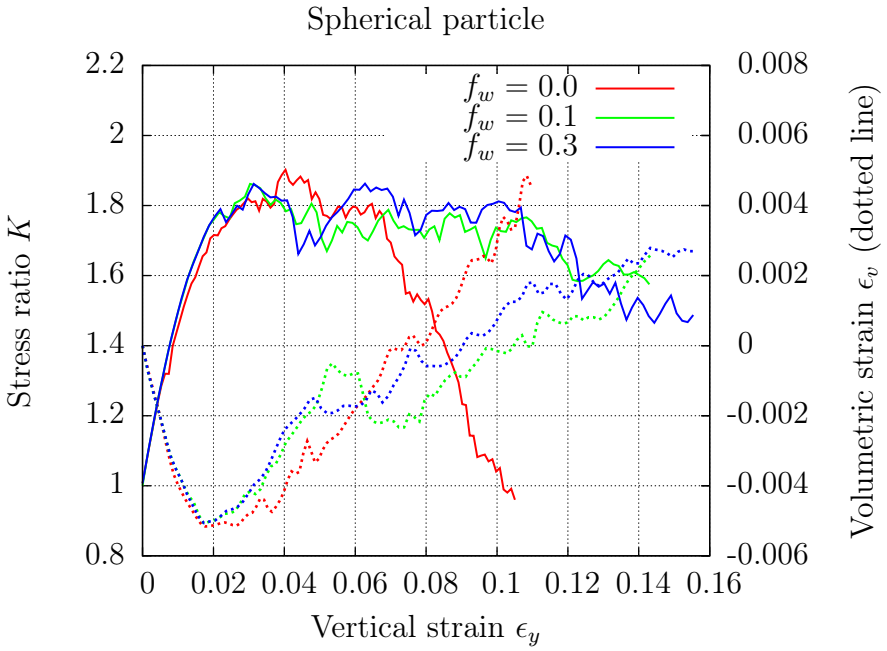

(a)

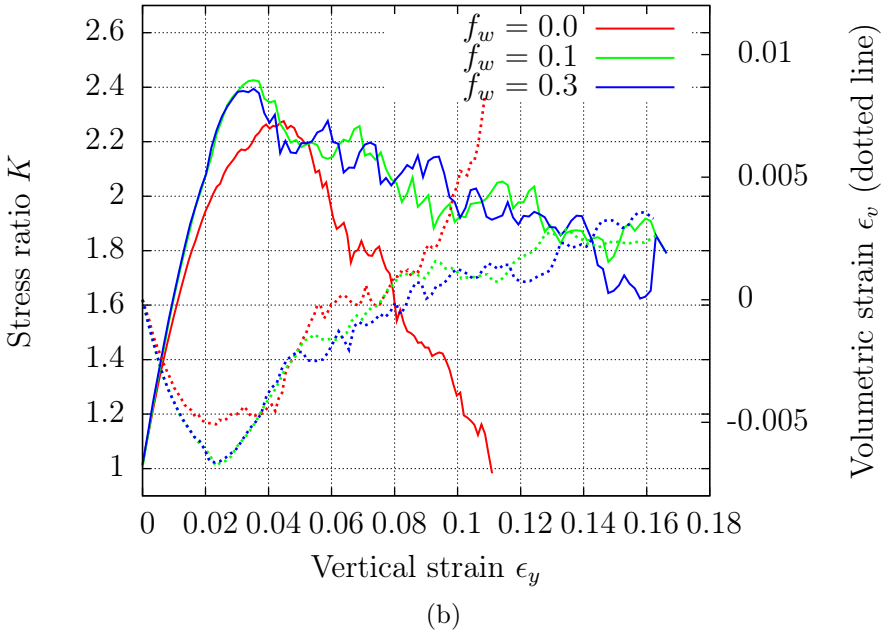

(b)

Figure 3.5: System responses with frictionless and frictional loading platens ($f_p = 0.3$)

can be clearly visualised in Figure 3.6 and 3.7, in which the particle configuration and displacement vectors were plotted. The displacement vectors were calculated for vertical strain increment from 0∼10% in order to cover the complete bulk deformation, together with a snapshot of the sample at 10% strain step with particles coloured in layers to show their relative movements. The colour scheme used in the plots of displacement vector ranges from blue to red, representing the minima and maxima, respectively.

It can be observed that there was a shear band formed of finite width. The sample was divided into two parts by this inclined band, while the two parts outside the band slides along the inclination plane in an opposite direction. These graphs well illustrated the failure mechanism in the sample with frictionless loading platens. Due to the lack of lateral restraint, after the onset of shear band, the system cannot maintain its stability to resist further deformation, thereby the upper and lower part continued to slide along the band which resulted in the severe stress drop and volume expansion as observed in the stress-strain-dilation curve. By having a closer look at the limited inclination zone, the amplified details show the formation of distinct vortex-like structure inside the shear band can be identified. Williams and Rege (1997) also noticed the existence of these vortex structures in deforming granular materials in DEM simulations. This phenomena was interpreted as part of the compatibility requirement for the deformation in a dense packing assembly, as the particles must form interlocking groups which slide against each other as rigid bodies before forming new groups.

For the cases in which friction was introduced to the loading platens, the stress-strain curves exhibited a much more progressive post-peak softening response. Previous experiments (Colliat-Dangus et al., 1988; Frost and Yang, 2003; Rowe and Barden, 1964) have observed that samples with lubricated ends present lower macroscopic strength and greater expansive volume change. Powrie et al. (2005) confirmed this tendency in DEM plane strain simulations using bonded

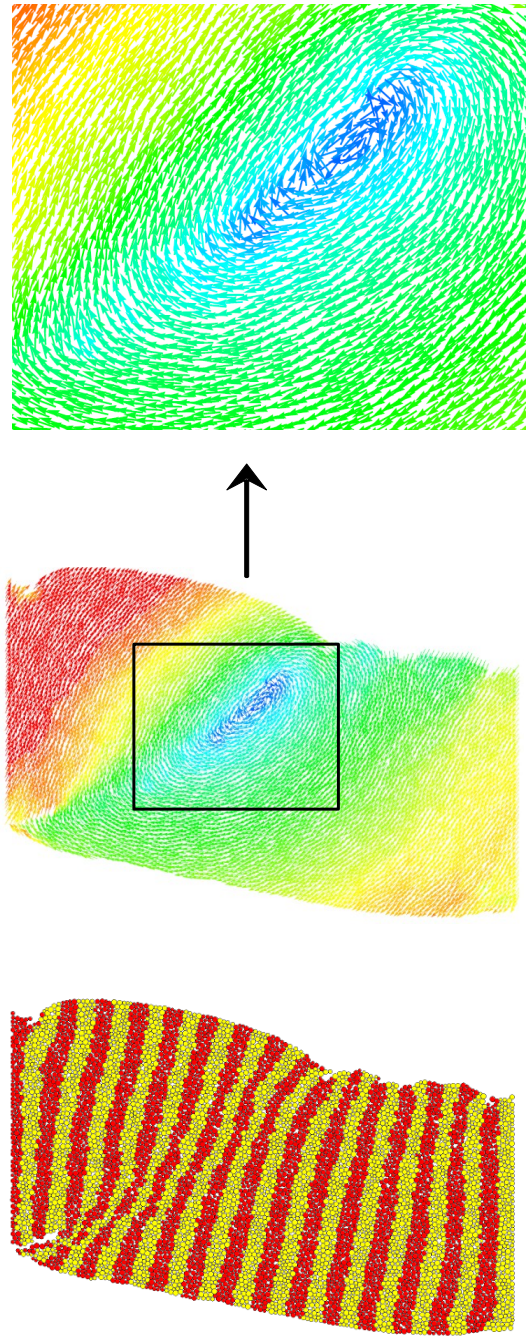

Figure 3.6: Biaxial test of spherical sample without end friction: particle layer configuration and displacement vectors at vertical strain of 10%

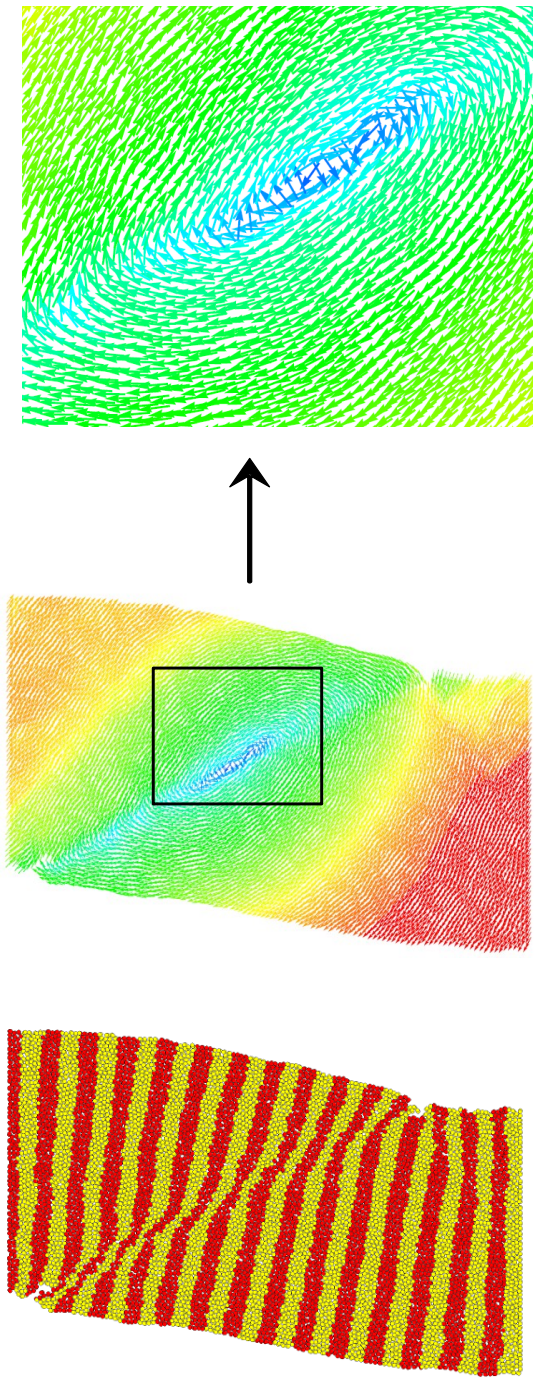

Figure 3.7: Biaxial test of non-spherical sample without end friction: particle layer configuration and displacement vectors at vertical strain of 10%

non-spherical particle. It was argued that the higher peak strength in the analysis with frictional platens was due to the possible arching which occurred between the top and bottom platens as the sample was compressed and the platen friction mobilised. This arching (with an arch on each side of the sample) allowed a column of high stress to form through the centre of the sample. Numerical results from the current DEM simulation reproduced and support these findings. In the sample composed of non-spherical particles, a significantly higher initial hardening slope and a higher peak stress were predicted when compressed by frictional platens. For the spherical particles, end friction was predicted to produce a slightly less initial loading stiffness but no noticeable effect on the peak failure stress. Similar results were also obtained in DEM simulations of triaxial test with spheres (Cui et al., 2007).

The effect of end friction was further investigated by comparing the case in which the end friction coefficient (f_w) was 0.1 with another simulation where f_w was increased to 0.3. The bulk responses yielded from these two simulations produced no noticeable difference for both types of particle, due to the fact that the bulk behaviour is mainly governed by particle interaction, as long as sufficient boundary roughness is present to provide the lateral stability. This suggests that a small value of end friction is sufficient to induce the lateral restraint, and any further increase in end friction does not affect the system response.

The end friction also plays an important role in the shear localisation pattern. In the samples compressed by frictional loading platens, cross shear bands developed rather than single band observed in the samples with frictionless loading platens. The progress of deformation for the non-spherical specimen in the current DEM simulation was compared with the experiments carried out by Alshibli and Sture (2000) as shown in Figure 3.8. It is noticed that the current numerical results are quite similar and comparable to the experimental work, in which a single band first formed followed by the development of conjugate shear bands

towards the end of simulation. The introduction of friction on the loading platens provided necessary lateral resistance at the two ends of sample, which prevented the sample from sliding along the inclination plane by triggering another shear band with an opposite orientation to the one that first formed. Without the end restraint, the pathways for force transmission in vertical direction cannot be continuous, thus caused the rapid and significant drop in the bulk strength.

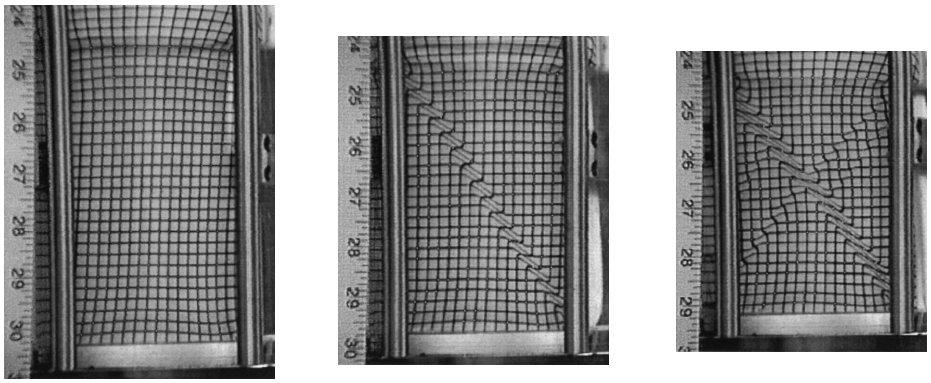

(a) Experiment tested on fine silica sands (Alshibli and Sture, 2000)

(b) Current DEM simulation (non-spherical particles ($f_p = 0.9, f_w = 0.3$)

Figure 3.8: Evolution of shear band patterns in experiment and the current DEM simulation

To conclude, shear band consistently occurred in all tests regardless of the end condition. However, zero end friction yielded an unstable bulk responses, showing a rapid drop in the stress ratio after reaching the peak strength accompanied by significant volume expansion. The simulations with frictionless loading platens produced one single shear band, whereas rough platens gave rise to two intersecting shear bands. These can be ascertained with respect to the lateral stability provided by the end restraint. The numerical results also indicate that different roughness of loading platens lead to practically the same mechanical behaviour. This suggests that laboratory attempts in end lubrication must reduce the friction to a very small value in order to achieve the desired smooth loading ends.

3.4.2 Influence of particle friction

Cohesionless granular materials carry and transmit the applied forces imposed at the boundary through interparticle contact forces. Therefore, the contact friction is expected to have a significant influence on the overall mechanical response of the granular mass. Here, the effect of interparticle friction was investigated by assigning two different friction coefficients (0.3 and 0.9) to the particles. The predicted loading responses are plotted in Figure 3.9.

The plots show the macroscopic strength of the assembly was significantly influenced by the interparticle friction, where the initial loading stiffness increased with larger interparticle friction coefficient. Spherical and non-spherical particles produced similar outcome in a qualitative manner. For the small particle contact friction ($f_p = 0.3$), the stress ratio reached the maximum value and decreased gradually under increasing vertical strain. When particle friction was set at 0.9, it is evident that a significantly higher peak stress ratio was predicted, followed by a sharp stress drop in the strain softening regime. An increase in the particle

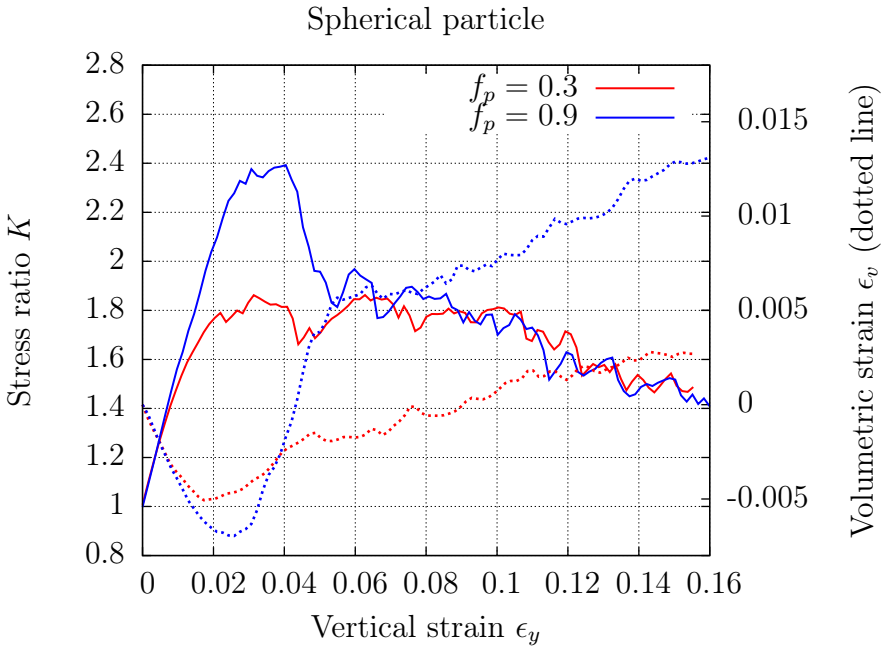

(a)

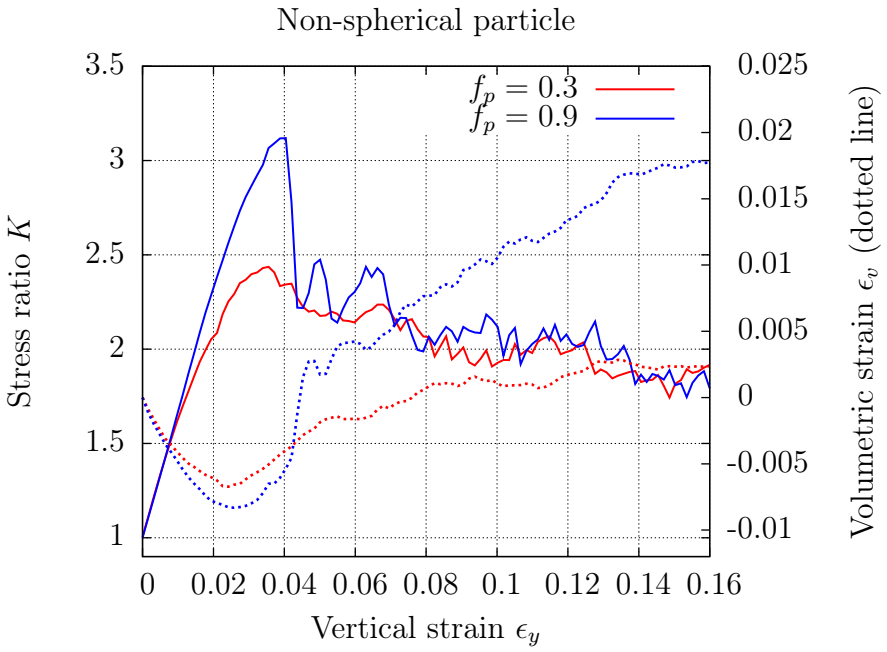

(b)

Figure 3.9: System response with different particle friction ($f_w = 0.3$)

sliding friction will lead to a greater amount of tangential force can be sustained at the contact without interparticle slip. Therefore, the higher bulk strength in the case with $f_p = 0.9$ is attributed to the greater resistance to relative particle movement developed at interparticle contacts. In terms of volumetric behaviour, increasing particle roughness generated a higher rate of dilatancy at the end of the loading.

The coordination number provides a good measurement of the particle contact intensity in a given assembly, which was defined earlier in Equation 2.1. The variation of coordination number during the biaxial loading is shown in Figure 3.10 as a function of vertical strain. The initial volumetric compression in the hardening phase was responsible for the increase of coordination number. After reaching the peak strength, the number of contacts decreased along with the sample dilation, where a large amount of voidage was generated. The loss of contacts is directly linked with the microstructural changes in the force network during the development of strain localisation, which will be further demonstrated in the subsequent analysis.

3.4.3 Width and inclination angle of shear band

The most direct manner to quantitatively characterise shear band is measuring its width and inclination angle. Results obtained from various triaxial and biaxial experiments (Alshibli and Sture, 2000; Lade and Wang, 2001; Oda and Kazama, 1998) showed that the values of shear band inclination angle are widely scattered with values ranging from 45° to 65°. The inclination angle of the shear band in the current DEM simulation was measured by scanning the sample at the end of the test (e.g. Figure 3.11). Table 3.2 lists the measured inclination angles of shear band from simulations with different interparticle frictions. The values of predicted inclination angle are comparable to the experimental measurements as

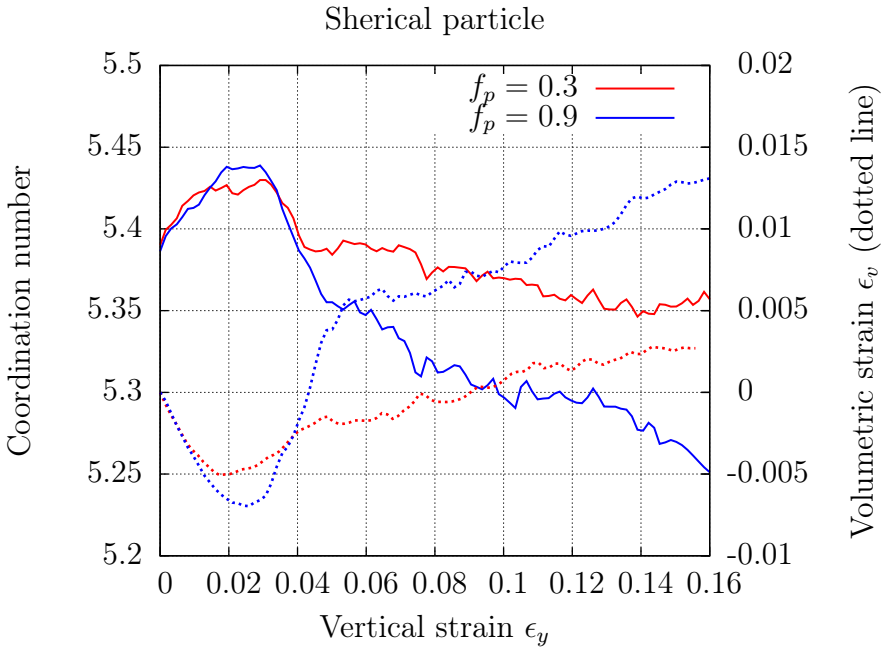

(a)

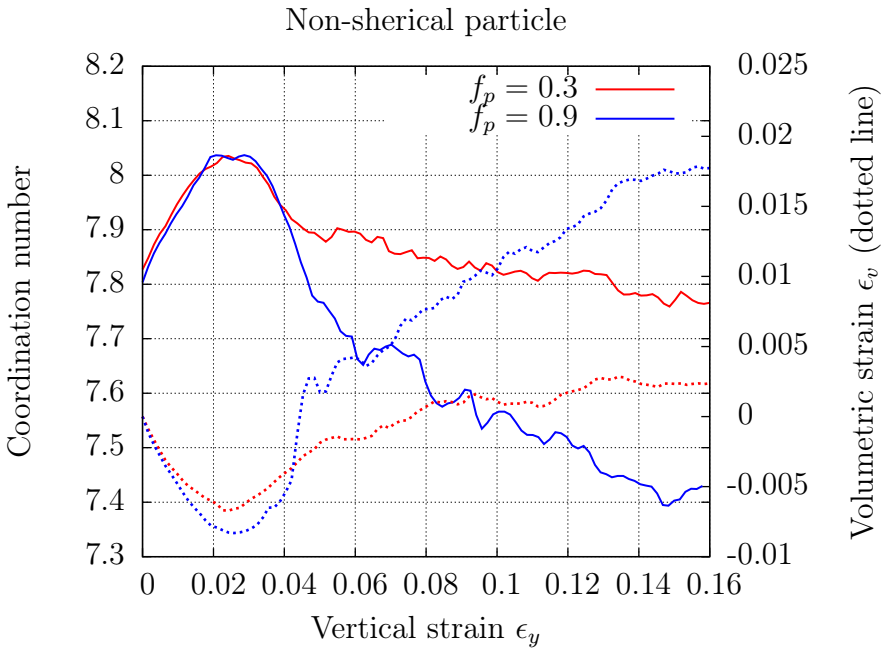

(b)

Figure 3.10: Coordination number and volumetric strain ($f_w = 0.3$)

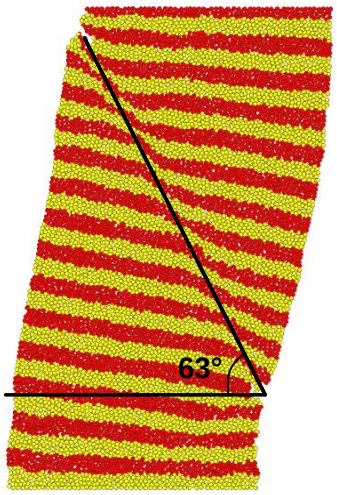

Figure 3.11: Measurement of shear band inclination angle

reported in the literature.

Table 3.2: Shear band inclination with different particle shapes and frictions

Particle friction	Inclination of shear band (degree)	
	Spherical	Non-spherical
0.3	52	51
0.9	45	53

In granular materials, a shear band is visible and it involves many particles in the direction perpendicular to the axis of the shear band. Valuable insight can be gained by analysing the variation of the shear band width. The width of shear band is often normalised by the mean particle size (D_{50}). In this study, the displacement field was employed to calculate the width of shear band. Following the work of Bardet and Proubet (1992), a local coordinate (ξ, η) is established, in which ξ-axis is parallel to the shear band and the η-axis is perpendicular to the shear band. Here, the possible and approximate shear band zones were divided into several subregions along the ξ-axis as shown in Figure 3.12(a). For each sub-

region, the average displacement along the ξ-axis direction can be approximately estimated as follows:

$$\overline{u}_{\xi}^{i} = \frac{1}{N_i} \sum_{j=1}^{N_i} u_{\xi}^{j} \tag{3.1}$$

where N_i is the number of particles that located within the ith subregion. When two conjugate shear bands develop within the assembly as illustrated in Figure 3.12(b), the sample can be divided into four subregions. Then four local coordinate systems are set up and the average width of the four shear bands is evaluated.

The width of shear band can be calculated by plotting the variation of u_{ξ} versus η for each segment in the local coordinate system as discussed above. It is assumed that u_{ξ} is constant outside the shear band and varies linearly inside the shear band. Thus typically a ramp area is formed with two horizontal lines connected by an inclined line. The width of the shear band is determined from the width of the ramp in the η-direction. Figure 3.13 gives an example of the calculation of shear band width using local and global displacement fields. It is shown that employing the whole displacement fields in the evaluation of the shear band width will lead to a significant overestimation. A more accurate width determination can be achieved by dividing the global displacement field into several local regions accordingly where only one shear band is dominating the deformation, and then perform the calculation in each shear zone separately.

Over the past decades, measurements of shear band width have been reported from samples with different types of grain. The width of shear band in samples of Toyoura sand was determined to be $8\sim15D_{50}$ by Oda et al. (2004), with the aid of microfocus X-ray computed tomography. A higher value of width, over $30D_{50}$, was found in loose sand (Finno et al., 1997; Harris et al., 1995b). DEM simulations (Bardet and Proubet, 1992; Hu and Molinari, 2004; Iwashita and Oda,

Figure 3.12: (a) Definition of global and local coordinates for analysis of width of shear band; (b) Schematic view of four local subregions

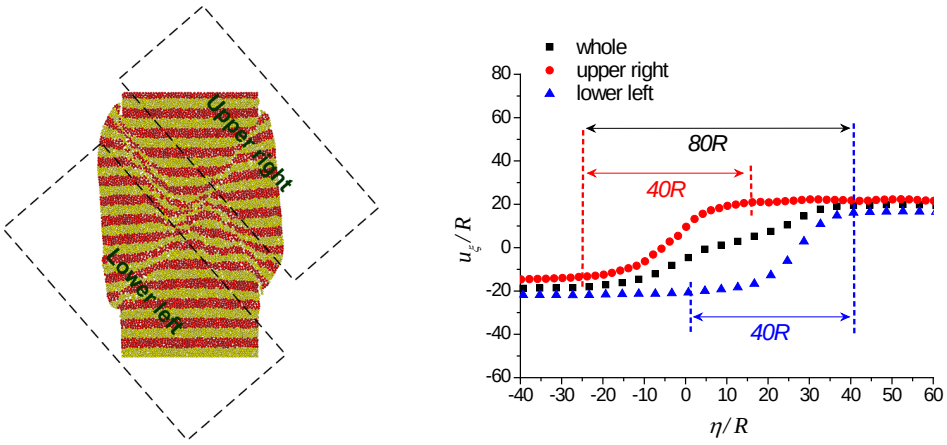

(a) Definition of different shear zones

(b) Definition of shear band width

Figure 3.13: Calculation of shear band width using displacement field

1998; Tordesillas, 2007) predicted the shear band width in the range of $15\sim30D_{50}$. Desrues and Viggiani (2004) concluded that both the thickness and orientation of shear bands depended on a number of factors including the initial state of the material (mean effective stress and void ratio), its grading (grain size, uniformity, etc.), and the size and slenderness of the specimen. For example, the shear band width in dense Hostun sands reduced from 22 to $13D_{50}$ as the effective confining stress increases from 100 to $800kPa$; A similar trend is observed for loose Hostun sand, the range of measured shear band widths being 31 to $17D_{50}$ over the same range of confining stress. The widths of shear band predicted using different particle shapes and contact frictions from the present study are listed in Table 3.3.

The width of shear band was predicted to increase as the particle friction decreases. Also the shear band developed in spherical particles was slightly wider than the one from non-spherical particles. This is mainly caused by the greater interlocking effect of the non-spherical particles, which confined the particle move-

Table 3.3: Shear band width with different particle shapes and frictions

Particle friction	Width of shear band (D_{50})	
	Spherical	Non-spherical
0.3	25	20
0.9	17	14

ment and hereby impeded further propagation of shear band. Overall, the predicted values of shear band width from the current simulations are slightly greater than, but comparable to, the measured values reported from experiments. This may be attributed to the two-dimensional nature of the current DEM model (although 3D shaped particles were employed). When the particles are constrained to two dimensions, they are unable to move out of the constrained plane, thus the dilation of the shear band may become more pronounced than that observed in three-dimensional experiments.

3.4.4 Void ratio

A constant volume change or a stabilisation of void ratio under large shear deformations is often considered to indicate that a limit or critical state has been reached within the granular assembly. Experimental results (Oda et al., 1982) showed that the value of void ratio inside the shear band was significantly greater than the one obtained from the whole sample. Desrues et al. (1996) pointed out that the homogeneity of the void ratio distribution over the specimen during loading, especially approaching the peak strength, must be considered as an important element in the characterisation of the overall volume change. Kuhn (1999) noticed the interrelations between the local void fabric and deformation pattern, where sample with vertically elongated void cells tends to dilate and

sample with obliquely elongated void cells tends to undergo slip deformation. Therefore, it is of interest to study the evolution and distribution of void ratio during biaxial loading.

Here, the void ratio is defined as the ratio of the area of voids to the area of solid particles. Therefore, the obtained value will be significantly smaller if compared to that from a 3D packing case. Two approaches were adopted to calculate the distribution of local void ratio. Firstly, a digital image analysis technique is developed to work out the void ratio based on pixel information. High resolution images (2000 $\times$ 2000 pixels) containing all the particles were output directly from PFC^{3D} at the end of the DEM simulation. Another method makes use of the PFC measurement circle, in which the void ratio is averaged within the specified geometry. The interrogation cell and measurement circle were set up accordingly to crop the sample into a rectangular shape, in order to eliminate the blank margins and to contain the main body of particle assembly. For both methods, the local void ratio was calculated within an averaging cell of side length or diameter of $5D_{50}$. The cell boundary moves by $1D_{50}$ in both vertical and horizontal direction at the same time for each evaluation (moving average technique). This was chosen to give a balance between the very high scatter if the cell is too small, and the loss of detail if it is large. These spot values of void ratio were then used to plot the contours of local void ratio distribution.

Figure 3.14 compares the distribution of local void ratio obtained from pixel analysis and PFC measurement circle. Overall, the contour patterns particularly the concentration of large voidage evaluated from these two methods are similar. However, the spot values are completely different, in which the pixel analysis produced a much higher local void ratio. Figure 3.15 shows an example of a binary image containing the particle sample and an amplified local view. It can be observed that the image extracted from PFC^{3D} model is able to adequately indicate the large voidage distributed in the region of shear band. However, a

close inspection of the amplified view suggests that the image contains voids between adjacent particles which are in contact and the outline of particle shape is far more than smooth, although a high output resolution has been specified. These two factors gave rise to the overestimation of local void ratio. Therefore, measurement circle is adopted to calculate the local void ratio in the subsequent analysis. Admittedly, the pixel-based analysis approved to be not accurate and cannot be used for quantitative investigation. Nevertheless, it does provide an easy implemented approach to calculate the local void ratio, particularly when the sample contains particles of irregular shapes. Future study should pay special attention to the accuracy and precision of the pixel data.

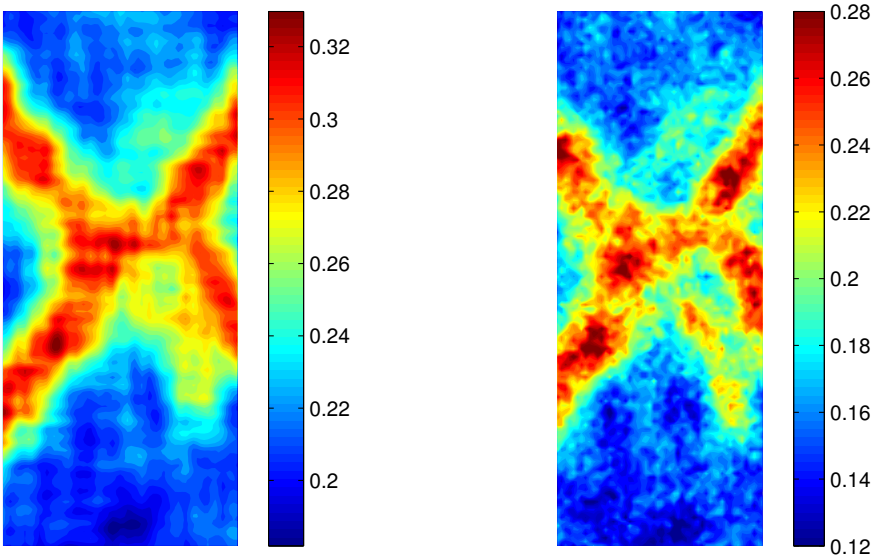

(a) Pixel analysis (b) Measurement circle

Figure 3.14: Calculation of local void ratio using two different methods

Figure 3.16 and 3.17 show the contours of these subregional void ratios at the end of each simulation with different interparticle friction coefficients. Each contour is presented in pair with the particle placement of different coloured layers to permit a better visualised comparison with shear band pattern. It is

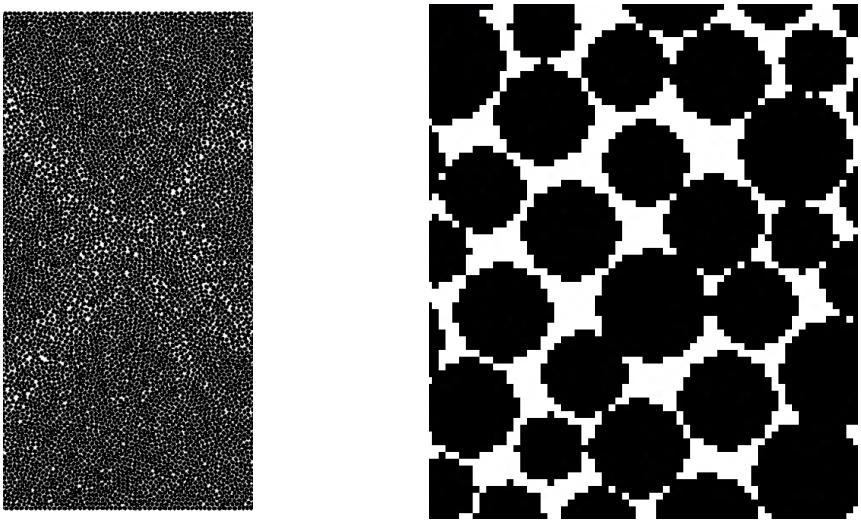

(a) Entire image (b) Amplified view

Figure 3.15: Example of a binary image output from PFC in the use of void ratio calculation

worth of mention that the void ratio calculation was based on the image obtained instantaneously, which may subject to change shortly. So a temporal averaging was carried out over a global strain interval of 0.5%, and the results (not shown here) show no significant changes. It suggested that these plots are sufficient to represent the distribution of local void ratio in the sample. The results are in line with the critical state theory proposed by Muir Wood (2008), i.e. at the end of a continuing shear deformation, all aspects of the packing fabric within the granular assembly should on average have reached a steady state, such as void ratio, particle orientation and contact orientation.

For spherical particles, the location of large local void ratio was diversely distributed when the interparticle friction is small; increasing the particle friction, in turn, produced a more well structured distribution, where concentration of large local void ratio occurred within the shear band. On the other hand, due to the strong particle interlocking effect, the calculations performed on specimens

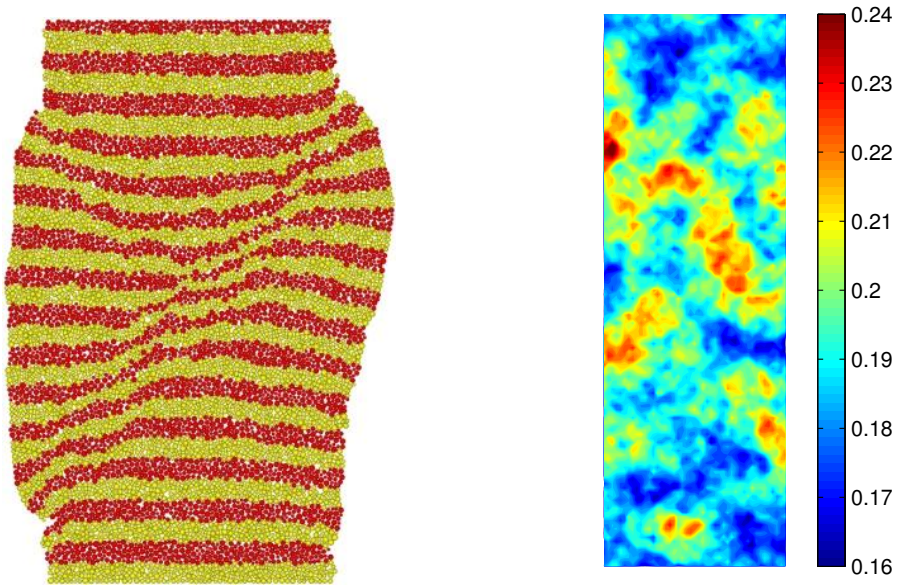

(a) $f_p = 0.3$

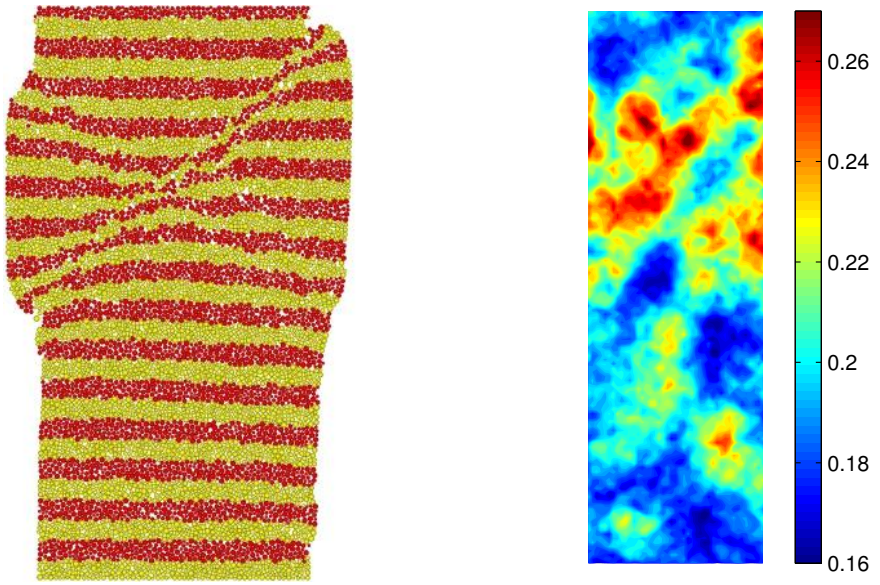

(b) $f_p = 0.9$

Figure 3.16: Particle layer configuration and contours of void ratio for spherical particle at vertical strain ϵ_y=15%

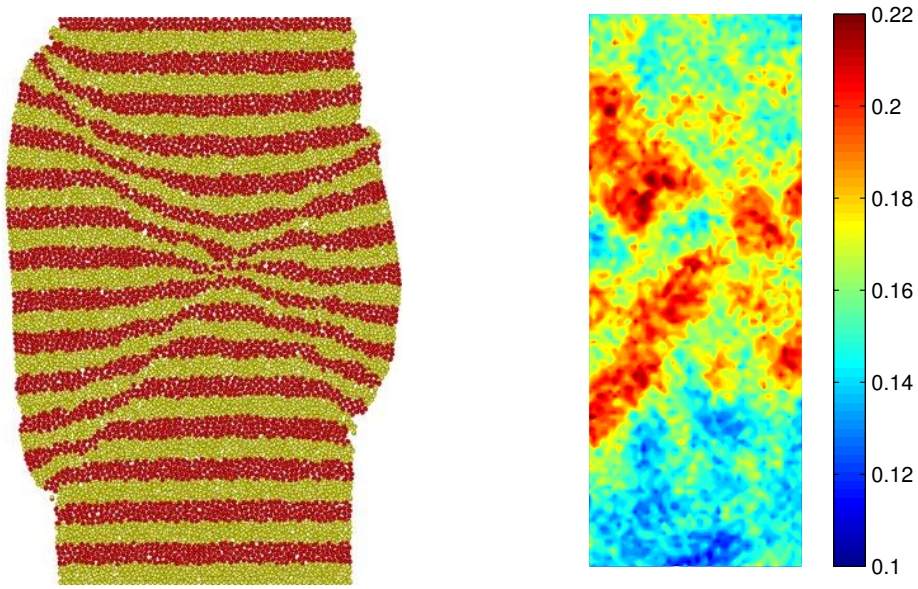

(a) $f_p = 0.3$

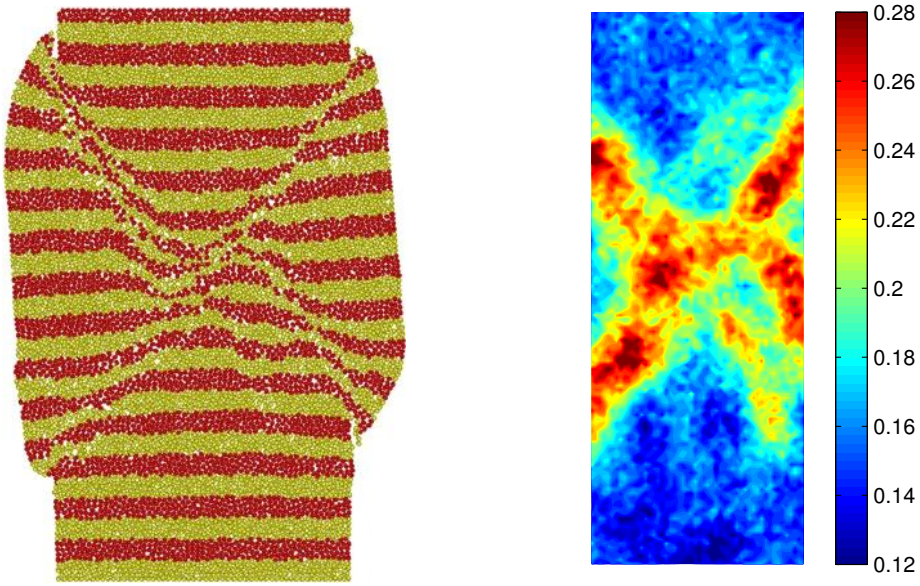

(b) $f_p = 0.9$

Figure 3.17: Particle layer configuration and contours of void ratio for non-spherical particle at vertical strain ϵ_y=15%

with non-spherical particles clearly demonstrate the existence of distinct zones of large voids which coincided with the shear band pattern predicted earlier. Meanwhile, it is evident that the localisation pattern was sensitive to the particle shape, i.e. conjugate shear bands can be easily identified in the specimen with non-spherical particles, while single band mechanism is more dominant in spherical particles. The presence of these large voids can be associated with the buckling of force chains that transect the shear band which will be investigated later.

The contour plots indeed reveal the interrelation between localisation pattern and void ratio distribution. In order to obtain more quantitative information to calibrate the microstructure variation, the local void ratios obtained from sub-regional image analysis were further investigated to construct the histograms of local void ratio within the whole specimen at different loading stages. Considering the development of voidage in the specimen is a gradual and progressive process, the frequency distribution of the local void ratio at four strain steps as illustrated in Figure 3.18 were calculated.

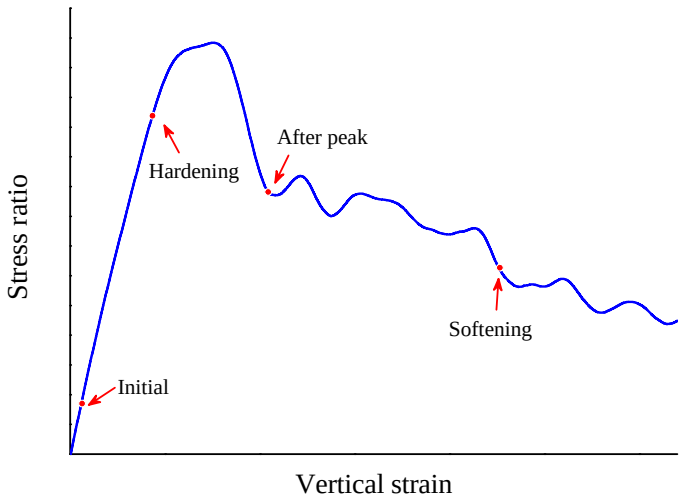

Figure 3.18: Four strain stages in the analysis of void ratio distribution.

Firstly, the variations of void ratio in the specimen at different strain stages

are presented as histograms in Figure 3.19 and 3.20 for spherical and non-spherical particles, respectively. The distribution percentage was normalised by the maximum value occurred in each specimen, while the mean void ratio of the whole unsheared specimen ($\bar{e}$) was adopted to scale the x-coordinates.

These histograms suggest that both particle shape and interparticle friction played important roles in the development of voidage during the loading. For example, when the interparticle friction was small ($f_p = 0.3$), it is apparent that void ratio did not vary greatly across the the whole specimen from unsheared to sheared state. However, the scenario became significantly different when f_p was increased. The common features at each loading stage are summarised separately:

- Initial: the local void ratio in both types of particles exhibited Gaussian distribution, representing a random packing of granular materials (Shahinpoor, 1980).

- Hardening: the sample experienced a compaction process, resulting in a decrease of the mean void ratio which shifted the histogram peak to the left of the horizontal axis.

- After peak: the tail of the distribution extended to the right of x-axis, indicating a portion of voids have developed in certain locations within the specimen. Also, a large interparticle friction ($f_p = 0.9$) gradually caused a gamma-like distribution, which was a significant deviation from the initial normal distribution.

- Softening: there was an continuing formation of large voidage. Particularly, as shown in Figure 3.19b and 3.20b, the maximum local void ratio in the sheared spherical and non-spherical specimen was 60% and 80% larger than its mean value before shearing ($\bar{e}$), respectively. This is indicative of an considerable increase of the heterogeneity in the distribution of local void

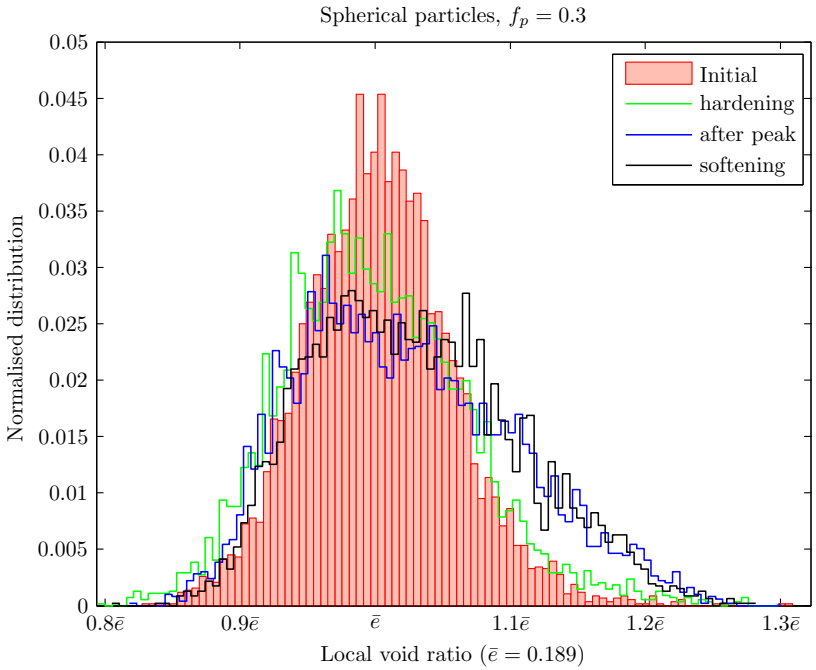

(a)

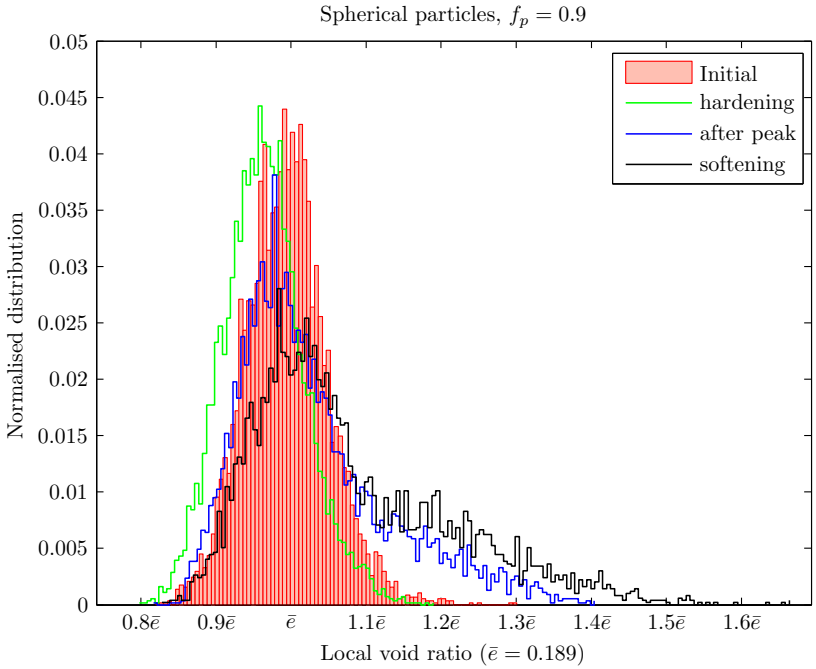

(b)

Figure 3.19: Evolution of the local void ratio distribution in the whole specimen composed of spherical particles

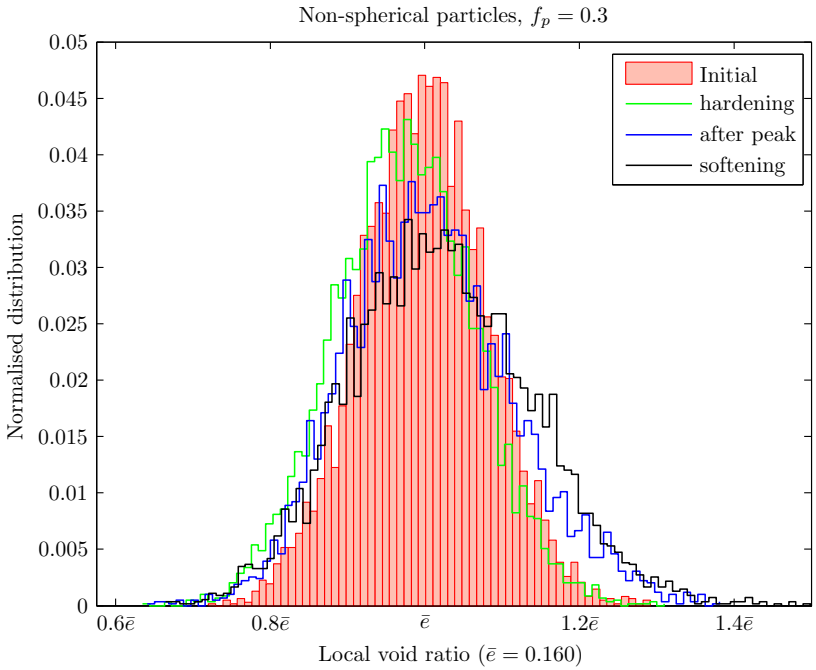

(a)

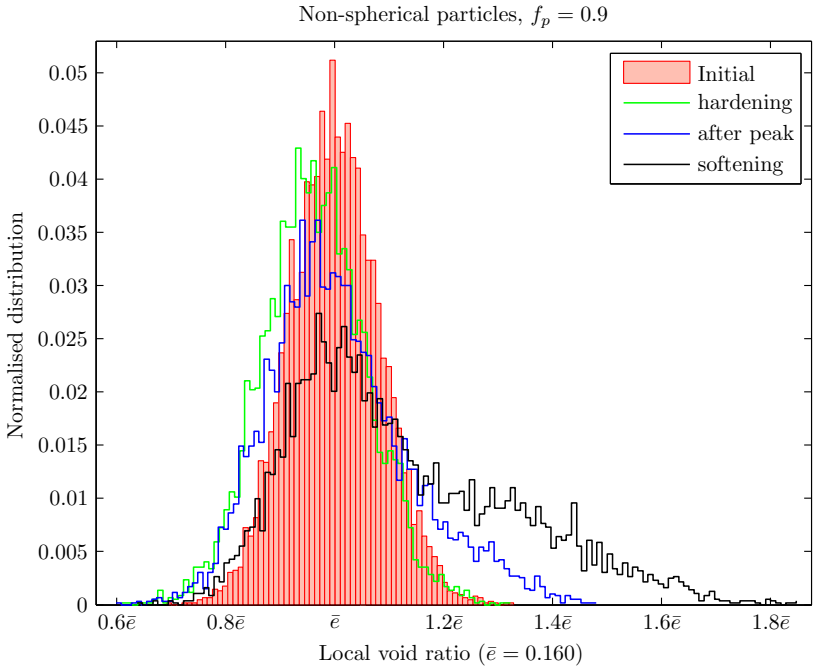

(b)

Figure 3.20: Evolution of the local void ratio distribution in the whole specimen composed of non-spherical particles

ratios and a strong dilation within the specimen.

Compared to sample composed of spherical particles, it is noted that non-spherical particles exhibited a broader range of local void ratio distribution at the end of the simulation, suggesting a more pronounced dilation in the sheared sample. The higher packing density (i.e. a smaller initial void ratio) in the unsheared non-spherical sample and the particle interlocking effect are likely to be the primary sources. Noticeably, after the achievement of the peak strength when a number of voidage have developed within the sample, the lower end of the histogram remained less changed on the horizontal axis, indicating that the dilation took place in certain regions was not accompanied by some local compressions in other areas. Regarding the observed normal and gamma-like distribution in the unsheared and sheared specimen, statistical characterisation can be carried out to further quantify the histograms of local void ratio.

The study using the displacement field to calculate the width and inclination angle of shear band (section 3.4.3), enables a careful determination of the boundary of shear band within a sample. Here, the microstructural differences inside and outside the shear band were examined at increasing strain levels. Consequently, three regions are considered to construct the histogram of local void ratio distribution, i.e. the whole specimen, inside and outside the shear band. These results from specimens with different combinations of particle shape and interparticle friction are presented in Figure 3.21, 3.22, 3.23 and 3.24.

The analysis of void ratio in different regions of the sample shows a noticeable change in its profile across the shear band as deformation proceeded. Comparing the sheared sample with unsheared one, both the mean value and standard deviation of local void ratio tended to increase within the shear zone, while the variation outside the strain localisation region was relatively less significant. This phenomenon became more pronounced in the sample with higher interparticle

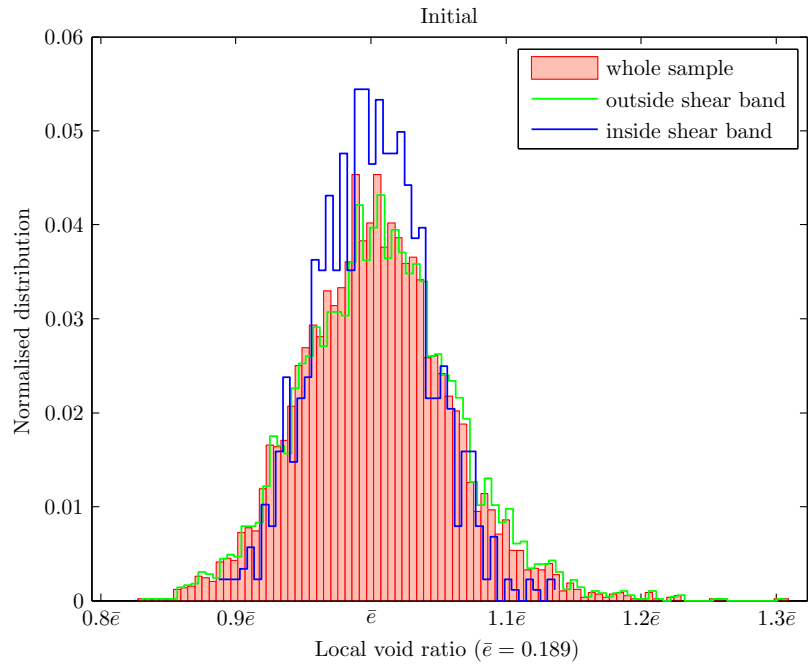

(a)

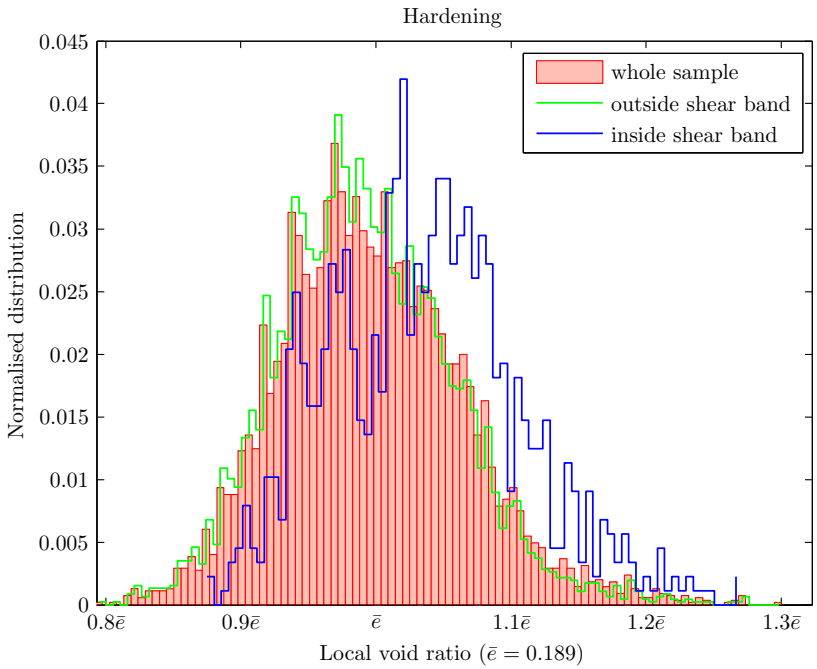

(b)

Figure 3.21: Histogram of local void ratio distributions at different loading stages, spherical particles $f_p = 0.3$.

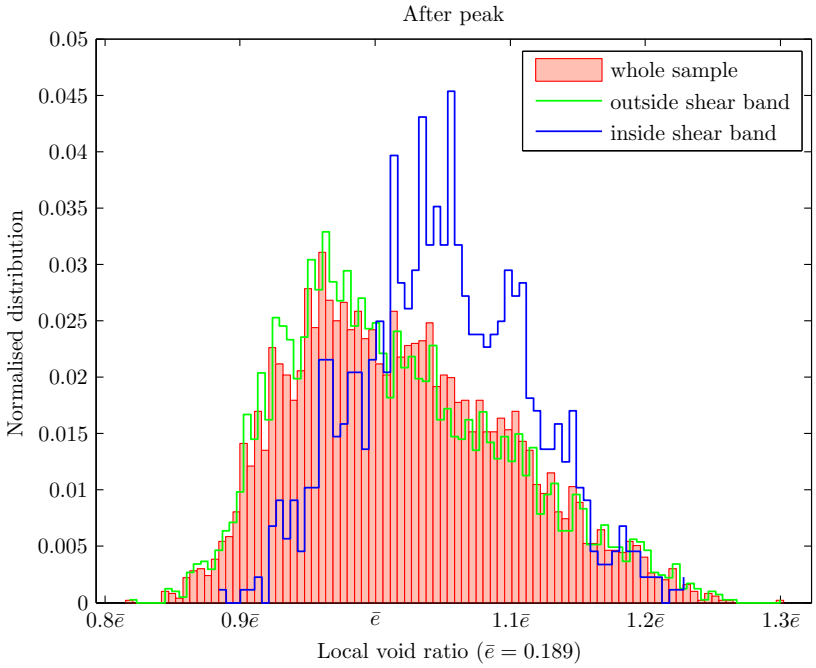

(c)

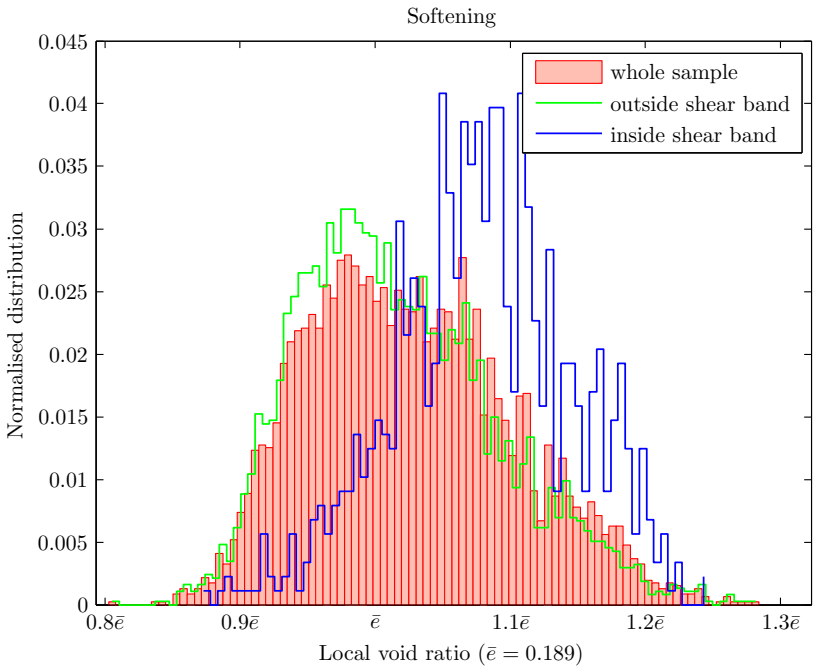

(d)

Figure 3.21: (*continued*) Histogram of local void ratio distributions at different loading stages, spherical particles $f_p = 0.3$.

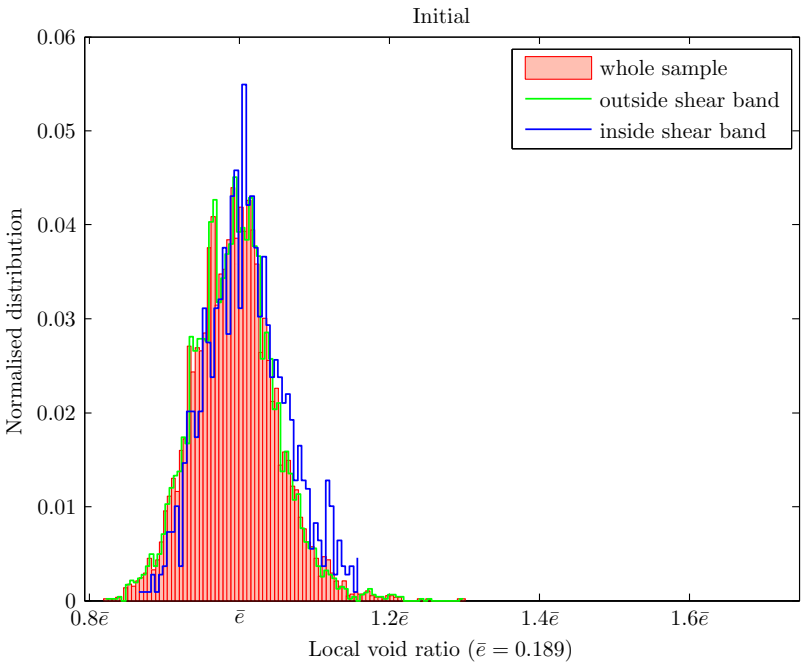

(a)

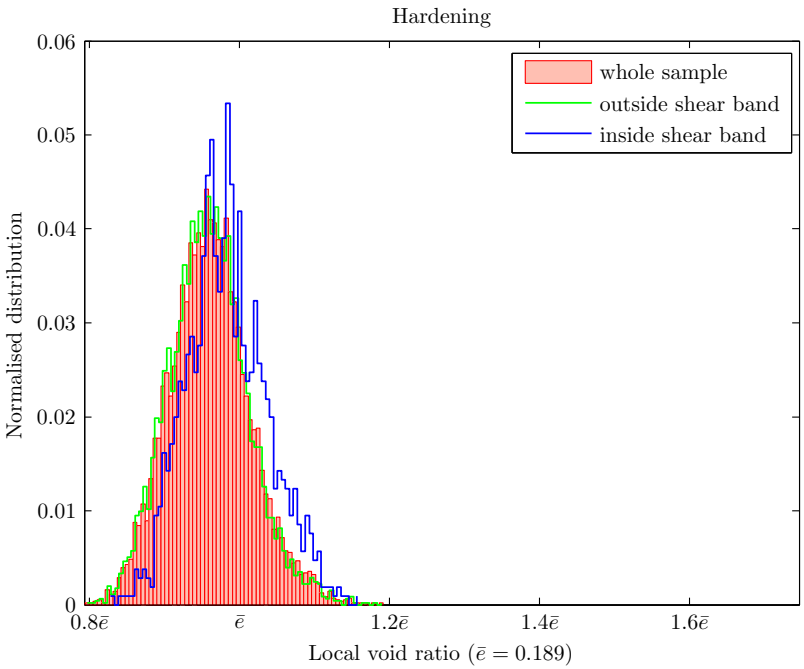

(b)

Figure 3.22: Histogram of local void ratio distributions at different loading stages, spherical particles $f_p = 0.9$.

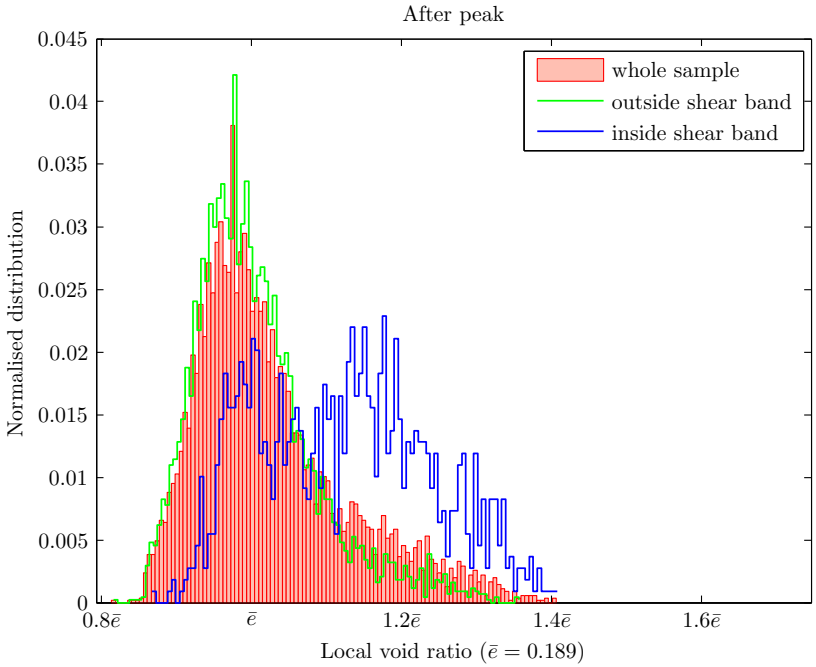

(c)

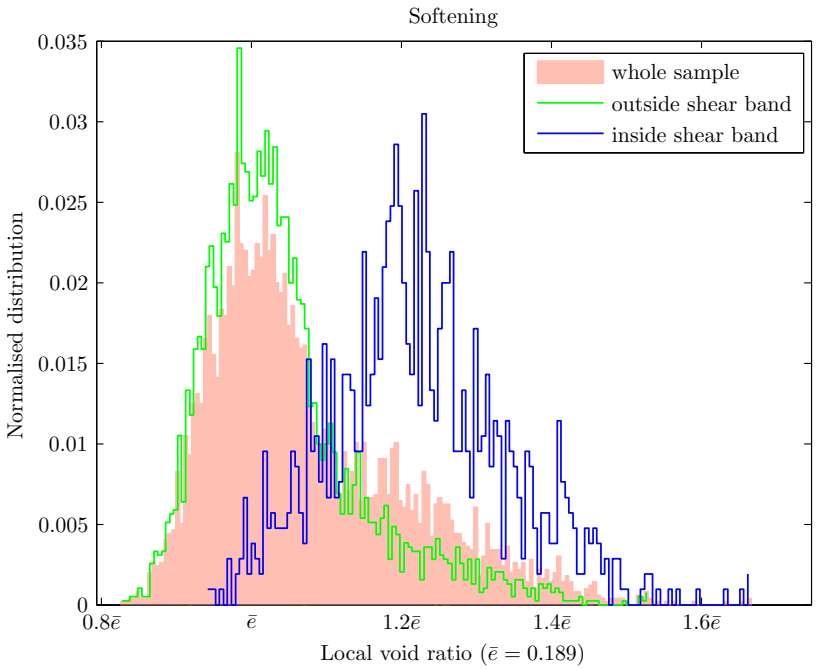

(d)

Figure 3.22: (*continued*) Histogram of local void ratio distributions at different loading stages, spherical particles $f_p = 0.9$.

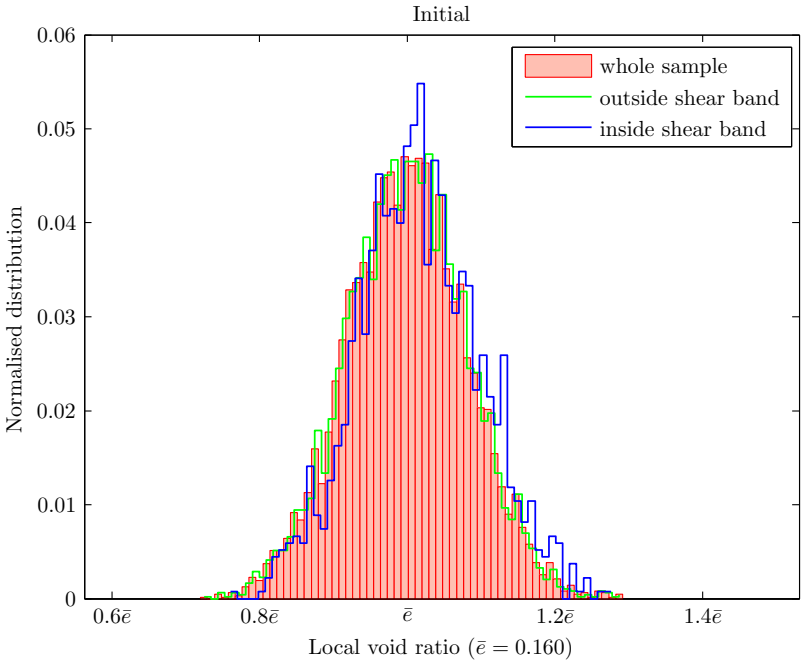

(a)

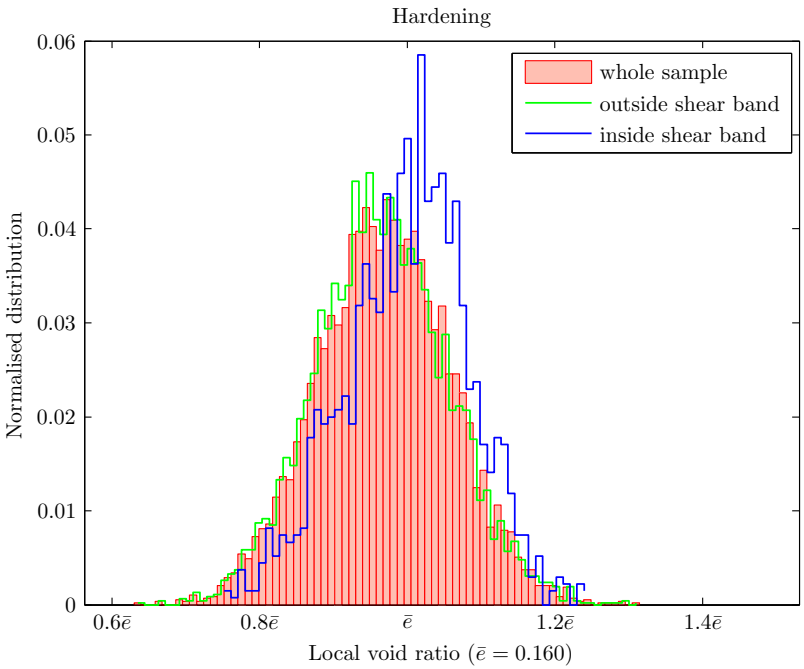

(b)

Figure 3.23: Histogram of local void ratio distributions at different loading stages, non-spherical particles $f_p = 0.3$.

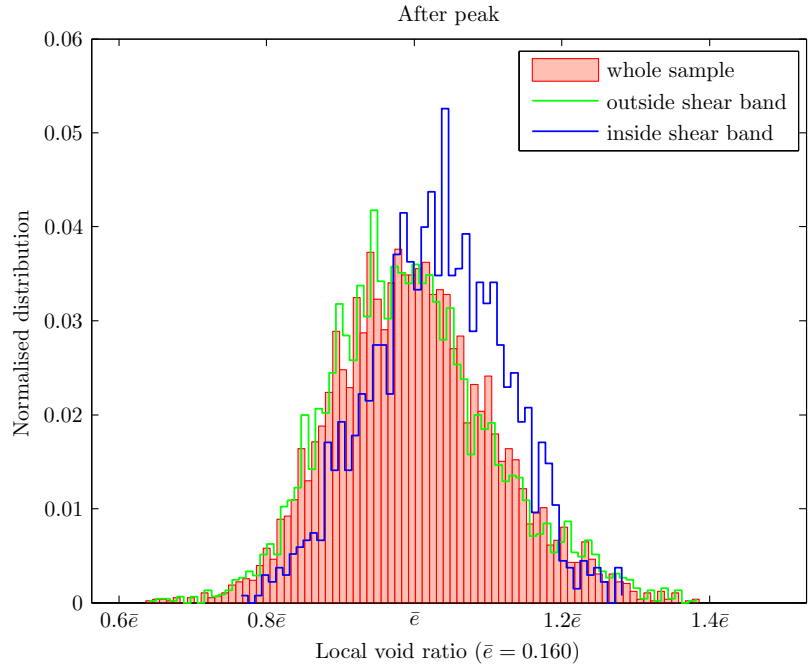

(c)

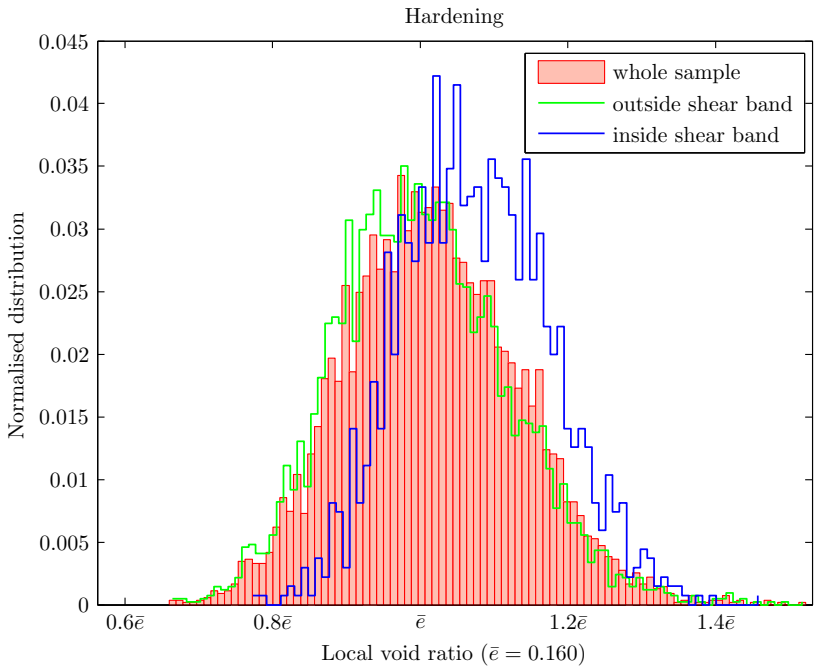

(d)

Figure 3.23: (*continued*) Histogram of local void ratio distributions at different loading stages, non-spherical particles $f_p = 0.3$.

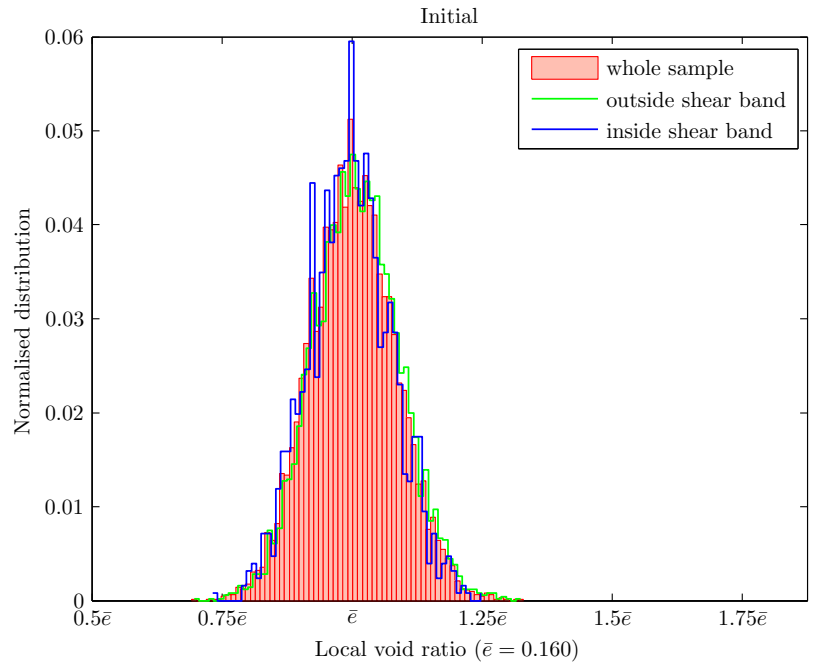

(a)

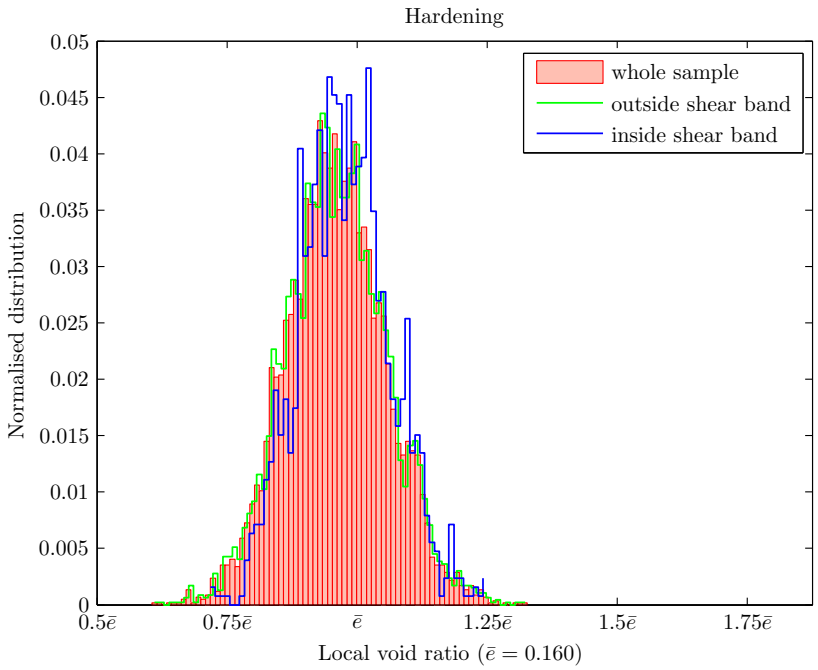

(b)

Figure 3.24: Histogram of local void ratio distributions at different loading stages, non-spherical particles $f_p = 0.9$.

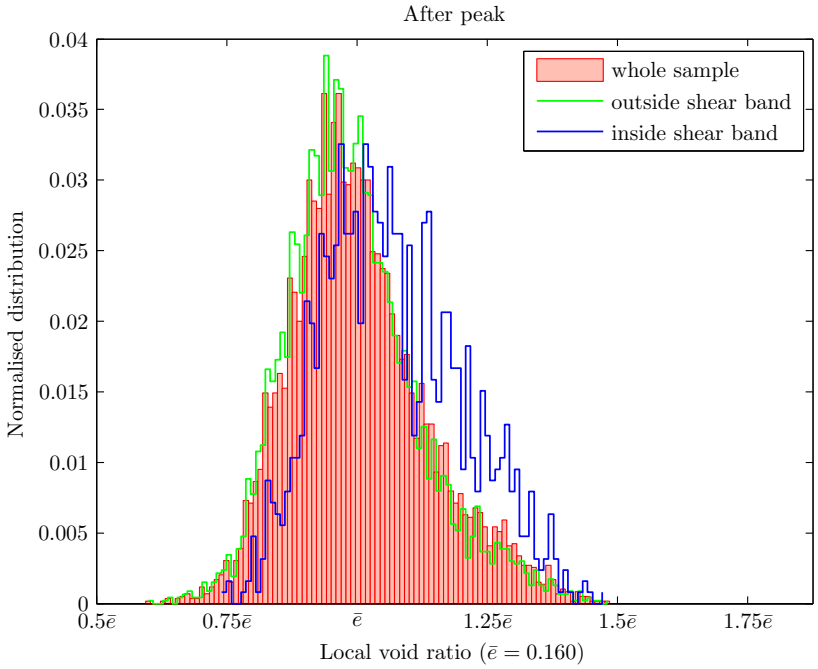

(c)

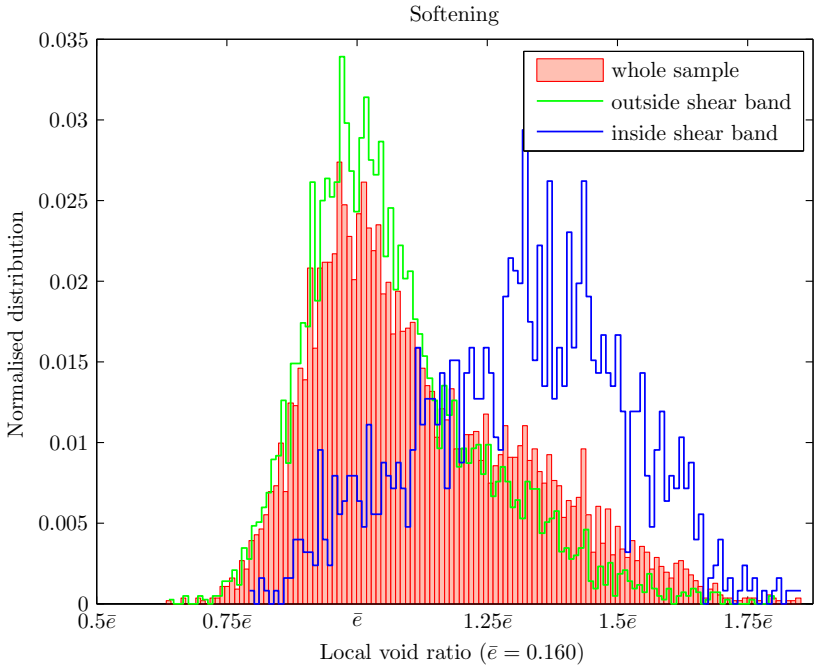

(d)

Figure 3.24: (*continued*) Histogram of local void ratio distributions at different loading stages, non-spherical particles $f_p = 0.9$.

friction (Figure 3.22 and 3.24), where the local void ratios within the shear band increased dramatically relative to those outside of the shear bands, which shifts the peak of histogram in the shear zone further to the right of x-axis. Although previous research (Kuhn, 1999; Oda et al., 1982) have reported that there were noticeable voids developed within a shear band, the current results provide quantitative information regarding the local voidage distribution and its evolution.

To summarise the variation of void ratio in different regions, Figure 3.25 and 3.26 plot the mean local void ratios both inside and outside of the shear band as a function of global axial strain. These figures show the that mean void ratio firstly decreased as a result of sample compaction during strain hardening, followed by a gradual increase with the most significant increment occurring inside the shear band after the onset of strain localisation. The behaviour of the two types of particles was similar, in which an increase up to 24% (Figure 3.25b) and 32% (Figure 3.26b) of the void ratios inside the shear bands (relative to the value from initial unsheared sample) can be observed from spherical and non-spherical samples with high interparticle friction, respectively; whereas only less than 8% increase in the samples with low interparticle friction (Figure 3.25a and 3.26a), irrespective of the particle shape. Interestingly, observing the mean void ratio inside shear band at the hardening stage, the decrease during the compaction course was insignificant compared to the one outside the band. This information suggests that at least at the hardening point in the current analysis, there was a tendency of bifurcation in the zone where shear band would eventually developed.

3.4.5 Particle rotation

Considering particle rotation, the mean clockwise rotation $\bar{\omega}_{cl}$ and the mean counterclockwise rotation $\bar{\omega}_{cc}$ were calculated for each specimen and plotted as a function of the loading stages. For spherical particles (Figure 3.27), the mean clock-

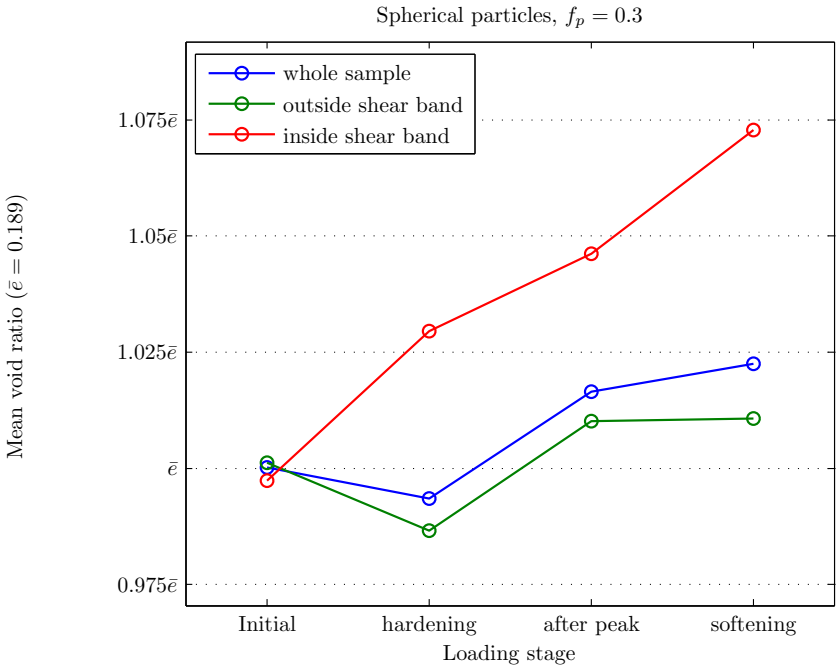

(a)

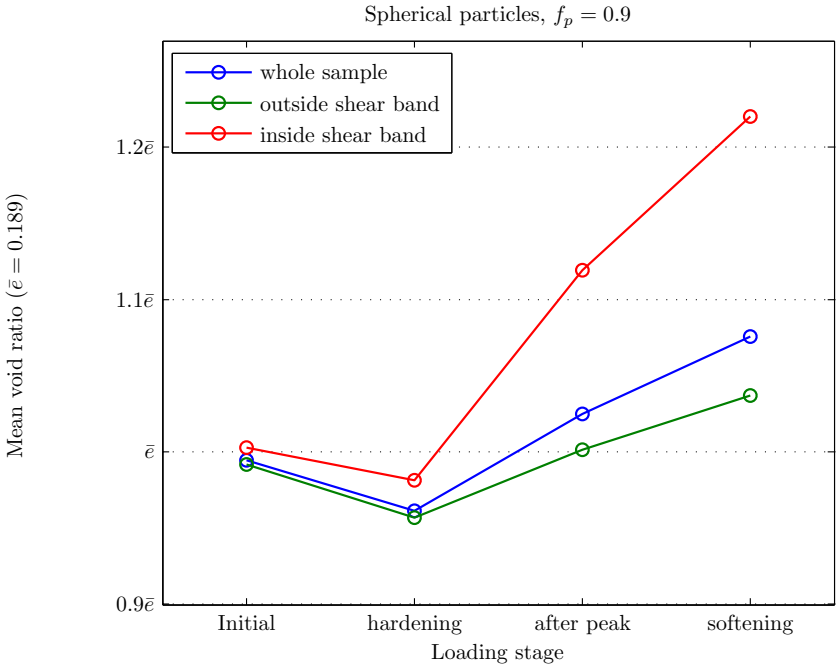

(b)

Figure 3.25: Evolution of mean void ratio in different regions of the specimen composed of spherical particles

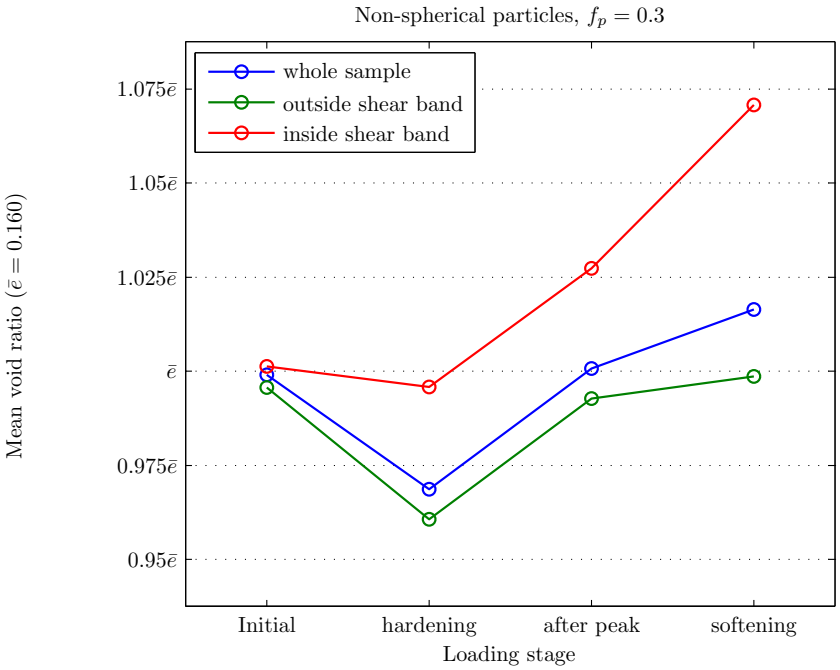

(a)

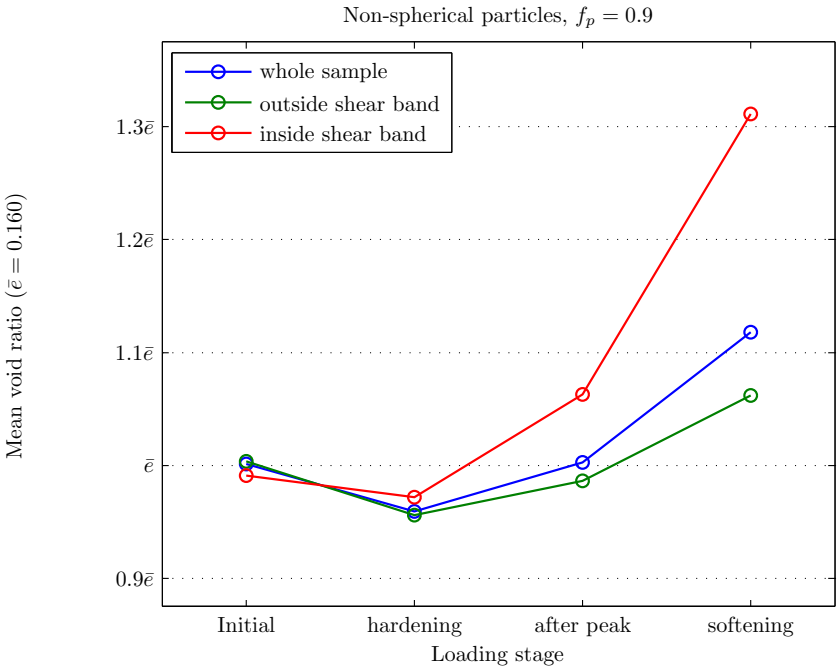

(b)

Figure 3.26: Evolution of mean void ratio in different regions of the specimen composed of non-spherical particles

wise rotation is approximately equal to the one in counterclockwise until reaching the post-peak stage, and the difference only becomes significant at the end of the deformation, where the shear bands have fully developed. Different magnitudes of particle rotation in two directions was observed earlier in the non-spherical particles, which took place after the strain hardening stage as shown in Figure 3.28. The interlocking propensity in non-spherical particle, and a smaller degree of surface roughness (interparticle friction) will both advance the rotational motion, as quantified by the magnitude of the mean particle rotation. Linking with the stress-strain curves as shown earlier (Figure 3.9), when particle rotation was restraint (larger interparticle friction and non-sphericity), stronger dilation, higher strength and initial loading stiffness were found compared to the case in which the rotation was easier to take place. It also suggests that DEM simulations using spheres reported in the literature, may overestimate the particle rotation.

The particle rotations that are greater in magnitude than the mean values were then plotted and the rest will be omitted. Different colours were adopted to represent the direction and magnitude of particle rotation, as given in Table 3.4. Figure 3.29, 3.30, 3.31 and 3.32 show the cumulative field of large particle rotation in the specimens with different combinations of particle shape and interparticle friction. Each figure systematically presents four plots at the loading stages defined in Figure 3.18.

Table 3.4: Colour scheme in the plot of particle rotation

Orientation	Magnitude	Colour
Clockwise (ω_{cl})	$\omega_{cl} > 2\bar{\omega}_{cl}$	red
	$\bar{\omega}_{cl} < \omega_{cl} < 2\bar{\omega}_{cl}$	yellow
Counterclockwise (ω_{cc})	$\omega_{cc} > 2\bar{\omega}_{cc}$	blue
	$\bar{\omega}_{cc} < \omega_{cc} < 2\bar{\omega}_{cc}$	light blue

It can be observed that clockwise rotations were dominant in the band which

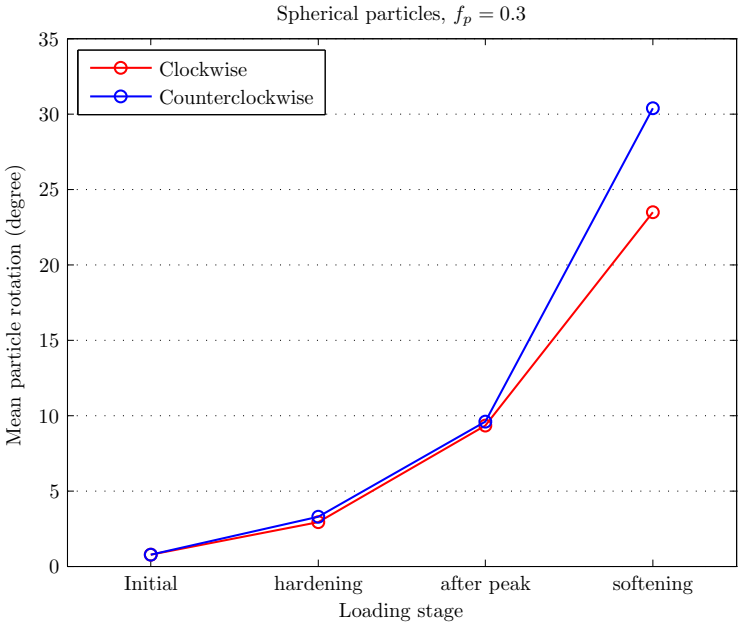

(a)

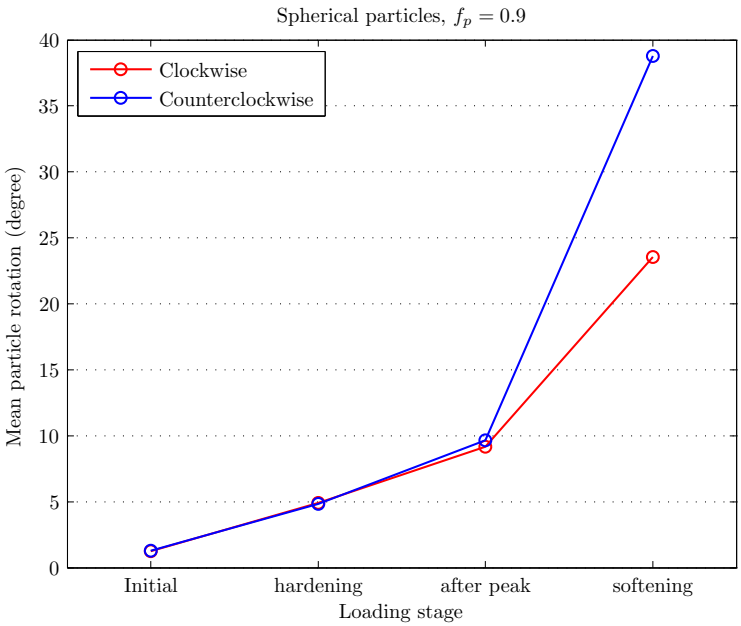

(b)

Figure 3.27: Evolution of mean particle rotation in the specimen composed of spherical particles

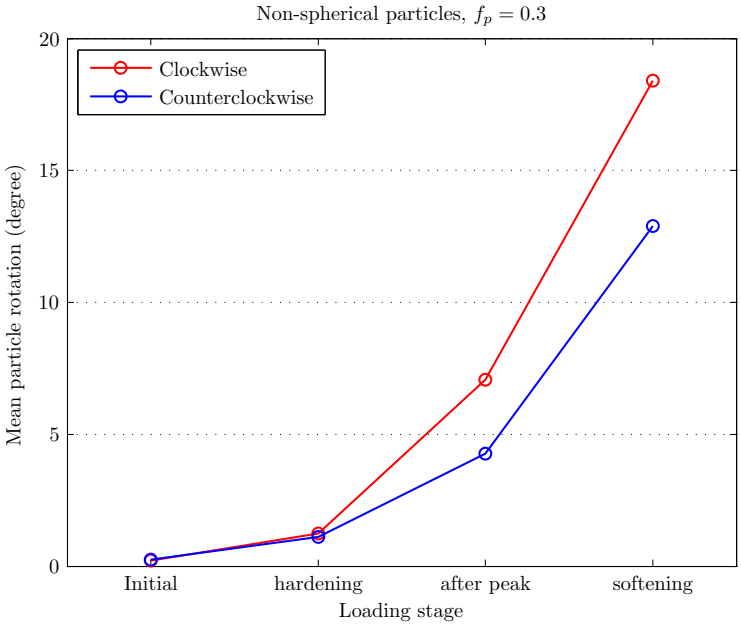

(a)

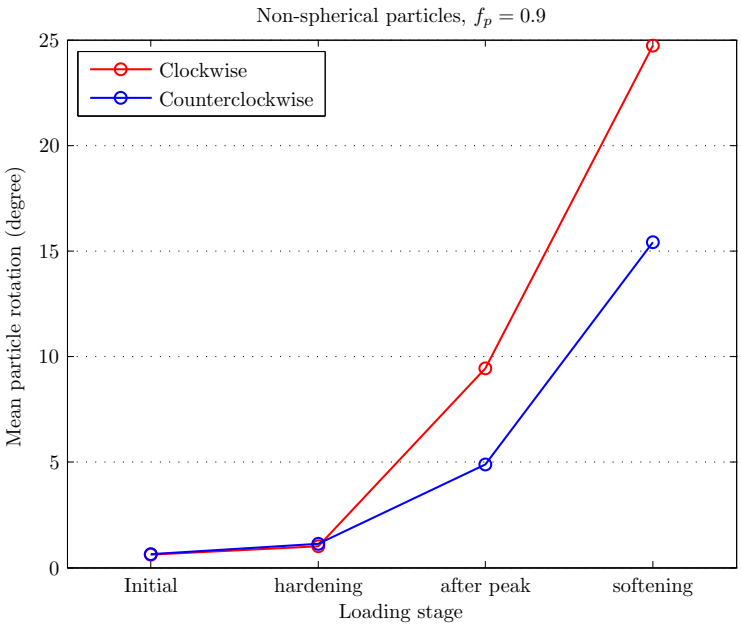

(b)

Figure 3.28: Evolution of mean particle rotation in the specimen composed of non-spherical particles

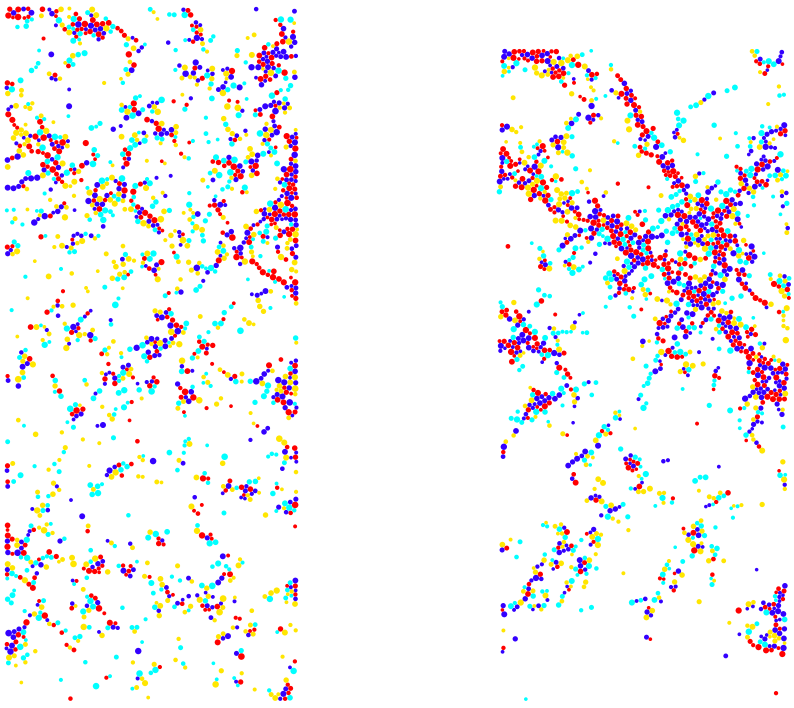

(a) Initial

(b) Strain hardening

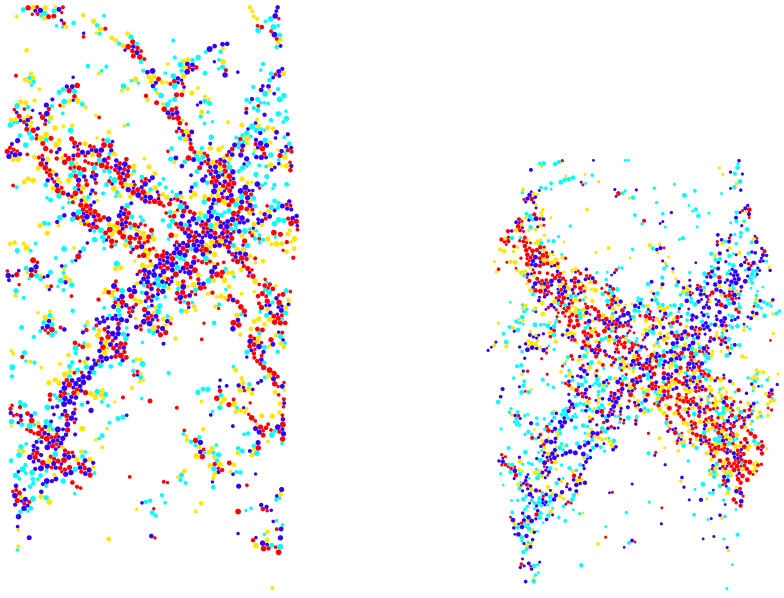

(c) After peak stress

(d) Strain softening

Figure 3.29: Large particle rotation in the specimen composed of spherical particles, $f_p = 0.3$

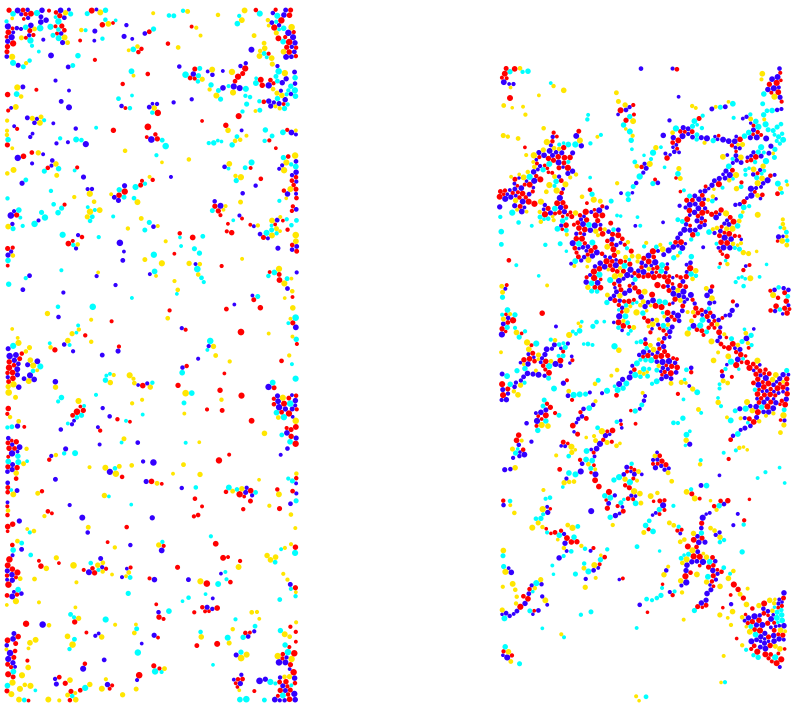

(a) Initial

(b) Strain hardening

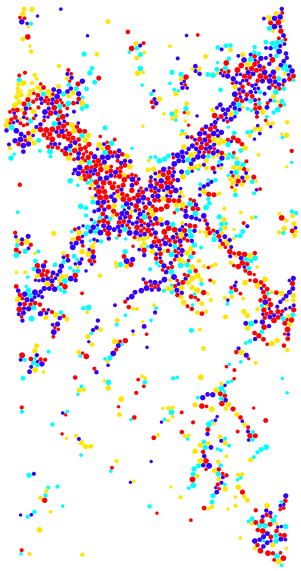

(c) After peak stress

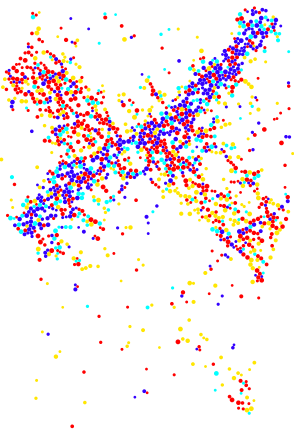

(d) Strain softening

Figure 3.30: Large particle rotation in the specimen composed of spherical particles, $f_p = 0.9$

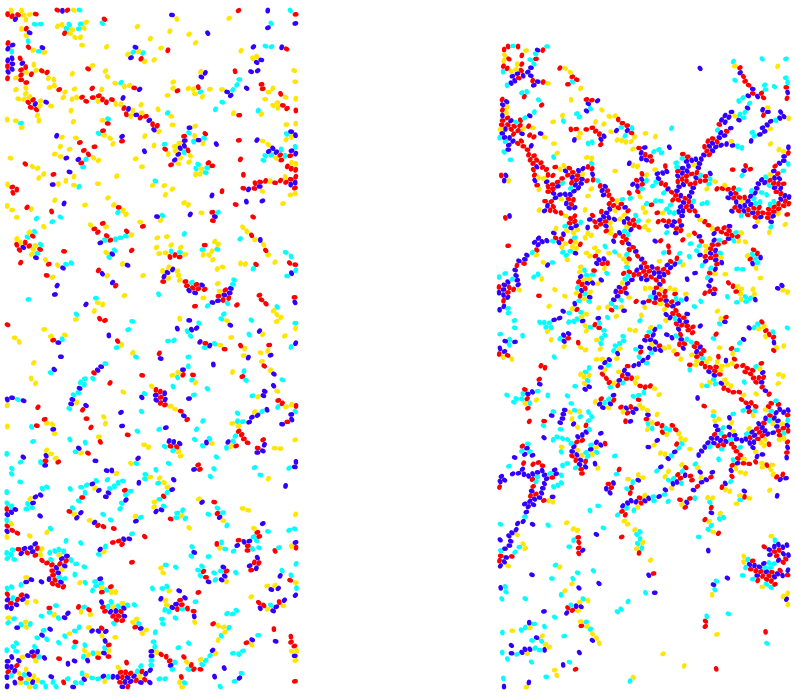

(a) Initial

(b) Strain hardening

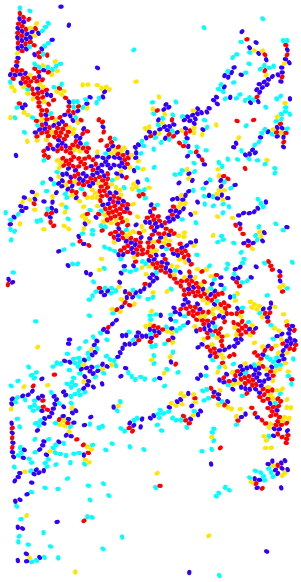

(c) After peak stress

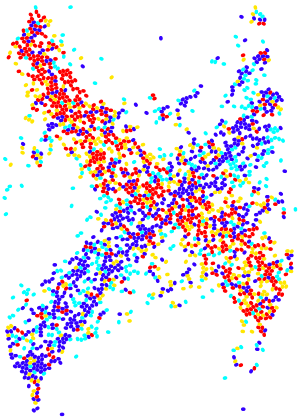

(d) Strain softening

Figure 3.31: Large particle rotation in the specimen composed of non-spherical particles, $f_p = 0.3$

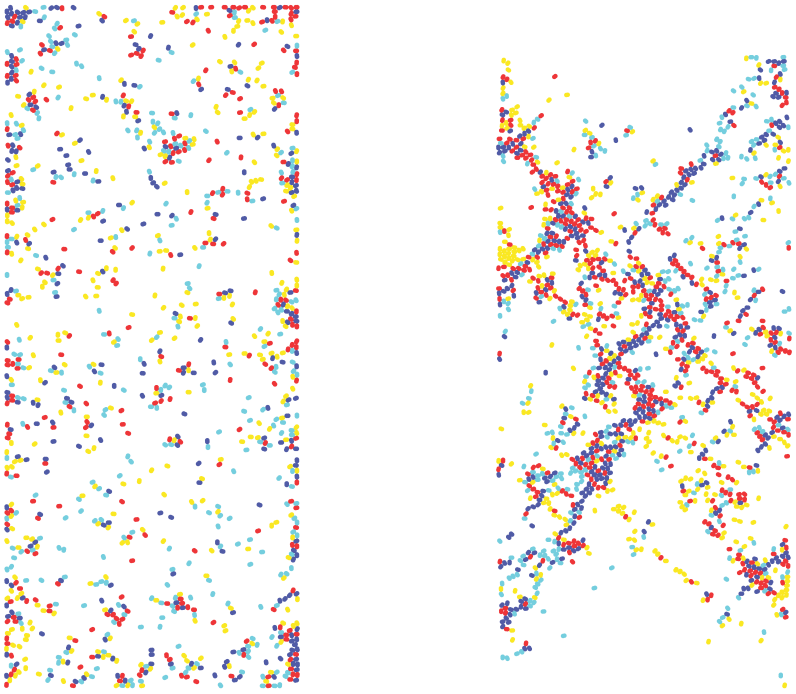

(a) Initial

(b) Strain hardening

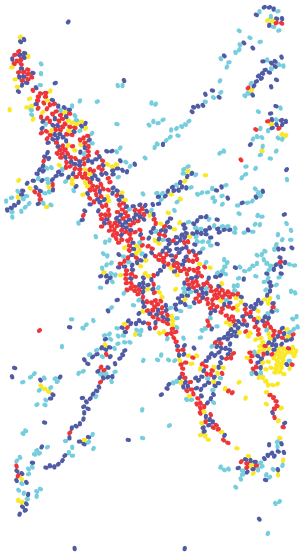

(c) After peak stress

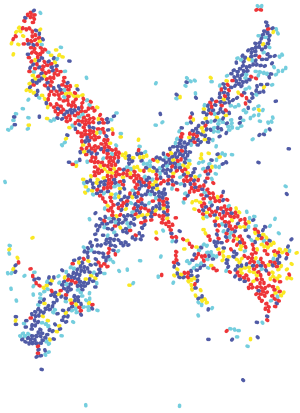

(d) Strain softening

Figure 3.32: Large particle rotation in the specimen composed of non-spherical particles, $f_p = 0.9$

dips to the right, while the rotations in the band that dips to the left tended to be counterclockwise. At initial stage, particles whose rotations exceed the mean value were dispersed randomly within the sample and no clear pattern can be observed. During the hardening phase, several inclined strips which contained most of the large particle rotations began to emerge. After the peak stress, pronounced concentration of particle rotation occurred in some limited inclined zones. Eventually, well structured patterns of large particle rotation at strain softening stage can be easily identified, which are comparable with the particle layer configuration as previously shown in Figure 3.16 and 3.17, indicating the shear bands have fully developed and were highly localised. By visually comparing the above figures, it can be concluded that a larger interparticle friction gave rise to a narrower band, while the band width in the sample composed of spherical particles is wider than that of non-spherical ones. The finding is in accordance with the previous calculation of shear band width, which was based on the particle displacement fields (Table 3.3).

3.4.6 Contact orientation and force chain network

The evolution of shear band is expected to be progressive and the deformation patterns are not necessarily simple. The intrinsic mechanism leading to failure is extremely difficult to justify by simply measuring the boundary load and displacement. DEM simulation has the added advantage of monitoring of variation of several micromechanical descriptors. The changes in the packing fabric can be examined by tracking the evolution of the particle contact orientations and the magnitudes of contact force transmitted in the system. In order to fully investigate the development of anisotropy, the distribution of contact angle and force chains from contacts carrying forces which are larger and smaller than the mean force are analysed separately. The results show that more than 65% of contacts

carry less than the average force, which is similar to the numerical findings of Muthuswamy and Tordesillas (2006a).

To cover the onset of non-homogeneous deformation and the formation of a shear band, the microstructure was analysed at similar vertical strain steps as outlined previously in Figure 3.18. Considering that the force chains are subject to instantaneous change approaching the peak strength, therefore one additional stage is introduced at that point. The stages at which key changes occurred and thus the micromechanical analysis were applied are (O) before the loading started; (A) strain-hardening; (B) the peak of stress ratio was achieved; (C) sudden drop from the peak stress; and (D) large deformation at the end of loading when the shear band has fully developed. By way of illustration, interparticle and boundary friction were selected as 0.9 and 0.3, respectively. Figure 3.33 and 3.34 show the distribution of the contact orientation as radial plots at different loading stages for spherical and non-spherical particles, respectively. In these plots, the frequency of occurrence for each contact angle is normalised with the maximum value in the total contact network and 0° represents two particles in contact horizontally whilst 90° represents vertical contact orientation.

The information in the plots suggests that the evolution of contact orientation for both types of particles are rather similar. Before the loading started, both strong and weak force network exhibited no preferred direction, representing a typical isotropic packing at Stage O. As the vertical loading increased, the large contact forces progressively orientated themselves towards the direction of vertical loading, indicating the initial isotropic state has gradually disappeared during the course of loading. This contact anisotropy was primarily generated by a reduction in the number of normal contacts with orientations close to the direction of maximum extensional deformation, i.e. the horizontal direction. These observations indicated that the early decrease of coordination number as shown in Figure 3.10 can be attributed to the loss of contacts in the horizontal direc-

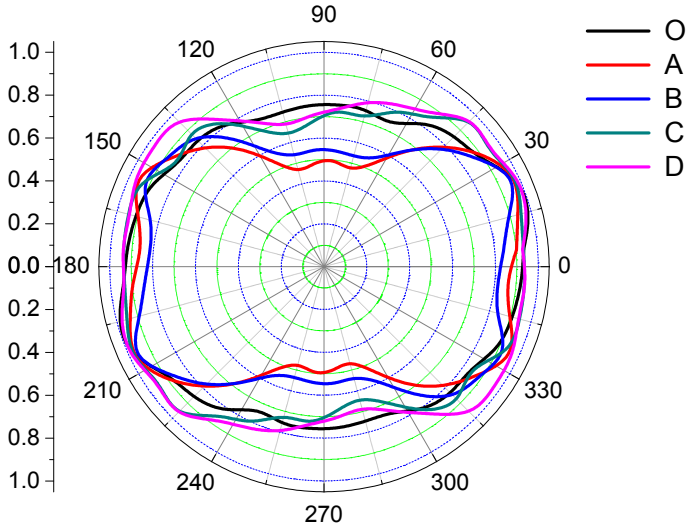

(a) $F_i < \bar{F}$

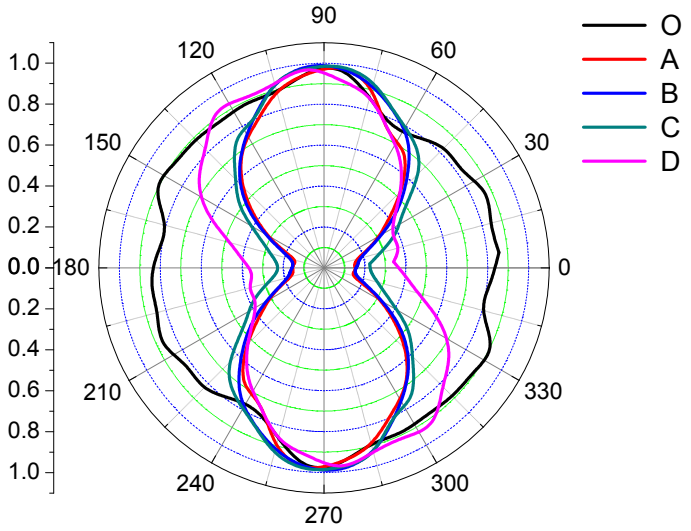

(b) $F_i > \bar{F}$

Figure 3.33: Polar distribution of contact orientation for spherical particles

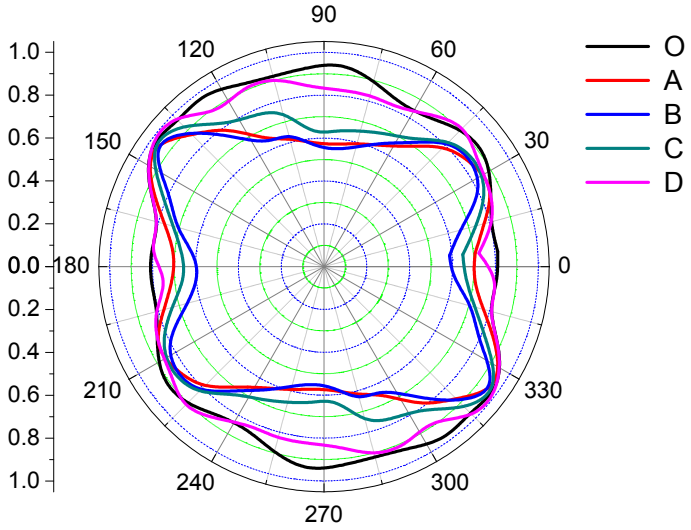

(a) $F_i < \bar{F}$

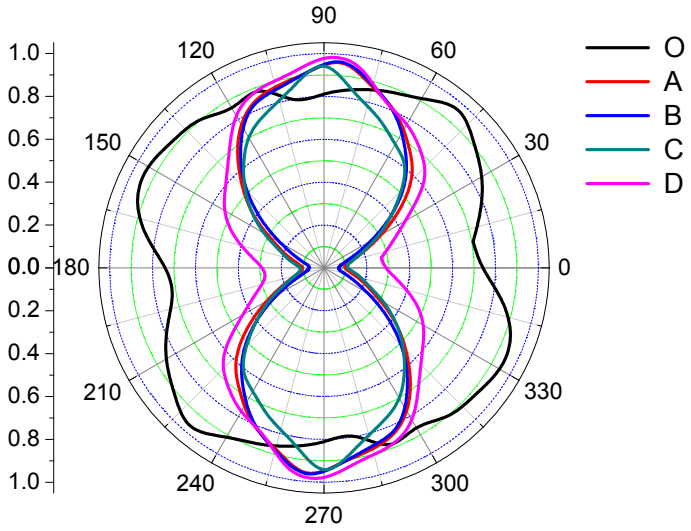

(b) $F_i > \bar{F}$

Figure 3.34: Polar distribution of contact orientation for non-spherical particles

tion. During the rest of the loading course, the contact orientation distribution for the strong force network were very similar, with the predominant preference in the vertical direction. These force chains aligned themselves in the direction of biaxial compression induced at the boundary, which maintained the structural stability as the deformation proceeded. For spherical particles, the peak of contact orientation in strong contact network rotated from the vertical plane and fell in the range between 90° and 120° at the end of the simulation. This is most probably due to the excessive rotations of spherical particles within the sample, which promoted the breakage of force chains and thus compromised the ability for the system to sustain further deformation.

Although the induced anisotropy was clear in the strong contact network for both types of particles, the distributions of contact angle from the weak force network did not change considerably. Muthuswamy and Tordesillas (2006a) pointed out that the persistence of a force chain not only requires a constant imposition of external loading throughout its length, but also the aid of its adjacent chains which mostly come from the weak contact network, to brace the long chains and to resist the repulsive forces that push away the particles belonging to the chain. Therefore, despite carrying only a small portion of force, these chains belonging to the weak network provide the necessary balanced equilibrium for the strong force structure to persist and grow.

Since the bulk behaviour of a granular sample depends on the interparticle contacts through which the forces are transmitted, visualisation of force chains can provide substantial information pertaining to the nucleation and propagation of strain localisation. As already discussed in Chapter 2, the force transmission within granular solids is sensitive to particle shape and arrangement, and distributed in a complex, non-uniform manner. In search of structural features of the strong force network that bears the largest proportion of stress, only force chains which carry the above-average normal contact forces were plotted. For

better visualisation, each single force chain will be depicted via a bar connecting the centres of two particles that are in contact, the colour of which is assigned according to the magnitude of contact force it is carrying, as given in Table 3.5. The evolutions of the strong force network throughout the deformation were plotted in Figure 3.35 and 3.36 for spherical and non-spherical particles, respectively.

Table 3.5: Colour scheme in the plot of force chains

Magnitude of force chain (F_i)	Colour
$F_{mean} < F_i < 2F_{mean}$	blue
$2F_{mean} < F_i < 3F_{mean}$	green
$F_i > 4F_{mean}$	red

It is observed that the plots of force chains give a reasonable visual approximation to the predominant trends as the deformation proceeds. At stage O, the directions of chains are evenly distributed, which again supports the findings from contact orientation. Once the loading started (Stage A), column-like structures were generated in the whole specimen, which adjusted the distribution of contacts aligned to the maximum principal stress axis in the early course of compression. A proportion of chains formed during the hardening process (stage A) became unstable and buckled as observed in Stage B, when the peak stress was achieved. This process then promoted buckling of the neighbouring force chains, which gradually concentrated into an inclined band (Stage C). The collapse of force chains thus contributed to the growth of large voids within the shear band. This mechanism provides supporting evidence of the reduction in bulk strength. At the end of the compression (Stage D), a significant amount of contact losses were clearly noticed within the specimen. Several long force chains carrying the largest normal contact forces (red bars) formed in the sample composed of non-spherical particles, serving as new pathways for force transmission and thus maintaining the structural stability.

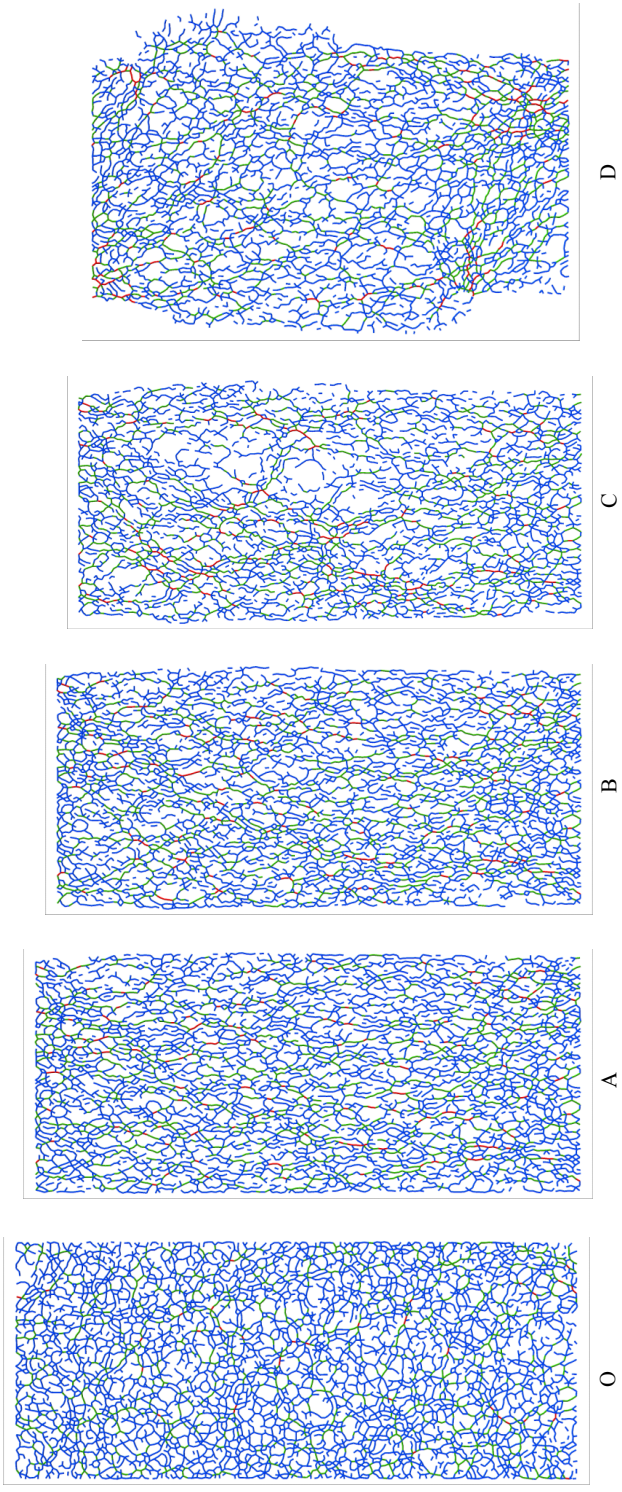

Figure 3.35: Force chains for spherical particles

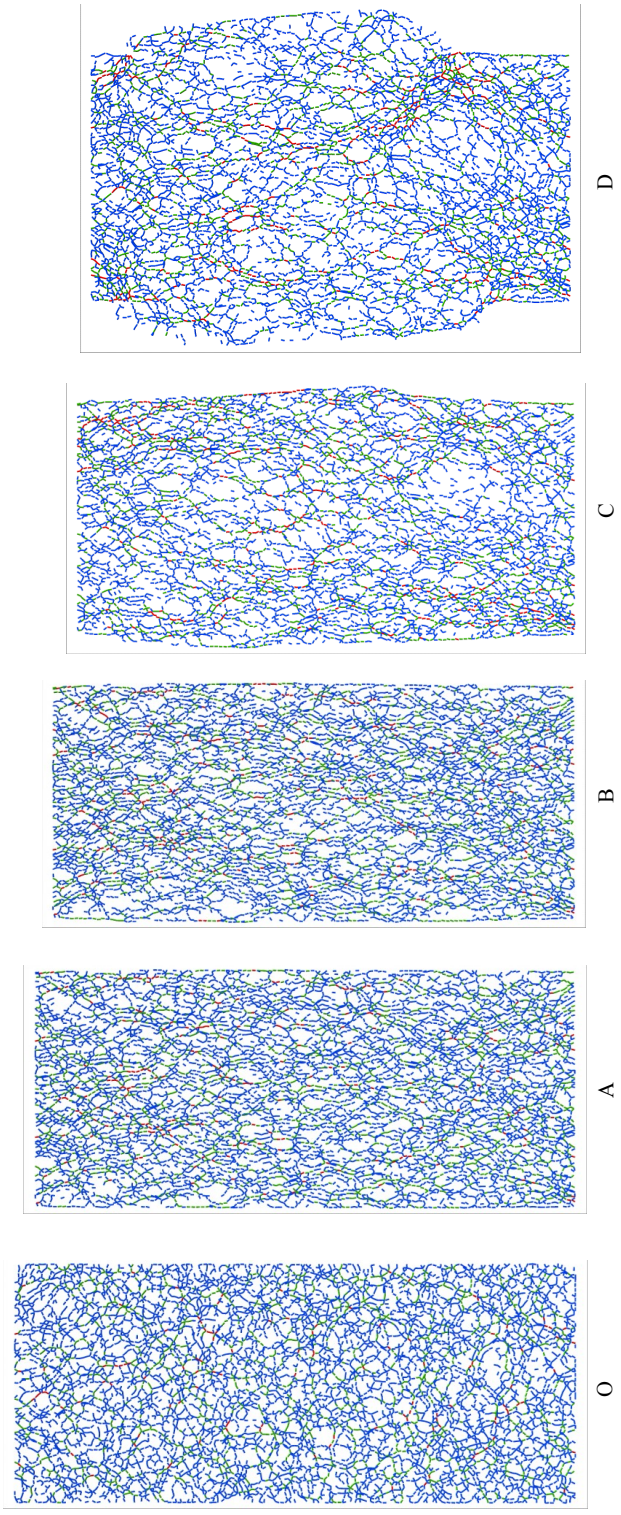

Figure 3.36: Force chains for non-spherical particles

3.4.7 Stress distribution

The rather ramified network of force chains as shown in earlier section suggests that not all the particles carry the same loads. Therefore, it can be assumed that the stress distribution in the sample is highly heterogeneous. Here, the stress development within the specimen is investigated based on the algorithm of measurement sphere as introduced in Section 2.8. By way of illustration, only the case with interparticle friction of 0.9 are presented for both spherical and non-spherical particles.

Before performing systematic stress analysis, studies using different combinations of radius and spacing of the measurement spheres (Table 3.6) were carried out, which will affect the stability and accuracy of the measured quantity. Figure 3.37 illustrates the resulting field of vertical stress for a given loading stage. All the contours show similar patterns of stress concentration at certain locations within the sample. Along with the decrease of averaging diameter, it started to pick up the discrete behaviour, showing the chain-like structures. Muir Wood (2004) pointed out that stress is only relevant when the averaging scale is larger than both individual particles and the force chains. After the comparison, it is determined that MS3 (i.e. radius of $5D_{50}$ with spacing of $1D_{50}$) is the ideal mesh scheme that can properly reflect the distribution of macroscopic stress in the current DEM simulation.

The stress development in the specimen at increasing strain levels are presented in contours. For spherical particles, horizontal stress (Figure 3.38), vertical stress (Figure 3.39) and shear stress (Figure 3.40) were considered at five loading stages as specified earlier. Similarly, these three stress components for non-spherical particles were presented in Figure 3.41, 3.42 and 3.43, respectively.

Looking at horizontal stress, once the loading started, there were noticeable stress concentration near the top and bottom of the sample, which can be at-

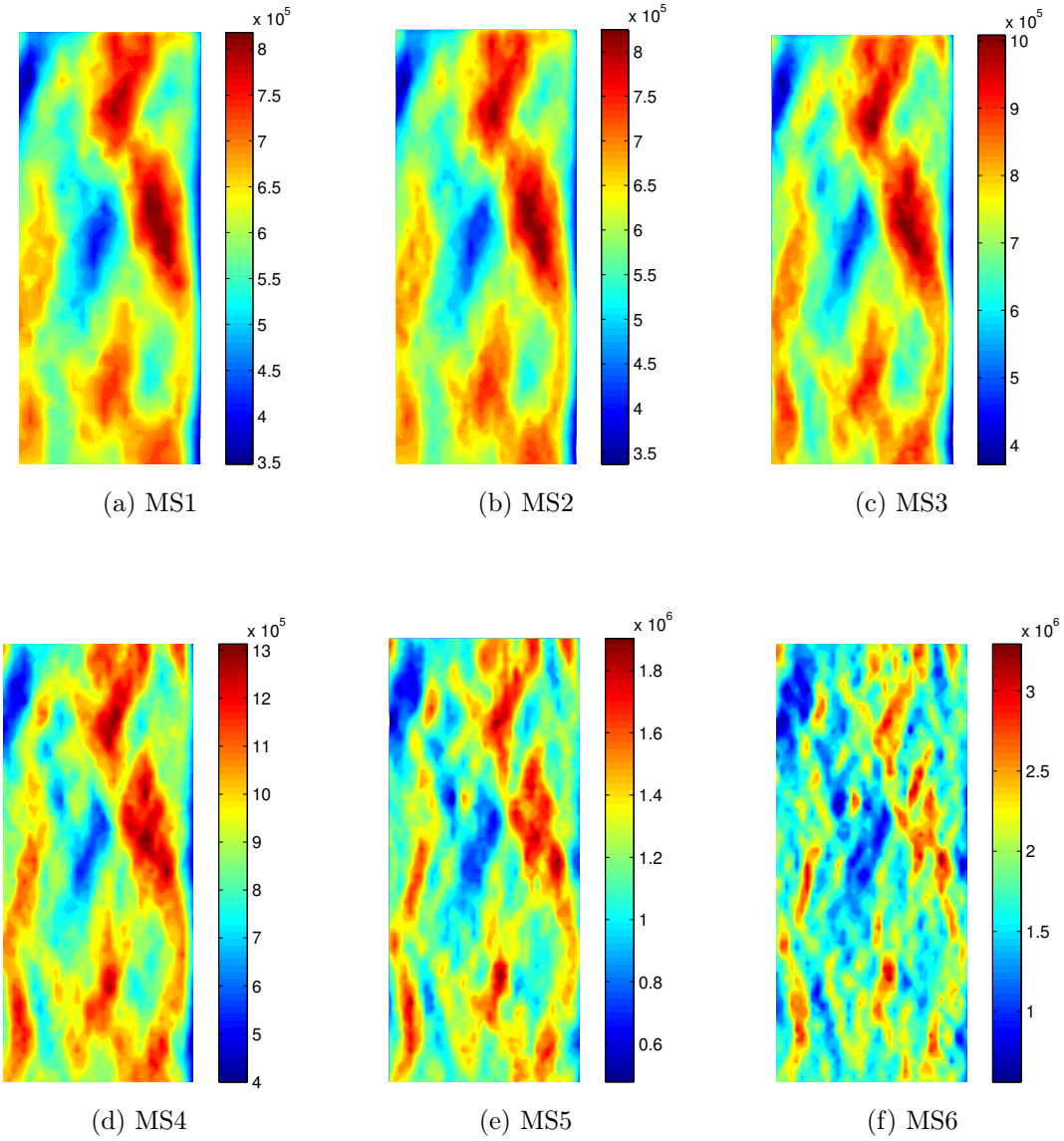

(a) MS1 (b) MS2 (c) MS3

(d) MS4 (e) MS5 (f) MS6

Figure 3.37: Evaluation of vertical stress in spherical particles using measurement spheres with different radius and spacing

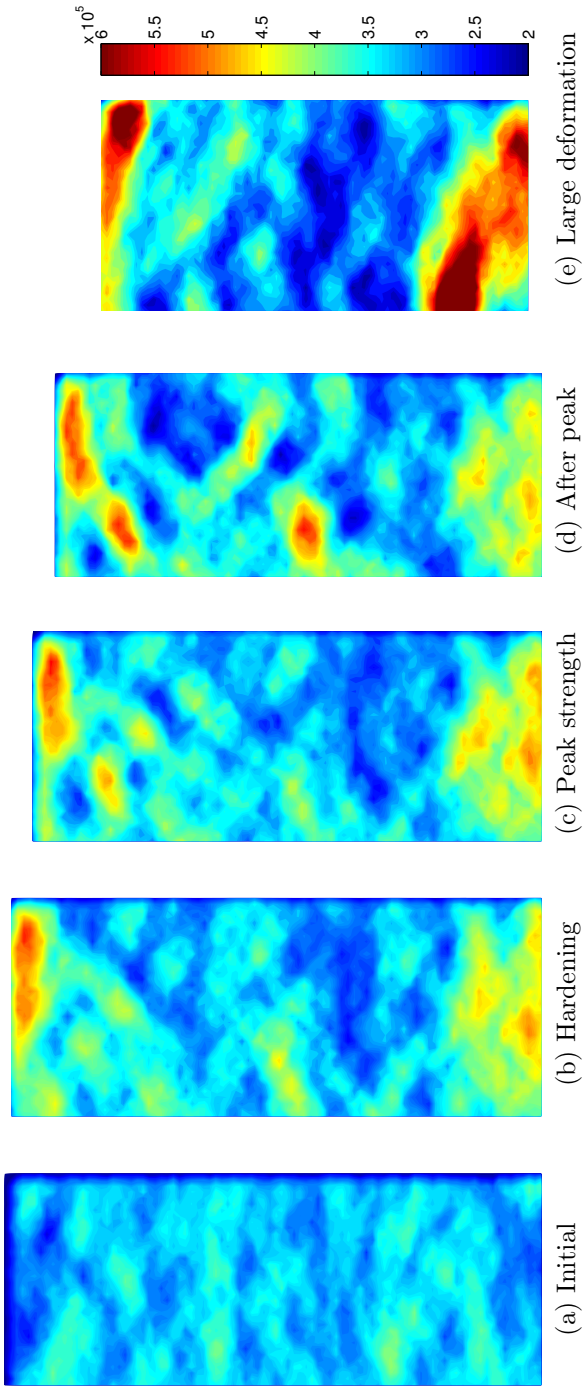

Figure 3.38: Horizontal stress in spherical particles

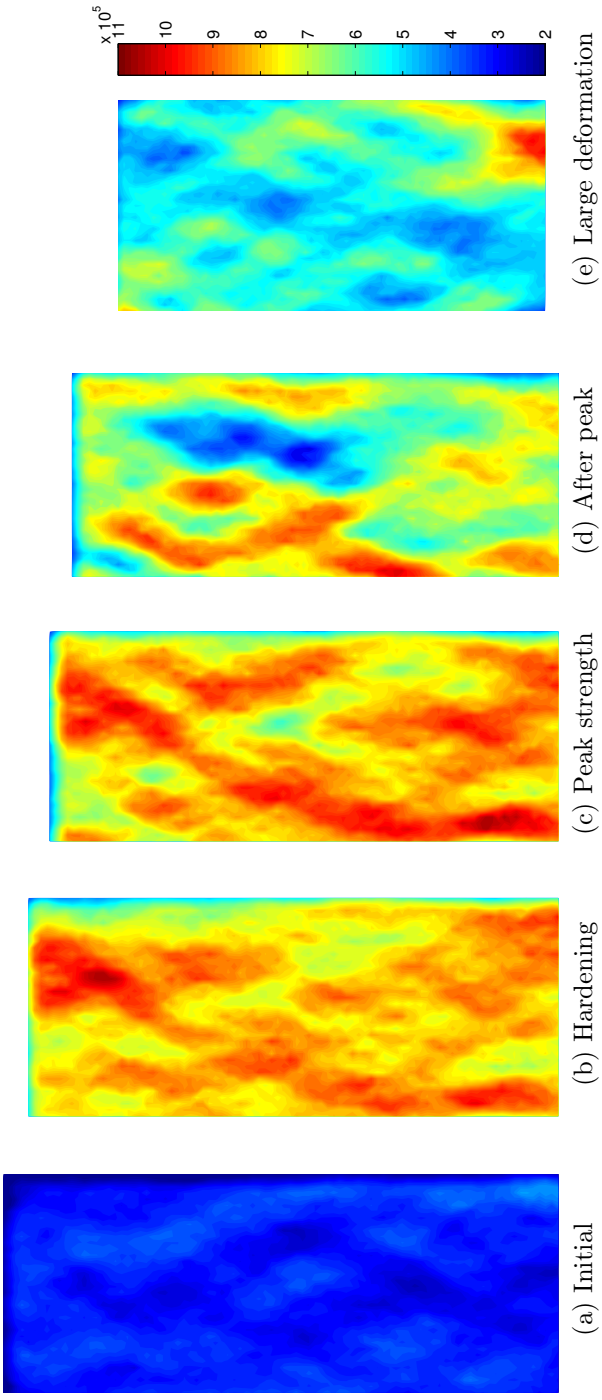

Figure 3.39: Vertical stress in spherical particles

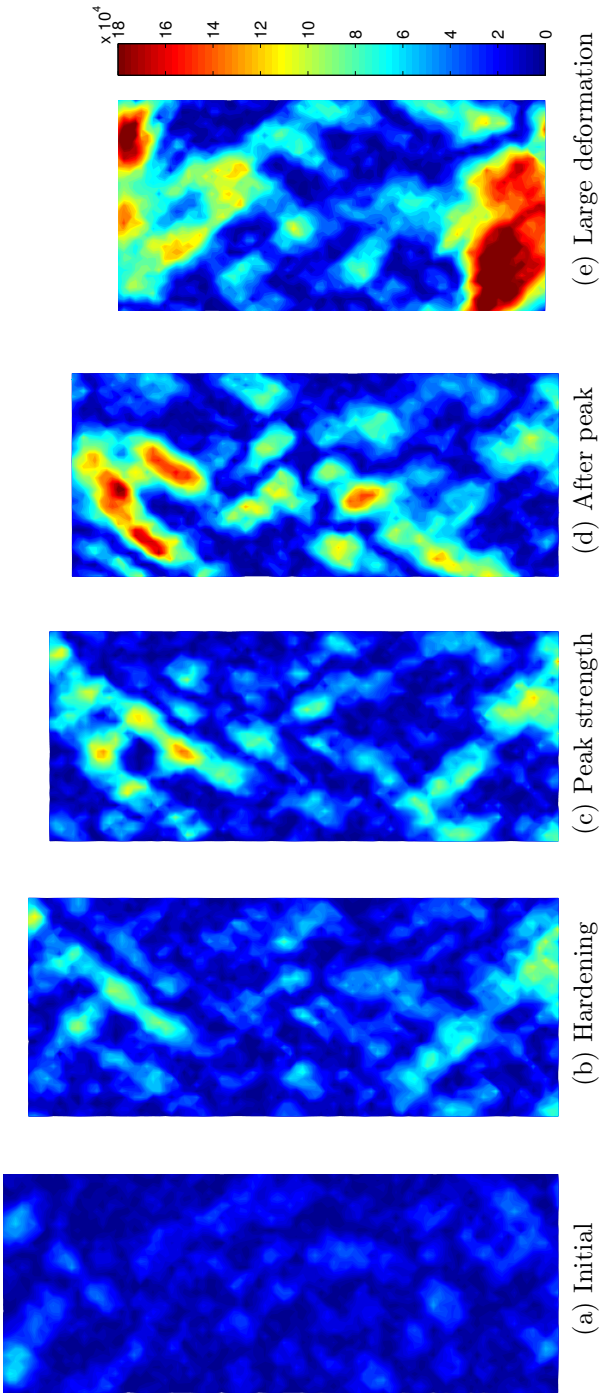

Figure 3.40: Shear stress in spherical particles

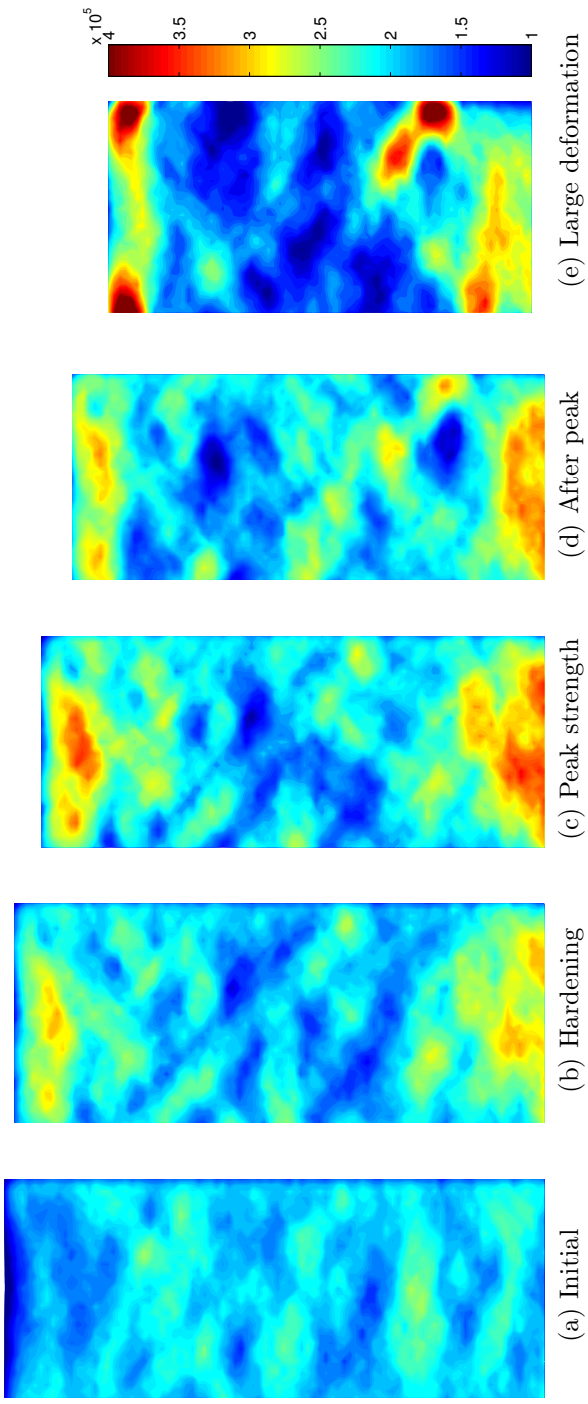

Figure 3.41: Horizontal stress in non-spherical particles

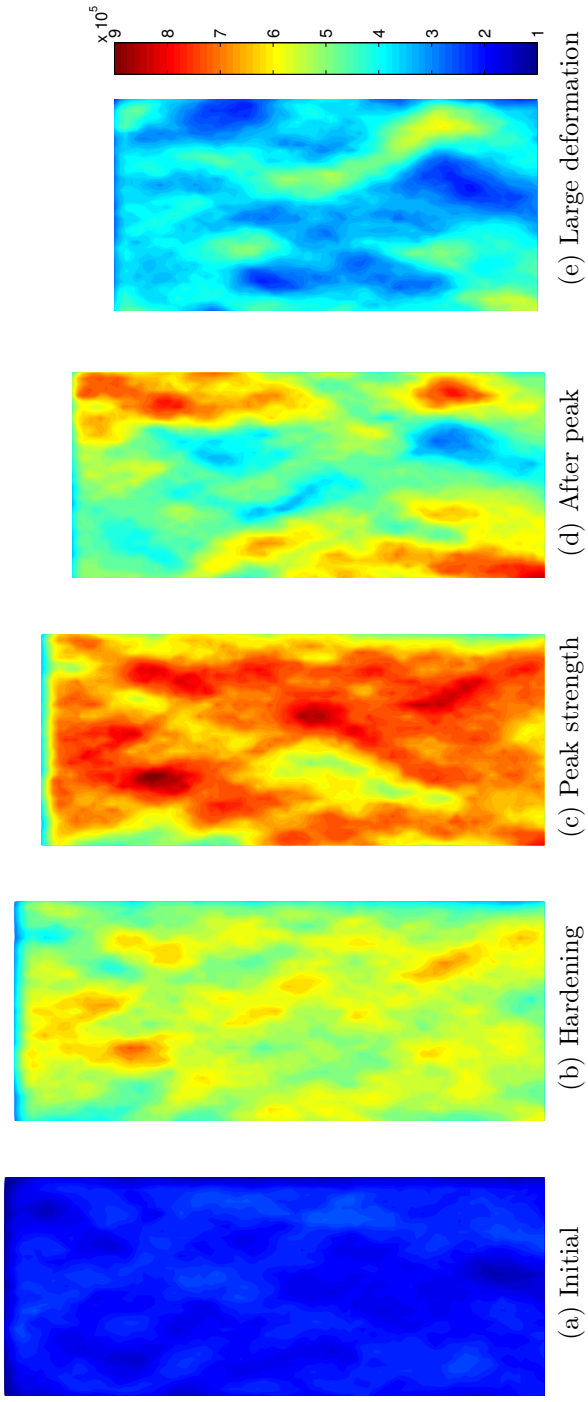

Figure 3.42: Vertical stress in non-spherical particles

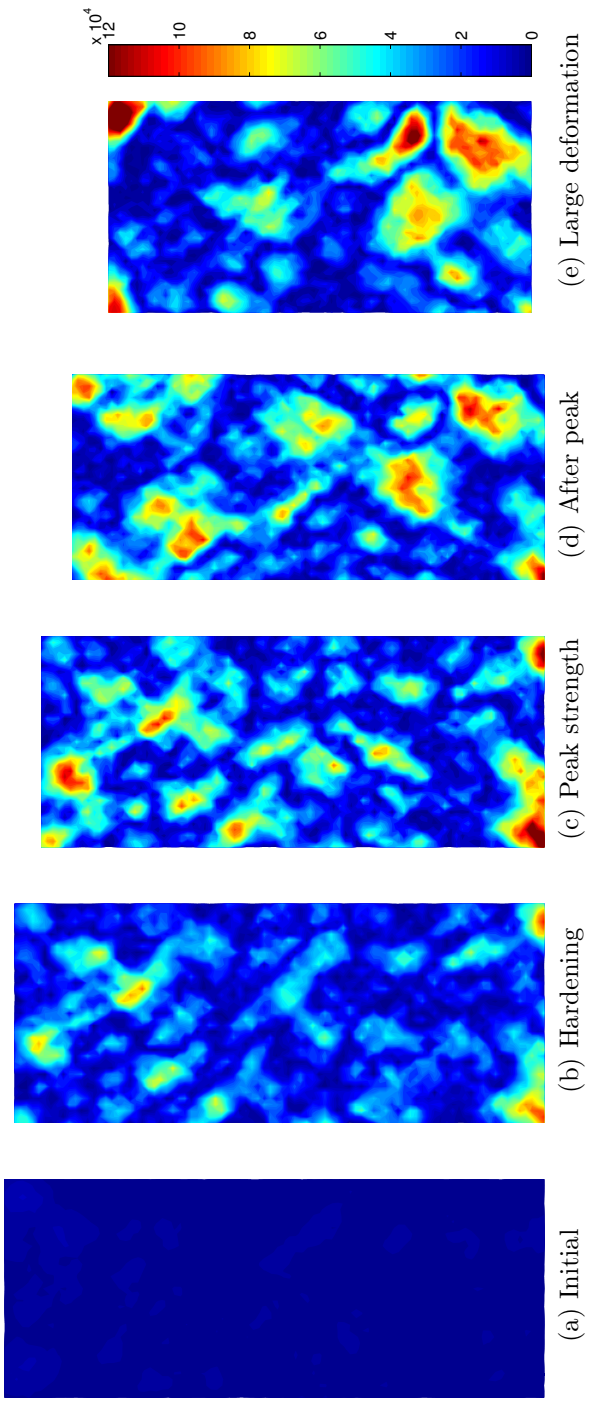

Figure 3.43: Shear stress in non-spherical particles

Table 3.6: Characteristics of measurement spheres used in stress calculation

ID	Radius (D_{50})	Spacing (D_{50})
MS1	6	3
MS2	6	1
MS3	5	1
MS4	4	1
MS5	3	1
MS6	2	1

tributed to the frictional forces acting on the loading platens, providing the necessary lateral stability. Recalling the fact that horizontal stress acting on the two membrane boundaries was kept as constant, therefore, the magnitude of horizontal stress did not change significantly elsewhere in the sample. Due to the external loading was applied on vertical direction, the patterns of vertical stress can be directly related to the formation and collapse of force chains. Until reaching the peak strength, the vertical stress experienced increasing concentration, followed by significant decrease along with the development of shear band in the softening regime.

3.4.8 Strain calculation

It is clear that DEM simulation is able to reproduce the shear band formation in granular solids under biaxial compression. In particular, the bulk responses have demonstrated the tendency that strain localisation can develop into one or two dominant shear bands eventually. However, what remains less understood is the precise evolutionary stage through which such diffused deformation develops to fully localised response. Obviously, analyses carried out over relatively large vertical strain increment (around 5%) in previous section unavoidably lost infor-

mation of such detail and interest. This section explores the application of PIV in DEM strain calculation over small time step. The results presented in this section are part of a more extensive research effort to understand the bifurcation instability at a far greater level of detail.

3.4.8.1 A hybrid PIV-DEM strain measurement

Here, a hybrid DEM-PIV approach was introduced to calculate the local strain field within a granular sample near the achievement of peak strength, attempting to further clarify the nucleation of shear band. A modified image recording technique is used to implement PIV in the current DEM simulation. High resolution images (5000×5000 pixels) containing the whole particle sample can be directly generated from PFC^{3D}. Whereas fluid requires seeding particles to produce characterisations upon which image processing can operate, similarly each particle in a discrete element model can be uniquely coloured between adjacent grains when plotted. The resolution and colour scheme are sufficient to detect and separate particles as illustrated in Figure 3.44.

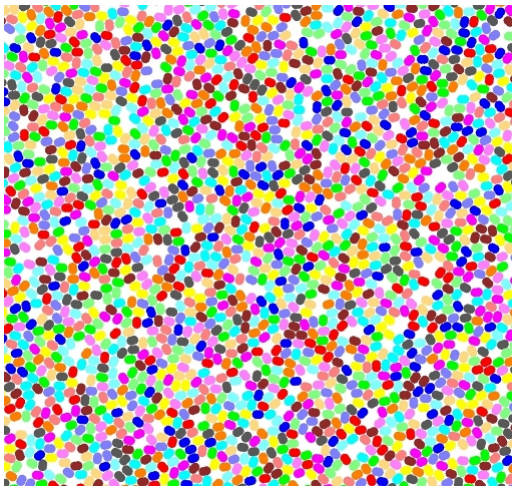

Figure 3.44: Coloured particle in DEM model

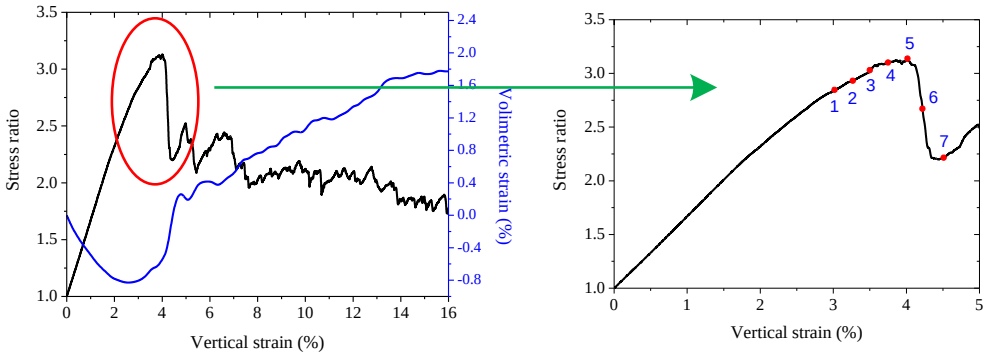

Figure 3.45: Data points indicate the strain interval for PIV analysis on global stress-strain curve

In order to establish a precise relationship between the achievement of peak stress and the nucleation of shear localisation, the peak stress region in the global stress-strain response is enlarged and shown in Figure 3.45. Each number noted on the curve represents a point at which an image was captured. There are 7 points marked on the curve with vertical strain increment of around 0.2-0.25%. The location of peak stress is denoted as "point 5", which divides the selected loading region into two parts, namely pre-peak (point 1, 2, 3 and 4) and post-peak (point 6 and 7) phase. PIV analyses were first conducted between images captured at two adjacent reference points abovementioned, from which the displacement fields were evaluated. Preliminarily, the size of interrogation window was 64×64 pixels (roughly equals to $6D_{50}$) while the spacing between two adjacent windows was set as 32 pixels. Strain components were then calculated based on the displacement data between adjacent interrogation windows.

The calculated shear strain compiled from the displacement fields in samples with different particle shapes and interparticle frictions are presented in contour plots. For the assembly composed of spherical particles ($f_p = 0.3$), the evolution of incremental shear strain is presented in Figure 3.46. In the first plot, a shear band initiated which was soon followed by several other localisations and

eventually one single dominant band emerging with an opposite inclination direction compared to the one firstly nucleated. The first four contour plots represent loading behaviour that took place prior to the achievement of peak stress. While slightly concentrated shear strain initiated from the middle right of the specimen can be discerned in the first two contours (stage 1-2 and 2-3), evidence of well defined strain localisation was not concrete. Interestingly, in the next strain increment (stage 3-4), three spots of highly localised deformation can be identified, with different locations and degrees of shear strain concentration. In the fourth plot (stage 4-5) leading up the peak stress point, one of the most prominent band from the previous stage that ranged from lower left to upper right of the sample started to manifest itself by exhibiting a strong strain concentration. This band continued to grow as seen in the last two plots (stage 5-6 and 6-7), and it eventually evolved into a dominant shear band during the softening phase.

Figure 3.50 shows the shear strain contours for non-spherical particles with $f_p = 0.3$. Clearly the strain concentration initiated from the upper left corner at quite an early stage before reaching the peak strength, followed by gradual intensification and smoothly developed into a definitive shear band, experienced less diffuse localisation compared to the spherical case. On the other hand, when the interparticle friction was increased ($f_p = 0.9$), for both spherical (Figure 3.48) and non-spherical (Figure 3.52) particles, a more intense competing mechanism was observed in the form of evidenced conjugate shear bands with a similar degree of strain concentration, indicated by the "V-shape" contour region in the colour of dark red.

The alternating patterns of shear localisation revealed from PIV analysis over small global strain increment provides more clarifications with regard to the bifurcation instability and temporal development of shear band, which is less clearly understood in Chapter 3. A number of the existing literature reported that the strain localisation occurred at or beyond the peak stress. Also, the buckling

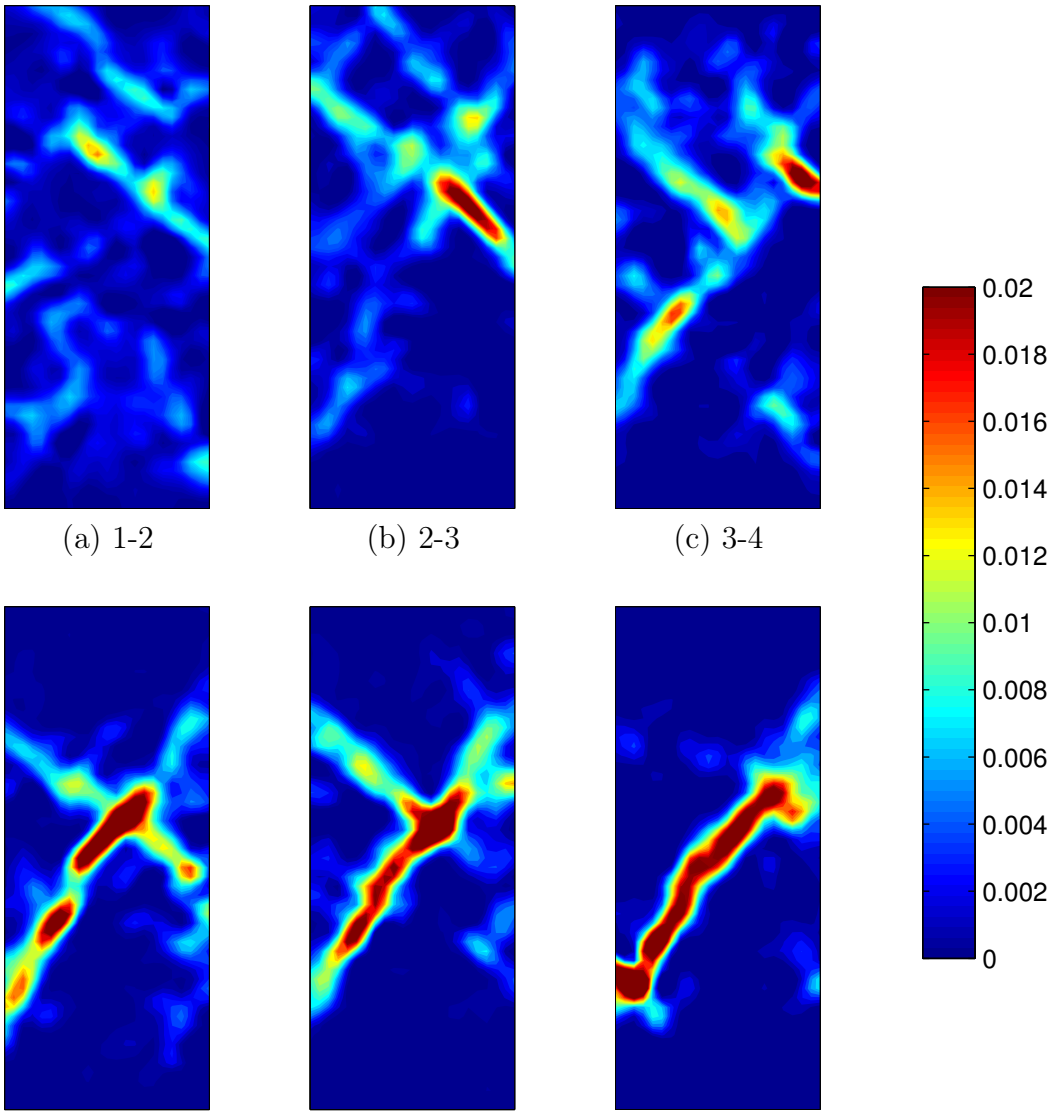

(a) 1-2 (b) 2-3 (c) 3-4

(d) 4-5 (e) 5-6 (f) 6-7

Figure 3.46: PIV calculated incremental shear strain for spherical particles, $f_p = 0.3$

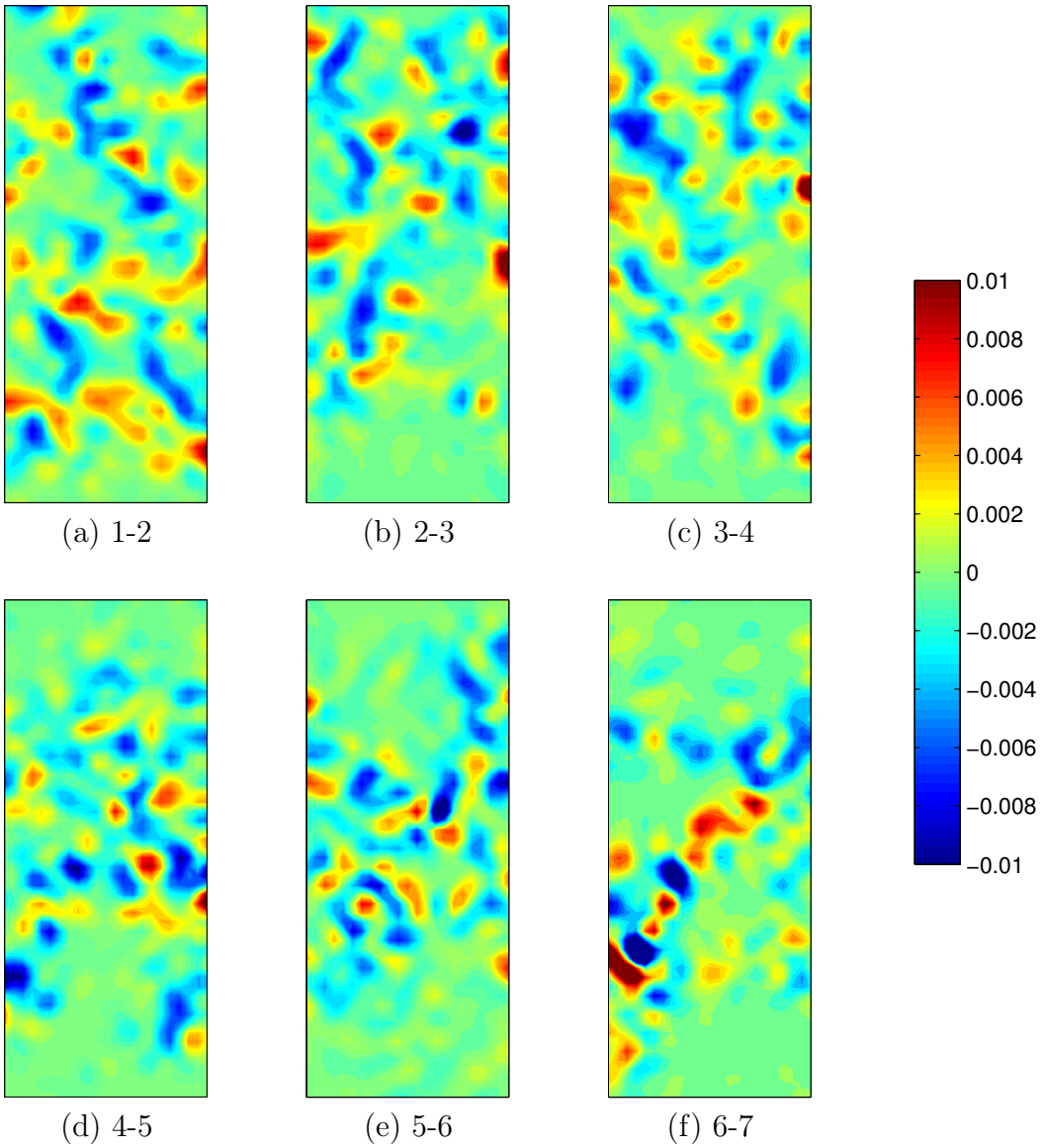

(a) 1-2 (b) 2-3 (c) 3-4

(d) 4-5 (e) 5-6 (f) 6-7

Figure 3.47: PIV calculated incremental volumetric strain for spherical particles, $f_p = 0.3$

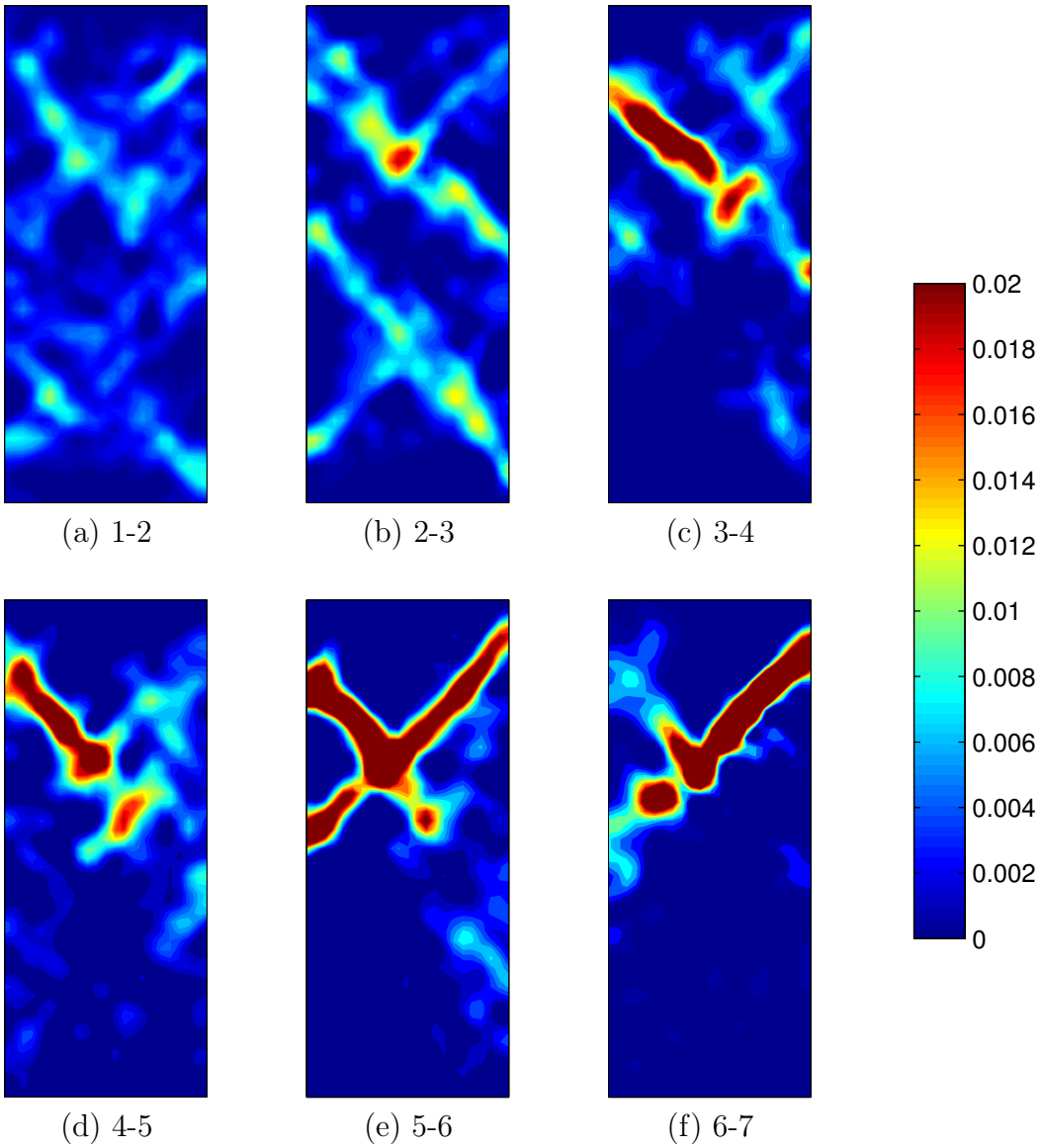

(a) 1-2 (b) 2-3 (c) 3-4

(d) 4-5 (e) 5-6 (f) 6-7

Figure 3.48: PIV calculated incremental shear strain for spherical particles, $f_p = 0.9$

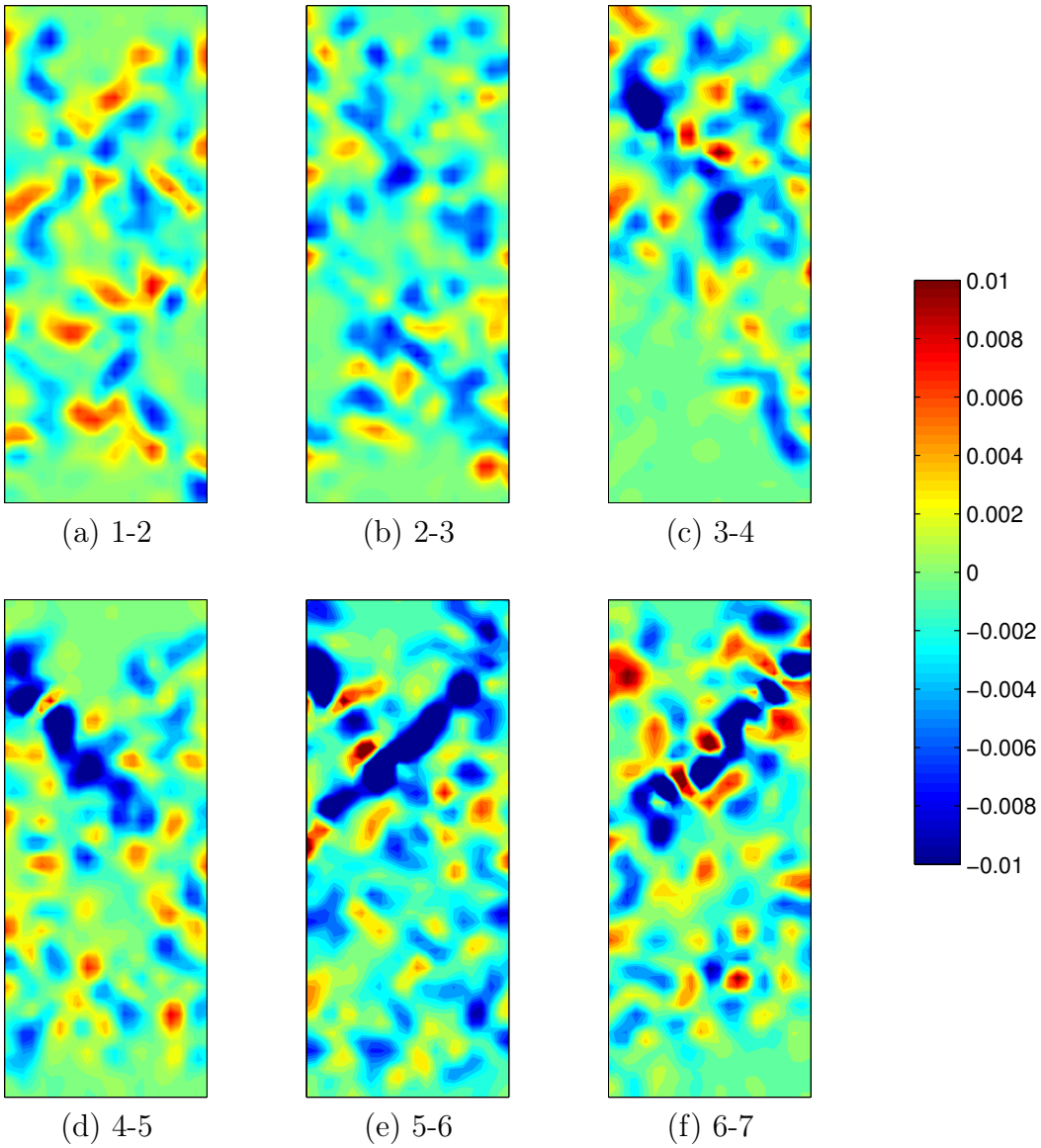

(a) 1-2 (b) 2-3 (c) 3-4

(d) 4-5 (e) 5-6 (f) 6-7

Figure 3.49: PIV calculated incremental volumetric strain for spherical particles, $f_p = 0.9$

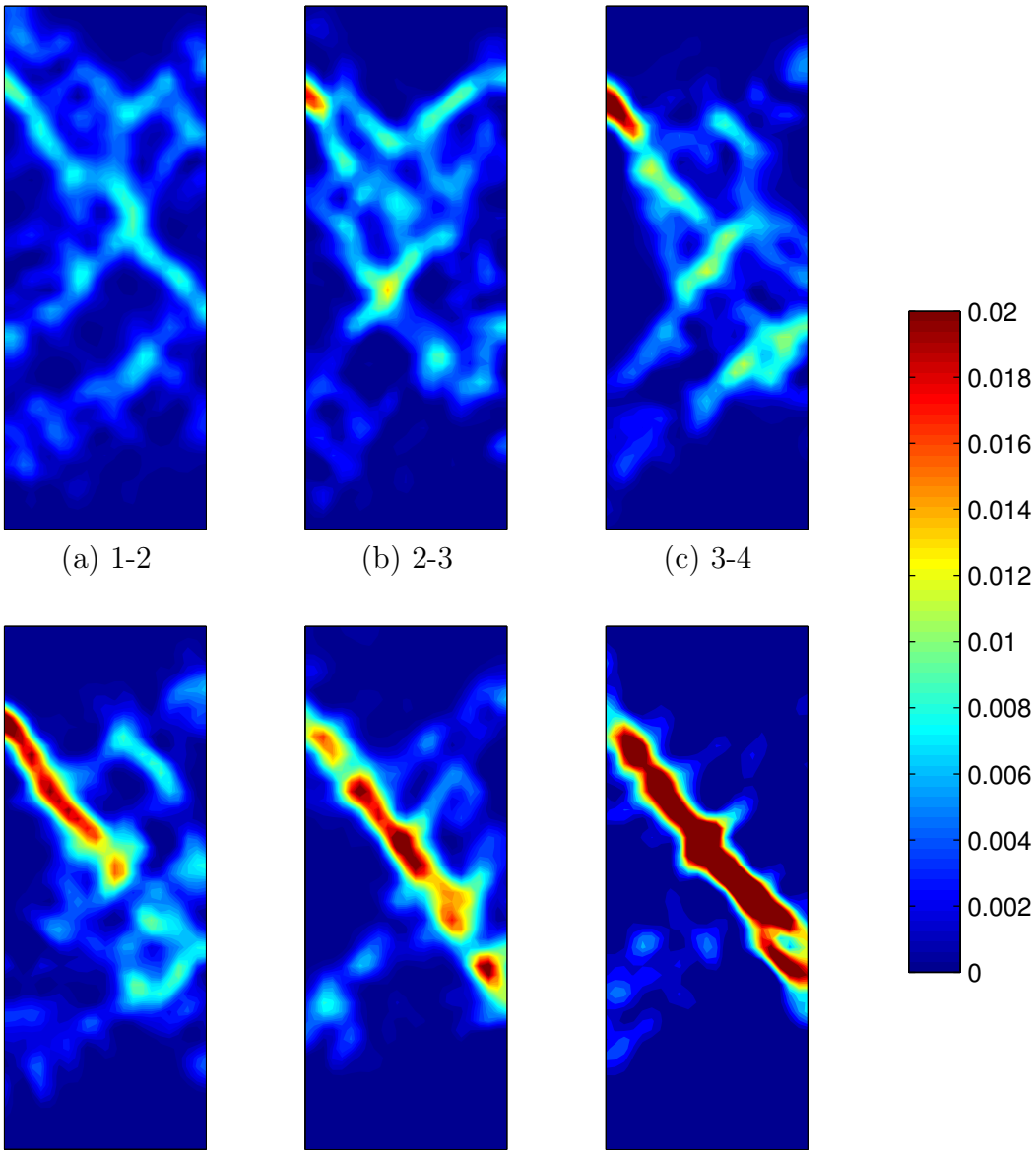

(a) 1-2 (b) 2-3 (c) 3-4

(d) 4-5 (e) 5-6 (f) 6-7

Figure 3.50: PIV calculated incremental shear strain for non-spherical particles, $f_p = 0.3$

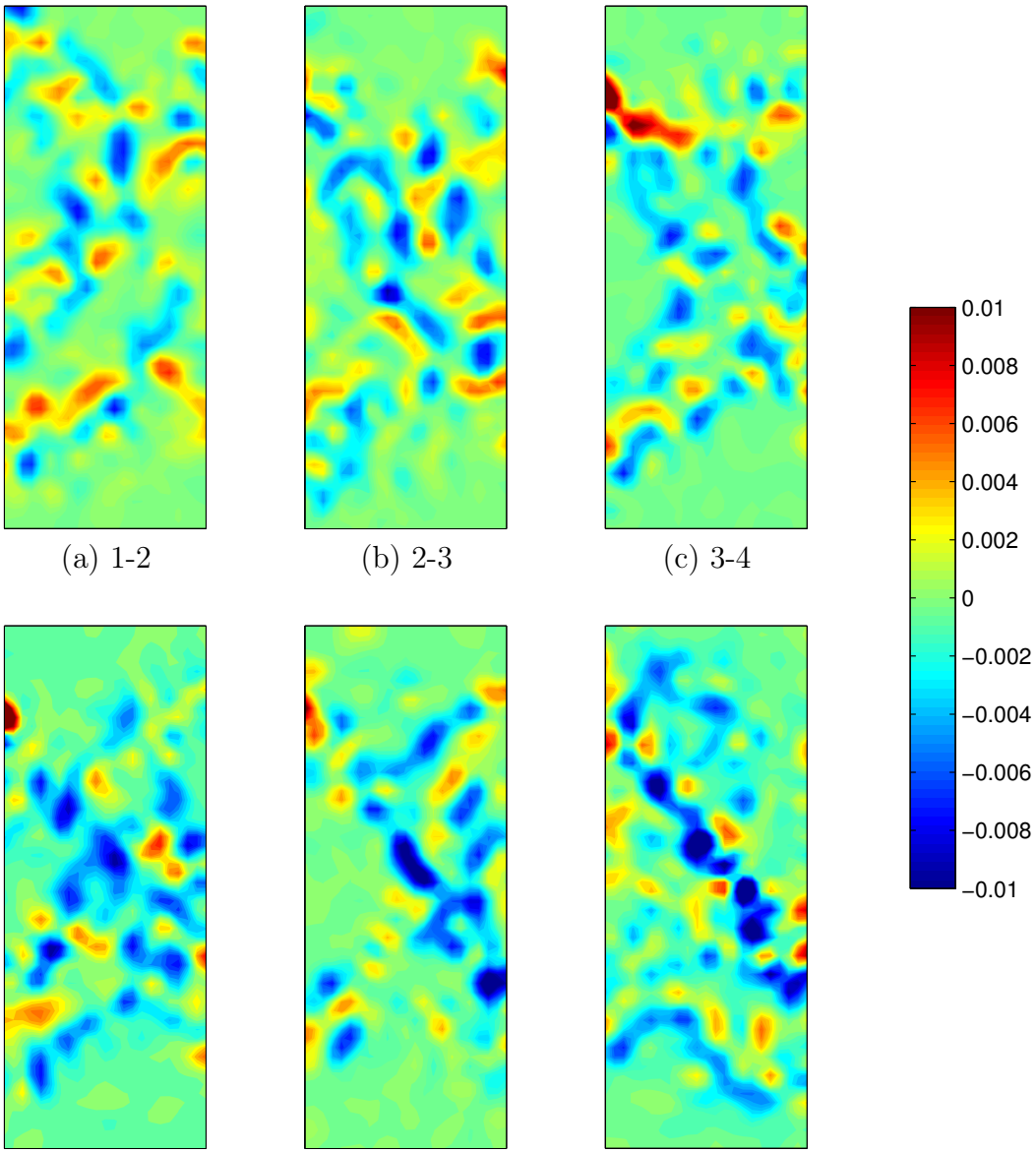

(a) 1-2 (b) 2-3 (c) 3-4

(d) 4-5 (e) 5-6 (f) 6-7

Figure 3.51: PIV calculated incremental volumetric strain for non-spherical particles, $f_p = 0.3$

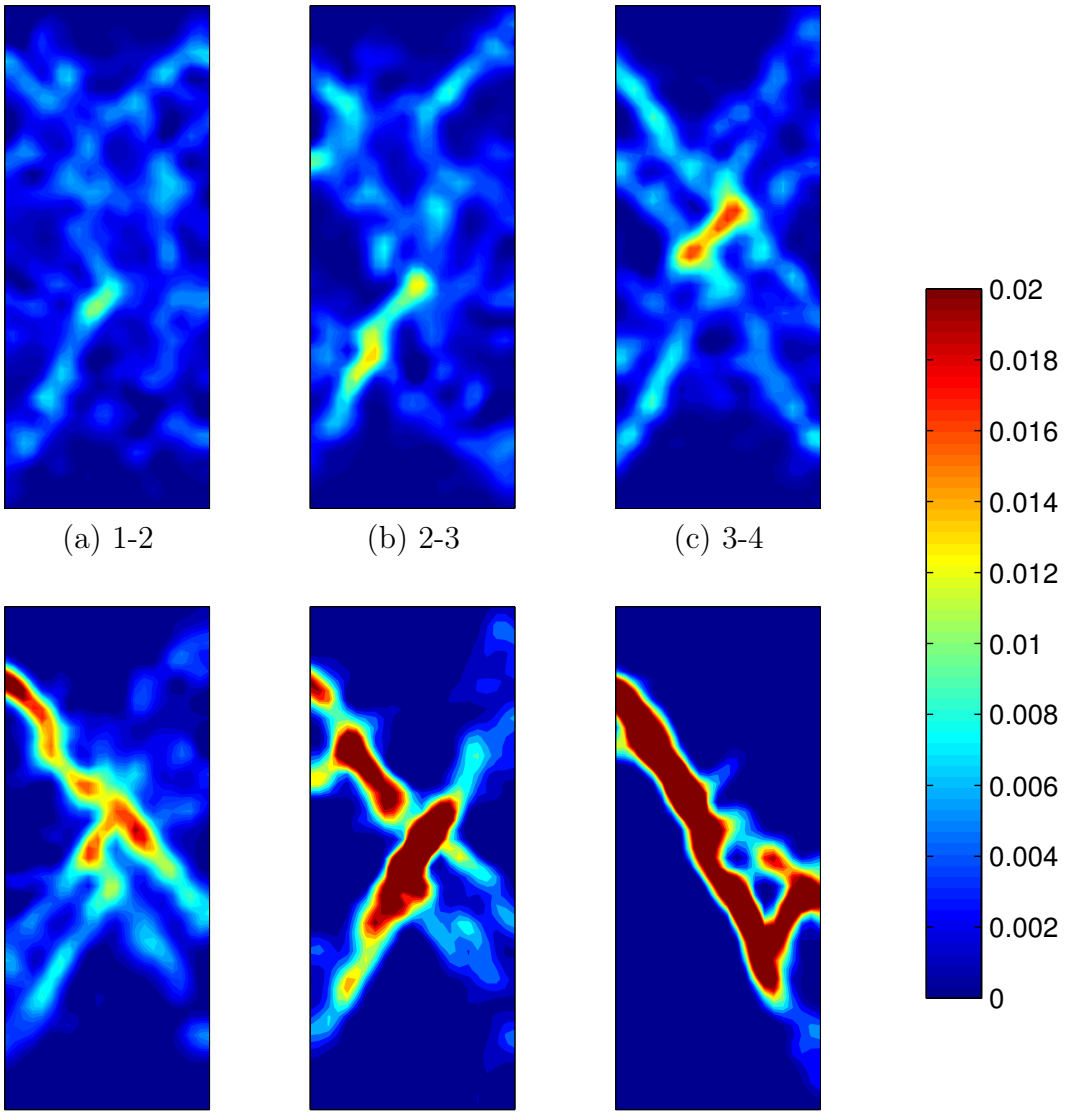

(a) 1-2 (b) 2-3 (c) 3-4

(d) 4-5 (e) 5-6 (f) 6-7

Figure 3.52: PIV calculated incremental shear strain for non-spherical particles, $f_p = 0.9$

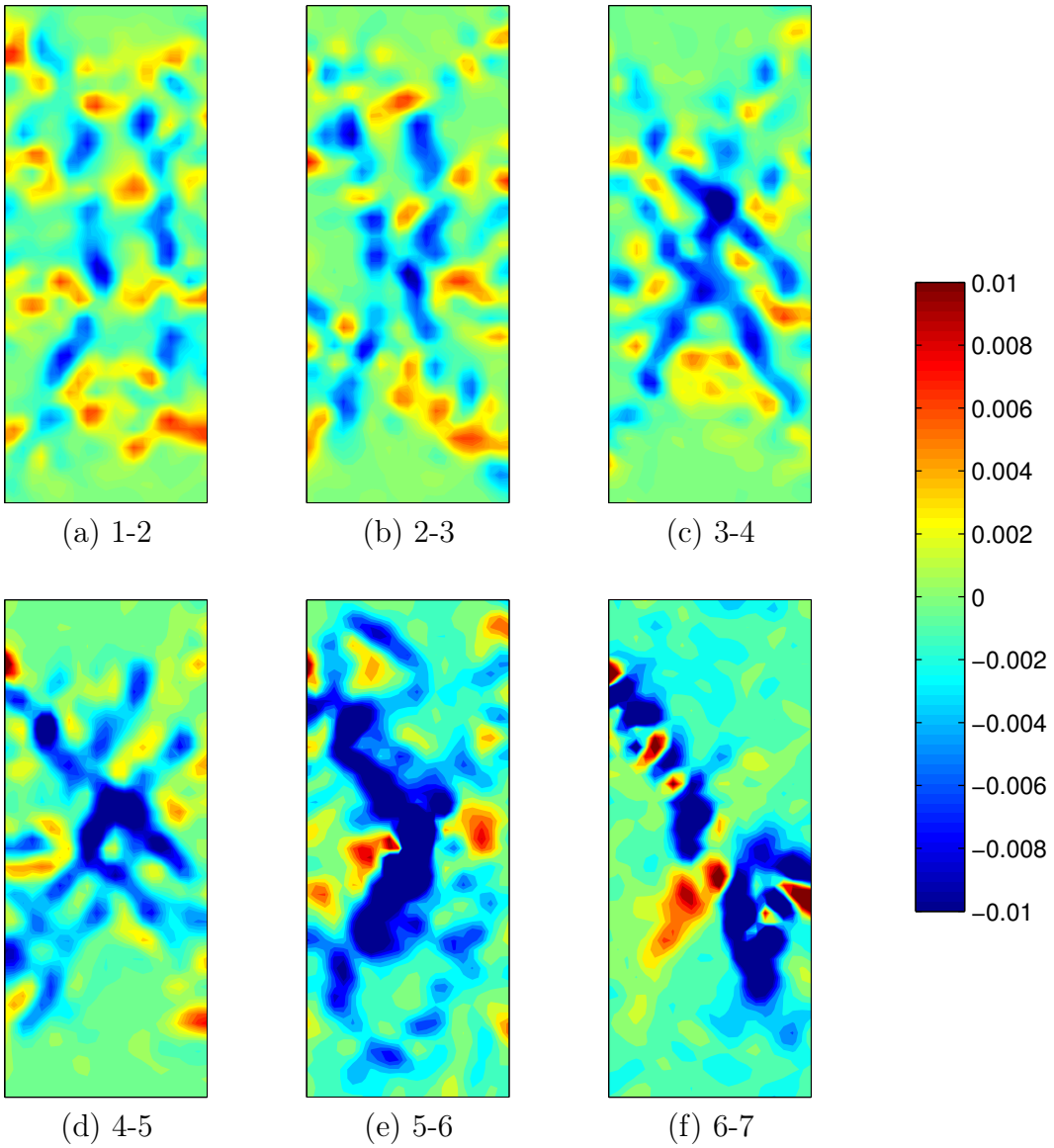

(a) 1-2 (b) 2-3 (c) 3-4

(d) 4-5 (e) 5-6 (f) 6-7

Figure 3.53: PIV calculated incremental volumetric strain for non-spherical particles, $f_p = 0.9$

of the force chains (e.g. Figure 3.35) associated with the shear band formation took place during the strain softening phase. However, it is important to bear in mind that there is no well defined criteria of the shear band onset. According to the PIV analysis, shear strain computed from displacement data indicates that strain localisation in the current DEM biaxial simulation initiated prior to the peak stress, whereas the evolution of the preliminarily initiated shear bands into a persistent shear band may take place after reaching the peak stress point.

It needs to be pointed out that the strain field presented in this section are all incremental and not cumulative, indicating that the information collected are only the new patterns of strain localisation emerging between such a strain range. Recent experimental work conducted by Hall et al. (2010) as briefly reviewed earlier, showed both incremental and cumulative strain maps of a 2D analogue granular sample during deviatoric loading. It was revealed that the shear strain was incrementally localised in space only for a given time step and moved between steps. This finding highlights the complexity of the kinematics and internal deformation in a granular material. A detailed comparison between the incremental and cumulative strain field in the current DEM biaxial simulation is indeed worthy of future investigation, which will provide more evidence to unveil the temporal and spatial evolution of shear band.

Concerning the volumetric strain (Figure 3.47, 3.49, 3.51 and 3.53), similar concentration patterns are observed if compared with the maximum shear strain. Unlike the well defined pattern of shear strain concentration, the contours of volumetric strain show significant alternations of expansion (blue) and contraction (red). However, expansive volumetric strain still dominates in the primary strain localisation zone, suggesting the initiation of shear band was accompanied by the increase of local voidage. Lesniewska and Muir Wood (2010) highlighted a micromechanism of developing volumetric strains which was not evident in the pattern of shear strains, which is also the case in the current PIV evaluations and

worth of future study.

Many new information of micromechanical features have been revealed from the above PIV analysis, illustrating the formation mechanism of shear band near the achievement of peak strength. However, it is generally agreed that the of PIV mesh refinement can significantly affect the precision of numerical outcome. Lesniewska and Muir Wood (2010) carried out an extensive convergence study of PIV analysis, determining the optimum mesh scheme in terms of patch size and grid spacing to evaluate the displacement and strain fields. It was observed that using finer meshes permits both study of overall deformation and inspection of local conditions. Similarly, this issue is also investigated in the current study, using six schemes of interrogation window with different size and spacing as listed in Table 3.7. Two cases (Figure 3.46(c) and 3.50(c)) were selected to perform the convergence analysis. The evaluated fields of shear strain (Figure 3.54 and 3.56) and volumetric strain (Figure 3.55 and 3.57) for the two cases were systematically presented.

Table 3.7: Characteristics of interrogation windows used in strain measurement

ID	Size of interrogation window (pixels)	Spacing (pixels)
IW1	64	32
IW2	64	16
IW3	64	8
IW4	32	16
IW5	32	8
IW6	16	8

The results clearly demonstrate that changing the interrogation mesh size of the PIV can have a significant effect on the resulting distributions of shear and

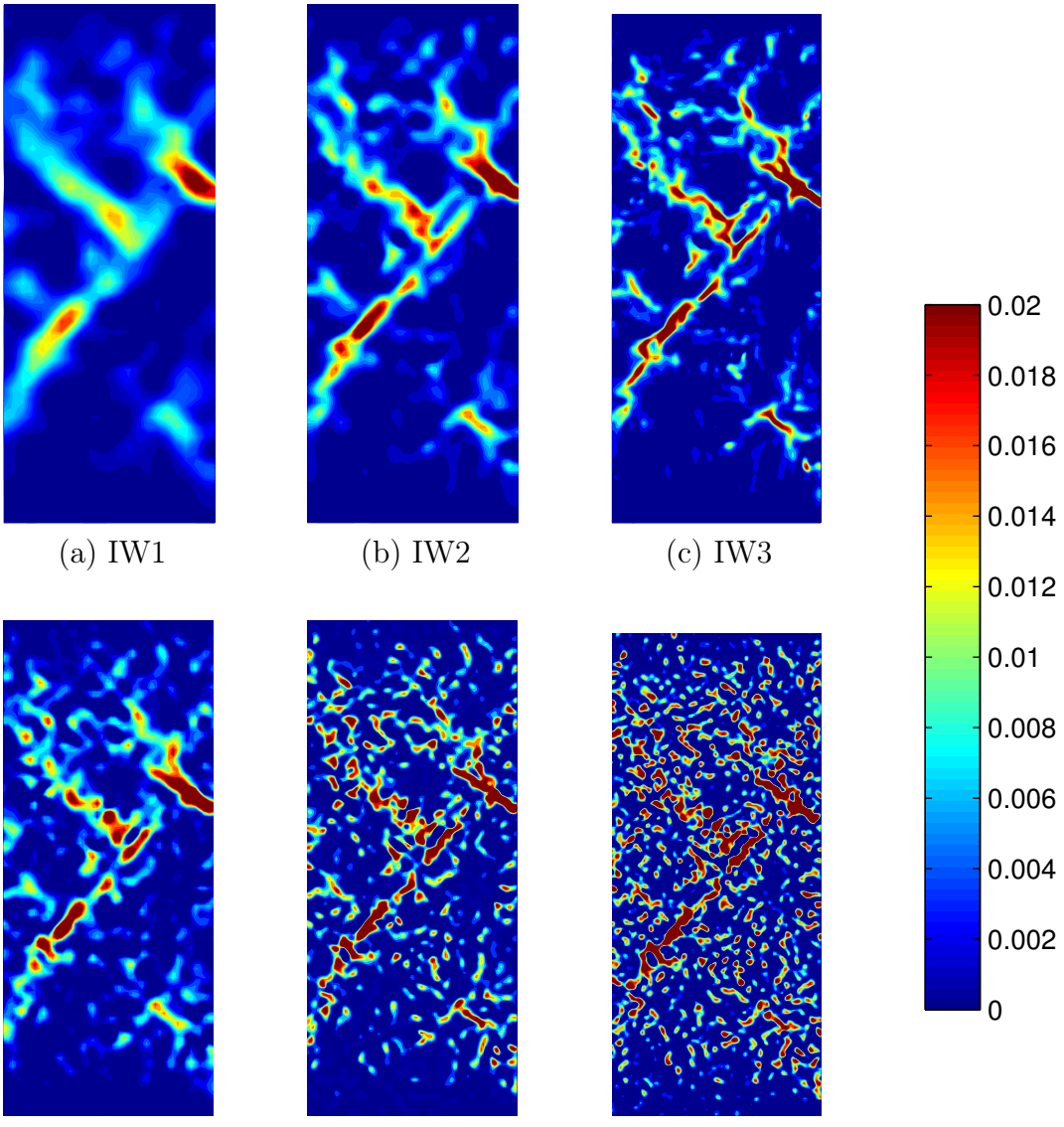

(a) IW1 (b) IW2 (c) IW3

(d) IW4 (e) IW5 (f) IW6

Figure 3.54: PIV calculated shear strain for spherical particles using different sizes of interrogation window (case: Figure 3.46(c))

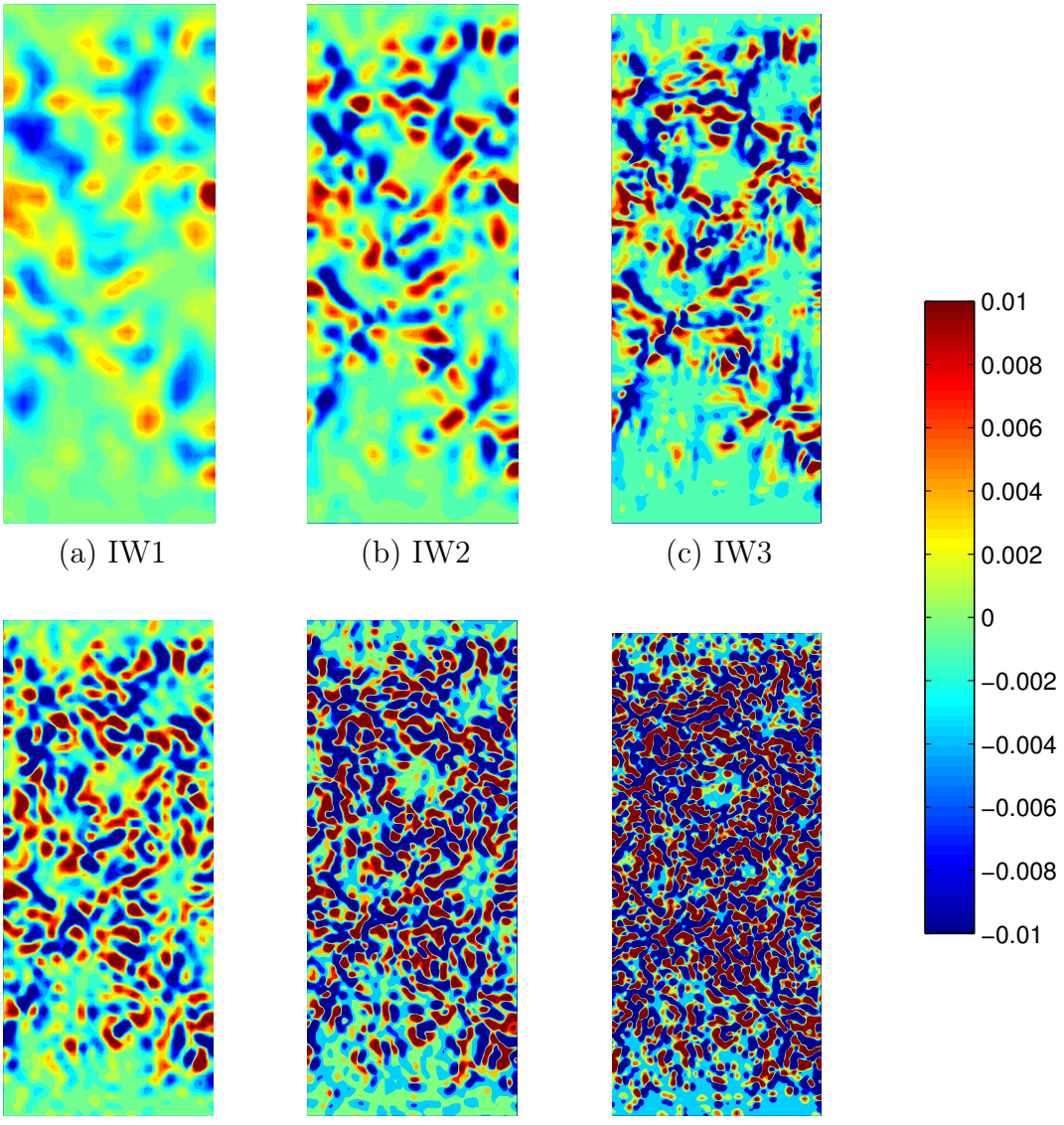

(a) IW1 (b) IW2 (c) IW3

(d) IW4 (e) IW5 (f) IW6

Figure 3.55: PIV calculated volumetric strain for spherical particles using different sizes of interrogation window (case: Figure 3.47(c))

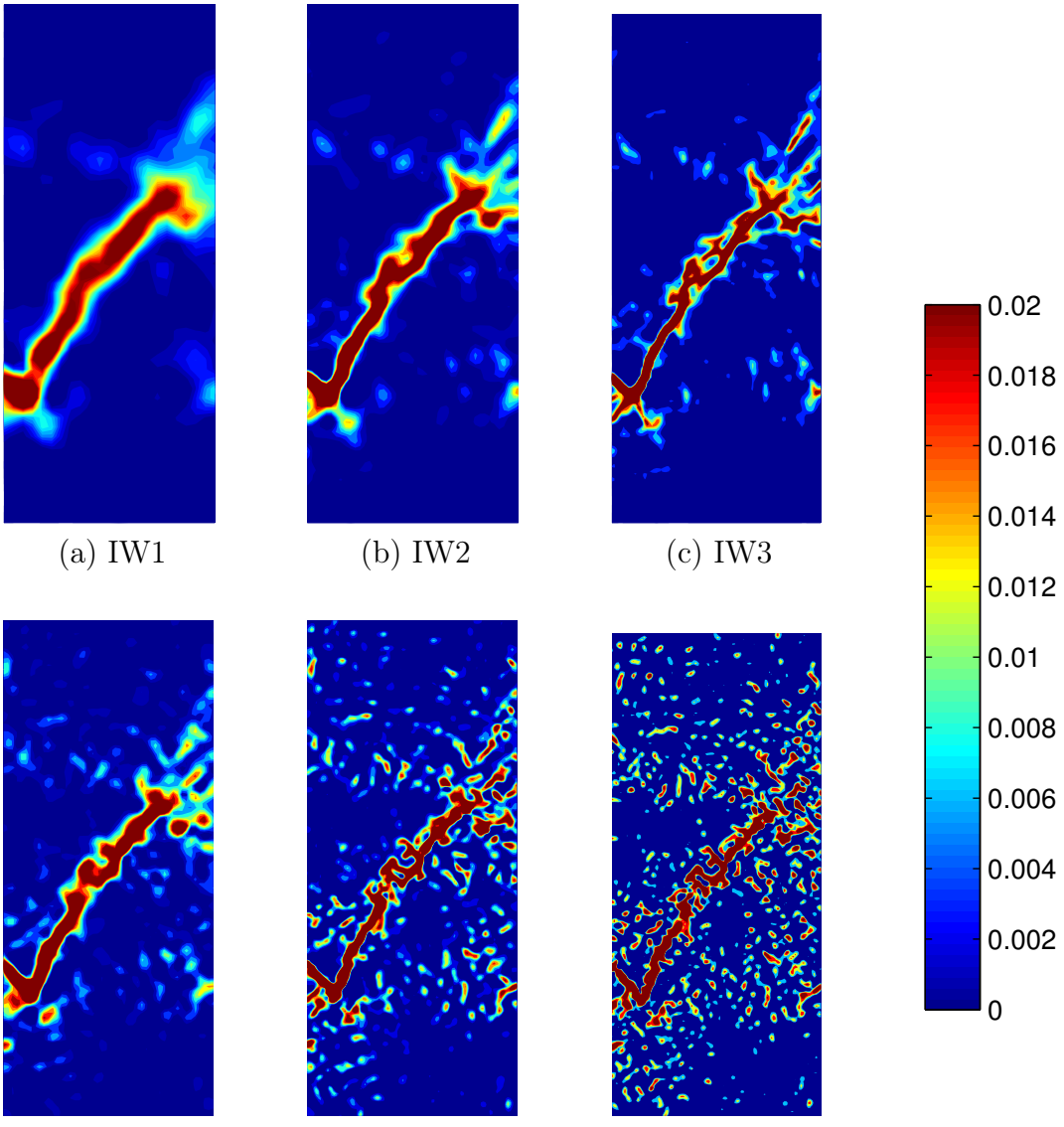

(a) IW1 (b) IW2 (c) IW3

(d) IW4 (e) IW5 (f) IW6

Figure 3.56: PIV calculated shear strain for spherical particles using different sizes of interrogation window (case: Figure 3.46(f))

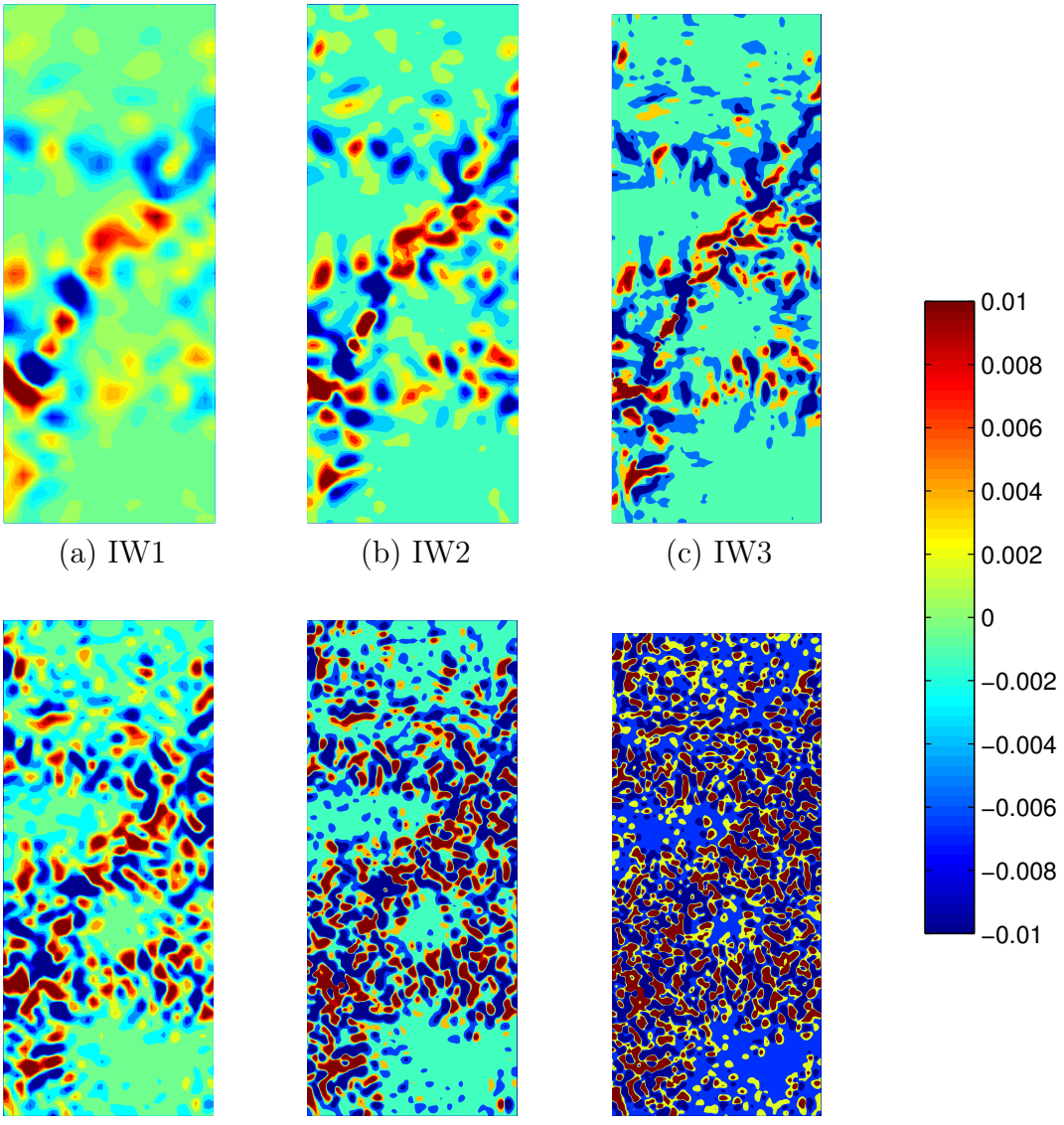

(a) IW1 (b) IW2 (c) IW3

(d) IW4 (e) IW5 (f) IW6

Figure 3.57: PIV calculated volumetric strain for spherical particles using different sizes of interrogation window (case: Figure 3.47(f))

volumetric strain. All the plots of strain contour using the six different mesh schemes show similar pattern of emerging shear band. As reported earlier, even the very rough mesh (IW1) vividly demonstrated a competing mechanism between bands with opposing directional tendencies. However, as can be seen from the plots using decreasing mesh sizes, using a coarser mesh for the calculation of strains can lead to a loss of information at smaller spatial resolution. For example, the computed strain pattern could fail to show some behaviour or mechanism at a more localised scale, particularly those related to local density changes occurring at a scale that may be larger than the individual particle size but smaller than the chosen PIV mesh size (Muir Wood, 2010).

Increasing the degree of mesh refinement further reveals new interesting features. For example, results obtained from IW2 and IW3 show some local branches of shear strain localisation within the shear band and more distinct zones in the volumetric strain with striking alterations of expansion and contraction. Hall et al. (2010) emphasised that those internal structures in the volumetric strain should not be simply treated as numerical artifacts from image correlation. In the cases where smaller interrogation windows were used (e.g. IW4, IW5 and IW6), a more erratic strain distribution was observed which is likely to contain a considerable amount of numerical noise, so a systematic evaluation of the numerical scatter would need to be undertaken in the interpretation of the results. Similar to the earlier mesh sensitivity analysis carried out in the stress calculation using measurement spheres in PFC3D, it is essential that the averaging volume should contain sufficient number of particles so that the particulate nature is not predominant and the predicted bulk quantity is representative. Overall, the current convergence study suggests that a good mesh scheme of interrogation windows can be achieved by using relatively large interrogation window while adopting small grid spacing (e.g. IW3), which provides reasonable inherent smoothing and meanwhile does not compromise the strain calculation.

3.4.8.2 Strain calculation based on DEM data

There are several candidate algorithms of strain calculation as reviewed in Section 2.4, which have been widely published in the literature. To provide another approach to calculate the strain and compare the results with those obtained from PIV analysis, here both the shear strain and volumetric strain are computed directly from DEM data.

For simplicity, an easy-implemented interpolation approach was adopted to calculate strain at this stage, which was coded in MATLAB and is briefly outlined. Firstly the sample domain was transformed into arrays specified by the spacing between two adjacent grids (`meshgrid`). Now at these regularly spaced grids returned by `meshgrid`, the value is interpolated based on the raw irregularly sampled data (each individual particle movement) by using `griddata`. Here, a triangle-based linear interpolation is adopted based on the Voronoi tellselation. Then the strain components were calculated by working out the gradients of the interpolated displacement fields as illustrated in Figure 3.58.

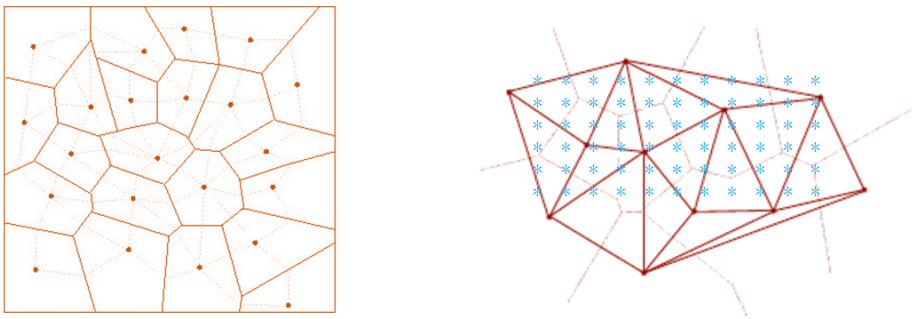

Figure 3.58: Voronoi diagram and triangle-based linear interpolation (solid dots: centroids of DEM particles, blue star: regularly spaced grids specified by `meshgrid`)

Two case were selected to extract the strain components (shear and volumetric strain) from DEM analyses, for both spherical (Figure 3.59, 3.60, 3.61 and 3.62) and non-spherical particles (Figure 3.63, 3.64, 3.65 and 3.66).

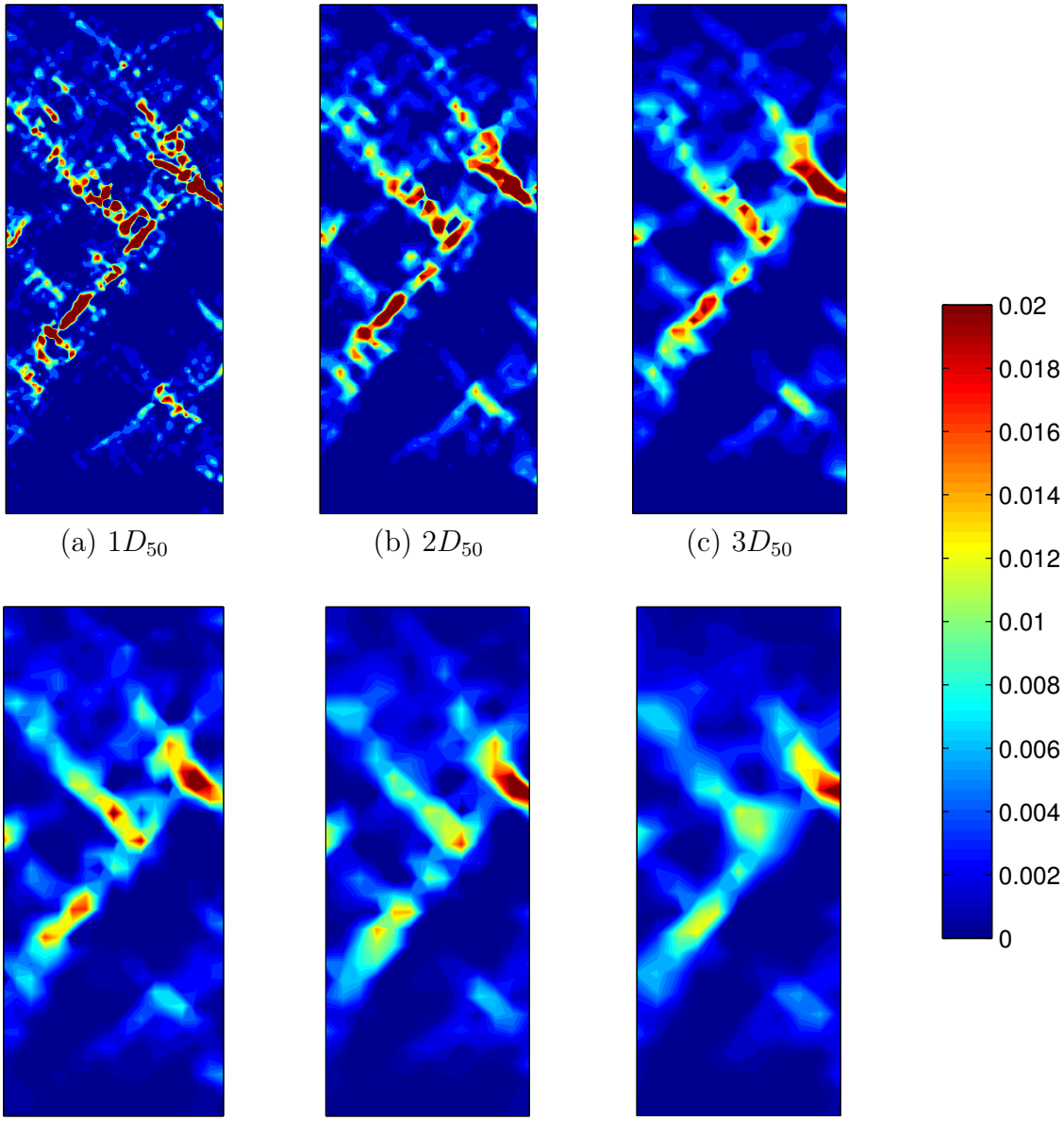

(a) $1D_{50}$ (b) $2D_{50}$ (c) $3D_{50}$

(d) $4D_{50}$ (e) $5D_{50}$ (f) $6D_{50}$

Figure 3.59: DEM calculated shear strain for spherical particles using different mesh spacing (case: Figure 3.46(c))

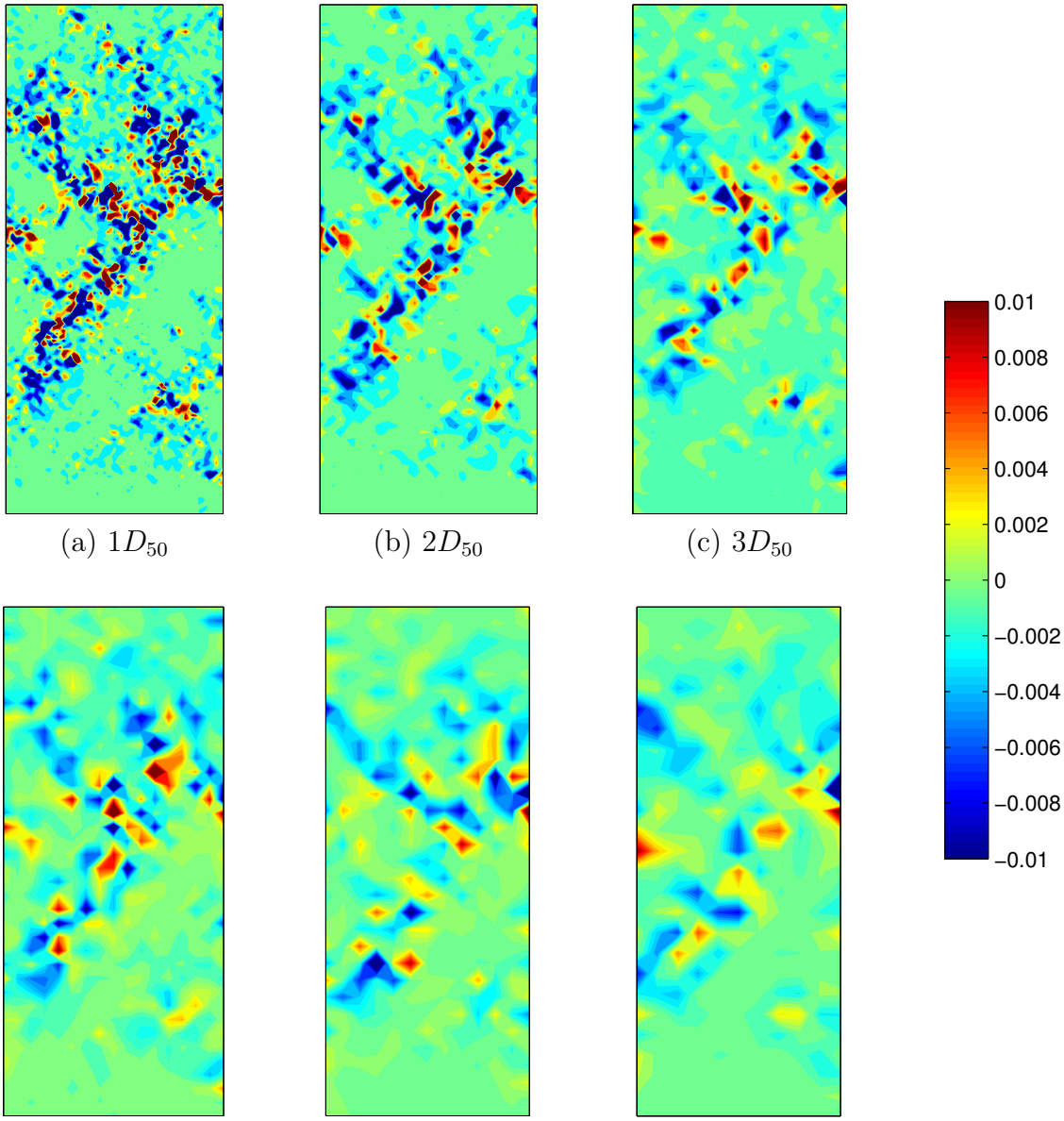

(a) $1D_{50}$ (b) $2D_{50}$ (c) $3D_{50}$

(d) $4D_{50}$ (e) $5D_{50}$ (f) $6D_{50}$

Figure 3.60: DEM calculated volumetric strain for spherical particles using different mesh spacing (case: Figure 3.47(c))

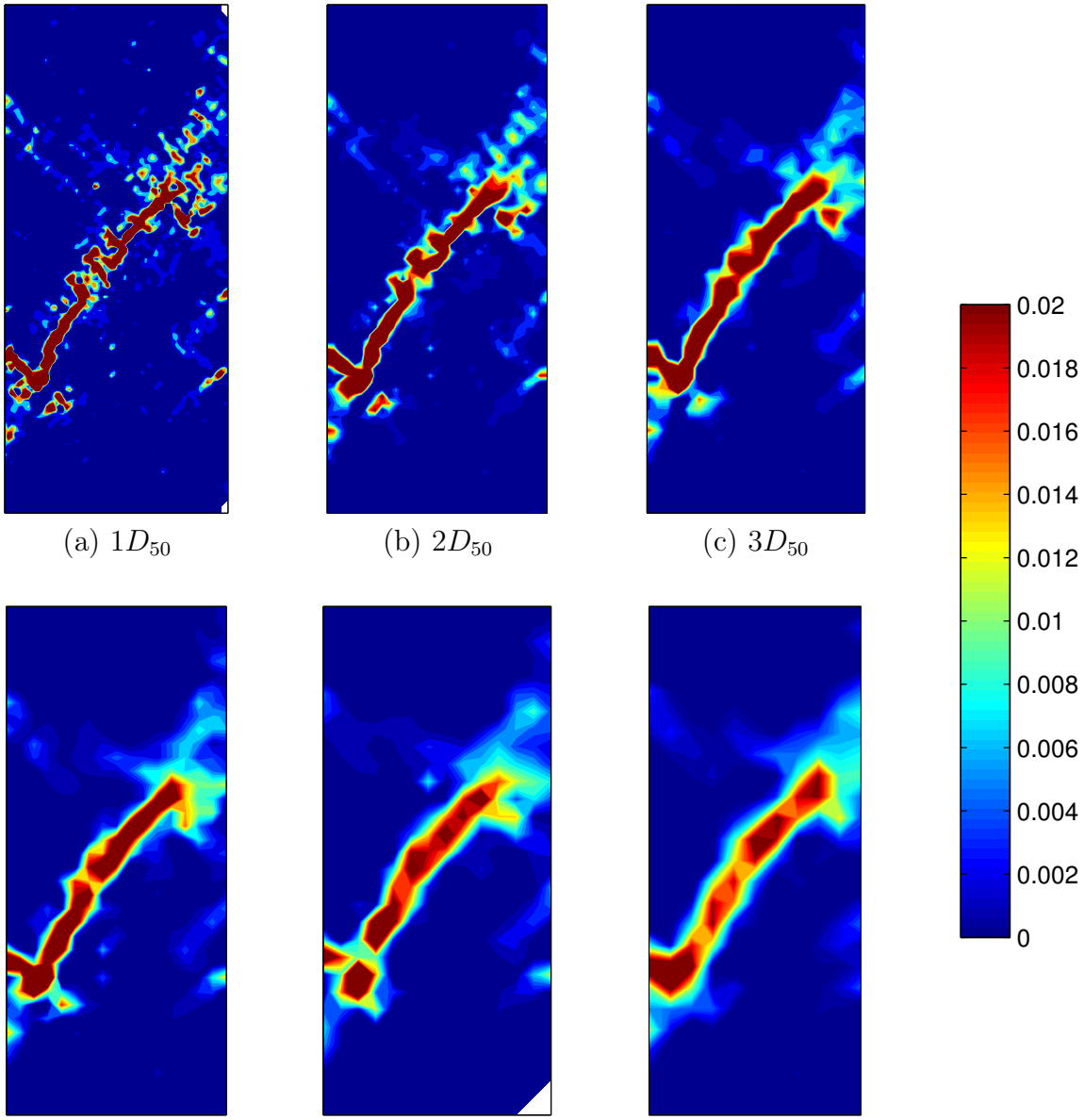

(a) $1D_{50}$ (b) $2D_{50}$ (c) $3D_{50}$

(d) $4D_{50}$ (e) $5D_{50}$ (f) $6D_{50}$

Figure 3.61: DEM calculated shear strain for spherical particles using different mesh spacing (case: Figure 3.46(f))

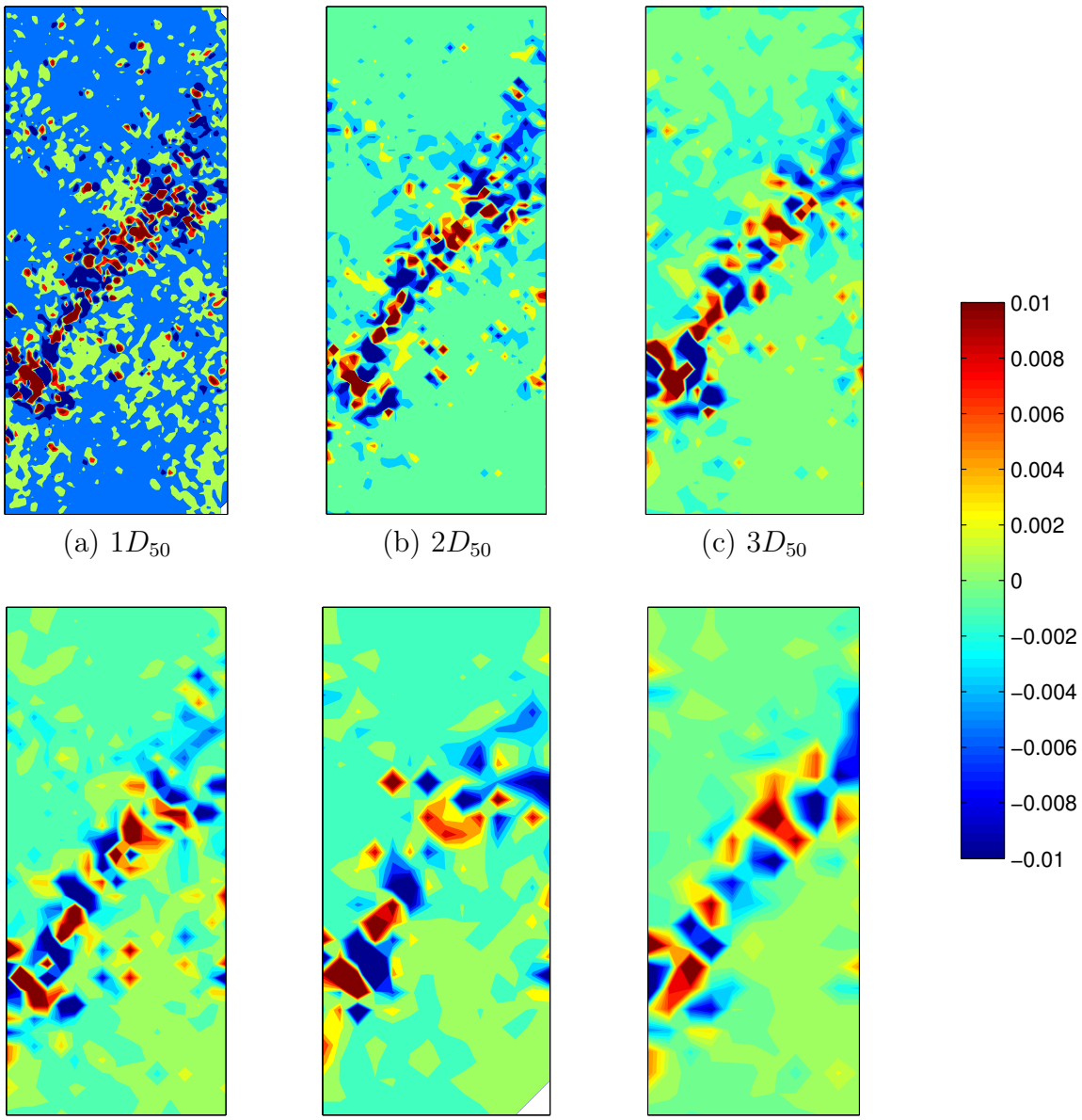

(a) $1D_{50}$ (b) $2D_{50}$ (c) $3D_{50}$

(d) $4D_{50}$ (e) $5D_{50}$ (f) $6D_{50}$

Figure 3.62: DEM calculated volumetric strain for spherical particles using different mesh spacing (case: Figure 3.47(f))

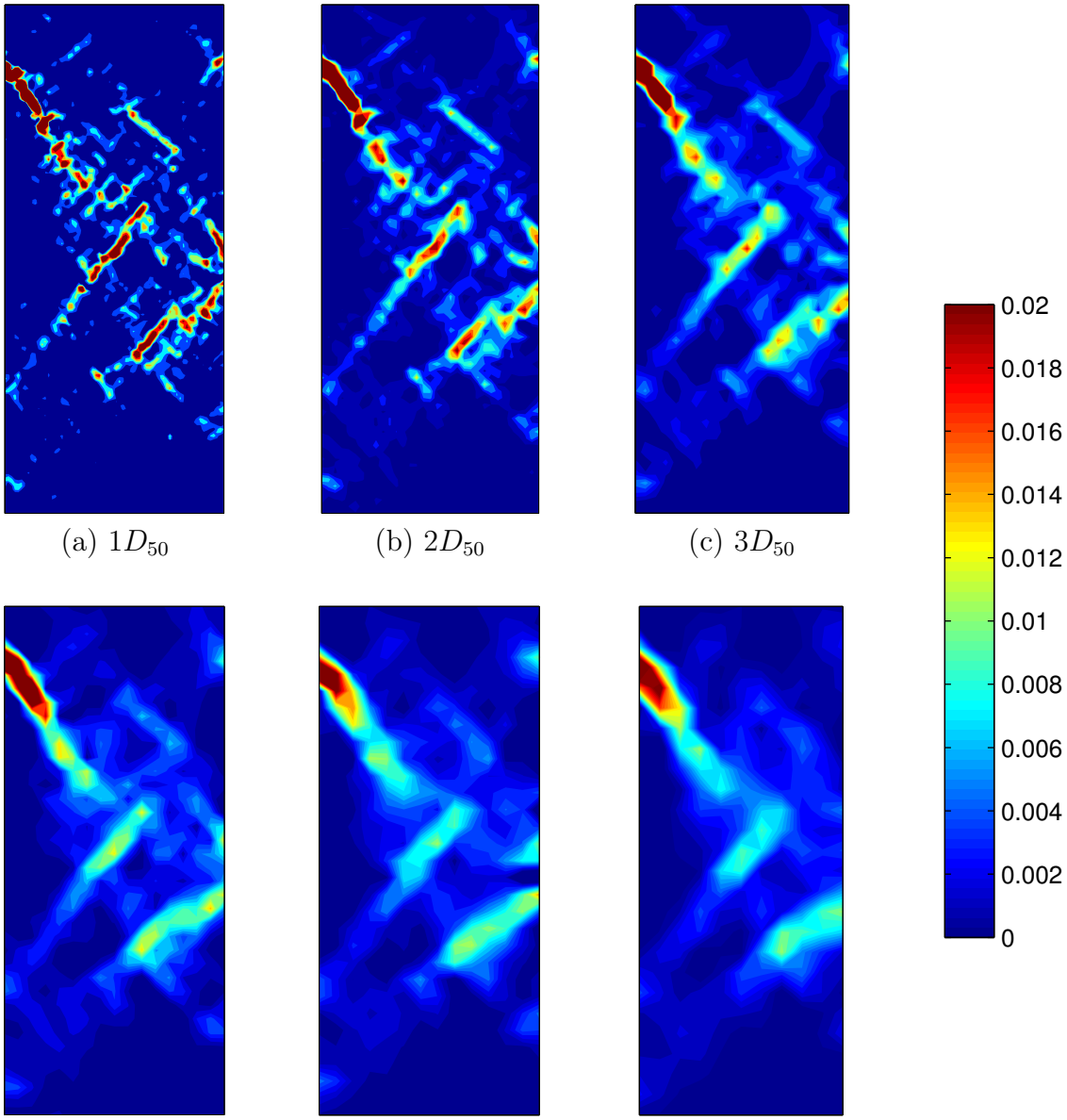

(a) $1D_{50}$ (b) $2D_{50}$ (c) $3D_{50}$

(d) $4D_{50}$ (e) $5D_{50}$ (f) $6D_{50}$

Figure 3.63: DEM calculated shear strain for non-spherical particles using different mesh spacing (case: Figure 3.50(c))

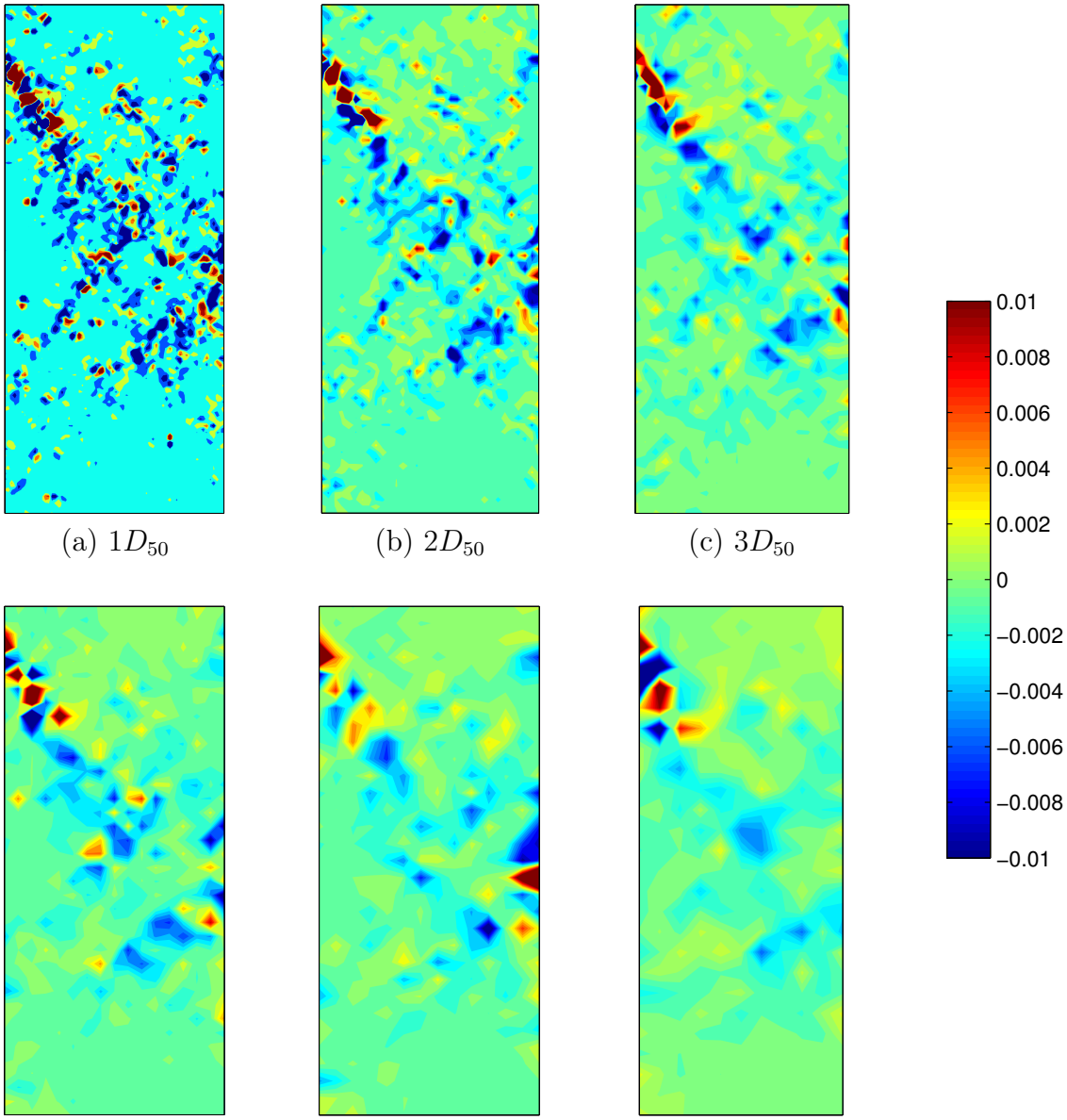

(a) $1D_{50}$ (b) $2D_{50}$ (c) $3D_{50}$

(d) $4D_{50}$ (e) $5D_{50}$ (f) $6D_{50}$

Figure 3.64: DEM calculated volumetric strain for non-spherical particles using different mesh spacing (case: Figure 3.51(c))

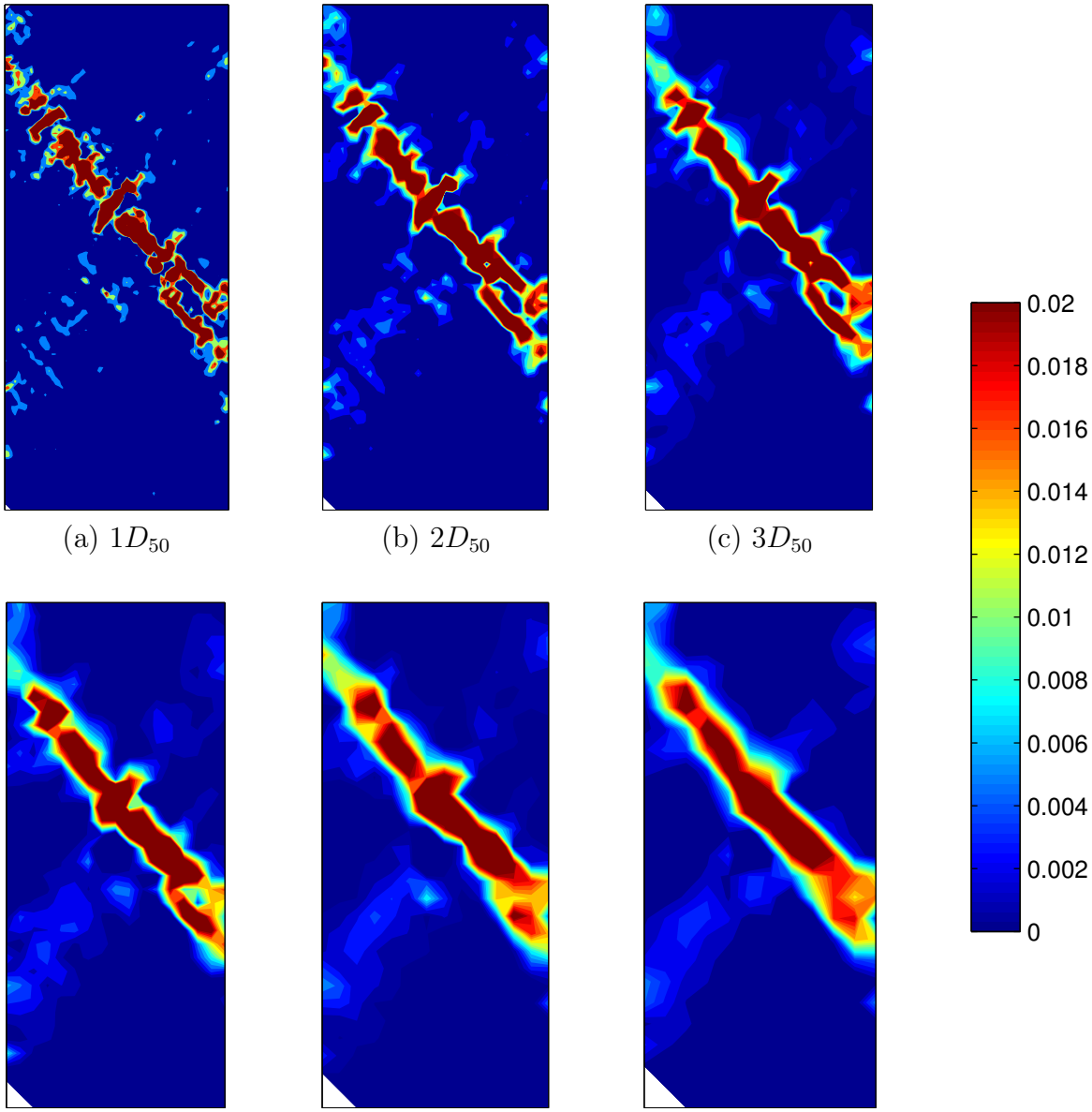

(a) $1D_{50}$ (b) $2D_{50}$ (c) $3D_{50}$

(d) $4D_{50}$ (e) $5D_{50}$ (f) $6D_{50}$

Figure 3.65: DEM calculated shear strain for non-spherical particles using different mesh spacing (case: Figure 3.50(f))

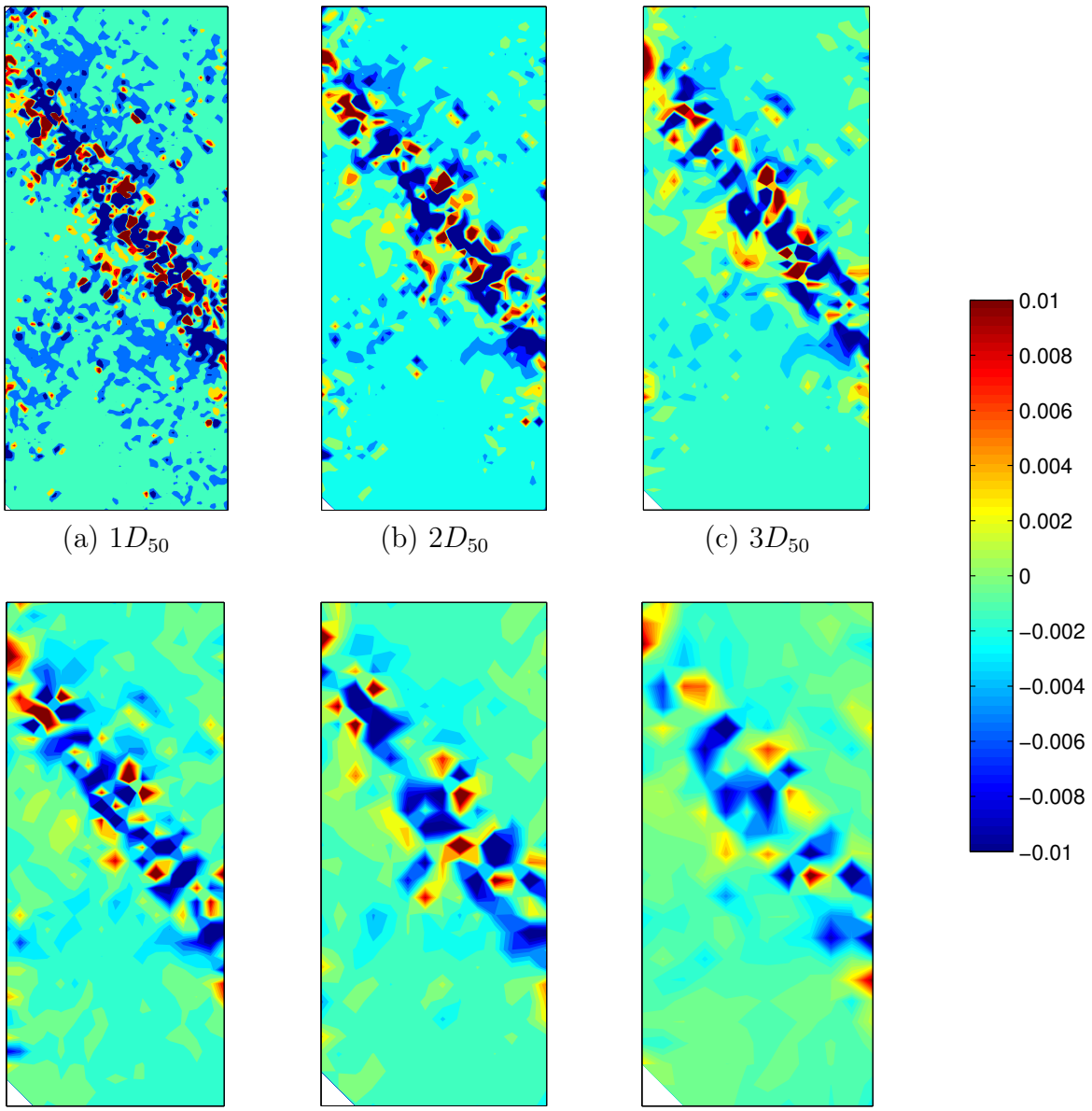

(a) $1D_{50}$ (b) $2D_{50}$ (c) $3D_{50}$

(d) $4D_{50}$ (e) $5D_{50}$ (f) $6D_{50}$

Figure 3.66: DEM calculated volumetric strain for non-spherical particles using different mesh sizes (case: Figure 3.51(f))

Overall, the DEM calculated strain distributions show a high level of similarity to the results from PIV analyses. Noticeably, there is one distinct difference between the two methods of strain calculation. In PIV image correlation, it averages the displacement of all the particles within one interrogation window. On the other hand, the displacement value at each grid is interrogated from DEM data of the three nearest particles in voronoi diagram. As a result, using finer grid spacing in the DEM interpolation produces much smoother displacement gradients and gives rise to abundant rich information with many local details, while smaller interrogation window in PIV analyses unavoidably generates a strain field containing a large number of noisy data.

Although quantitative comparison of strain calculations between the PIV interrogation and the current DEM interpolation is not practical at this stage, the results does provide an easy implemented approach to inspect the strain distribution and thus guide the research attention to areas of special interest. Future study focus on a more mathematically rigorous algorithm is necessary and under investigation.

3.4.9 Evaluation of shear band orientation using local information

The angle of shear band reported in section 3.4.3 was obtained by measuring the inclination pattern based on the layered particle configuration. Here, as the local information concerning the stresses and incremental strains have been obtained from DEM analyses, the orientation of shear band was further calculated according to some classical solutions. There are three most widely used analytical solutions to the inclination angel (θ) of shear band with respect to the minor principal stress, which are introduced as follows:

1. Coloumb solution assumes a shear band forms in the direction of the planes

where maximum mobilised angle of friction occurs.

$$\theta_C = 45^\circ + \frac{\phi}{2} \tag{3.2}$$

where ϕ is the friction angle of the soil;

2. Roscoe solution treats the shear band as a layer of intensely shearing material which coincides with the zero extension direction.

$$\theta_R = 45^\circ + \frac{\psi}{2} \tag{3.3}$$

where ψ is the dilation angle and can be defined by:

$$\sin\psi = -\frac{\delta\epsilon_v}{\delta\gamma} = -\frac{d\epsilon_1 + d\epsilon_2}{d\epsilon_1 - d\epsilon_2} \tag{3.4}$$

where $\delta\epsilon_v$ is incremental volumetric strain and $\delta\gamma$ is incremental shear strain, respectively.

3. Arthur-Vardoulakis solution gives an average of the Coulomb and Roscoe solutions.

$$\theta_V = 45^\circ + \frac{\phi + \psi}{4} \tag{3.5}$$

Hall et al. (2010) further illustrated the Coloumb and Roscoe directions of shear band by using Mohr's circle (Figure 3.67). Here, two strain increments were selected to evaluate the orientation of shear band using both global and local conditions in the region of the shear band. By way of illustration, only the case with interparticle friction of 0.9 are presented for both spherical and non-spherical particles. The first global strain increment (4-6%) covers the the significant stress drop after the peak strength was achieved. Another reference

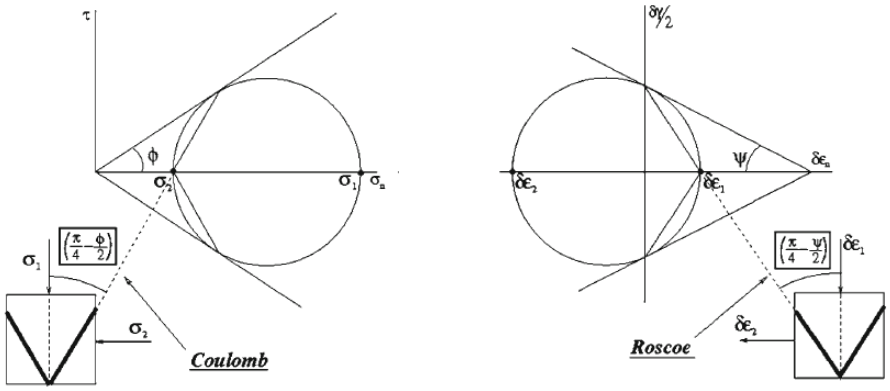

Figure 3.67: left: Mohr's circle of stress indicating the Coloumb directions; right: Mohr's circle of strain increment indicating the Roscoe directions (Hall et al., 2010)

stage (14-16%) was chosen in the large deformation regiem, when the shear bands have fully developed. Shear and volumetric strain fields of spherical (Figure 3.68) and non-spherical particles (Figure 3.69) at these two stages are presented, in which the regions enclosed by the white lines representing the shear zones used for local analyses.

In the global analyses, both stress and strain components were measured at the sample boundaries. For the local analyses using the conditions in the shear band region, the stresses were calculated through measurement spheres while the strains were extracted from gradients of particle displacements, both as introduced in the previous sections. Table 3.8 and 3.9 list the evaluated orientations of shear band for spherical and non-spherical particles, respectively. The results suggest that the Arthur-Vardoulakis solutions gave a better approximation of the shear band orientation if compared to the DEM observations, while the Coloumb and Roscoe solutions being the upper bound and lower limit, respectively. Additionally, there was no significant difference between the values obtained from global and local calculations. Although shear band is a local phenomena that

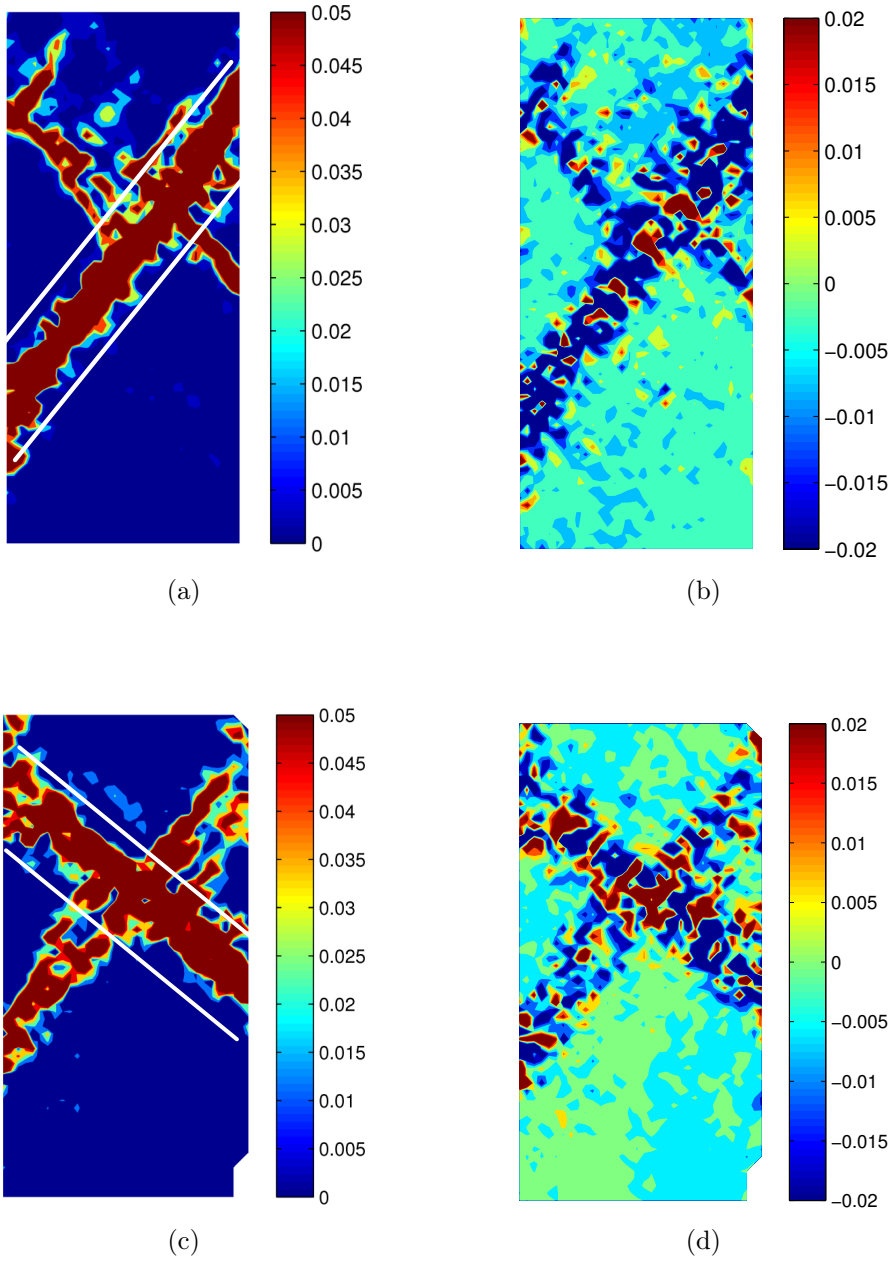

Figure 3.68: Shear and volumetric strain fields of spherical particles (top row: global strain increment 4-6%; bottom row: global strain increment 14-16%)

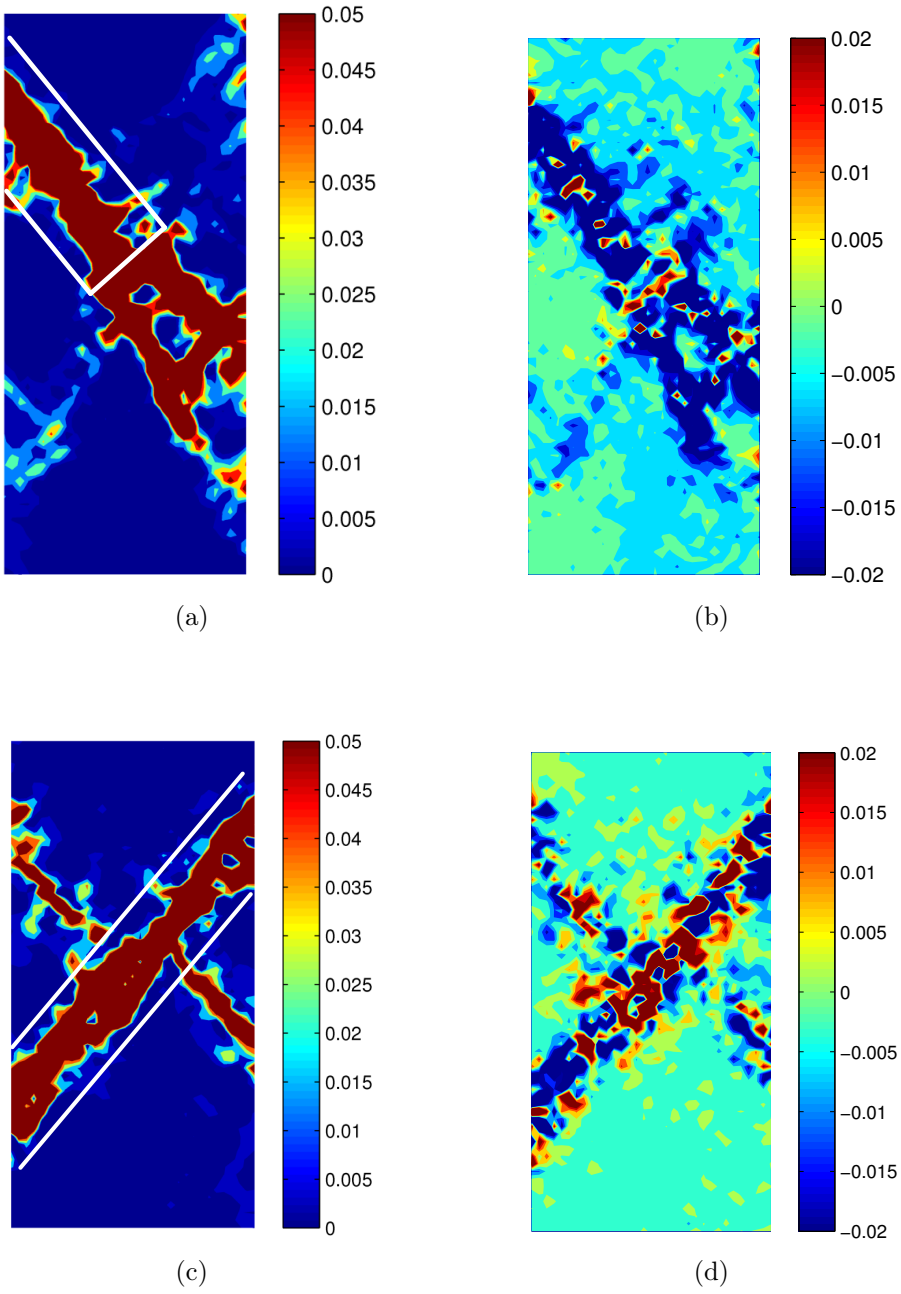

Figure 3.69: Shear and volumetric strain fields of non-spherical particles (top row: global strain increment 4-6%; bottom row: global strain increment 14-16%)

causes significant strain localisation, it also largely affect the global mechanical conditions (e.g. stress and strain). The current results suggest that using global stress and strain is adequate in the calculation of shear band orientation.

Table 3.8: Shear band orientation for spherical particles

Strain increment	Global			Local			DEM observation
	θ_C	θ_R	θ_V	θ_C	θ_R	θ_V	θ_D
4-6%	53.3	50.0	51.7	53.1	47.1	50.1	50.8
14-16%	50.5	46.4	48.5	52.6	45.2	48.9	40.5

Table 3.9: Shear band orientation for non-spherical particles

Strain increment	Global			Local			DEM observation
	θ_C	θ_R	θ_V	θ_C	θ_R	θ_V	θ_D
4-6%	56.7	50.8	53.8	57.9	49.7	53.8	53.1
14-16%	53.3	45.7	49.5	56.6	45.1	50.9	49.2

3.5 Summary

This chapter presents the DEM simulations of biaxial compression test conducted on specimens composed of spherical and non-spherical particles, in which special attention was given to the micromechanics associated with strain localisation. The servo-controlled particle membrane boundaries used in the numerical model was able to reproduce the natural nucleation of shear band. The macroscopic behaviour predicted from DEM simulations showed that the current densely packed samples under biaxial loading exhibited a strain-softening response and accompa-

nied by volumetric expansion at large deformations, which is in agreement with experimental results on dense granular materials in the literature.

The effect of several factors on the phenomenon of strain localisation were carefully investigated through a set of parametric DEM simulations. Both the bulk responses and patterns of shear band were affected significantly by the end friction. One single shear band was dominant in the sample with frictionless loading platens, and the sample rapidly reached an ultimated failure by sliding along the inclined shear plane. On the other hand, the introduction of end friction provided necessary lateral restraint, leading to the commonly observed conjugate bands and a relatively steady state after the peak strength was achieved. With regard to the interparticle friction and particle shape, both were observed to have strong influence on the bulk strength. Generally, a higher coefficient of interparticle friction led to a macroscopically stronger assembly, showing a more pronounced peak strength followed by a distinct stress drop, whereas a small interparticle friction gave rise to a more moderate softening process. The interlocking asperity of non-spherical particle allowed a greater amount of tangential force to be sustained at the contact, and thus exhibited larger resistance to biaxial compression compared to spherical sample. Additionally, the width and inclination angle of shear band were measured to characterise the strain localisation. The width of shear band was 14$\sim$25 times of the mean particle diameter on average and the inclination angle varied from 45° to 53°, which are comparable to the experimental measurements in the literature.

Compared to unsheared specimens, the local void ratio distributions in sheared specimens showed both higher mean values and standard deviations. This relation became more pronounced with the increase of interparticle friction. The histograms constructed from the subregional analysis quantitatively showed that local void ratios within the shear band increased dramatically relative to those outside the shear zones. Also, shear band formation was evident in all the cases

by observing the excessive particle rotations. The interlocking propensity in non-spherical particles generated more resistance to the particle rotation, and thus produced stronger dilation and higher bulk strength. Meanwhile, a considerable amount of microstructural changes occurred during the biaxial compression. The development of contact orientation proved a good descriptor of the force network, which implied that an initial isotropic packing was gradually destroyed and a pronounced anisotropic structure was yielded. The strong force network was visualised by plotting the force chains carrying above-average contact forces at varying strain levels, in which the buckling processes can be discerned and associated with the development of large voidage.

This chapter also concerns the constitutive response in terms of stress and strain, aiming to establish a link between particle analyses and continuum interpretation. The average stress tensor was calculated based on the algorithm of measurement sphere while the strain components were evaluated through the application of PIV correlation. A hybrid DEM-PIV approach was developed to understand the micromechanical processes underlying the evolution of localised shear band, with the objective of determining the displacement field and hence strain over a short time step. Around the achievement of the peak stress, where the shear band was anticipated to initiate and propagate progressively, PIV analysis was carried out over a global strain step of $\Delta\epsilon_y \approx 0.25\%$. The incremental shear strain fields computed from the displacement data derived from PIV measurement suggested that multiple shear bands formed initially in the hardening phase, i.e. before reaching the peak stress. However, the persistent pattern of strain localisation was not definitive until the softening regime. This temporal information provides much insight into the mathematical formulation and continuum modelling of bifurcation instability. The importance of choosing different diameters of the measurement sphere and PIV interrogation windows was also highlighted, in order to determine the optimum mesh scheme. Finally, the shear

band orientation was further evaluated using the local stress and incremental strain in the regions of shear band. The results show no significant differences compared to the values calculated using the global conditions measured on the sample boundaries.

Chapter 4

Analysis of pressure distribution beneath granular piles

4.1 Introduction

Bulk handling and processing of granular solids are vital operations in a wide range of industries. Granular materials are commonly stored and transported as stockpiles. In agricultural and mining industries, the height of these open stockpiles typically range from 20 to 50 meters. At such a scale, the consequence of failure due to the incorrect estimation of base pressure will be catastrophic. Therefore, the design of gravity reclaim has received increasing research attention, which involves the evaluation of progressive load on the base and the determination of foundation capacity. The base pressure distribution of such a static pile is one of the most classic problems in granular mechanics, which has been extensively studied by both scientific and engineering communities in the last decades. Intuitively, it is anticipated that the maximum vertical pressure at the base of a pile occurs directly underneath its apex, where the height of overlying material is a maximum. In contrast to liquids, the pressure under a granular pile does not

increase linearly with the depth, but shows a central dip instead. For this reason, the base pressure profile is sometimes described as a "M-shape" distribution.

4.2 Literature review

The measurement of base pressure in granular heaps provides a useful manner to verify mathematical formulation and constitutive models of the way that forces transmit within cohesionless granular solids. This problem has been the subject of a number of analytical, numerical and experimental studies. It is noticed that the great majority of stockpile experiments in which a significant pressure dip was measured came from non-spherical particles. These include sand and fertilizer granules, elliptical particles and iron ore pellets. Meanwhile, it can be observed that many experiments using 3D spherical or 2D circular particles produced a less significant pressure dip and often with considerable stress fluctuation. Notably, contradicting theories have been given regarding the explanations of pressure dip. Many theoretical models published to date show the occurrence and the magnitude of the minima depend on different parameters, such as particle shape, its material properties, segregation and base deflection. This section reviews the literature in experimental base pressure measurement, continuum and discrete element modelling of pile formation.

4.2.1 Experimental study

Two pioneering experimental work in measuring the base pressure under conical stockpiles will be firstly reviewed. Jotaki and Moriyama (1979) used pressure cells to measure pressure distributions along the central baseline of conical piles of sand ($300 \sim 700\mu m$) up to $70mm$ height. Smid and Novosad (1981) conducted similar experimental work on granular heaps ($60cm$ height) using sand and granu-

lar fertilizer, which were funnelled onto a horizontal steel plate. Both experiments demonstrate that the vertical stress distribution did not reach a maximum beneath the apex of the conical stockpile, but instead showed a local dip at the center, as shown in Figure 4.1.

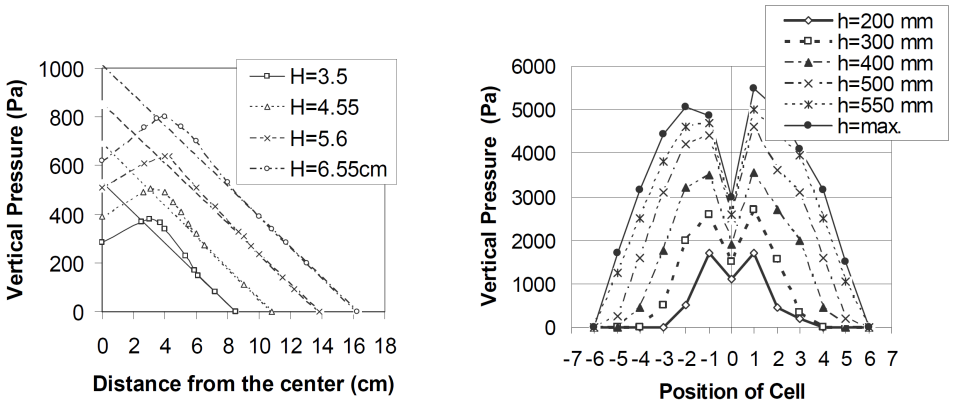

(a) Jotaki and Moriyama (1979) (b) Smid and Novosad (1981)

Figure 4.1: Early experimental study of vertical pressures along the base of a heap of sand

Vanel et al. (1999) further explored the influence of preparation history on the base stress distribution. Two construction techniques, namely "localised source" and "raining procedure" were used to form the piles. Figure 4.2 compares the experimental setup and stress profile obtained. It is obvious that the construction history dramatically affects the base pressure profiles of conical and wedge-shaped piles formed on a rigid base. The point source deposited sandpile shows the presence of reduction in the central pressure, whereas the pressure dip disappears in the heap prepared from the raining procedure. The postulated mechanism producing the dip is that the flow of particles during the localised-source procedure forms stress chains oriented preferentially in the direction of the slope.

Zuriguel et al. (2007) and Zuriguel and Mullin (2008) employed discs, elliptic cylinders and pear-shaped cylinders in photoelastic experiments to study the

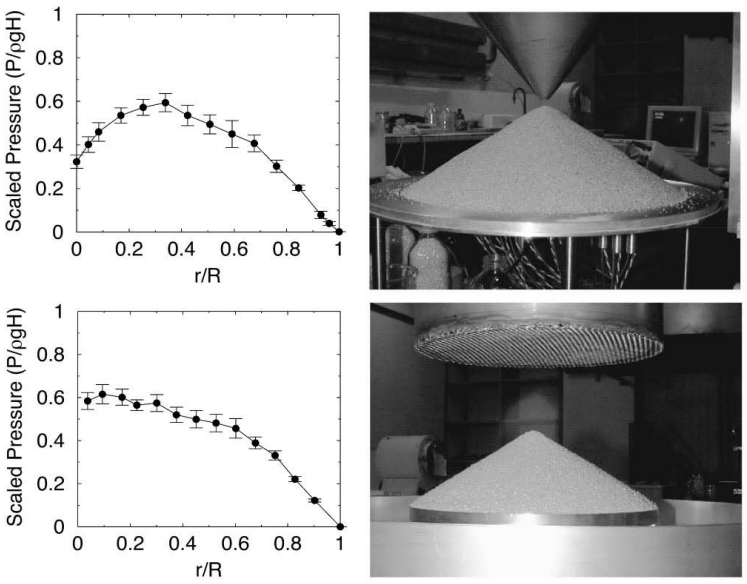

(a) Conical piles

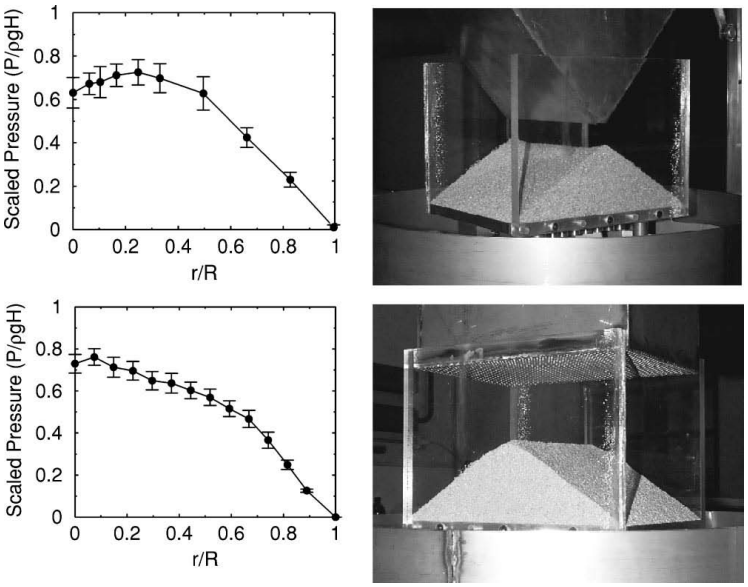

(b) Wedge-shaped piles

Figure 4.2: Normal stress profiles from different construction techniques (Vanel et al. (1999))

role of particle shape on the stress distribution in a sandpile. The results clearly suggested that a larger degree of particle nonsphericity will produce a more significant pressure dip. The authors attributed the amplification of the effect to orientational ordering induced by the shape of the grains which eliminates the degeneracy of circular particles. Additionally, as the orientation of principal stress in photoelastic particles was readily made visible, optical image analysis suggests that there is direct correlation between the size of the dip and the mean chain orientation within the pile.

Recently, a number of carefully designed experiments were carried out within granular solids and silo group at the University of Edinburgh. The experimental investigation measured the pressure distribution underneath a conical pile as the pile grows. Approximately spherical iron ore pellets with a mean diameter of $3mm$ was used to build up the pile. Figure 4.3 shows the vertical pressure measured at the end of the pile formation on the base at several radial positions, plotted against the normalised radius (relative to the mean base radius R_p deduced from diametral measurements). The results show a robust and reproducible pressure profile with a significant dip under the apex, rising steadily from a minimum pressure at the centre to a peak at the radius of $r \approx 0.3R_p$, before falling off towards the edge of the pile. Furthermore, it was also pointed out that base deflection, elongated particles and particle size segregation are not pre-requisites for the pressure dip formation.

4.2.2 Analytical study and continuum modelling

Owing to the complexity of granular systems, mathematical formulation in solving the base pressure in granular piles has attracted significant interest particularly from the physics community. Cates et al. (1998) summarised the difference of research motivation faced in a broad range of disciplines as:

(a) Pile composed of iron ore pellets

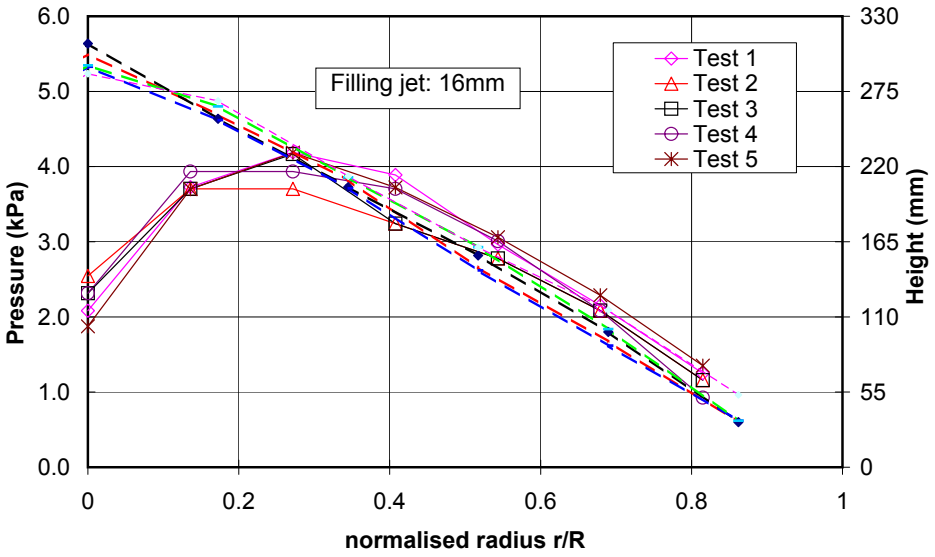

(b) Base stress compared with hydrostatic pressure

Figure 4.3: Experiments carried out at the University of Edinburgh (Ooi et al., 2008)

> *From the perspective of geotechnical engineering, the problem of calculating stresses in the humble sandpile may appear to be of only marginal importance. The physicist's view is different: the sandpile is important, because it is one of the simplest problems imaginable in granular mechanics.*

It thus highlights the complexities of granular mechanics even when the particles are deposited in the simplest form. Physicists (Bouchaud et al., 1995) tended to reflect the true physics of poured cohesionless grains rather than the conventional elasto-plasticity in applied mechanics. Wittmer et al. (1996) proposed a postulation that principal stress axes have a fixed angle of inclination to the vertical direction, and it was therefore called the fixed principal axes (FPA) model. Comparing to previous continuum models, this hyperbolic model assumes that external load is supported by a skeletal network of force chains, and the stress dependence on construction history is embodied through a local anisotropy in grain organisation. This FPA model is highly speculative and has not received general acceptance.

Tejchman and Wu (2008) performed FEM analysis on vertical stress distribution under sandpiles, in which a micro-polar hypoplastic constitutive model was incorporated. A striking feature of this model is the fact that the constitutive equation is incrementally non-linear in deformation rate and the inclusion of the critical states. Their results confirms the experimental findings reported by Vanel et al. (1999), where the methods of the heap construction largely affect the pressure profile. Additionally, it is suggested that the vertical pressure distribution did not depend upon the initial void ratio, mean grain diameter, heap inclination and base roughness.

4.2.3 Discrete element simulation

Zhou et al. (2003) performed DEM simulations with spheres for wedge-shaped sandpiles formed on bases of different degrees of deflection. The numerical prediction demonstrates that base deflection has a significant effect on the normal pressure distribution. However, it is also suggested that base curvature is not the sole factor leading to a normal pressure distribution with a dip, particularly when a sandpile is constructed with monosized spheres.

Matuttis et al. (2000) introduced 2D convex polygonal particles in DEM simulation to study the influence of particle shape on the base pressure of granular piles. It is found that both the angle of repose and pressure profile depend on the polydispersity of particle employed. Increasing the particle sphericity leads to a reduction in the measured angle of repose. The results support the evidence of a dip in the vertical stress under the apex of the heap when the pile is constructed from a point-like source, where the resulting avalanches and particle rearrangement will significantly enhance the arching.

4.3 Implementation of DEM model

The widely used non-linear visco-elastic Hertz-Mindlin no slip contact model was adopted in all simulations reported in this chapter. For simulations involving spheres, rolling friction was found to be necessary to produce a pile with a realistic angle of repose, so a simple rolling friction model first proposed by Zhou et al. (1999) was used, in which a rolling friction torque acts opposite to the relative rotation between particles and between particles and boundary. A classical Coulomb sliding contact friction was considered for all cases, in which particle contact is modelled using a spring-dashpot model with a tangential slider satisfying the Columb friction. The commercial code EDEM was used to simulate

spherical particles because the rolling friction model of Zhou et al. (1999) has been fully implemented in EDEM and is not available in Itasca PFC^{3D}.

The particles were centrally charged onto a rigid horizontal frictional base to form piles of varying dimensions. The three groups of simulation (single layer pile, wedge-shaped pile and conical pile) were conducted and presented in the next three sections. Table 4.1 lists the material parameters used in this sandpile simulation.

Table 4.1: Values of the DEM parameters used

Name of the variable	Symbol	Value
Sphere radius (mm)	R	2
Particle density (kg/m^3)	ρ	3000
Poisson's ratio	ν	0.3
Young's modulus (MPa)	E	10
Damping coefficient	B	0.8
Sliding friction between particle and particle	f_p	0.3
Sliding friction between particle and base	f_w	0.2
Rolling friction for the spheres	f_r	0.3

For single layer and wedge-shaped piles, the base pressures were averaged on a base segment of length 10 times the mean particle diameter, with the segment boundary moving by one particle diameter for each evaluation (moving average technique). The averaging process on 10 diameters was chosen to give a balance between the very high scatter if the segment is small, and the loss of detail if it is large. The change of only one diameter indicates what an imaginary pressure cell might observe if placed at each point. Similarly, annular averaging segments were utilised in pressure evaluation for conical piles. Figure 4.4 illustrates the moving averaging scheme adopted in the current study. These evaluated distributions of

base pressure are presented and discussed in the following sections.

(a) Standard averaging method

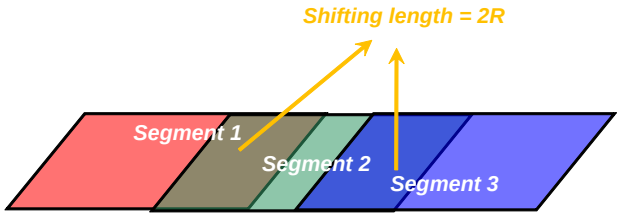

(b) Moving averaging method

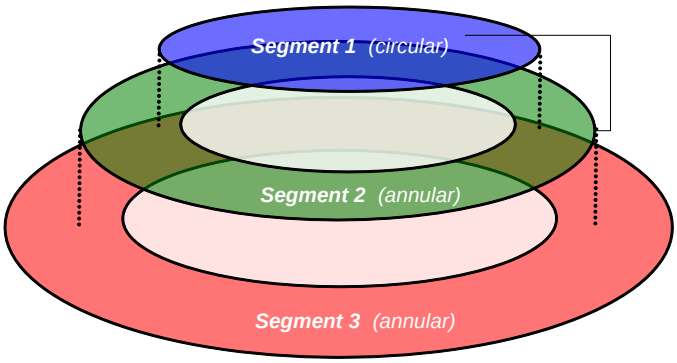

(c) Annular averaging segments used in conical pile

Figure 4.4: Moving averaging method in the evaluation of base pressure

4.4 Numerical results from DEM simulation

4.4.1 Single layer pile model

In this DEM model, all particles were generated to fall randomly with particle centres aligned in a vertical plane. The non-spherical particles were generated with random orientation of the particle longitudinal axis in the prescribed plane.

The simulation thus simulates the pile formation from a single layer of particles and resembles a 2D situation. The pouring jet was given a width of $10R$ to model a concentrated pouring jet but large enough to avoid mechanical arching. The jet was kept as close to the top of the growing pile as possible to reduce the impact energy on the pile. The distance between the apex of the pile and the jet source was maintained at a height in between 8 and 15 particle diameters. The charging rate was set at 500 particles per second. When the target number of particles has been generated, the assembly was simulated for a further 3 seconds to reach its equilibrium state before the data was analysed. The equilibrium state was confirmed by examining both average unbalanced force and total kinetic energy in the whole system, which were less than $1 \times 10^{-6} N$ and $5 \times 10^{-11} J$, respectively. To explore the scaling effect, the granular pile was continued to be built up gradually by pouring more particles onto the pile and evaluate the pressure distributions at increasing pile sizes.

Figure 4.5 shows the predicted vertical pressure distribution acting on the horizontal base of single layer granular piles for single sphere and paired-sphere assemblies at 3000, 6000 and 9000 particles. The pressure is normalised with the maximum computed value P_{max} and the base coordinate is normalised with the radius of the pile R_p. For the non-spherical paired-sphere assembly, the M-shaped vertical pressure distribution with a central pressure dip is clearly evident even for the smallest 3000 particle heap. The dip became more pronounced as the pile grew larger. On the other hand, for the spherical assembly, the pressure dip was not present at 3000 particles, could be discerned from the 6000 particle case and became pronounced only for the 9000 particle case. There is also a significant loss of symmetry in the base pressure for the spheres due to significant local rupture events that perturbed the symmetry (see for example the local plateau of pressure midway between the apex and the edge of pile). This is related to the crystalline structure that has formed in the monosized sphere assemblies.

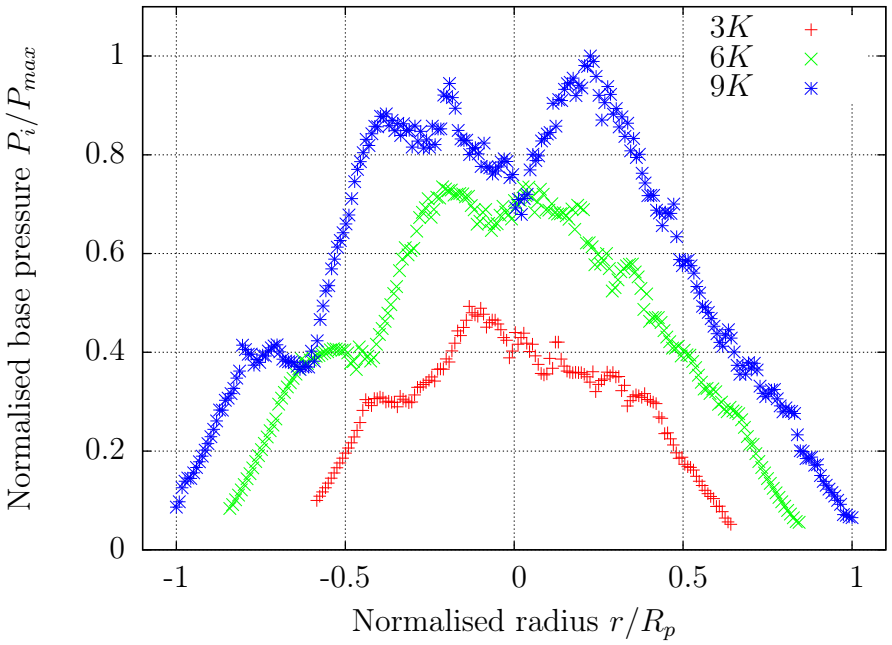

(a) Spherical particle

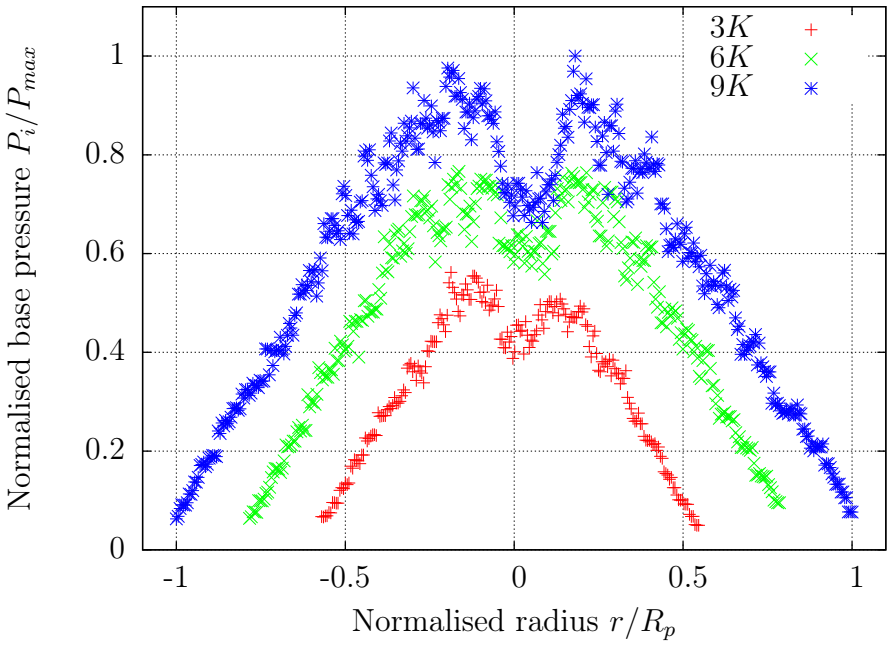

(b) Non-spherical particle

Figure 4.5: Base pressure distributions for single layer piles with 3000, 6000 and 9000 particles

The results in Figure 4.5 suggest that non-spherical particles with a greater degree of particle interlocking produced a more robust pressure dip. The base deflection as proposed by some researchers is not a prerequisite for the formation of the pressure dip since current simulations have predicted convincing pressure dips with a rigid horizontal base. The comparison between spherical and non-spherical assembly is also relevant since the great majority of the published simulations on granular piles are based on 3D spheres or 2D circular disks. Sphere with its perfect particle symmetry has the propensity for excessive particle rotation that can obscure the phenomena pertaining to real granular solids and would not have formed a stable pile on a horizontal plane. As explained above, rolling friction was introduced for the spherical assembly here which increased the rolling resistance and allowed a stable pile to be formed. The simulation without rolling friction was conducted (not shown here) and confirmed this occurrence. This also agrees with previous studies of Zhou et al. (1999) and others on the use of rolling friction to form stable granular pile. A detailed discussion on the various rolling friction models in DEM simulations and the influence on granular solid behaviour can be found in Ai et al. (2008).

The granular piles were further explored by studying the characteristics of the contact force network within the pile. For single layer model, all particle contacts occur within the prescribed plane, so the particle contact orientation can be evaluated as introduced in section 2.2. Since each contact always appears in pair, there exists a 180° rotational symmetry. Figure 4.6 shows the distribution of the contact orientation for all the particle-particle contacts in the pile presented as radial plots. In these plots, the frequency of occurrence for each contact angle is normalised with the maximum value in the total contact network and 0° represents two particles in contact horizontally whilst 90° represents vertical contact orientation.

For the monosized sphere, a crystalline packing structure has formed pro-

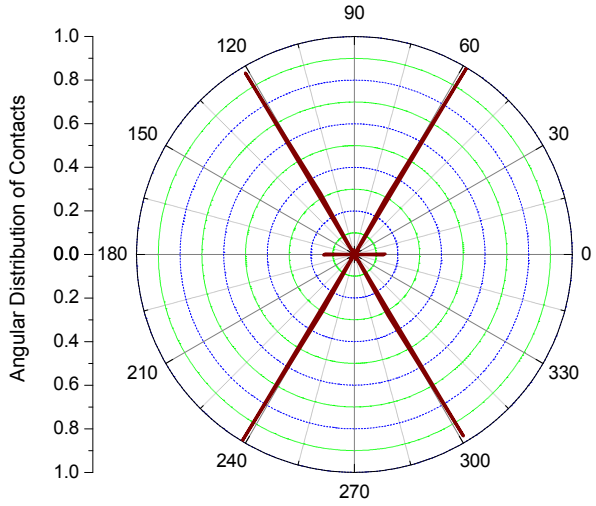

(a) Spherical particle

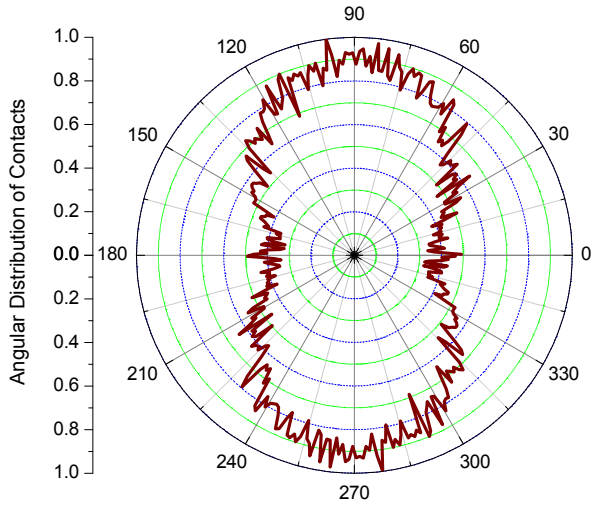

(b) Non-spherical particle

Figure 4.6: Distribution of contact orientation in the single layer pile with 9000 particles

ducing contact orientation predominantly in the 60° and 120° orientations. For the pile composed of paired-sphere particle, the contact orientations show a periodic distribution which can be approximated by a second-order Fourier expansion with a preferential vertical contact orientation. This distribution compares well with the DEM calculations of Nouguier-Lehon et al. (2005) where polydispersed polygonal particles were simulated, indicating that this form of contact distribution may prevail in most naturally deposited granular assemblies of non-spherical particles. The significant difference in contact orientation between spherical and non-spherical system shown here suggests caution in extending the results from studies based on 3D spheres and 2D disks to real granular solids that are not perfect spherical.

It is also interesting to explore the orientations of the particles in the granular pile formation. Figure 4.7 shows the orientation distribution of the particles' long axis for the paired-sphere pile in this single layer model with 9000 particles. The orientation of the paired-sphere particle is defined as the angle that its long axis makes with the normal to the base as illustrated in Figure 2.2. It can be observed that the particles are mainly oriented horizontally, being the optimally most stable position. This also explains the dominant vertical contact orientation noted above. Very similar particle orientation distribution has been observed in photoelastic granular pile experiments on elliptic cylinders as shown in Figure 4.7b (Zuriguel and Mullin, 2008).

In granular solids, contact force is transmitted by relatively rigid, heavily stressed chains of particles which form a sparse network of strong contacts carrying greater than average normal contact forces. The remaining groups of particles, which separate the strong force chains, are only lightly loaded. To better visualise the network of contact forces, Figure 4.8 shows the force chains which carry greater than average contact force in the single layer pile with 3000 paired particles. Observing the force chains near the base, it appears that there was a particle

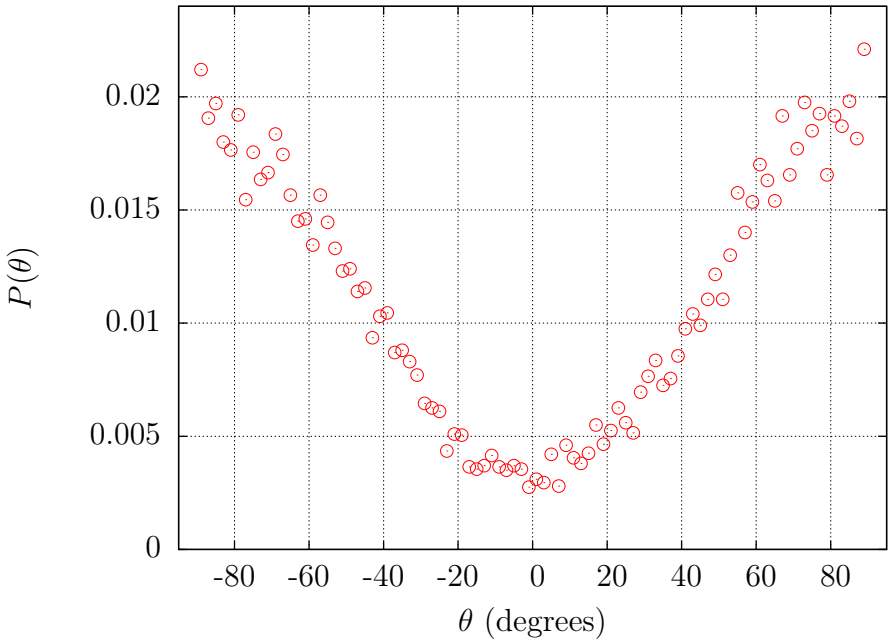

(a) Particle orientation in the 9,000 paired-sphere granular heap

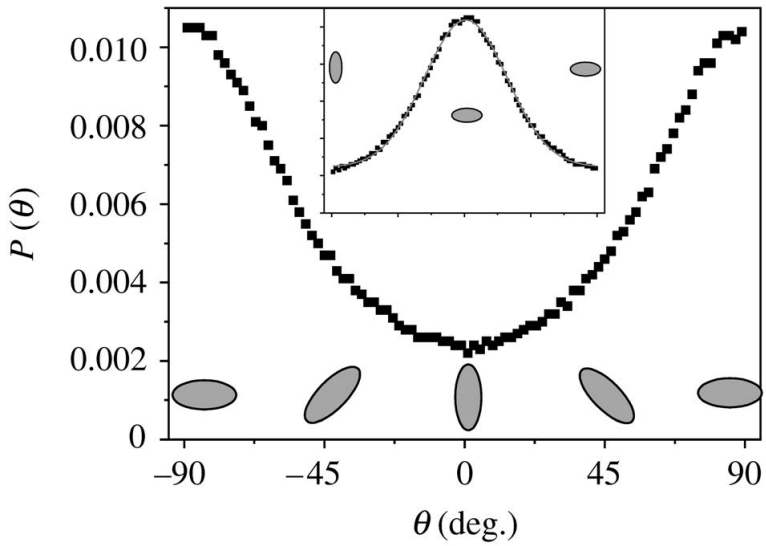

(b)) Particle orientation measured in photoelastic heap experiments of Zuriguel and Mullin (2008) using elliptic cylinders

Figure 4.7: Comparison of particle orientation distribution in simulation and experiment

arching seemed to develop under the apex of the heap, which may be responsible for the existence of central pressure reduction and needs further investigation.

4.4.2 Planar wedge model

The single layer model is further extended to wedge-shaped granular pile, which has been reported in studies of the pressure distribution beneath a sandpile (Vanel et al., 1999; Zhou et al., 2003). The wedge pile was simulated by confining with front and rear frictionless vertical walls to form a wedge pile with a thickness of 16 times the particle radius. Simulations were carried out with paired-sphere particles being centrally charged over the whole thickness onto a rigid horizontal base.

Several researchers have studied the influence of heap construction history on the formation of the pressure dip e.g. (Vanel et al., 1999). Recent 2D photoelastic experiments carried out by (Geng et al., 2001) provides evidence of the effect of width and falling height of the pouring jet. Here, planar wedge DEM models of granular piles were simulated using two pouring jet dimensions to investigate this effect: a wide extended pouring jet ($80R$ width) and a narrow concentrated jet ($8R$ width). The results show that the angles of repose arising from the two pouring dimensions are the same at 32°, so the difference in the base pressure distribution cannot be attributed to the repose angle or self weight of the material. The associated vertical base pressures underneath the pile are presented in Figure 4.9.

It is evident that for this pair of simulations, the run with a concentrated jet displayed a distinct dip whereas the one with the extended pouring jet did not. This supports the proposition that the method of pile construction play a significant role in the formation of the pressure dip. The results suggest that the concentrated jet charging leading to material avalanching down the conical

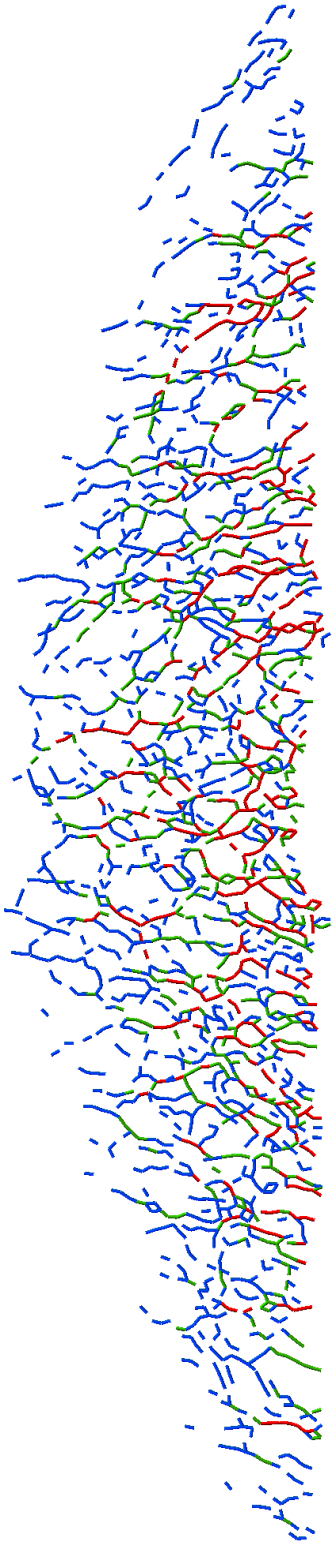

Figure 4.8: Force chains in a single layer pile with 3000 paired particles

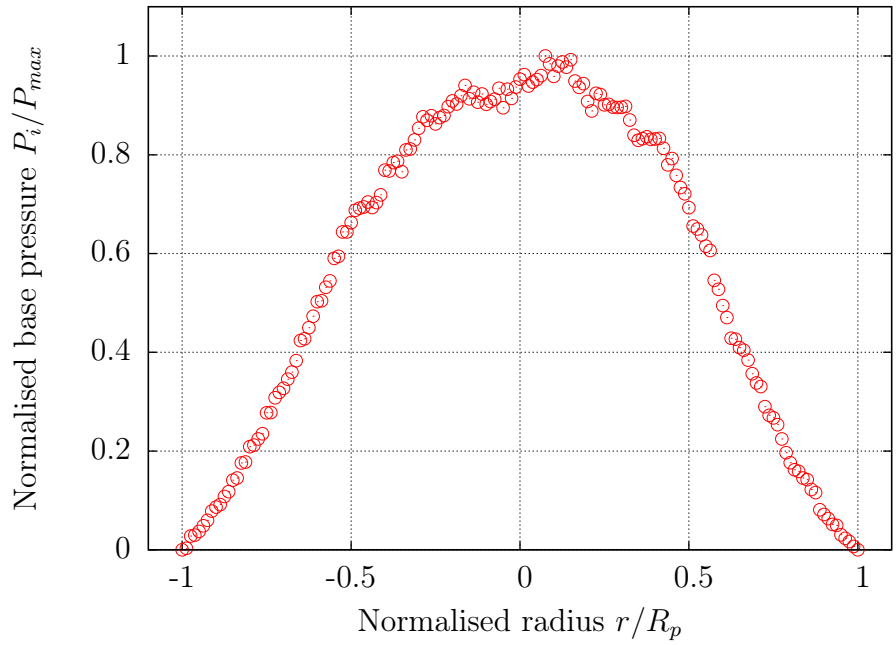

(a) Extended pouring jet

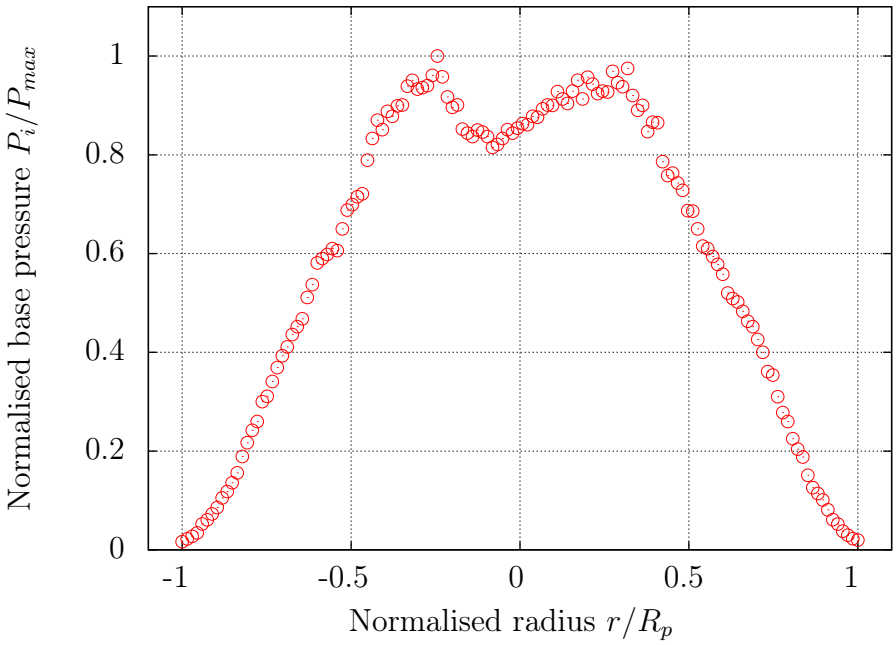

(b) Concentrated pouring jet

Figure 4.9: Base pressure profiles for 3D wedge pile of 5000 paired-sphere particles using two different pouring jets

slope during formation may be important in the pressure dip phenomenon. With the extended pouring source, this process may have been somewhat disturbed to the point that the resulting packing structure no longer exhibits the M-shaped pressure distribution. Further experimental results (Ooi et al., 2008) indicated that even for an extended pouring jet, the pressure dip will eventually take form as the pile grows larger. The dimension of the charging jet relative to the dimension of the pile is an important scaling issue which is under further investigation.

4.4.3 Conical pile model

This section presents the full 3D conical pile simulations using paired-sphere particles. The common proposition in explaining the pressure dip is some form of arching effect arising from the formation process which results in a significant part of the weight at the central zone being progressively carried by the outer radial zone. It is thus interesting to compare the results from the single layer model and the planar wedge model to this full three-dimensional conical pile where the arching action is significantly different.

Figure 4.10a shows the vertical base pressure under conical piles of 5000, 10000, 15000 and 20000 particles. Axial symmetry was assumed in the pressure evaluation with the averaging segmental area being an annulus section, so only half of the pressure profile is shown. Similar moving averaging was deployed so that every statistically possible pressure evaluation has been plotted. The averaging areas started from a circle with a radius of $6R$ at the centre of the conical pile, and then incrementally shifted by $1R$. The results showed the evolution of the pressure dip as the pile built up, which appears to have not been reported by any previous numerical studies. The base pressure appears to approach an asymptotic M-shaped pressure distribution as the pile size increases. The results may be compared with the physical stockpile experiments of Ooi et al. (2008)

using mini iron ore pellets (Figure 4.10b) where much similarity can be discerned. Also, the experiments showed a dip which approaches 50% of the maximum base pressure measured at a radial coordinate of $0.3R_p$: this also compares reasonably well with the DEM prediction here. Comparing with the single layer and planar wedge models, the conical pile appears to produce a larger central dip which is probably due to the greater degree of arching in a conical pile compared with the planar arching in the previous two models.

It is reasonable to assume that the averaging lengthscale of $6R$ chosen above can have a significant influence on the computed pressure distribution especially where the pressure is changing rapidly and the numerical pile is relatively small. The sensitivity to averaging lengthscale is explored further using $4R$, $5R$, $6R$ and $7R$ averaging segments and the results are shown in Figure 4.11. The scatter in the computed pressure increases as the averaging length decreases. This is expected since at small lengthscale, the discrete nature of the complex local contact force structure dominates, resulting in highly fluctuating averaged forces. To assist in characterising the pressure distribution and the magnitude of the central pressure dip, an empirical equation was proposed of the form:

$$P = a\cos\left[b\frac{\pi r}{2}\right] - ce^{-r/d} \tag{4.1}$$

with four fitting coefficients a, b, c and d and performed non-linear regression best fit to each of the four cases, which are also plotted in Figure 4.11.

The best fit trends for the four averaging lengths turn out to be very similar: the central minimum pressure, the maximum base pressure and its radial location are not particularly sensitive to the choice of these four averaging lengths trialled, which lends credence to base pressure evaluation here. Further information on the number of contacts per averaging segment is shown in Figure 4.12 for 20000 particle granular pile with $6R$ averaging length. The number of contacts per

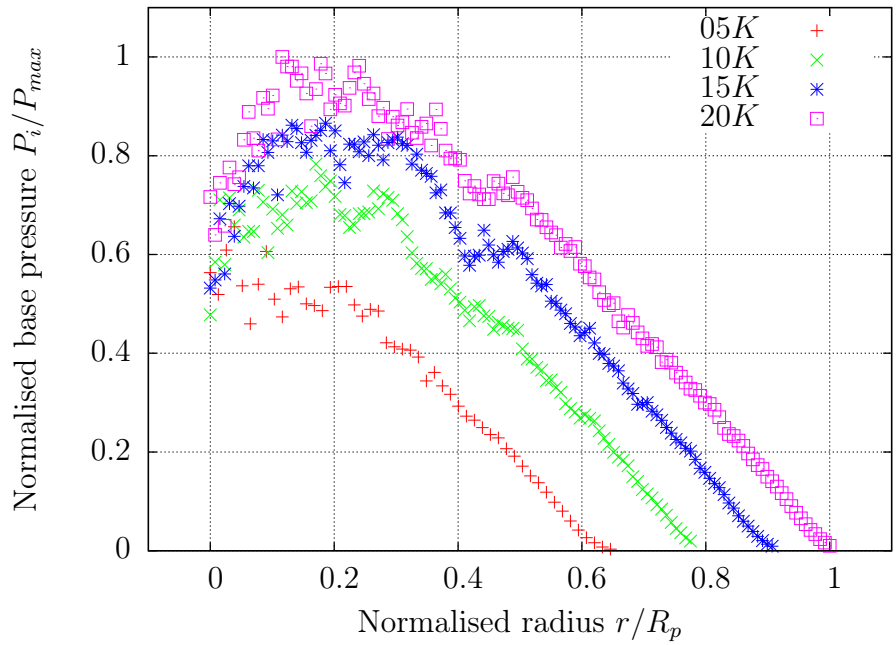

(a) Conical pile DEM simulations

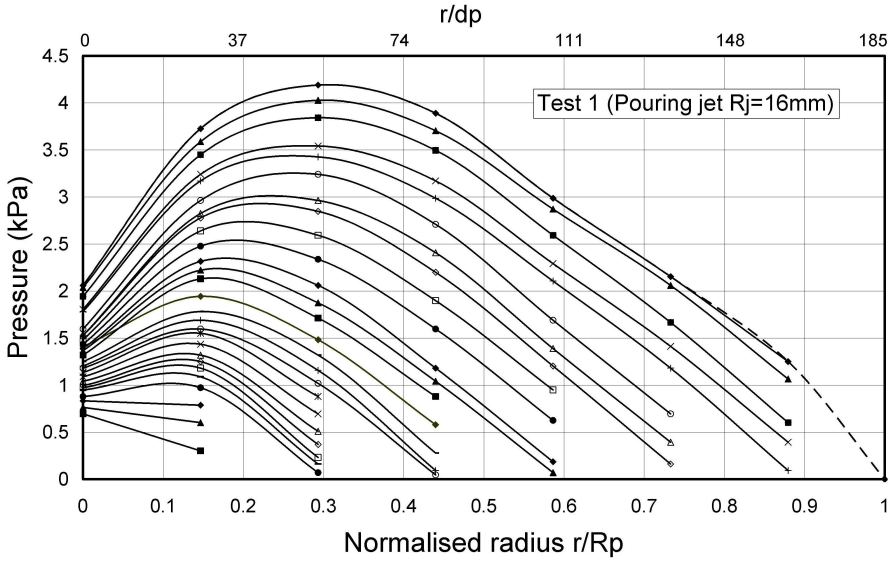

(b) Iron ore pellets experiments (Ooi et al., 2008)

Figure 4.10: Base pressure profiles for 3D conical stockpiles

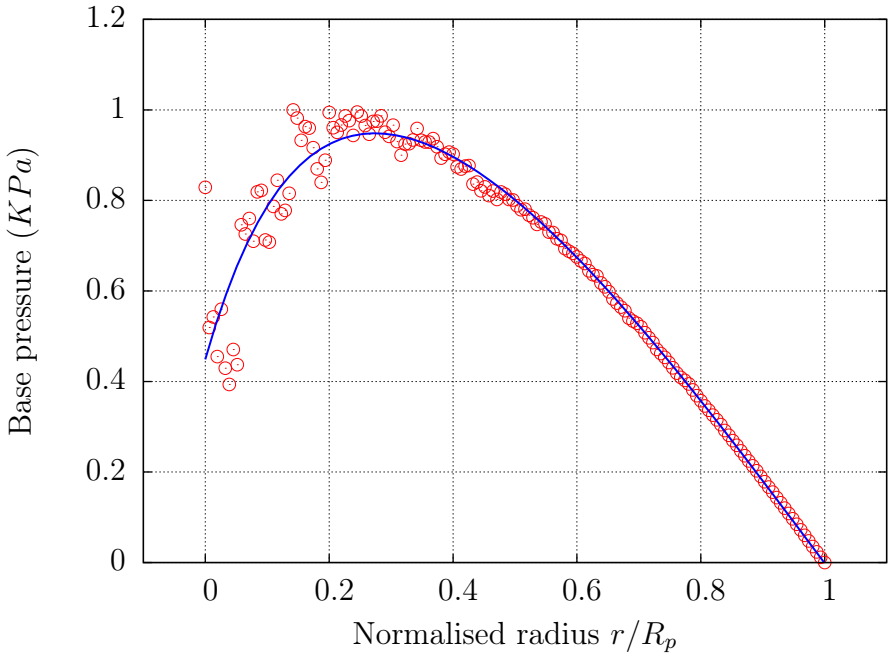

(a) $4R$

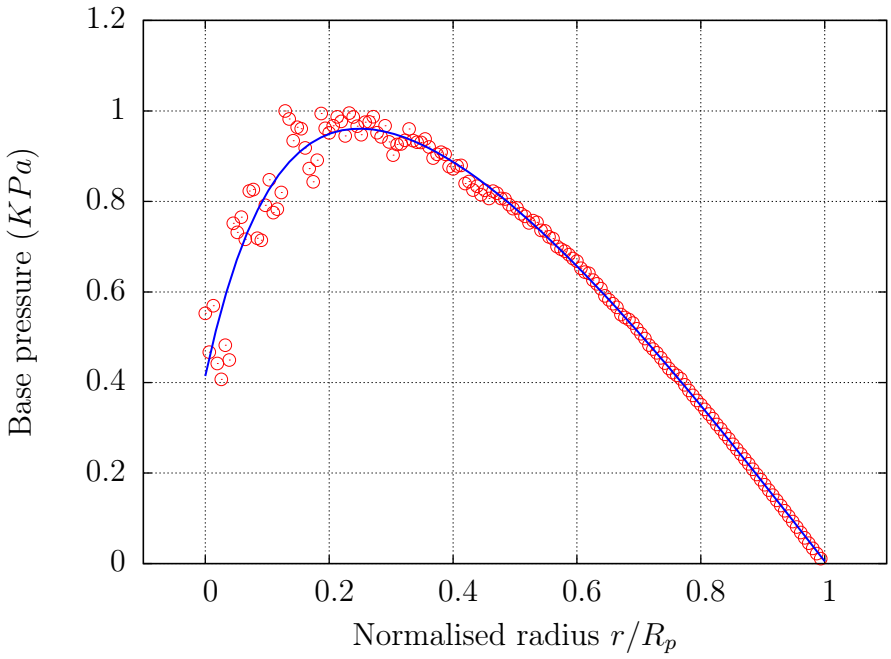

(b) $5R$

Figure 4.11: Base pressure evaluated with different averaging segmental lengths

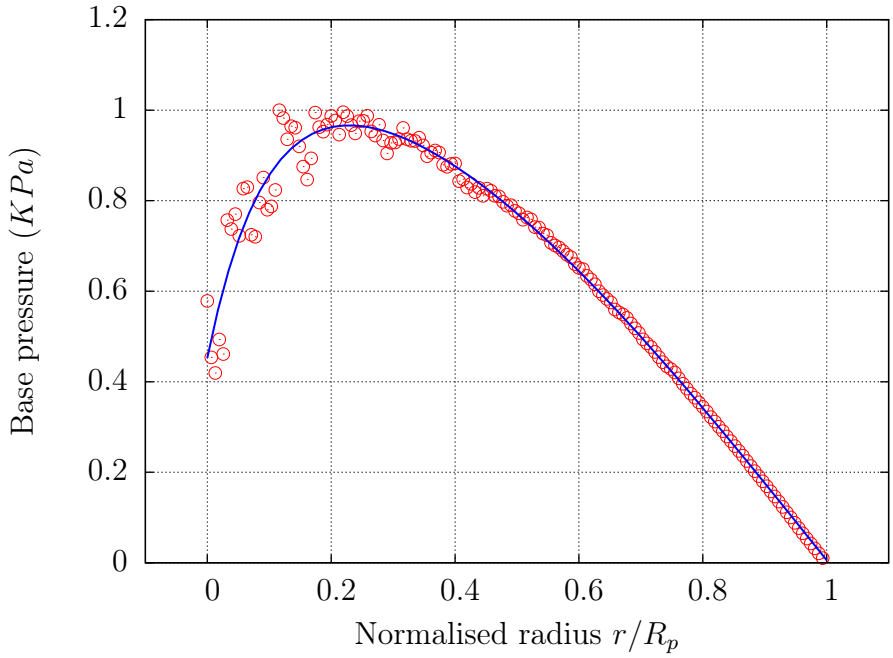

(c) $6R$

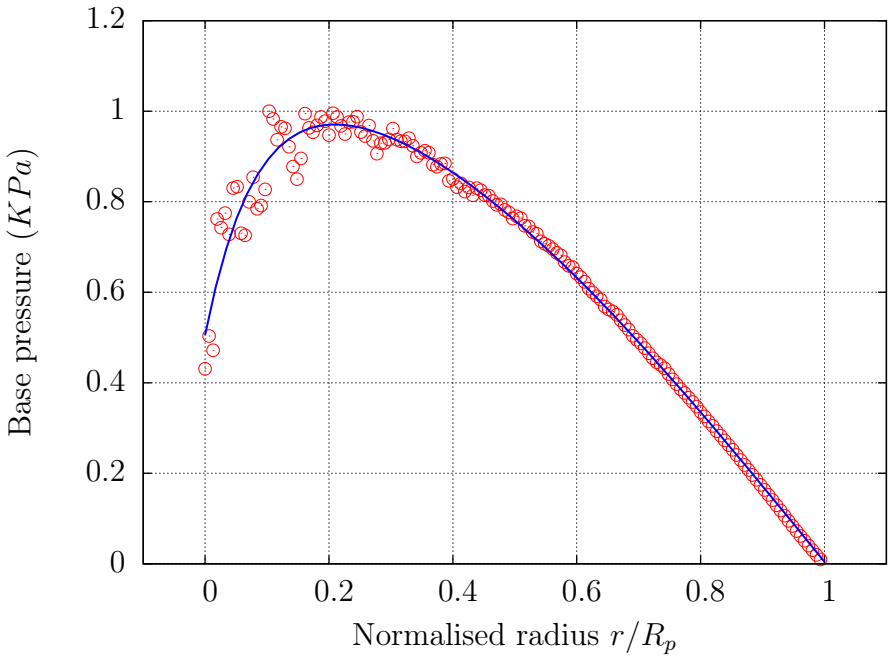

(d) $7R$

Figure 4.11: Base pressure evaluated with different averaging segmental lengths (*cont.*)

segment increases almost linearly as the averaging area increases, with more than 100 contact forces per averaging length for radial coordinate greater than 20% of pile radius. The average contacts per segment turn out to be relatively constant at 0.043 contact per mm^2.

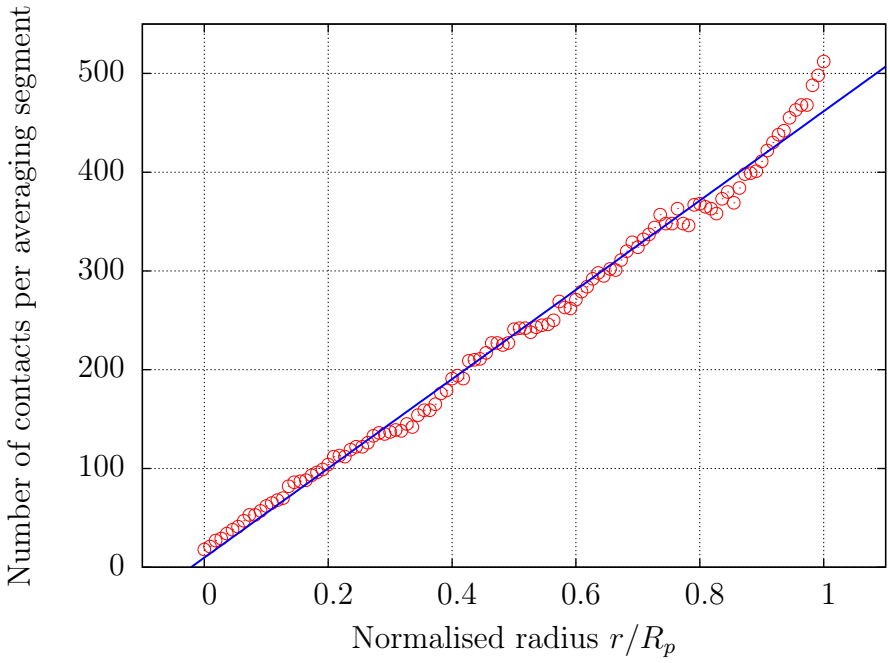

Figure 4.12: Number of contacts in averaging segment for a 3D conical pile with 20,000 particles

To further probe the magnitude of the contact force within the pile, the probability density function for the contact force F (normalised with the mean contact force for the whole population) is shown in a semi-logarithmic plot in Figure 4.13. The data shows that the strong contact forces (defined as $F > 1$) are well described by an exponential function of the form $P(F) = Ce^{-nF}$ indicating that the occurrence of the strong forces decreases exponentially with the magnitude of the force and there is a significant scatter at the tail end where the contact forces are large. For the weak contact forces (defined as $F < 1$), the distribution

deviates away from the exponential. These weak contact forces constitute the majority of the contacts in the system (more than 70% of all contacts), which is in agreement with the experimental observations of (Geng et al., 2001) and the numerical results of (Radjai et al., 1998). Similar contact force distribution has been reported in other densely packed granular solid systems (Coppersmith, 1997; Liu et al., 1995).

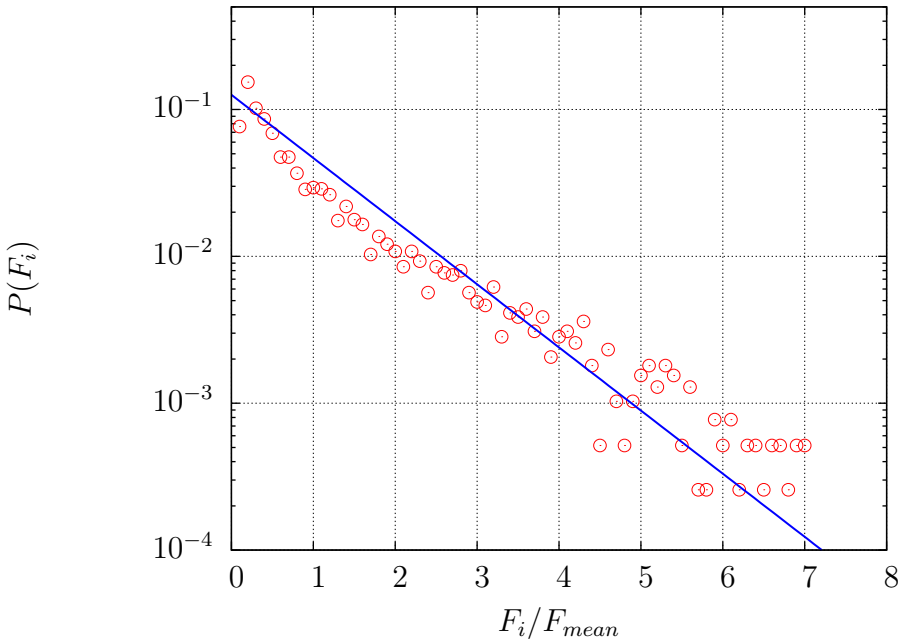

Figure 4.13: Normalised contact force distribution function $P(F_i)$ for a 3D conical pile with 20,000 particles

4.5 Summary

Discrete element simulations of granular piles using spherical and non-spherical particles have been presented. For spherical assembly, a stable granular pile with a realistic angle of repose is predicted only when rolling friction is incorporated. The resulting base pressure profile appears more erratic with a less robust central

pressure dip than the non-spherical particles. It is suggested that spherical particles with its perfect symmetry has the propensity for excessive rotation that can obscure the phenomena pertaining to real granular solids. The rest of the chapter focused on non-spherical particle in the form of a paired-sphere shape with an aspect ratio of 1.5. The results show that the paired-sphere assembly produced a robust M-shaped pressure profile with a significant dip under the apex when a sufficient pile size was achieved.

Apart from the smallest 5000 particle conical pile simulation, all paired-sphere simulations reported in this paper produced a central pressure dip. The results support the proposition that the M-shaped pressure distribution is a robust and natural pressure distribution for a typical stockpile where the scale is considerably larger than the mean particle size. In addition, the results indicate that base deflection is not prerequisite for the pressure dip whereas a relatively concentrated pouring jet with respect to the pile dimension appears to be essential. The base pressure distribution under progressive development of the granular pile suggests the base pressure approaches an asymptotic M-shaped pressure distribution as the pile size increases, which is in good agreement with experimental observations. The dimension of the pouring jet relative to the dimension of the pile is an important scaling issue which is under further investigation. The granular fabric in terms of magnitude of the contact force, contact orientation and particle orientation within a granular pile have also been described.

Typical industrial stockpiles can easily contain over 10^{10} particles. Recent advances in parallel implementation of DEM methodology coupled with increasingly cheap and powerful CPUs mean that it is now quite possible to model large stockpiles of the order of $10^5 - 10^7$ particles or more. However the present study suggests that the pressure dip phenomenon develops from relatively early stages of pile formation. One of the largest scale experimental investigation of stockpile confirmed that this is indeed the case (McBride, 2006). The capability of DEM

to predict the pressure dip phenomenon with a promising agreement with the experiments shows the potential of using this technique to explore the particle scale mechanics and the associated granular fabric which produce bulk responses that are still poorly understood.

Chapter 5

Rigid body penetration in granular solids

5.1 Introduction

Granular solids subject to a rigid body penetration can be related to a wide range of geotechnical applications, e.g. pile installation, soil samplers and in situ testing tools. Pile foundations have been extensively used to support buildings and structures by transferring load to deeper and more competent soil layers. The design and construction of displacement piles and offshore foundations have been recognised as challenging tasks with many uncertainties, which require a sound understanding in the soil classification and estimation of its mechanical properties (e.g. shear strength, bearing capacity). Such information can be best obtained from proper in situ tests. The standard penetration test (SPT) and cone penetration test (CPT) are among the most popular tools for the characterisation of a geotechnical site. The merit of these tests, and the main reason for the widespread applications is primarily due to the simplicity and economy. The measured resistance that the probe encounters in the ground can be extrapolated

to evaluate the bearing capacity of pile foundation. Although the inferred soil parameters are unavoidable approximate, it gives a useful guide for ground conditions where it may not be possible to obtain undisturbed borehole samples of adequate quality. Thus, investigation of penetration test and the underlying penetration mechanism, is of interest to both geoscience researchers and geotechnical engineers.

Noticeably, most of the numerical approaches used to study penetration problems have a rather weak representation of the discontinuities within the soil mass, where only the deformability and strength of the soil are considered in constitutive laws. Therefore some phenomena caused by the inherent inhomogeneity in granular materials at the grain scale are preserved. Recent advances in discrete element modelling offer unique opportunities to evaluate mechanical properties and behaviour of granular solids. In this chapter, DEM simulations of penetration test are carried out to study the bulk resistance to indentation and the force transmission mechanism. The chapter commences with a literature review of theoretical methods and numerical modelling of penetration test. The numerical implementations of the discrete element modelling was then outlined. Penetration resistance, deformation pattern, homogenised stress fields as well as contact network were analysed to interpret the progressive penetration mechanism. The way that particle shape and gravitational acceleration influence all these aspects were carefully compared and discussed. Although this is not a standard penetration test, and should not be regarded as such, it gives insight into the micromechanics involved and the application of DEM across multiple length scales of interest in geotechnical engineering. Another focus of this chapter lies into the PIV measurement of deformation field in physical experiments in which a model footing was indented into granular solids. The development of displacement, velocity magnitude, streamline and shear strain were presented. Finally, a set of corresponding DEM simulations of footing test were also conducted to access its capability in

quantitative prediction of bulk behaviour.

5.2 Literature review

This section deals with a brief review of the previous studies on the prediction and validation of penetration resistance in granular materials. It covers the principal ideas behind these methods, as well as their capabilities and limitations.

5.2.1 Analytical and theoretical methods

Over the past decades, a number of analytical theories have been proposed to evaluate the penetration resistance, which include bearing capacity theory, cavity expansion method and strain path method etc.

- Bearing capacity theory: The bearing capacity of a foundation is defined as the critical load per unit area at either the ground surface or at a certain depth below the ground surface that is necessary to mobilise the full shear strength of the soil. The critical load depends not only on the mechanical properties of the soil but also on the size and shape of the footing. Yu and Mitchell (1998) presented a detailed review of several bearing capacity solutions. The major advantage of this approach was summarised as its relative simplicity, which can be easily adopted in many engineering practices. However, its limitations were also pointed out, including insufficient consideration of both soil deformation around penetrator and initial stress state. These drawbacks suggest that the dependence of tip resistance on soil compressibility, which have been observed from many in situ tests, cannot be properly predicted.

- Cavity expansion method: Bishop et al. (1945) first proposed the analogy between cavity expansion and cone penetration. According to this method,

the penetration can be simulated by expanding a cavity of an initial zero or finite radius. The pressure needed to develop a deep hole in an elastic-plastic medium is proportional to the pressure required to expand a cavity of the same volume under similar conditions. Yu (2000) published a book regarding the cavity expansion theory and its applications in solid and rock mechanics. This method treats the penetration in a more realistic manner as both elastic and plastic deformation of the soil during the large strain deformation can be taken into consideration. Additionally, the influence of initial stress state and stress rotation occurred near the penetrator are also approximately examined.

- Strain path method: Baligh (1985) noticed that deep steady penetration are mainly strain governed. This finding suggested that if the strain path around the cavity can be reproduced in a suitable laboratory test, the soil stresses could then be estimated. This analytical analogy is thus known as the "strain path method". Furthermore, it was explicitly pointed out that this method offered the means of extending penetration solutions in an approximate form to more practical situations of interest, particularly anisotropic clays, rough piles, compressible soils etc. In this method, strain rates are firstly calculated from pre-estimated velocity fields. Based on the streamline profiles, strain paths for each element can be obtained by integration of those strain rates. At this stage, constitutive properties are introduced to compute stress fields from the equilibrium relation.

5.2.2 Experimental work

The repeatability and reliability of the standard penetration test (SPT) have increased its application as a main choice in in situ testing techniques. Figure 5.1 shows a standard split-spoon sampler which is driven into the soil through

a supported borehole. The test procedure is described in the British Standard (BS EN ISO 22476-3) and American Society for Testing and Materials Standard (ASTM D1586). The usefulness of SPT results largely depends on the soil type, with fine-grained sands giving the most reliable results, and clays and gravelly soils yielding results which may be poorly representative of the true soil conditions. Despite these flaws, the reason being that SPT results are often the only test results available. It has become common practice to directly correlate SPT results with soil properties relevant for various geotechnical engineering design.

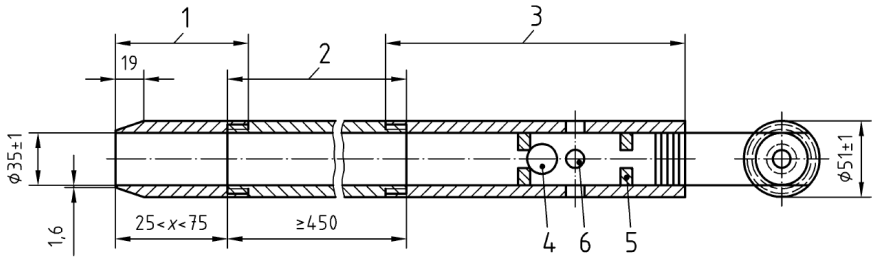

Key

1 Drive shoe
2 Split barrel
3 Coupling
4 Non return valve (ball diameter: recommended 25 mm; ball seating: recommended 22 mm)
5 Ball retaining pins
6 Four vent holes (min diameter 12 mm)
x Length of the drive shoe

Figure 5.1: Longitudinal cross section of a SPT sampler (BS EN ISO 22476-3)

In many geotechnical tests performed at earth gravity of $1g$, the loads primarily depend on the soil cohesive strength but not on gravitational forces. These tests give little information about the stress dependent behaviour of the soil. To overcome the expense and delay of carrying out full scale tests, centrifuge tests have been widely employed. Centrifuge modelling refers to the testing of a reduced scale model in a radial acceleration field of n times earth gravity, in which the self weight stresses at corresponding points are the same as in the field. Powrie (1996) pointed out that the low stresses in $1g$ tests in sands can give

misleading results, because the dilation effect may be way more significant than they would be at higher stresses in field constructions; in clays, the stresses which drive failure may be too small in relation to the undrained shear strength. Experimental work carried out by Allersma (1995) suggested that one major advantage of centrifuge test was that the shear stress can be more practically realised with the same magnitude as in a soil layer. In that sense, centrifuge tests constitute a valuable input in the understanding of large discontinuous displacements of earth segments at a large depth. Muir Wood (2004) presented the underpinning mechanics of centrifuge modelling and site investigations to study the in situ soil properties at such augmented acceleration levels. More details of centrifuge test can be found in Taylor (1995), in which the main feature was summarised as:

> *With this technique, self weight stresses and gravity dependent processes are correctly reproduced and observations from small-scale models can be related to the full-scale prototype situation using well established scaling laws. Centrifuge model tests have proved to be particularly valuable in revealing the mechanism of soil deformation and collapse and in providing data for validating numerical analysis.*

5.2.3 Finite element method

A considerable amount of research has been contributed to the simulation of penetration tests by using finite element method (FEM) in the past decades. FEM can provide an easy access to describe the initial stress state and soil stiffness, while the stress and strain fields can be determined through constitutive laws. However, during the penetration process, the occurrence of large mesh distortion in large deformation zones around the penetrator is difficult to to be avoided. This can lead to the severe loss of numerical accuracy and control of computational convergence. To overcome these difficulties, Arbitrary Lagrangian Eulerian (ALE)

method has been incorporated in the FEM formulation of penetration problems. In this method, the movement of the element nodes and the material points is decoupled, which enables the constraint of the excessive mesh distortion. Van Den Berg et al. (1996) applied ALE algorithm to simulate cone penetration in layered soil. The mesh refinement significantly reduced the influence of the boundary condition. Furthermore, by associating the updated Lagrangian description with an Eulerian formulation, the soil strength showed strong dependency on the the stiffness ratio between the layers. Huang et al. (2004) carried out a finite element analysis of cone penetration test, in which the soil was considered as homogeneous. Parametric study suggested that the horizontal displacement of soil around the cone was controlled by the size of the penetrometer shaft, whereas the vertical displacement depended on the elastic properties of the soil, the friction at the cone-soil interface and the strength of the soil.

5.2.4 Discrete element method

Discrete element modelling has been applied in granular systems where large deformation is involved including penetration problems. Muthuswamy and Tordesillas (2006a) carried out DEM simulation of granular assembly subjected to indentation by a rigid flat punch. It was concluded that interparticle friction, packing density and polydisersity played major role in the force propagation under penetration. Based on the contact data from DEM, a novel quantitative characterisation of force chain was proposed, in terms of the length, curvature and degree of branching. The quantification of force chains was further linked with the macroscopic strength. Findings indicated that straighter and shorter force chains, combined with a stronger degree of branching in the force chain network, resulted in a macroscopically stronger granular material. Lobo-Guerrero and Vallejo (2007) studied the effect of pile shape on the penetration resistance

in crushable granular materials. Piles with three different shapes (flat tip, open pile and triangular tip) were chosen to drive into a densely compacted sample. The highest penetration resistance was observed in a flat ended pile, which also induced the highest amount of particle crushing surrounding it. The simulation also considered the influence of the installation of a second pile after the first pile was driven. The penetration of the first pile resulted in a considerable densification in the sample, which in turn produced an increase in the penetration resistance of the second pile and more particle crushing. Jiang et al. (2008) employed DEM to simulate a cone shaped penetrator being quasi-statically pushed into the granular ground. Several particle motion patterns were observed during the penetration, featured by velocity fields. The penetration caused the granular solids near the penetrator undergoing both loading and unloading process, which also accompanied by large rotations of principal stress. It is noticed that all of these DEM studies reviewed only used spherical particles, while the effect of particle shape was not addressed.

5.3 Numerical implementation of penetration test in DEM

In the current study, the granular ground was simulated as a single layer of particles and subject to penetration by a rigid flat punch. There were 20,000 particles in the DEM model, for both spherical and non-spherical particles. The non-spherical particle was formed by clumping two spheres ($2mm$ in radius) giving an aspect ratio of 1.5. The mean particle radius of spherical particles was set as $3.6mm$, in order to give an equivalent volume to the non-spherical particle. In an effort to avoid the crystal packing arrangement in monospherical system, the radius of spherical particles followed a linear distribution of $3.6 \pm 1mm$. The

dimension of the granular assembly is $1400\times750mm$ and the penetrator width is $80mm$, which allows up to 10 particle contacts at the punch base and reduces any boundary effect. The rainfall filling method was used to form the assembly, which gives the particles more freedom to form a random packing structure during the course of settling down under earth gravity ($g = 9.81m/s^2$). Table 5.1 lists the DEM input parameters.

This study also concerns a numerical investigation of how the granular solids will respond under different gravitational accelerations, which will provide a useful contribution to the research of extraterrestrial mechanics. An amplified gravity field ($100g = 981m/s^2$) was applied to the whole sample similar to centrifuge modelling. Table 5.2 lists the initial sample void ratio for the four cases with different particle shapes and gravity accelerations. The punch is then introduced and indented into the particle mass at a constant rate of $10mm/$s. A snapshot of the particulate assembly during penetration is presented in Figure 5.2.

Table 5.1: Values of the DEM parameters used

Name of the variable	Symbol	Value
Particle density (kg/m^3)	ρ	3000
Young's modulus (GPa)	E	1.0
Poisson's ratio	ν	0.3
Damping coefficient	B	0.8
Sliding friction between particle and particle	f_p	0.5
Sliding friction between particle and punch	f_w	0.3

Table 5.2: Initial sample void ratio before penetration

Gravity	Particle shape	
	Spherical	Non-spherical
$1g$	0.2610	0.2327
$100g$	0.2292	0.2111

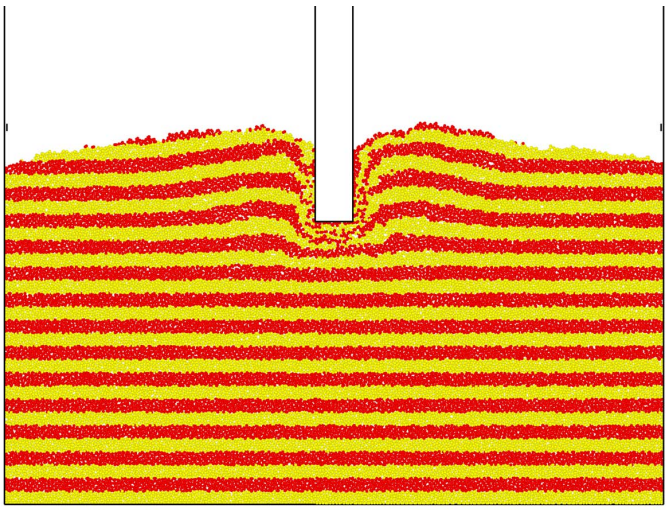

Figure 5.2: DEM setup of footing test

5.4 Results of DEM penetration tests

5.4.1 Penetration resistance

The reaction forces acting on the punch base were measured and recorded every 10^3 computational cycles (approximately 10^{-4} second) throughout the DEM simulation, which is much higher than the reading frequency in laboratory experiments. Figure 5.3 shows the base resistance as a function of penetration depth. The measured force fluctuated significantly as the punch was pushed into the sample, which is not usually reflected in continuum models. To reduce the noise in the raw data, temporal averaging was performed over a time span of 0.1 second, representing an output frequency of 10Hz. As observed in Figure 5.3, the averaged curve became much smoother and the variations in the loading response can be characterised. The general trend is that the penetration resistance increased linearly as the penetration proceeded, with the initial gradient higher than the one achieved later. In general, the bulk strength to resist the penetration is provided by interlocking asperities and interparticle frictional forces. The current results show that non-spherical particles produced a much higher resistance to penetration than spherical particles with the same contact friction. This implies that system using non-spherical particles was less apt to be stirred by the penetration, mainly due to the strong interlocking effect. Muthuswamy and Tordesillas (2006a) confirmed that as particle sliding friction was increased, the macroscopic penetration strength also increased, although not linearly.

Here, special attention will be given to the large amount of noises in the DEM predicted penetration resistance. These fluctuations have been widely reported from previous DEM simulations in the literature, and they can sometimes be as large as or even larger than the mean stress value (Liu et al., 1995). Figure 5.4a shows the bulk response of crushable granular solids subject to driven pile in-

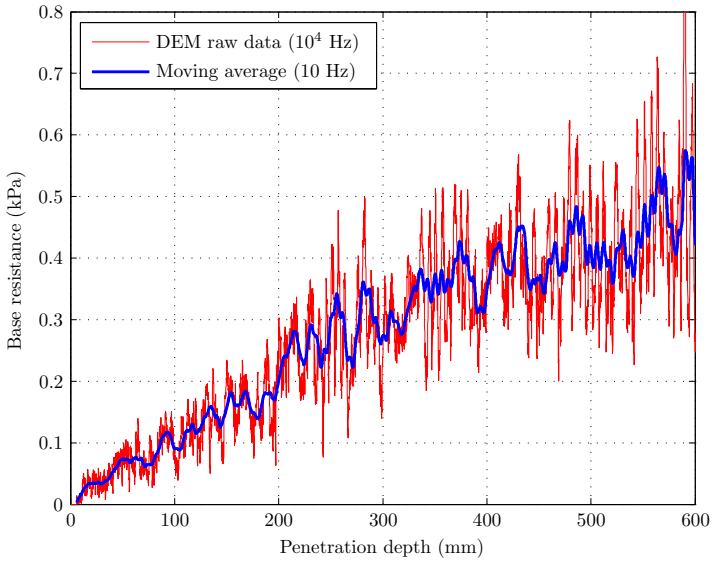

(a) Spherical particles

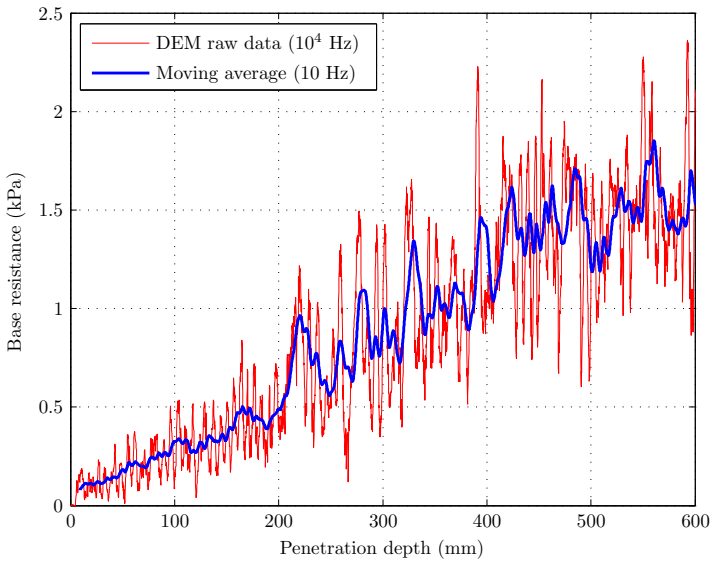

(b) Non-spherical particles

Figure 5.3: Base resistance response under earth gravity field

stallation from DEM simulation conducted by Lobo-Guerrero and Vallejo (2007). In their study, the spike drops were attributed to the particle crushing under high stress concentration beneath the punch tip. However, all the particles in the current DEM model were rigidly bonded and not crushable. Therefore, the explanation proposed by Lobo-Guerrero and Vallejo (2007) cannot be applied to the current simulation. Kheiripour Langroudi et al. (2010) investigated the spatial non-uniformities and temporal fluctuations in the normal stress transmitted across a sheared granular layer through DEM simulations of Jenike shear test. A dynamic sensor measuring the normal stress was set up and moved relative to the cylindrical side walls at the shearing velocity, similar to the moving punch in the current simulation. The sensor diameter D_s was varied to explore the spatial averaging effect. As shown in Figure 5.4b, there was a direct link between the spatial inhomogeneities and temporal fluctuations in the stress recorded, where the fluctuations became smaller as the sensor area increased. The implication was interpreted as considering the relatively small number of particles in the DEM model, each particle carries a large portion of force induced from external loading. This large portion is then transmitted to the transducer that either senses the presence of the particle (when the particles roles over it) or not (when the particle rolls off the sensor), giving rise to fluctuations that are smaller with smaller particles and larger with large particles. This understanding provides physical insight into the cause of the numerical fluctuation observed in the current small scale penetration model.

Taking advantage of the microstructural analysis of contact force network, the origin of these numerical fluctuations was further examined. Two key stages representing a typical significant drop in the bearing load were marked in Figure 5.5, during which the punch moved only $0.5D_{50}$ whereas the reaction force drooped from $20.9N$ to $8.2N$. The instantaneous force chain at these two stages with a zoomed view in the region directly under the punch were presented in Figure 5.6,

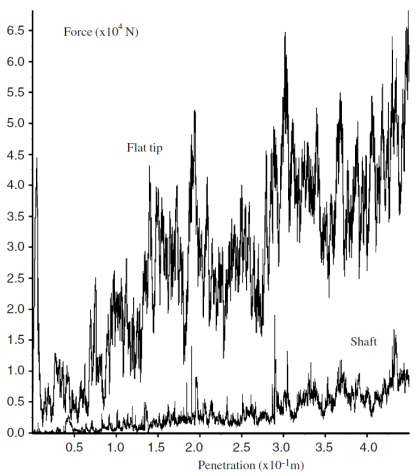

(a) Driven pile installation in crushable particles (Lobo-Guerrero and Vallejo, 2007)

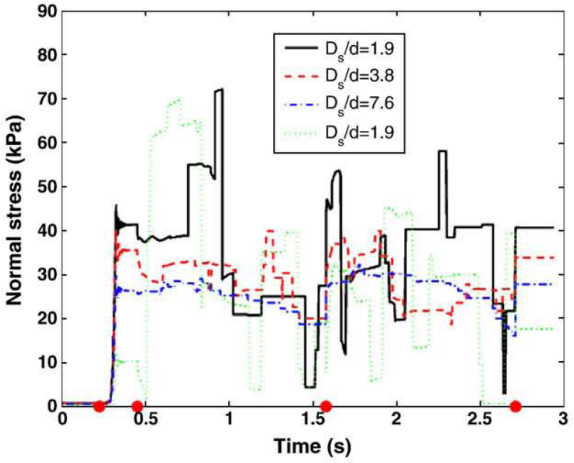

(b) Recording from the dynamic sensor with different areas in DEM simulations (Kheiripour Langroudi et al., 2010)

Figure 5.4: Data fluctuation observed in DEM simulation

where only the chains carrying above-average normal force were plotted. At the point when the peak load was achieved (stage A), a well structured strong force network was formed immediately under the punch base. After the sudden drop occurred at stage B, the existing contact network underwent a remarkable change, where many force chains have collapsed and there were less force chains directly supporting the punch. The results suggest that the pronounced fluctuation in the DEM prediction can be attributed to the successive collapse and reformation of force chains. This finding is consistent with past experiments studying the drag behaviour (Geng and Behringer, 2005) and stress propagation (Muthuswamy and Tordesillas, 2006b) in two-dimensional granular media.

The influence of gravity field was illustrated in Figure 5.7, where the penetration depth was presented in terms of punch breadth B and mean particle diameter D_{50}. Noticeably, the normalised loading response under the amplified gravity is practically equal to the one obtained from earth gravity, indicating

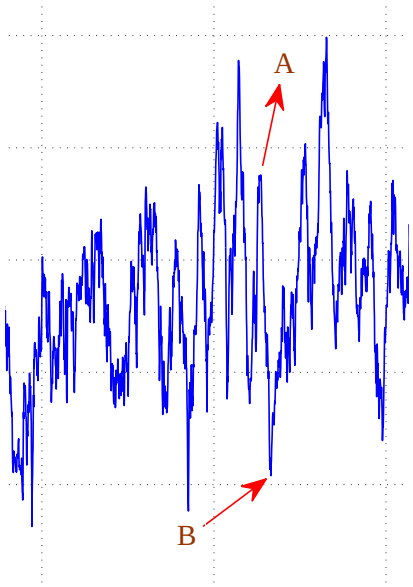

Figure 5.5: Two key stages in the loading response curve

that the forces exerted by the particles on the punch was linearly proportional to the gravitational acceleration. Furthermore, the data plotted in the curve from the $100g$ case was output at every 10^{-4} second without any smoothing operation, whereas the penetration resistance from simulation with $1g$ was averaged over 0.1 second as abovementioned in Figure 5.3. It suggests that an amplified gravity field can considerably reduce the noise in DEM predicted macroscopic response. To provide more detailed information regarding the force transmission under these two gravity fields, Figure 5.8 compares the differences in the resulting force network at the penetration depth of $4B$, in which once again only the above-average normal contact forces were shown. Under an amplified gravity field, the packing density dramatically increased and the whole sample became more compacted. As a result, the spatial arrangement of the force chains became highly ramified and tangled, producing a considerable enhancement in the system capability to sustain severe external perturbation. These findings implies that the much higher alleviation of numerical fluctuation in the reaction force under $100g$ can be re-

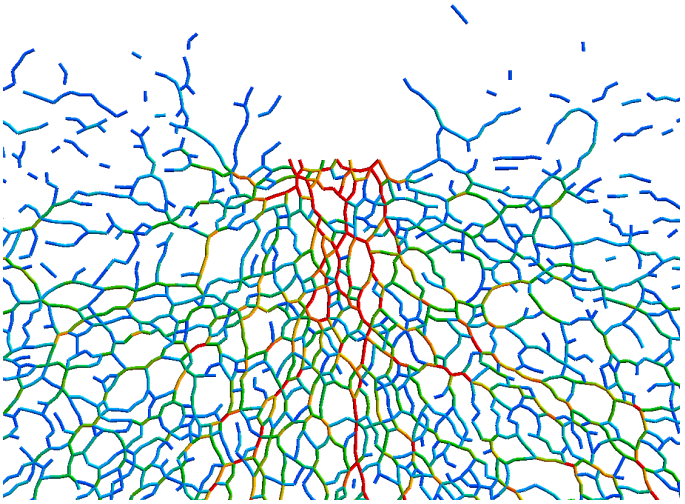

(a) Force chain at stage A

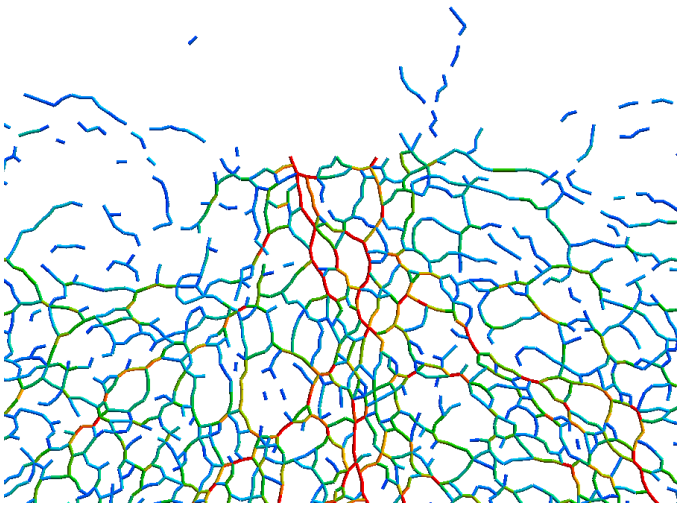

(b) Force chain at stage B

Figure 5.6: Force chains (beneath the penetrator) carrying above-average contact forces

lated to the large amount of available pathways for force propagation, thus the influence caused by force chain collapse has been reduced significantly.

5.4.2 Stress adjacent to the penetrator

The stress concentration in granular materials may eventually cause a much quicker end bearing failure of foundations. It is thus useful to investigate the stress fields in the current penetration simulation. In geotechnical engineering, when the depth of penetration is less than the breath of footing, the mechanical behaviour can be considered as shallow foundation. The development of three stress components (i.e. horizontal stress σ_{11}, vertical stress σ_{22} and shear stress σ_{12}) at two penetration stages ($1B$ and $4B$) were calculated via measurement sphere algorithm in PFC^{3D} which was introduced in Chapter 2. In order to measure the stress over a representative area, the diameter of the measurement sphere was chosen as $5D_{50}$ and has 50% overlap with its neighbours. Haertl (2008) comfirmed that averaging over such an area is suffcient to obtain stable and representative results. Figure 5.9, 5.10, 5.11 and 5.10 show the contours of the stress distribution beneath the punch base.

Before the penetration started ($0B$), both the horizontal σ_{11} and vertical stress σ_{22} became concentrated at the base where the self weight of sample was carried, and no clear pattern in the shear stress σ_{12} was observed. The differences in the magnitudes of σ_{22} between spherical and non-spherical particles were insignificant, due to the similar overlaying grain mass. However, the σ_{11} in spherical particles was larger than the one in non-spherical particles. This can be attributed to the greater interlocking propensity in non-spherical particles, which led to a more stable packing configuration in which the particles can support each other mainly in vertical direction under gravity. Without the interlocking asperity contributing to the frictional resistance in spherical particles, the spheres can easily move

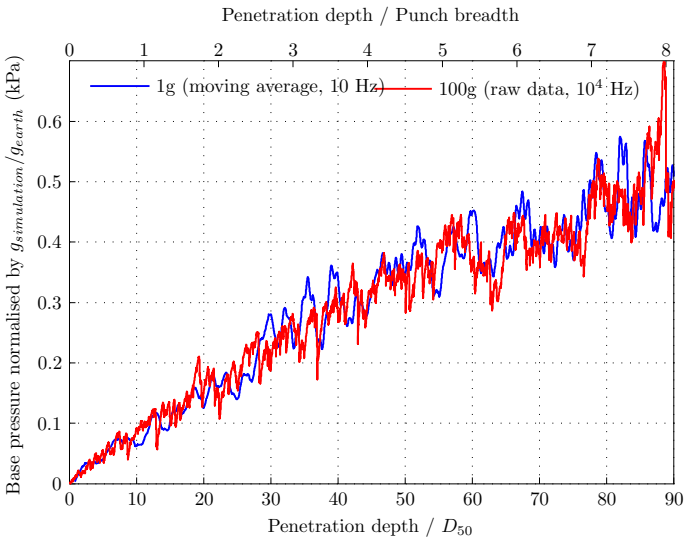

(a) Spherical particles

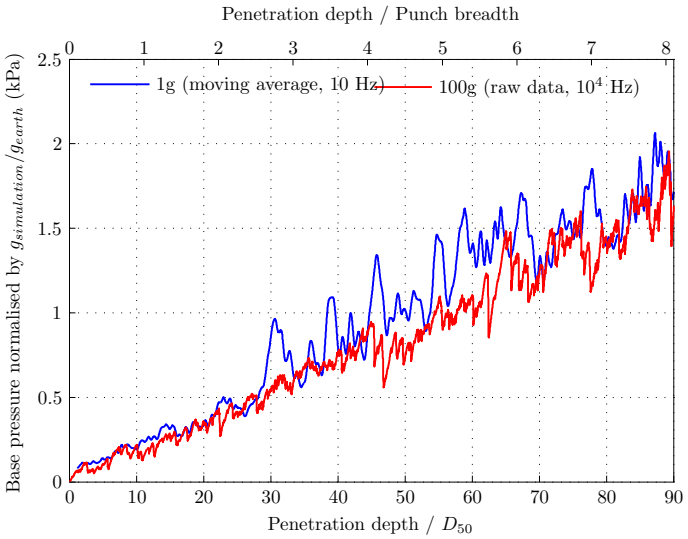

(b) Non-spherical particles

Figure 5.7: Comparison of the base resistance response with different gravity fields

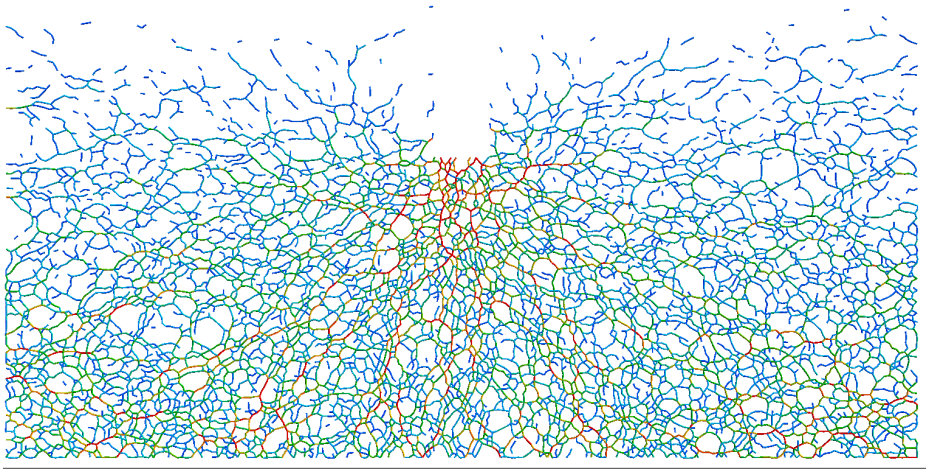

(a) Gravity $1g$

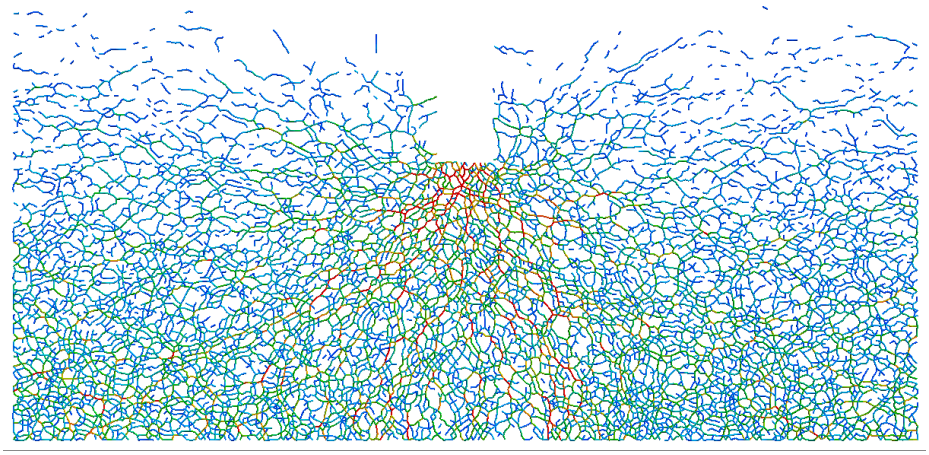

(b) Gravity $100g$

Figure 5.8: Comparison of strong force network in spherical particles at the penetration depth of $4B$

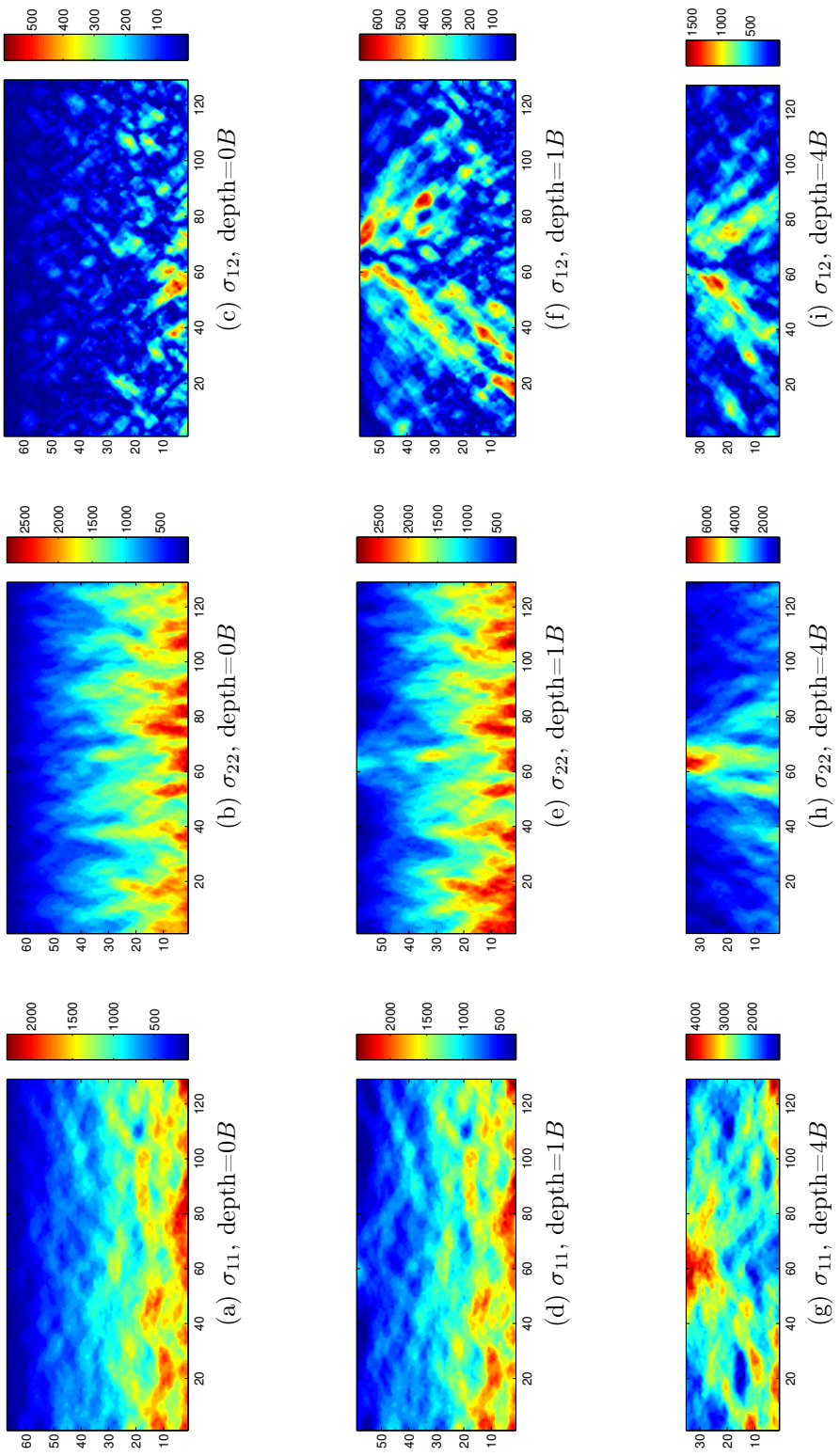

(a) σ_{11}, depth=$0B$ (b) σ_{22}, depth=$0B$ (c) σ_{12}, depth=$0B$

(d) σ_{11}, depth=$1B$ (e) σ_{22}, depth=$1B$ (f) σ_{12}, depth=$1B$

(g) σ_{11}, depth=$4B$ (h) σ_{22}, depth=$4B$ (i) σ_{12}, depth=$4B$

Figure 5.9: Stress components for spherical particles under $1g$ gravity field

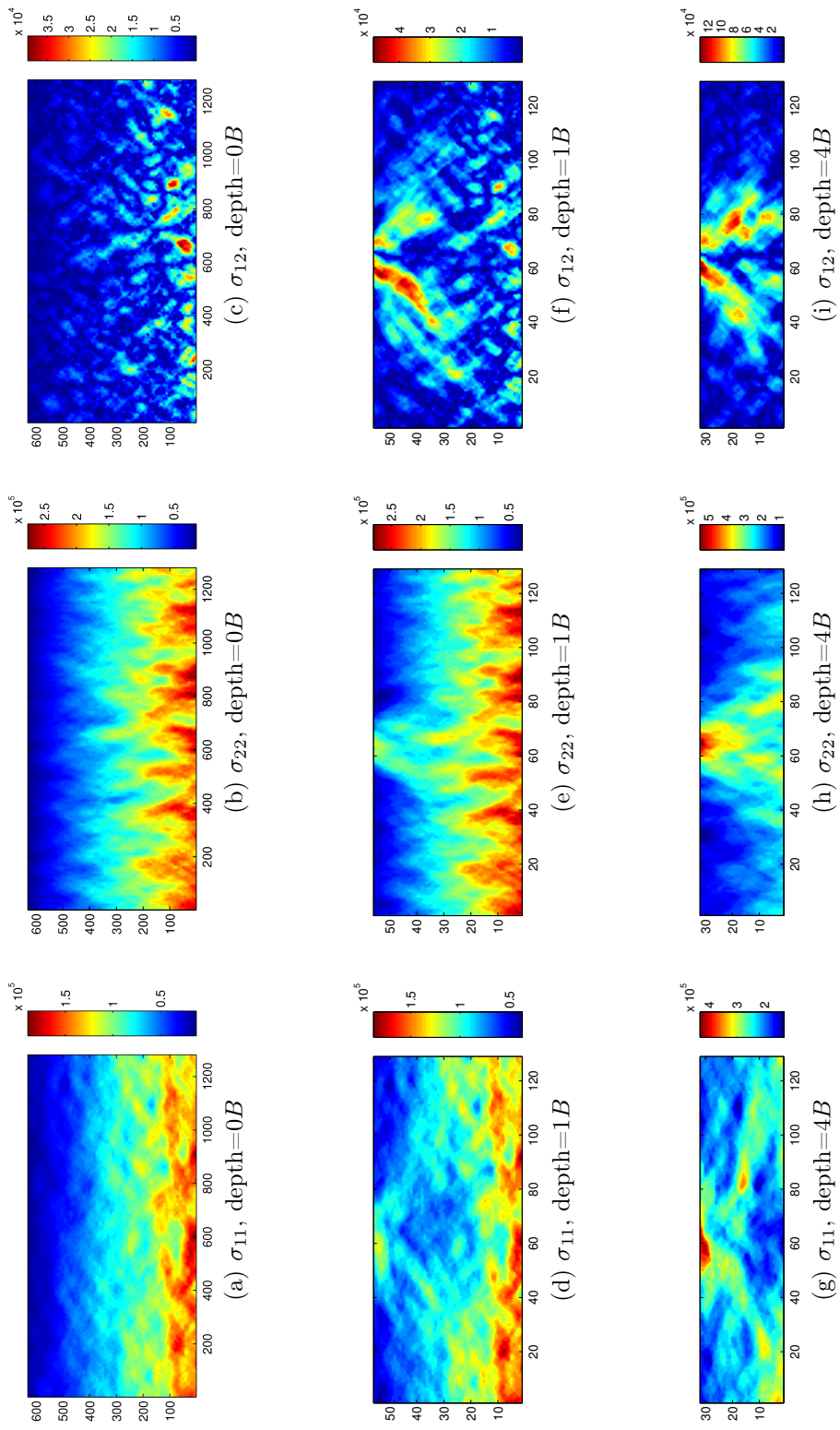

(a) σ_{11}, depth=$0B$ (b) σ_{22}, depth=$0B$ (c) σ_{12}, depth=$0B$

(d) σ_{11}, depth=$1B$ (e) σ_{22}, depth=$1B$ (f) σ_{12}, depth=$1B$

(g) σ_{11}, depth=$4B$ (h) σ_{22}, depth=$4B$ (i) σ_{12}, depth=$4B$

Figure 5.10: Stress components for spherical particles under $100g$ gravity field

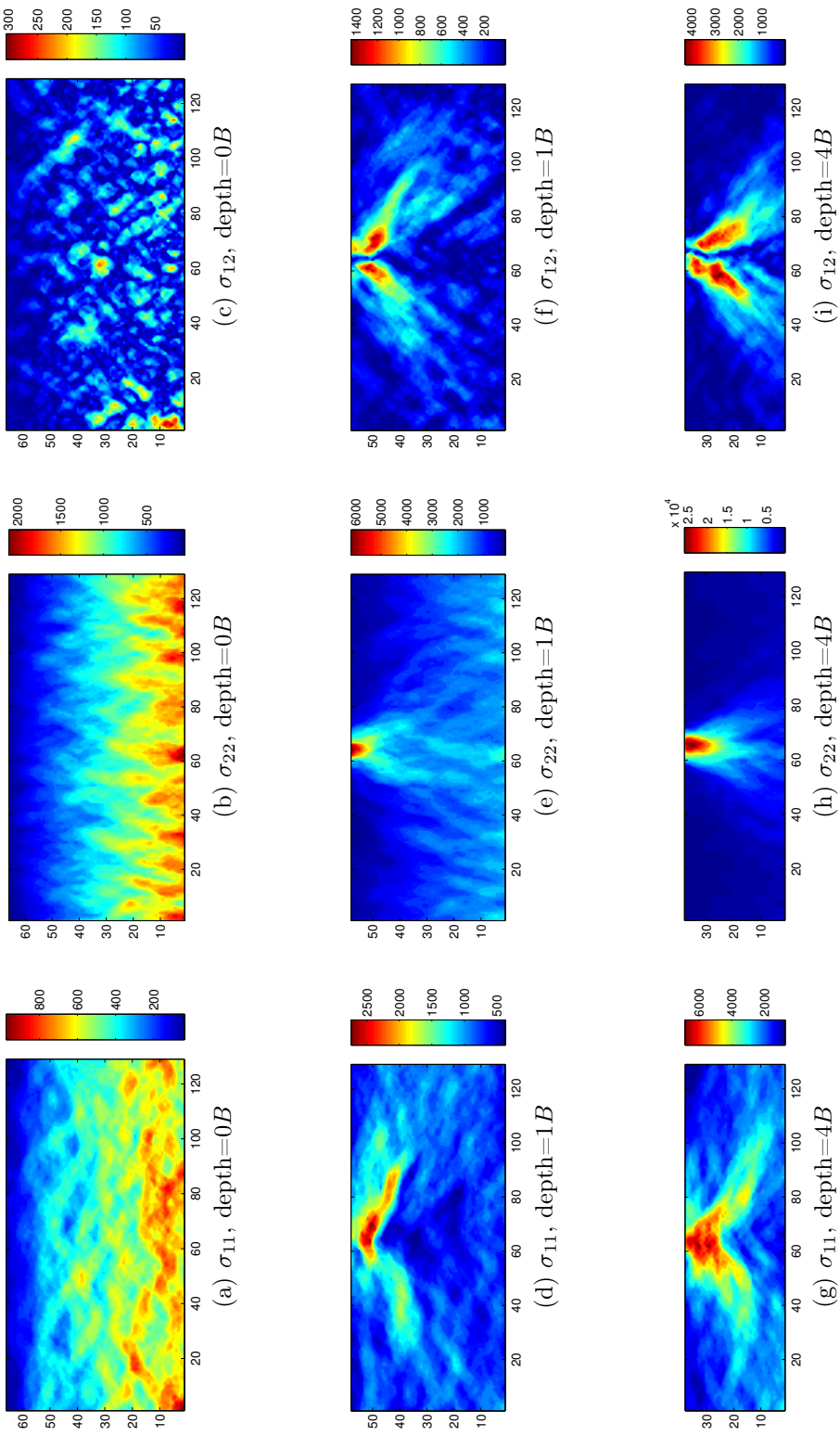

(a) σ_{11}, depth=$0B$ (b) σ_{22}, depth=$0B$ (c) σ_{12}, depth=$0B$

(d) σ_{11}, depth=$1B$ (e) σ_{22}, depth=$1B$ (f) σ_{12}, depth=$1B$

(g) σ_{11}, depth=$4B$ (h) σ_{22}, depth=$4B$ (i) σ_{12}, depth=$4B$

Figure 5.11: Stress components for non-spherical particles under $1g$ gravity field

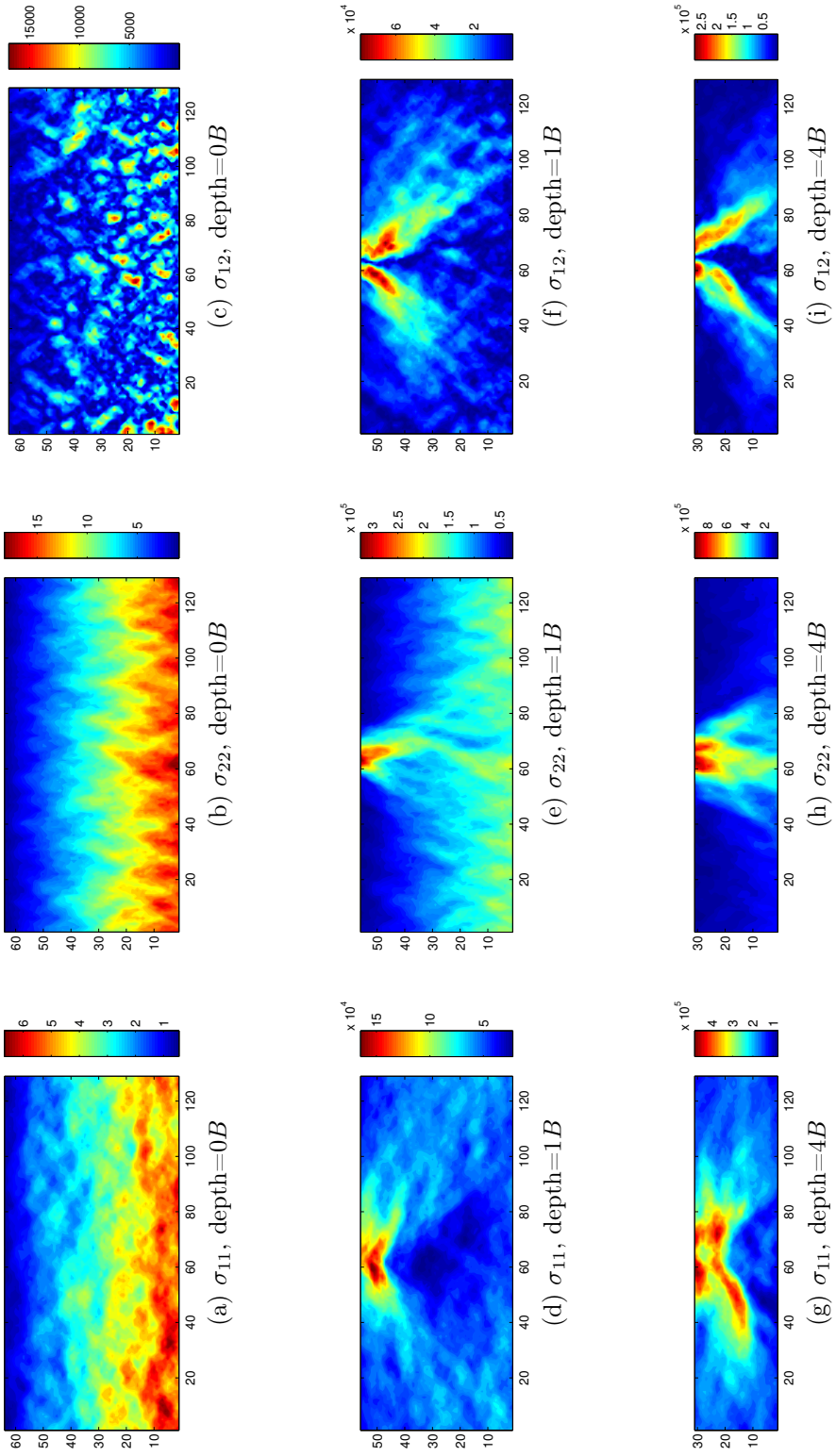

(a) σ_{11}, depth=$0B$ (b) σ_{22}, depth=$0B$ (c) σ_{12}, depth=$0B$

(d) σ_{11}, depth=$1B$ (e) σ_{22}, depth=$1B$ (f) σ_{12}, depth=$1B$

(g) σ_{11}, depth=$4B$ (h) σ_{22}, depth=$4B$ (i) σ_{12}, depth=$4B$

Figure 5.12: Stress components for non-spherical particles under $100g$ gravity field

laterally during the formation of the sample and thus produced higher horizontal stresses.

It is anticipated that the stress would become concentrated around the punch tip and increase significantly as the penetration proceeds into the bulk solids. However, for spherical particles, when the penetrator reached the depth of $1B$, the stress developed underneath the punch base was not much influenced by the penetration. With continued penetration, the stress concentration became discernible near the punch at the depth of $4B$. This information suggests that granular samples composed of spherical particles possessed extremely weak resistance to external perturbation, particularly to global or local shearing, such as the current particle-punch interface.

More attention is paid to the stress distribution in the sample composed of non-spherical particles, where the resulting stress fields are seemingly more comparable to those obtained from finite element method (Figure 5.13). In contrary to spherical particles, here strong stress concentration became obvious under the penetrator at the penetration depth of $1B$, indicating the non-spherical sample was able to withstand a higher penetration loading. This information suggests that non-spherical particles give a better representation of real granular system. Then the stress components of σ_{11} and σ_{22} expanded predominantly in horizontal and vertical direction, respectively. The shear stress σ_{12} initiated from the corner of punch, and propagated along an inclined direction. It is noticed that the particles near the punch were heavily stressed, whereas the far field stresses were less affected. The largest stress occurred very close to the punch, and rapidly decreased at points farther from the punch. This implies that the significantly stressed area was relatively localised and the stress gradient around the penetrator can be considerably high. In order to calibrate the highly stressed zone, the concept of pressure bulb was utilised to characterise the distribution of each stress component. In geotechnical engineering, pressure bulb is a term that rep-

resents the volume of soil below a foundation within which the applied surface loads induces appreciable stress. In the current study, stresses considered as contributing to the stress concentration were those of the magnitude ranging from $0.5\sigma_{max}$ to σ_{max}. By way of illustration, only the results from non-spherical particles in the deep penetration stage performed at $1g$ were presented, as shown in Figure 5.14. Under the penetration loading, the bulb of each stress component spread out into the sample both laterally and vertically, with different intensities and shapes. Considering the region enclosed by the dark blue contour line, the depth and width at which the vertical stress propagated from σ_{max} to $0.5\sigma_{max}$ are approximately $1.75B$ and $1B$, respectively. The shear and horizontal stress underwent such a change with a much larger area. This reveals that vertical stress exhibited the highest gradient close to the punch. Lebert et al. (1988) explored the effect of stress duration on the pressure transmission in physical experiments. It was found that pressure will be transmitted deeper down the soil layer with the longer stress duration at the soil surface, as illustrated in Figure 5.15. This phenomena is worthy of further investigation and can be evaluated based on the current DEM model.

5.4.3 Force chains and contact orientations

The information collected from the stress distribution as presented in the previous section was derived from the interparticle contact forces. Care should therefore be given to the force network which governs the micro- and macroscopic response. Both the magnitude and direction of the contact forces, particularly those contacts belonging to the strong network will be carefully examined. By way of illustration, only the results from non-spherical particles under earth gravity is presented. Although not shown here, similar feature and trend were observed in the rest three cases. It is believed that the selected example is adequate to

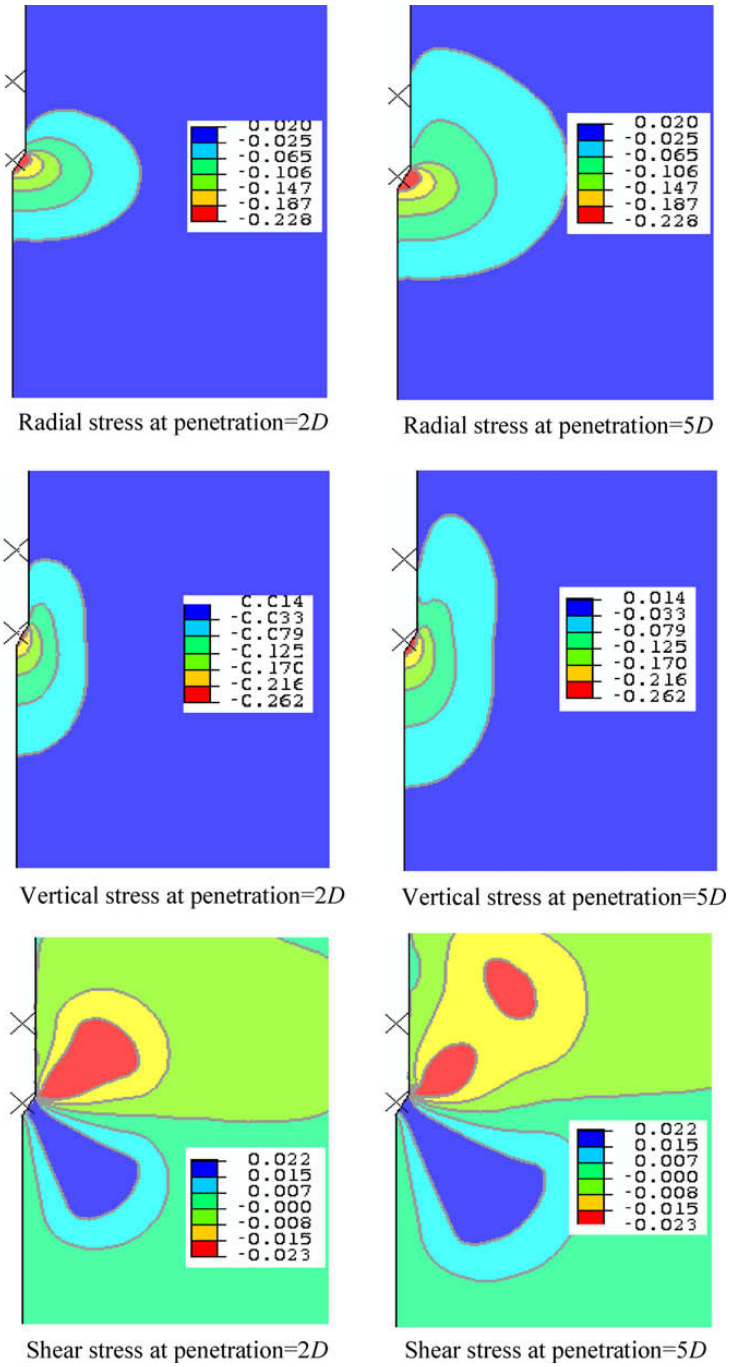

Figure 5.13: Stress distributions Liyanapathirana (2009)

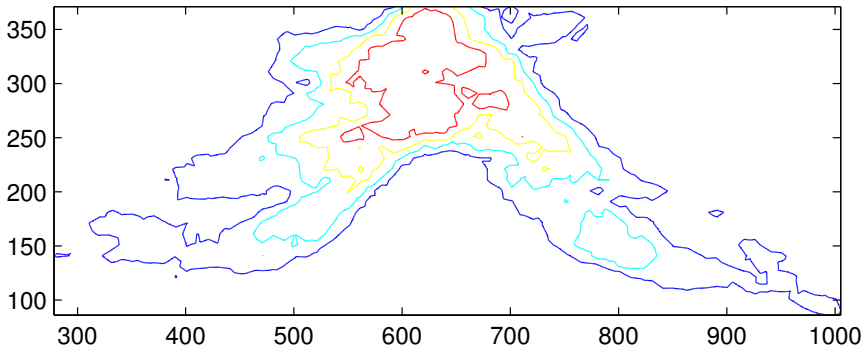

(a) σ_{11}

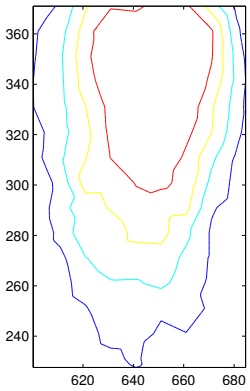

(b) σ_{22}

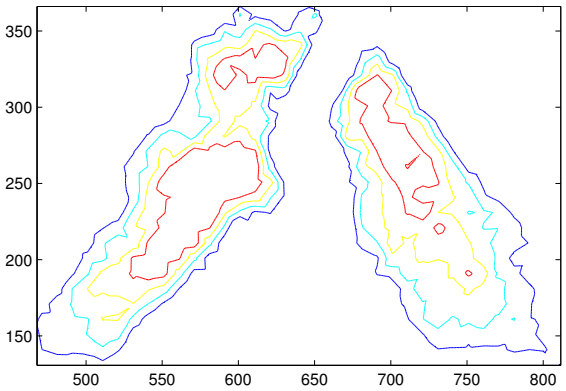

(c) σ_{12}

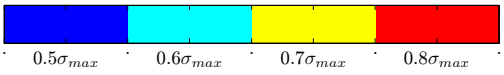

(d) Colour scheme

Figure 5.14: Stress bulb developed in the sample with non-spherical particles (depth=$4B$, gravity=$1g$)

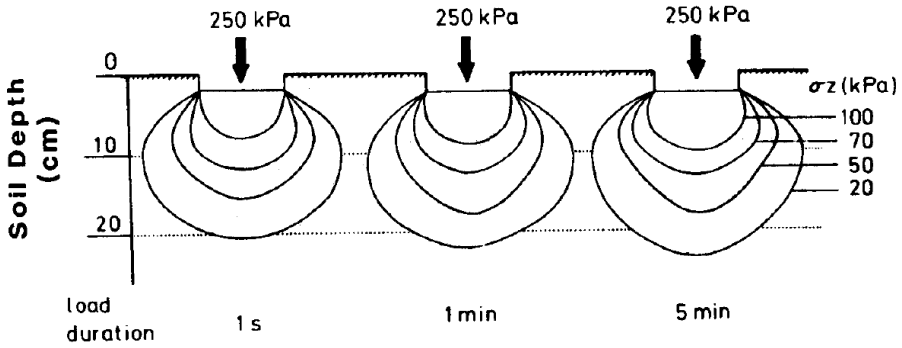

Figure 5.15: Time dependent alteration of the stress lines (Lebert et al., 1988)

describe the contact network evolution.

In the samples composed of non-spherical particles under $1g$ gravity, there were over 60,000 contacts within the entire contact network. As reported in Figure 5.14, stress concentration induced by the penetration occurred in a rather localised area, which indicates that only a small portion of grains were highly stressed and groups of particles outside the concentration zone were only lightly loaded. Consequently, the contact forces of special interest are those whose magnitudes are three times lager than the mean value ($F_i > 3F_{mean}$), which takes approximately 3∼4.5% of the whole contact population. Note that the average contact force F_{mean} is different at various penetration stage and approximately increases linearly with the penetration depth. For each penetration depth considered (normalised by the punch breadth B), the contact network is presented by two plots, which are the force chains combined with the contact orientation. These results are shown in Figure 5.16, 5.17, 5.18, 5.19, 5.20, 5.21 and 5.22.

The force chain configuration provides a clear visulisation of the spatial arrangement of interparticle forces. As shown in these figures, the force chains spread out principally from the penetrator base in various directions and eventually transmitted to the base. The most heavily stressed chains were formed and propagated along vertical punching direction. The preferred contact orientation

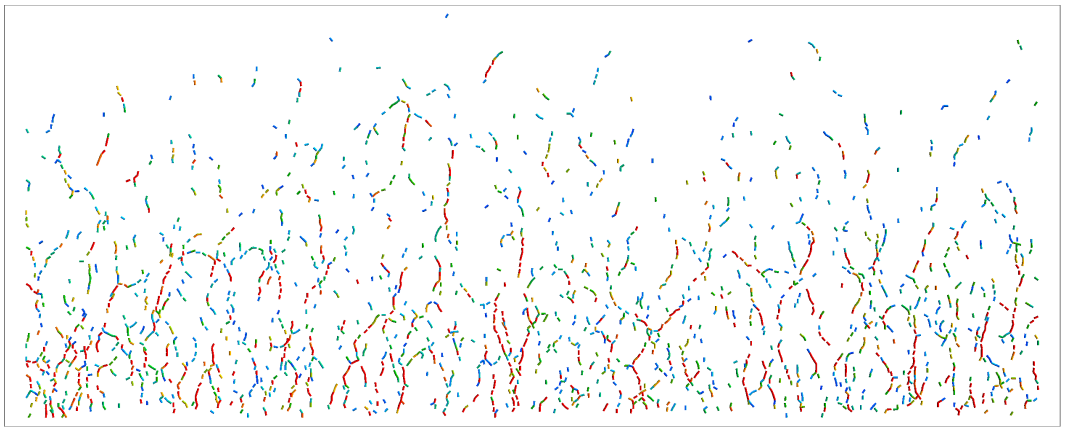

(a) Force chains

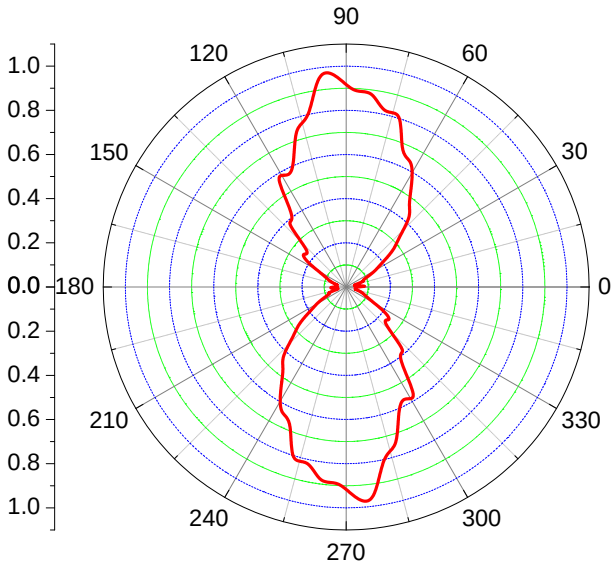

(b) Contact orientation

Figure 5.16: Force chains and contact orientations ($F_i > 3\bar{F}$) at penetration depth $0B$

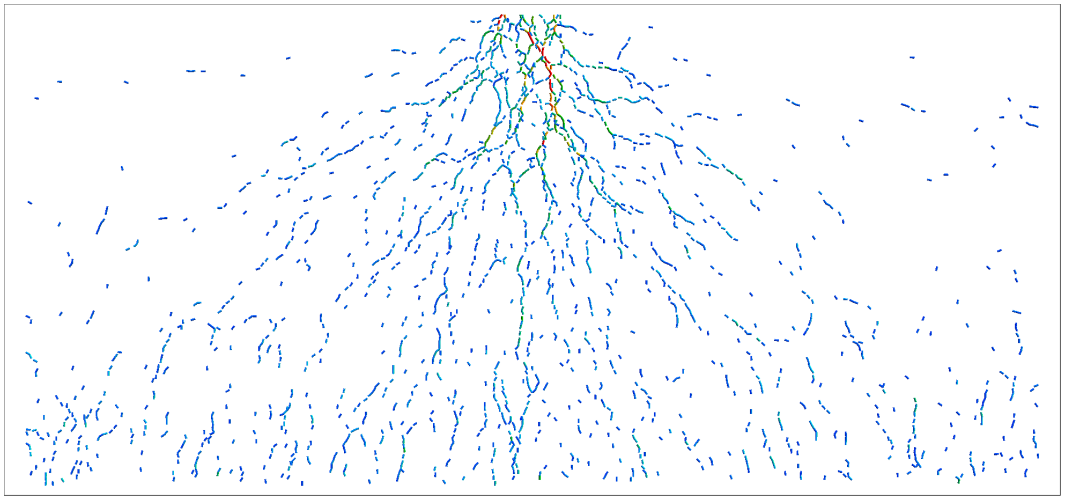

(a) Force chains

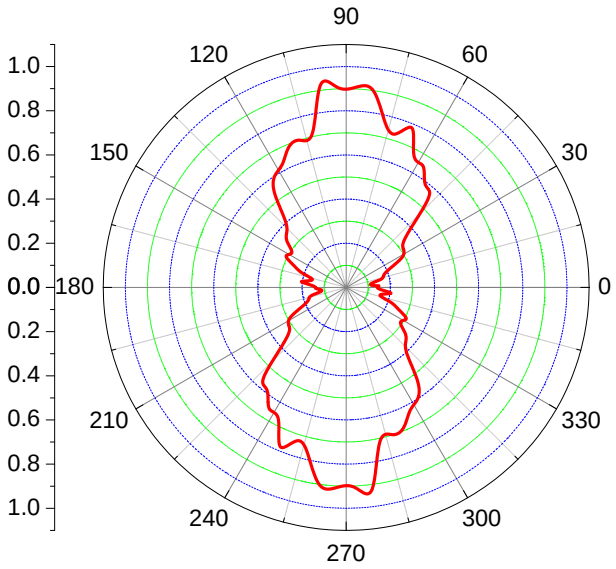

(b) Contact orientation

Figure 5.17: Force chains and contact orientations ($F_i > 3\bar{F}$) at penetration depth $1B$

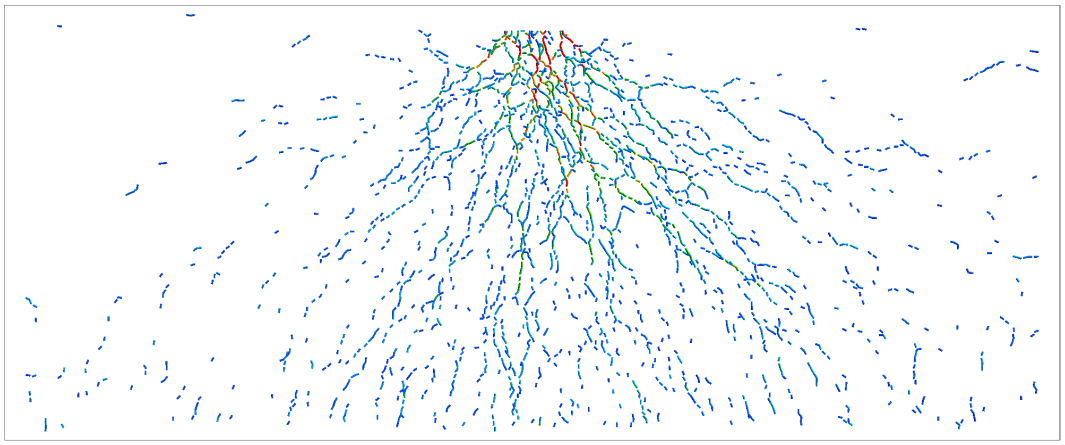

(a) Force chains

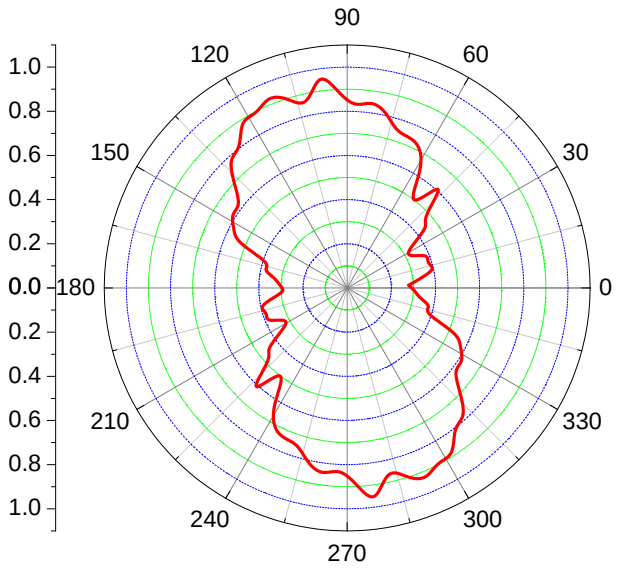

(b) Contact orientation

Figure 5.18: Force chains and contact orientations ($F_i > 3\bar{F}$) at penetration depth $3B$

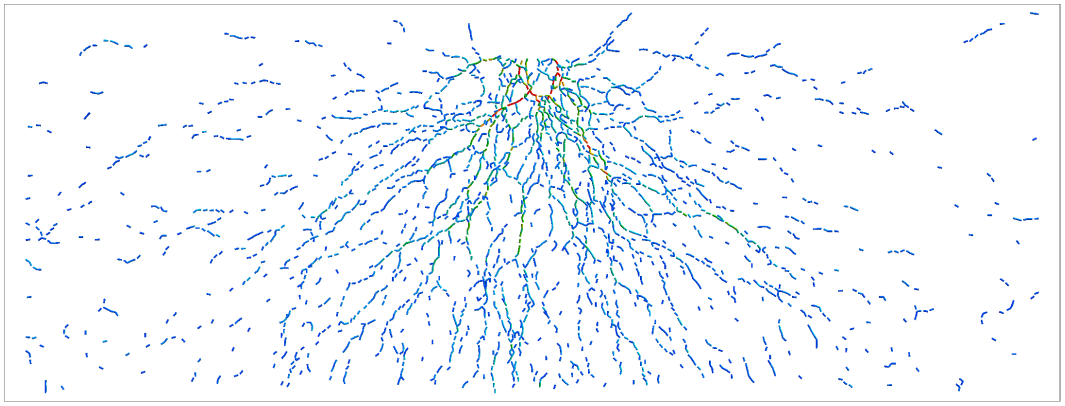

(a) Force chains

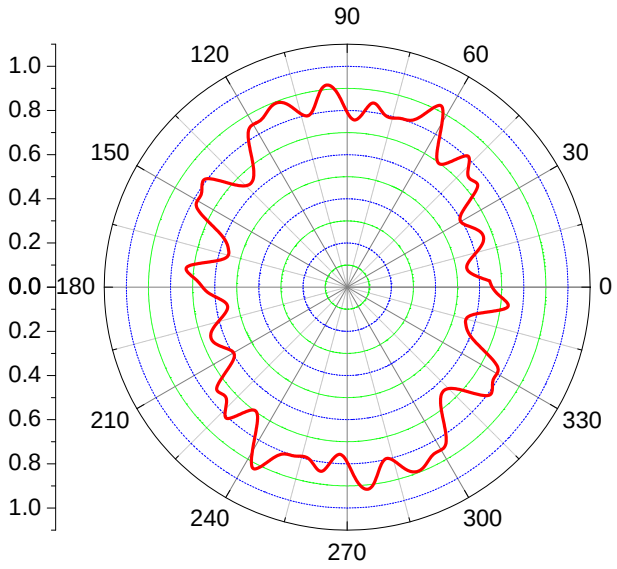

(b) Contact orientation

Figure 5.19: Force chains and contact orientations ($F_i > 3\bar{F}$) at penetration depth $4B$

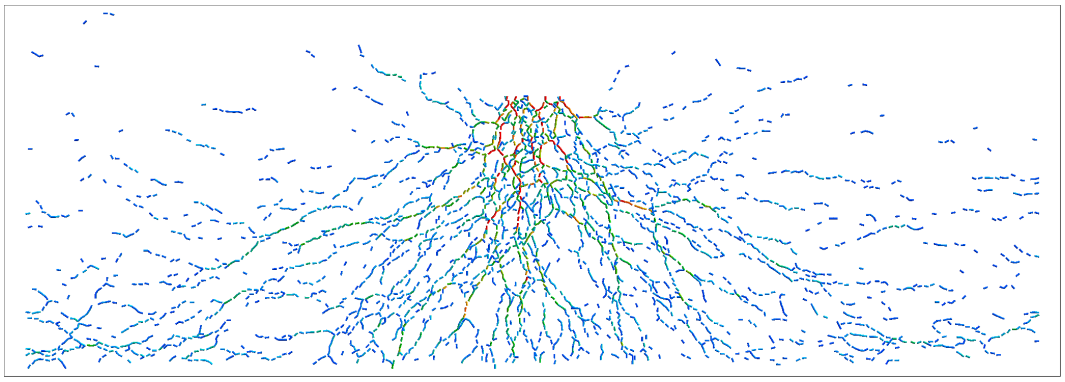

(a) Force chains

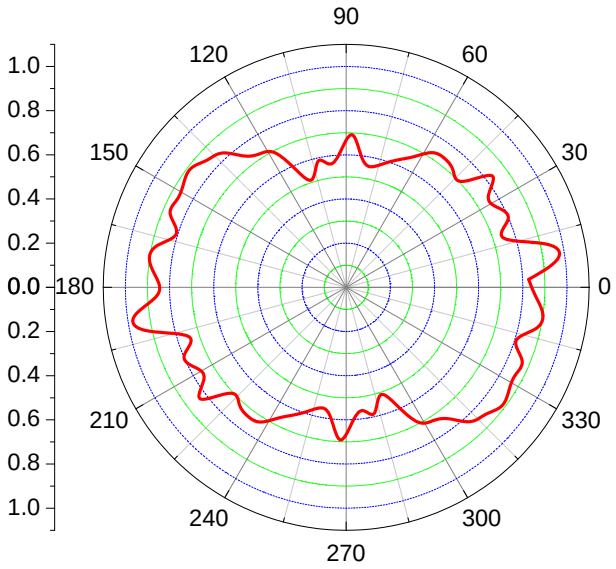

(b) Contact orientation

Figure 5.20: Force chains and contact orientations ($F_i > 3\bar{F}$) at penetration depth $5B$

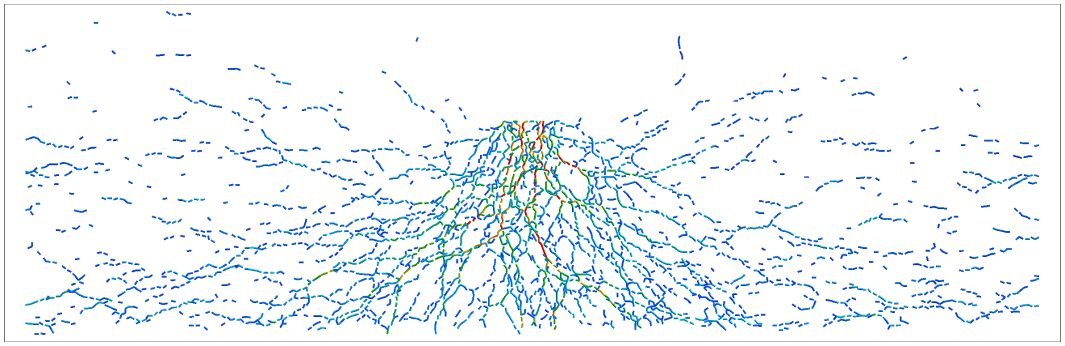

(a) Force chains

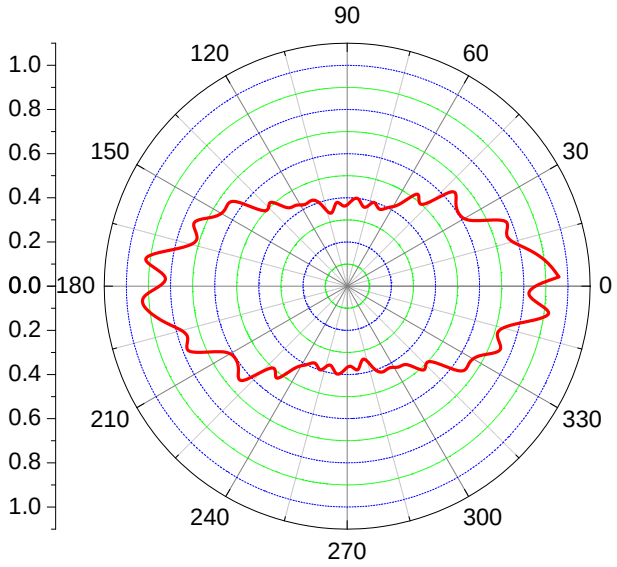

(b) Contact orientation

Figure 5.21: Force chains and contact orientations ($F_i > 3\bar{F}$) at penetration depth $6B$

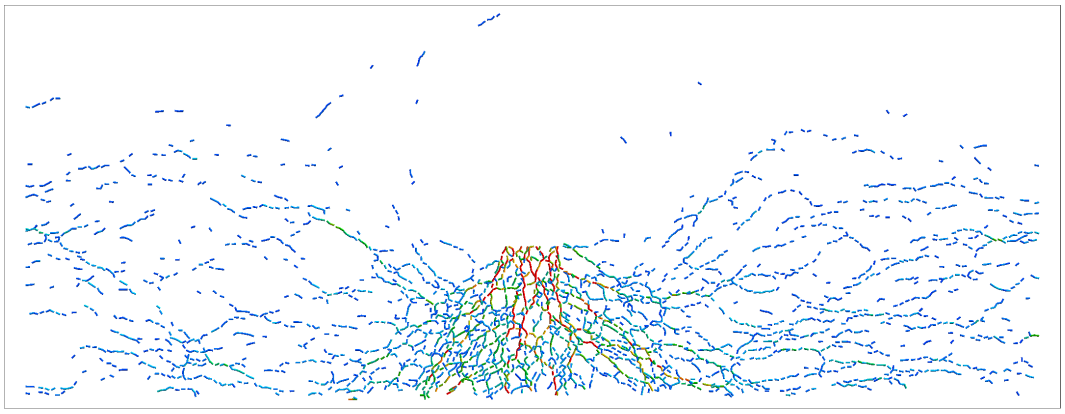

(a) Force chains

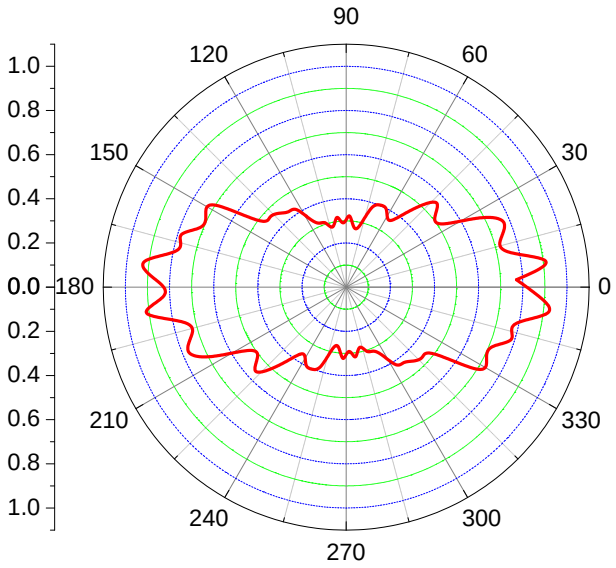

(b) Contact orientation

Figure 5.22: Force chains and contact orientations ($F_i > 3\bar{F}$) at penetration depth $7B$

in the strong network progressively evolved from vertical to horizontal direction as penetration proceeded; this effect can also be visually verified from the plots of force chain at increasing penetration depth.

- $0B$: Prior to the penetration, the basewall carried the whole self weight of the granular sample, where the development of the large contact forces originated vertically from the bottom under gravity deposition (Figure 5.16);
- $1B$: As the punch moved downwards and came into contact with the particles, the contact orientation still exhibited evident preference at 90°, but the underlying mechanism was different from the previous stage. Here, a group of strong contact forces became apparent immediately beneath the penetrator and propagated all the way to the rigid horizontal base (Figure 5.17);
- $3B$: The strong tendency of most contacts to orient vertically gradually reduced by showing a slight rotation from the vertical plane. This deviation can be verified from the degree of branch in the force chains, which increased remarkably and resulted in the formation of a more complex network around the punch (Figure 5.18b);
- $4B$ and $5B$: Interestingly, the contact orientation exhibited in Figure 5.19b and 5.20b became more evenly distributed, not showing any strongly preferred contact angle. Comparing to the contact network at the depth of $3B$, there were a large amount of newly formed chain segments in horizontal direction extended to the side walls, which further promoted the development of a highly ramified network;
- $6B$ and $7B$: As the penetrator approached the base of the model, the contact network depicted in Figure 5.21 and 5.22 demonstrated that the strong

normal forces mainly propagated laterally, accompanied by the strong boundary effect coming from the base wall.

The anisotropy observed in the distribution of interparticle contact orientation gives an insight into the local deformation and force transmission mechanism during loading. As the penetration started, the area immediately under the punch was highly densified and grains in this region moved primarily downwards with the punch, which produced the strong vertical preference in the contact orientation (Figure 5.17). When the penetrator progressed deeper, particle movement became increasingly constrained within a rather limited zone. Meanwhile, those previously formed strong vertical chains became highly stressed and can easily get buckled. At this stage, laterally supporting chains were developed to provide the necessary balanced equilibrium for these strong vertical force structure to persist and thus maintained the structural stability. As a result, the vertical force chains were capable of withstanding larger compressive forces induced from the increasing penetration loading. In other words, new pathways for force propagation were formed horizontally. This explains the significant growth of force chains in horizontal direction as observed from Figure 5.18 to 5.20. This process turned into accentuated in Figure 5.21 and 5.22 when the penetrator was close to the base wall. Apparently, the principal contact orientation was horizontal, indicating a significant amount of lateral force chains bracing those highly stressed vertical chains beneath the penetrator.

One quantitative manner to study the inhomogeneities of force network is to measure the probability density distribution. Figure 5.23 plots the probability density distributions of normal contact forces within the entire network at three representative stages, i.e. before, during and near the end of the penetration simulation. The granular sample contains a large number of particles, the majority of which were not influenced by the indentation due to the relatively small size

of penetrator compared to the sample dimension. Consequently, the probability density of these normal contact forces decayed exponentially and the peak occurred in the interval with the smallest value. As the penetration proceeded, the tail of exponential distribution became longer and more skewed, indicating a stronger penetration resistance and more intense interaction between the penetrator and granular solids. This exponentially decaying distribution can be related to a number of factors, such as penetration resistance and packing fabric etc, which will be further investigated.

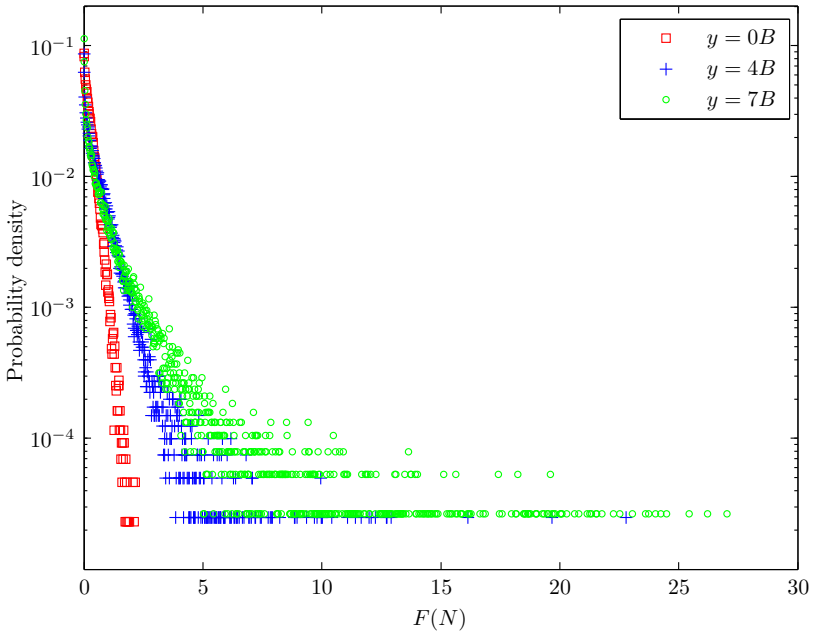

Figure 5.23: Probability density distribution of interparticle contact forces

5.4.4 Discussion on the failure mechanism

The penetration process is indeed a large strain phenomenon, where the bulk sample experiences severe and complex deformation pattern. Throughout the penetration course, particles were pushed downwards, outwards and sidewards

to accommodate the punch, during which considerable particle movement took place particularly beneath the punch base. Therefore, particle movement during the penetration was tracked and investigated. The displacement fields are presented at penetration depths of $1B$ and $4B$, which represent the shallow and deep penetration stage, respectively.

Given the fact that there were 20,000 particles in the current DEM model, it is impractical to plot all the displacement arrows. Therefore, only those with magnitudes greater than 10% of the penetrator movement were plotted, and the rest were omitted. Figure 5.24 and 5.25 show the displacement fields at two penetration depths under earth gravity for spherical and non-spherical particles, respectively.

The deformation patterns illustrated by the excessive displacement vectors clearly showed a curved "rupture" surface, which will be associated with some classical failure theories in a qualitative manner. Figure 5.26 shows two profiles of slip line with regard to the ultimate bearing capacity of foundations. These theories assume that upon exceeding a certain stress condition, rupture surfaces are developed in the soil mass. Thus, the stress causing the formation of these rupture surfaces are considered as the ultimate bearing capacity of the soil.

- Terzaghi (1943) proposed the first bearing capacity equation based on general shear failure. The slip surface ends at the cone base level and no kinematic field is allowed above the footing shoulder. The effect of embedment depth is replaced by a surcharge pressure acting at the level of the footing base, and the shear strength of the overburden is not considered.

- Meyerhof (1951) included the shear strength of soil above the base of footing, which was neglected in Terzaghi's solution. This means that beneficial effects of the foundation depth is included in the analysis. The failure plane analysis is slightly more complex as the soil is still in plastic equilibrium

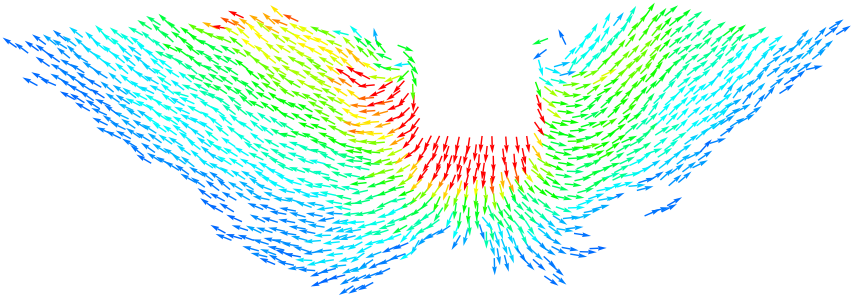

(a) Penetration depth=1B

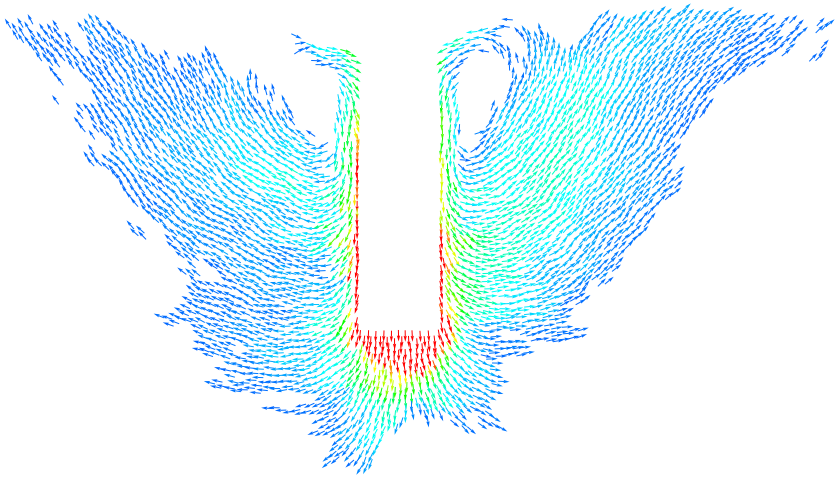

(b) Penetration depth=4B

Figure 5.24: Displacement vectors at different penetration depth for spherical particles under 1g

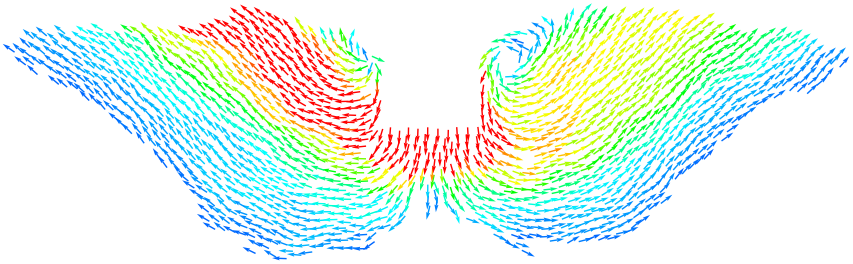

(a) Penetration depth=1B

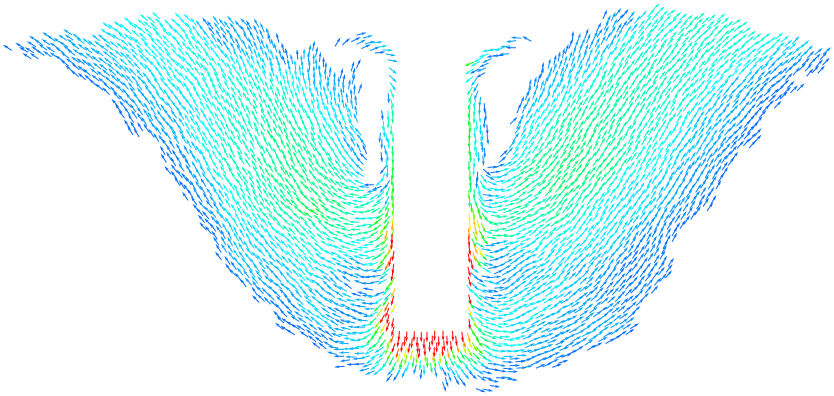

(b) Penetration depth=4B

Figure 5.25: Displacement vectors at different penetration depth for non-spherical particles under 1g

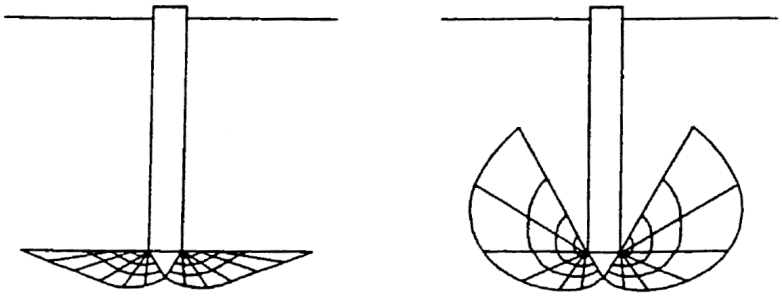

(a) Terzaghi (1943) (b) Meyerhof (1951)

Figure 5.26: Profiles of failure surface in the literature (reproduced from Durgunoglu and Mitchell (1975))

but has a log spiral failure surface that includes shear above the base of the foundation.

As shown in Figure 5.24 and 5.25, similar patterns of particle movement can be observed between spherical and non-spherical particles at the same penetration depth. At the penetration depth of $1B$, most particles started to flow outwards and upwards to the surface which promoted the heaving process. Visual inspection of these excessive displacement vectors suggests that the failure surface proposed by Terzaghi (1943) gives a reasonable description of shallow penetration mechanism. In the triangular active zone that immediately underneath the penetrator, all the particles were highly compacted and moved primarily downwards. Also, the radial shear zone and the Rankine passive zone can be well identified. Through the course that the penetrator moved from $1B$ to $4B$, there was a large kinetic zone above the punch base, where more particles moved sidewards and upwards. Initial observation of the particle trajectories are qualitatively in agreement with the shape of failure surface assumed by by Meyerhof (1951). This similarity implies the theory proposed by Meyerhof (1951) is a proper assumption in deep penetration region.

Admittedly, the patterns of displacement vector presented in this section are rather subjective, which completely depend on the arbitrarily adopted scaling quantity (10% of the penetrator movement in the current study). In the case under the amplified gravity field, where the sample was more compacted and has a higher bulk stiffness, accordingly the average particle movement was much smaller compared to the one under earth gravity. Therefore, the patterns of displacement vectors plotting with the same scale as abovementioned will be completely different, although the maximum particle movement should be the similar which is the penetration depth. Therefore, the results need to be treated with some caution since the analysis itself was developed to offer a direct visualisation and general understanding of the kinematic fields, rather than an evaluation of the failure criteria. More importantly, it serves the purpose of providing an easily implemented probe to examine the structure of local particle rearrangement and the dynamics leading to failure.

5.5 Model footing test in granular solids

Much knowledge of footing foundation is based on vast amount of empirical data from controlled experiments and field observations, which have largely contributed to the knowledge of soil mechanics. One main challenge is that the soil deformation remains unclear, which usually cannot be accurately measured in field tests, as often only the footing resistance and its displacement are recorded. Verification of engineering calculations thus becomes complicated, with rather limited knowledge of the soil movement and internal shearing mechanism. The goal of this study is to obtain a quantitative assessment of solids deformation with high spatial resolution during a footing installation process by using PIV. Special attention is paid to the influence of filling method and packing density on the loading response and failure mechanism, in terms of displacement field,

flow path and shear strain. Furthermore, DEM simulations corresponding to the current footing tests were also performed to access its capability in quantitative prediction.

5.5.1 Experimental procedures

5.5.1.1 Slice model

To carry out the footing experiments, a slice model was designed and constructed to satisfy both the mechanical and optical requirements. Firstly, the model has to be able to contain a large number of granular particles, and to sustain the external loading while minimising the out-of-plane deformation. The second requirement being that to enable an image recording equipment to look directly at the front face of the slice, the model must has a clear unobstructed view of the materials contained within it. The final slice model has an internal dimension of $1000 \times 600 \times 30mm$, comprised of two $10mm$ thick Perspex sheets as front and rear walls.

Footing size has been found as an important factor in loading response and will also be investigated in the current study. Three footings of 50, 100 and $150mm$ width were used in the tests. The gap between the footing and the Perspex walls was kept small to allow no particle to pass by, and yet not too tight that resisting frictional forces would be generated. To meet these requirement, PVC which has a relatively low friction coefficient was selected to construct the strip footing. Therefore, the footing should remain undeformed during test, meanwhile the friction between the footing and particles can be reduced. Figure 5.27 shows the complete setup of the footing test in the current study, which includes a SLR camera in front of the designed slice model that located in the Instron machine.

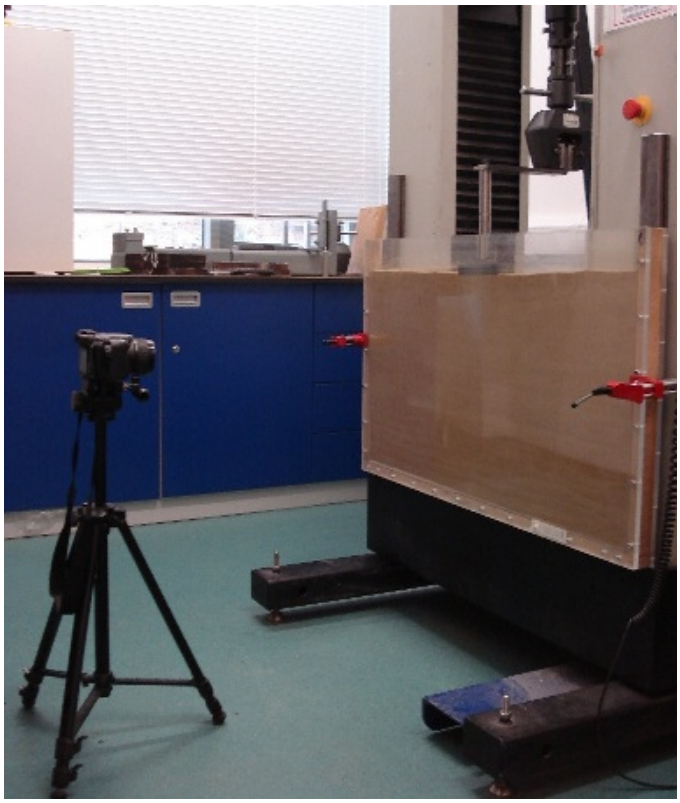

Figure 5.27: Laboratory apparatus of footing test

5.5.1.2 Test solids

Two test materials were chosen in the study: Leighton Buzzard sand and barley grains (Figure 5.28). Leighton Buzzard sand (LBS) has been widely used and is well documented in a number of experimental studies. In terms of the optical appearance, natural sand has its own texture in the form of different colours from grain to grain, which will be further enhanced by the light and shadow formed between adjacent grains under illumination. This feature gives sufficient pixel characterisation to perform successful PIV operations. Barley grains were chosen in order to explore the particle shape effect. These elongated barley grains can orientate themselves into various directions in three dimensional space. Additionally, particle interlocking is prevalent in barley grains, and the degree of interlocking will vary locally within a sample. Theretofore, the resulting packing structure becomes an issue of special interest and will be explored in detail.

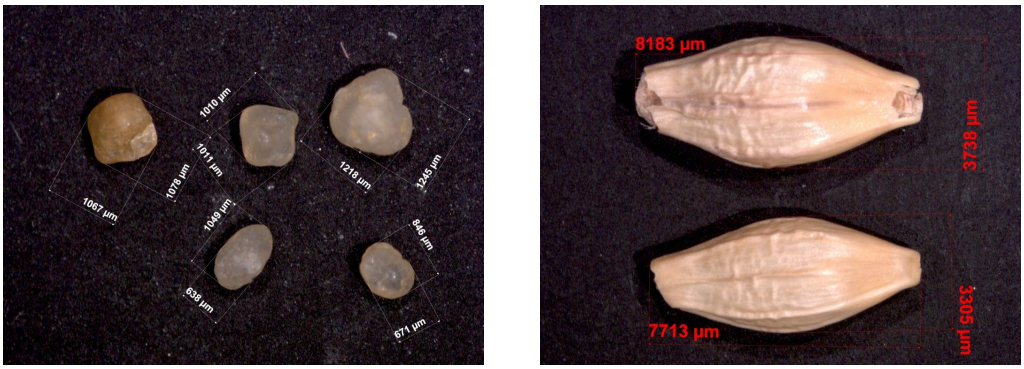

(a) Leighton Buzzard sand (b) Barley

Figure 5.28: Miscroscopic view of particle samples

5.5.1.3 Sample preparation

It is well accepted that the macroscopic behaviour of a particle assembly is rather sensitive to its packing structure, which can be largely controlled by the manner

that the bulk sample is prepared. A number of previous studies have noted that the method of filling affect the particle flow patterns in a silo and the bulk strength (Smid et al., 1993; Zhong et al., 2001). With the aim to explore the influence of packing structure, it is necessary to develop robust filling methods so that all the testing samples can be directly compared with each other. In the current study, two filling methods were employed to form different packing structures for both types of particles, as illustrated in Figure 5.29:

- Concentric filling: The sample was prepared by discharging the particles from a plastic funnel. The diameter of the filling pipe is slightly less than the inner width of the planar slice, in order to minimise particle movement in the out-of-plane direction. The filling apparatus was held in the centre of the planar model and moved upwards as the pile grew. Local densification caused by the impact energy was reduced by lifting the end of the filling pipe immediately above the apex, which in turn kept the particle falling height as constant. As the pile reached the top of the slice model, the remaining two triangular areas at left and right side were filled by following the pile along its angle of repose.

- Layered filling: The sample was prepared by moving the filling pipe along the width of planar model at a constant rate, such that the materials formed layers of approximately $20mm$. The process was repeated by tracking to one side of the model then back gain. Similarly, the falling height was minimised to reduce the impact energy.

The differences of the resulting packing structures yielded from two filling methods for two types of particles are apparent simply from visual inspection, as shown in Figure 5.30. For sand, the angle of repose during the concentric filling can be clearly identified, while layered horizontal bands were discernible in the sample prepared from layered filling. For barley, the concentrically filled

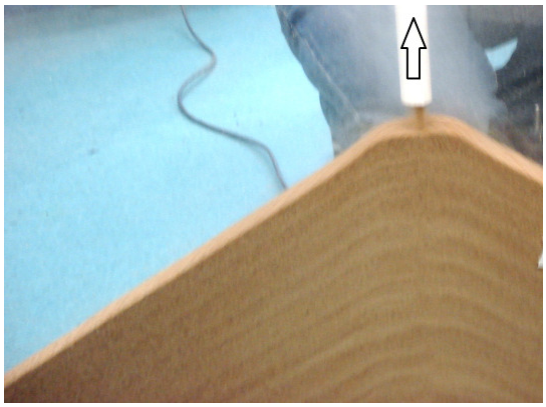

(a) Concentric filling

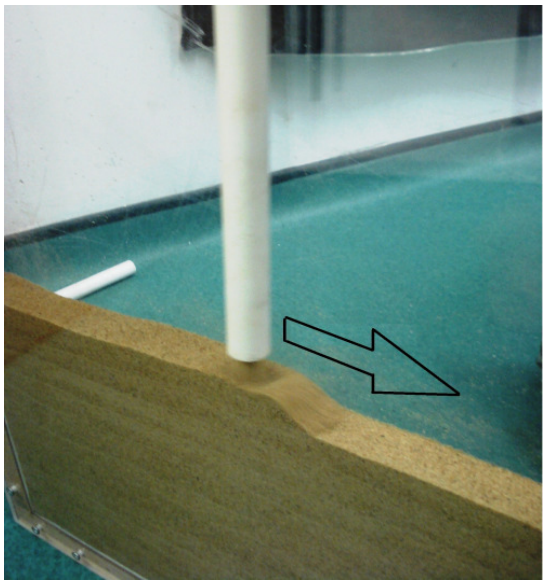

(b) Layer filling

Figure 5.29: Two filling methods

sample exhibited a well organised packing configuration, in which the majority of the grains positioned horizontally. It can be explained as that the concentric filling process allows the particles to accelerate freely down the top surface of the pile following the angle of repose, and eventually reached the optimally most stable position under gravity. Conversely, barley grains in the layered sample were randomly placed at various orientations and appeared more loosely packed.

(a) Sand: concentric filling

(b) Sand: layered filling

(c) Barley: concentric filling

(d) Barley: layered filling

Figure 5.30: Comparison of the resulting packing structures induced from two filling methods

The influence of packing density is also explored by using the vibratory compaction method to form a more densely packed sample (note for barley only). It should be noted that the internal pressure, as well as the frictional forces between particles and container walls can cause density nonuniformity within the sample.

To achieve a uniform distribution of density over the whole bulk volume, the sample was prepared in three layers of $200mm$ each. After each layer of filling, the model was placed on a vibrating shaker plate (Figure 5.31) for approximately 2 minutes to allow the material to compact.

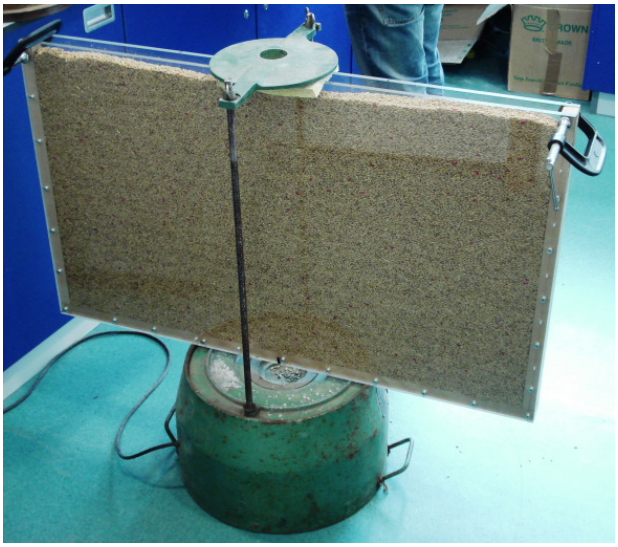

Figure 5.31: Slice model placed on vibrating shaker

5.5.1.4 Characterisation of particle and bulk sample

Prior to the footing experiments, both the particle and bulk sample were quantitatively characterised. It is important to distinguish between particle and bulk properties, whether referring to physical or mechanical properties.

The direct shear test (particularly the Jenike tester) has been widely used to measure the bulk material properties required for the design of storage and processing equipments that handle bulk materials. In the Jenike shear test, the particulate sample in a split box is sheared laterally under constant normal load by moving the top half of the box relative to the bottom half. The Jenike shear cell used in the current experiments (Figure 5.32) has a large diameter of $143mm$,

which is suitable for both sand and barley grains. The upper shear ring and the lid were displaced at a nominal rate of $1mm/\text{min}$, and three external loads were applied $(7.5/15/30kg)$ to achieve different normal stress levels.

It is well known that the failure of a granular mass can usually be adequately described by the Mohr-Coulomb failure criterion:

$$\tau_f = c + \sigma_n tan\phi \tag{5.1}$$

in which τ_f and σ_n are the limiting shear stress and the normal stress on the failure plane, and c and ϕ are the material constants termed the cohesion and the internal friction angle. Haertl and Ooi (2008) pointed out that a granular material can be treated both as a cohesionless material ($c = 0$), or a typical $c - \phi$ material (a frictional material with a small cohesion). Treating the non-spherical particles as a cohesionless material could lead to a larger bulk friction coefficient. Here, the bulk friction was determined by a regression best fit to each test series over the normal stress range as shown in Figure 5.33 and 5.34, in which the average shear stress acting on the split plane versus the horizontal relative displacement were plotted for all the samples with sand and barley, respectively. Table 5.3 summarises the measured friction coefficients and other particle properties of all test samples. The density listed is the density of solid particles, which is not dependent on the degree of sample compaction.

For ease of comparison and discussion, each test was assigned a name according to its material, filling method, bulk density and footing size. For example 100BCUD, is "B" for barley, "C" for concentrically filled, "UD" for uncompacted loose sample and testing under the $100mm$ footing. Also, "S" represents Leighton Buzzard sand, "L" represents layered filling and "DD" denotes a dense sample compacted by the vibrating shakers. To further quantify each testing sample, the achieved bulk density and void ratio are listed in Table 5.4. Measurements of bulk

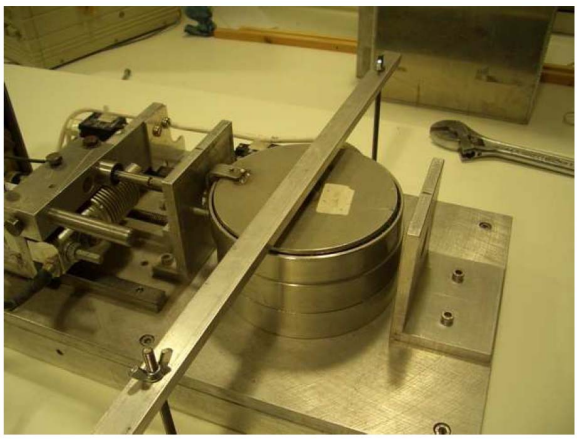

(a) Laboratory setup

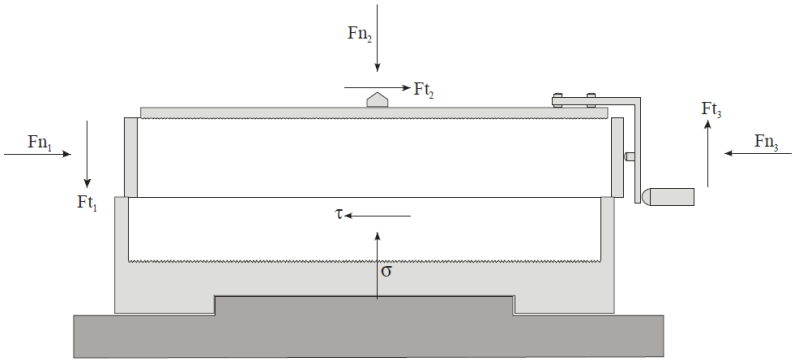

(b) Schematic diagram

Figure 5.32: Jenike shear test

Table 5.3: Particle properties

Particle properties	Sand	Barley
D_{50} (mm)	0.5	5.1[a]
Particle density (kg/m^3)	2650	1260
Interparticle friction	0.413	0.273
Boundary friction	0.152	0.136

[a] D_{50} was averaged from two axis.

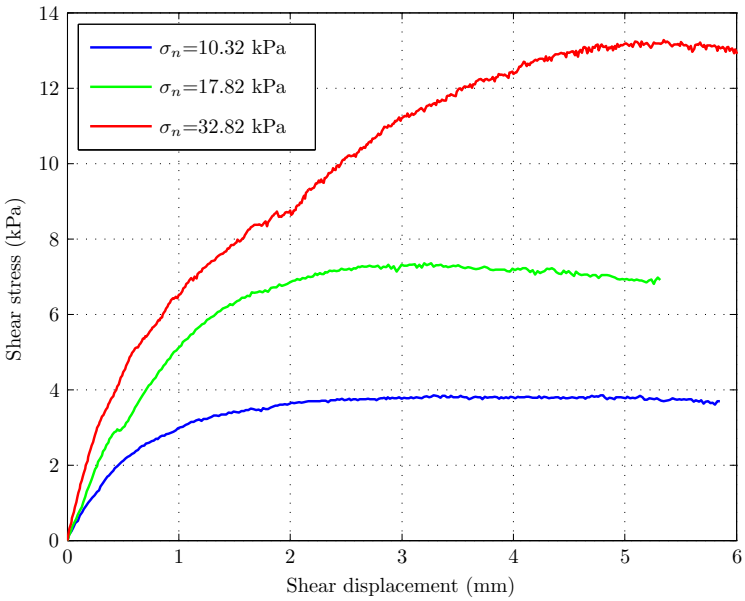

(a) Shearing response in th measurement of bulk friction

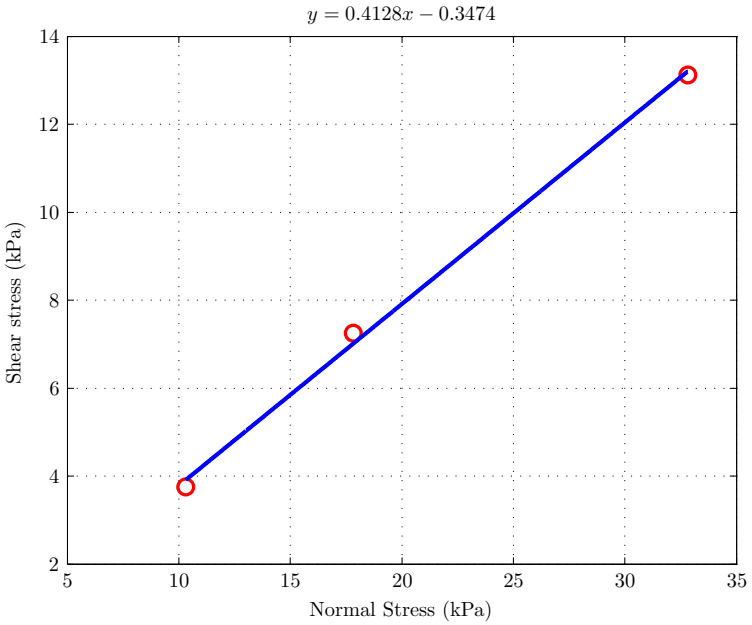

(b) Evaluation of friction coefficient using linear regression

Figure 5.33: Frictional properties of sand

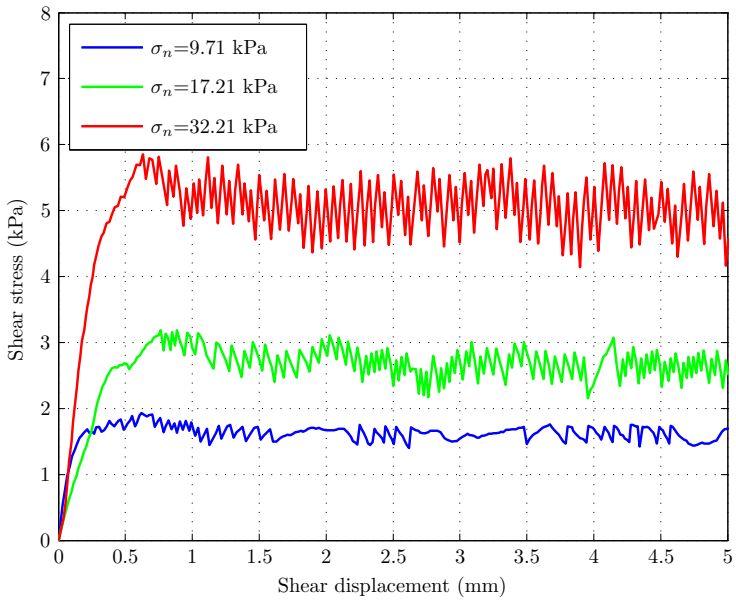

(c) Shearing response in the measurement of particle-boundary friction

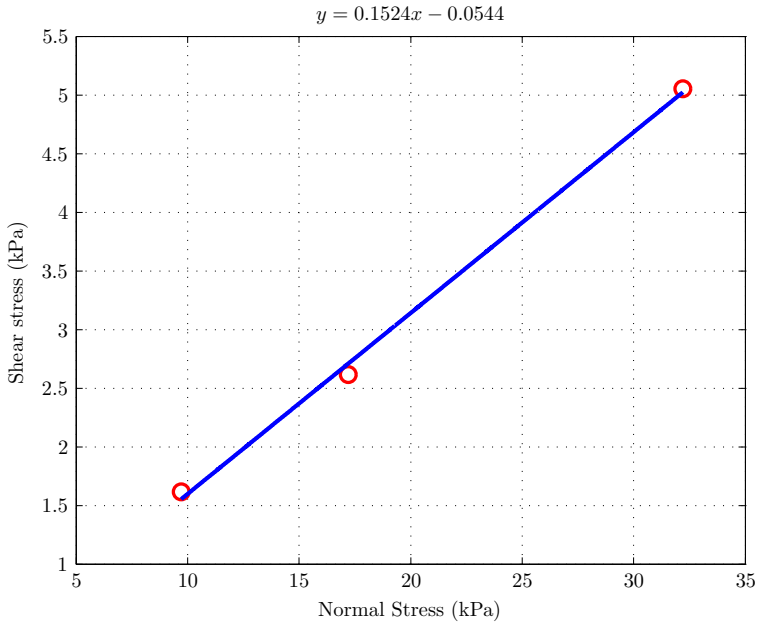

(d) Evaluation of friction coefficient using linear regression

Figure 5.33: (*continued*) Frictional properties of sand

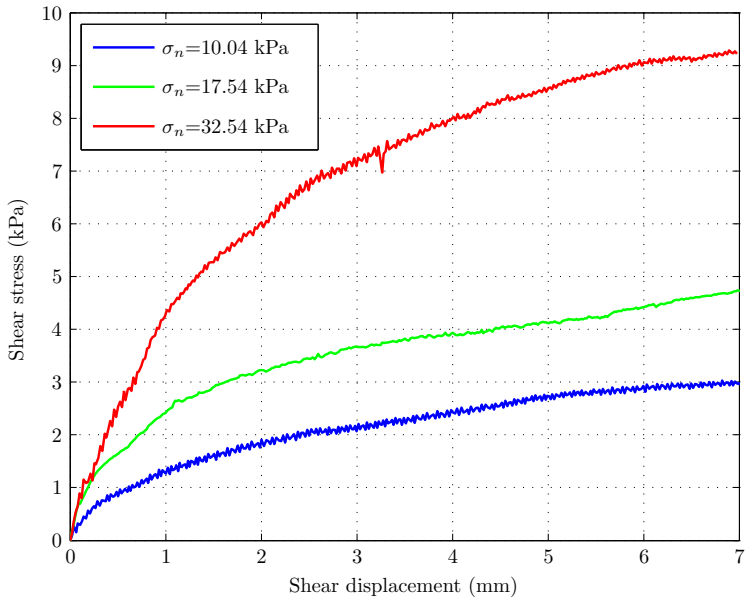

(a) Shearing response in the measurement of bulk friction

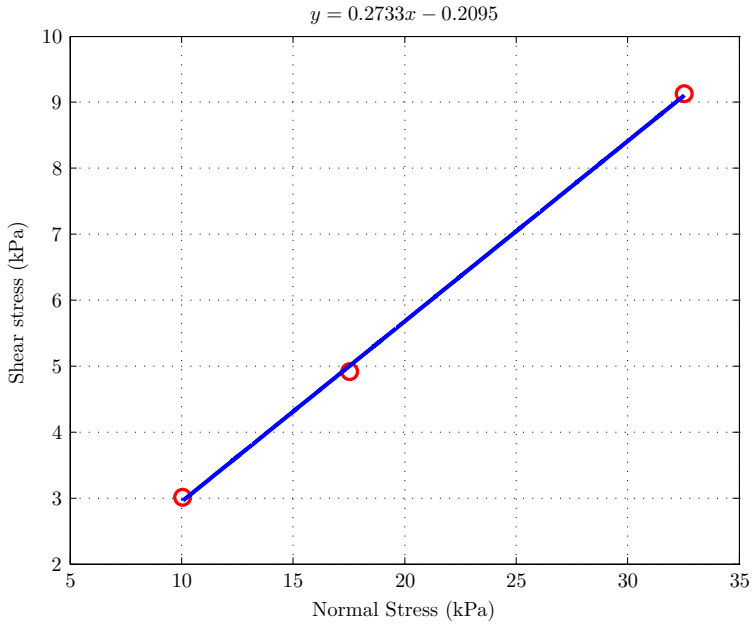

(b) Evaluation of friction coefficient using linear regression

Figure 5.34: Frictional properties of barley

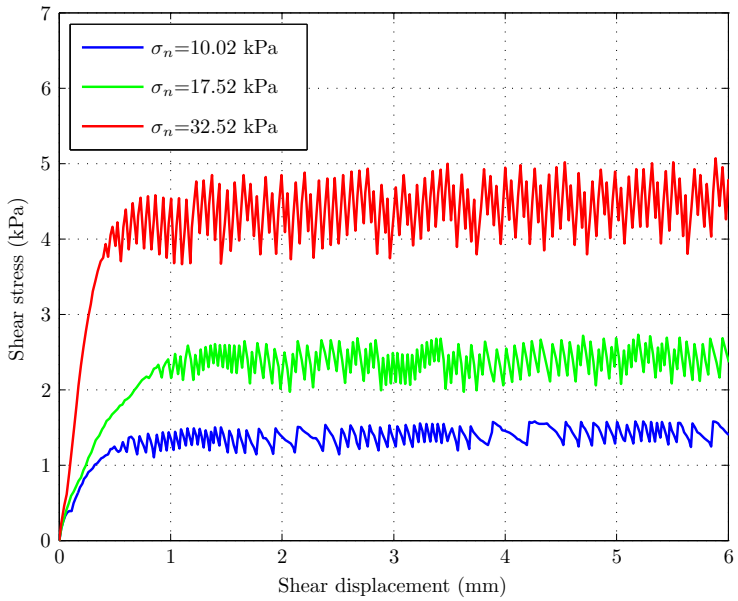

(c) Shearing response in the measurement of particle-boundary friction

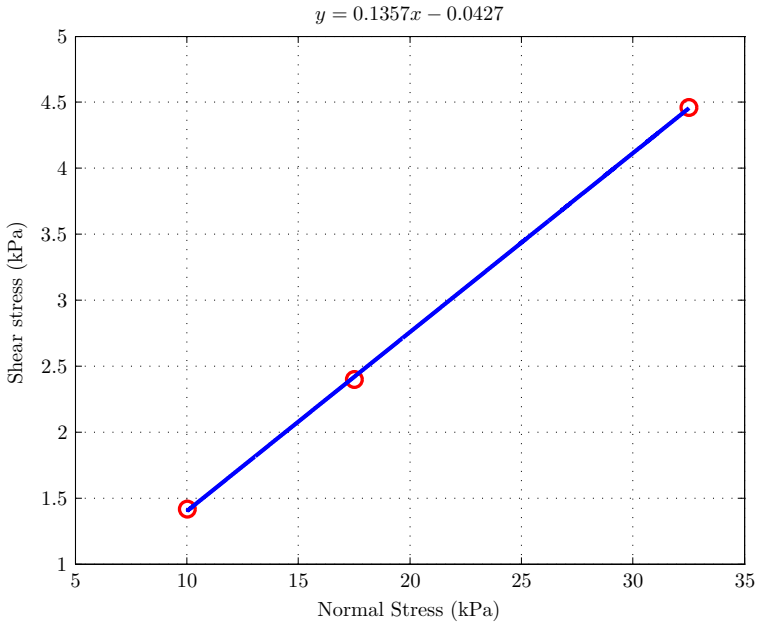

(d) Evaluation of friction coefficient using linear regression

Figure 5.34: (*continued*) Frictional properties of barley

density and void ratio can be easily made and are useful in developing meaningful interpretations of macroscopic behaviour. Bulk density is defined as the mass of particles divided by the total volume they occupy, which takes into account the total solid space as well as pore space (usually air). Unlike particle density, bulk density is not an intrinsic material property; it can change depending on how the material is packed. The void ratio is measured according to Equation 2.2, in which the volume V can be calculated from the inner dimension of the slice box, i.e. $V = AH$ where A is the cross section area of the box and H is the filling height of the particle sample. If the density and total mass of particles are known, Equation 2.2 can be expressed in another form:

$$e = \frac{V - V_s}{V_s} = \frac{AH}{M/\rho} - 1 \tag{5.2}$$

where M is the total mass of the granular assembly and ρ is the particle density. As reported in Table 5.4, the achieved bulk density in samples prepared by two different filling methods were insignificant, which leads to the expectation that the resulting loading responses would be similar. On the other hand, a much stiffer loading curve can be anticipated in densely compacted samples due to a much lower initial void ratio.

5.5.1.5 Loading setup

External loading to drive the model footing into the sample was carried out via the Instron testing machine with $100kN$ capacity at the University of Edinburgh. The slice model was firmly clamped at several positions to minimise any possible out-of-plane deflection during the test (Figure 5.35). The loading rate was kept constant throughout all the tests at a rate of $20mm$/minute, which was reasonably slow to simulate a quasi-static loading scenario. Footing displacement and reaction force on the footing base were recorded constantly by Instron machine

Table 5.4: Property index of testing samples

Test name	Footing breadth (mm)	Particle type	Filling method	Bulk density (kg/m^3)	Void ratio (e)	Vibrated
50-S-C-UD	50					
100-S-C-UD	100	Sand	Concentric	1538.69	0.72	No
150-S-C-UD	150					
50-S-L-UD	50					
100-S-L-UD	100	Sand	Layered	1545.59	0.71	No
150-S-L-UD	150					
100-B-C-UD	100					
150-B-C-UD	150	Barley	Concentric	768.97	0.64	No
100-B-L-UD	100					
150-B-L-UD	150	Barley	Layered	755.93	0.67	No
100-B-L-DD	100					
150-B-L-DD	150	Barley	Layered	810.91	0.55	Yes

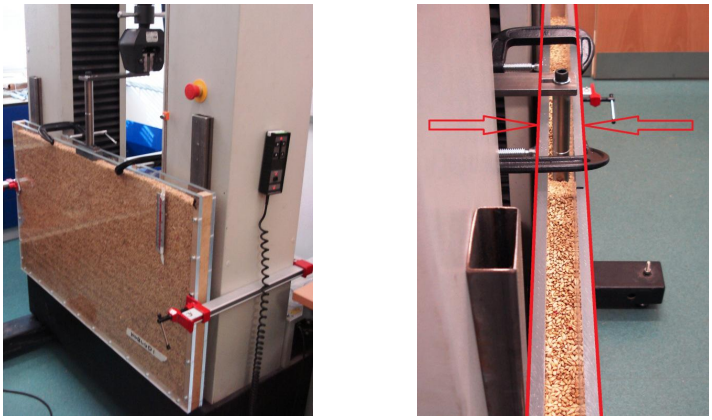

Figure 5.35: Clamping the model to minimised the out-of-plane deflection

and logged to a data file every second (1Hz).

5.5.1.6 Image recording

Images were captured by a high resolution SLR camera every 10 seconds (0.1Hz). This ensured sufficiently small particle movement between two successive images, which is of particular importance for the tracking of complex deformation zones (recalling loading rate of $20mm$/minute). Special attention was paid to minimise the reflection on the Perspx front surface, as well as the image distortion caused by camera lens not perpendicular to the measurement plane. Typical images recorded at various penetration depths using different footing sizes were shown in Figure 5.36. The pixel dimension of all the images is 2816×2112, which gives a scale that converts pixel to physical length at approximately 0.25-0.3mm/pixel.

Each captured digital image was cropped accordingly before putting through PIV operation. To focus on the primary deformation zone (i.e., the area immediately beneath the footing), typically only about 60-80% of the imaged face were evaluated by PIV correlation. This can also eliminate the effect caused by shadows and reflections in the image, which may obscure the granular solids from the background, especially those near the edges of specimen.

(a) 50mm

(b) 100mm

(c) 150mm

Figure 5.36: Typical images captured for PIV analysis using three footing sizes

5.5.2 Loading-displacement curve

In order to compare the bearing capacities of all the model footing tests and to identify key stages to perform PIV analysis, the loading-displacement curves plot the stress acting at the footing base against the settlement depth are first examined.

5.5.2.1 Sand

The tests on Leighton Buzzard sand investigated the influence of initial packing structure, dictated by the filling method (Figure 5.37); and the effect of footing size (Figure 5.38) on the bulk loading response.

Observations from Figure 5.37 suggest that the different filling methods appear to affect the loading response, where the common trend is that the initial loading gradients were similar while the layered filling method produced a larger base resistance as the footing settlement increased. This observation is in accordance with the higher bulk density achieved in the SLUD sample as reported in Table 5.4.

Figure 5.38 gives loading responses for different footing sizes on SCUD and SLUD samples. It can be seen that as footing breadth increased, the induced base resistance decreased irrespective of filling methods. Having a closer look at the loading-displacement curves, the smallest $50mm$ footing generated a relatively clear transition from the initial loading stage to the hardening phase. On the other hand, in the samples indented by the footing of $150mm$, the loading curve did not display such a distinct change and the transition point of loading stiffness is less well defined. It thus poses difficulty in the determination of the ultimate bearing capacity, which must be treated consistently for all the tests and will be further discussed in the subsequent section.

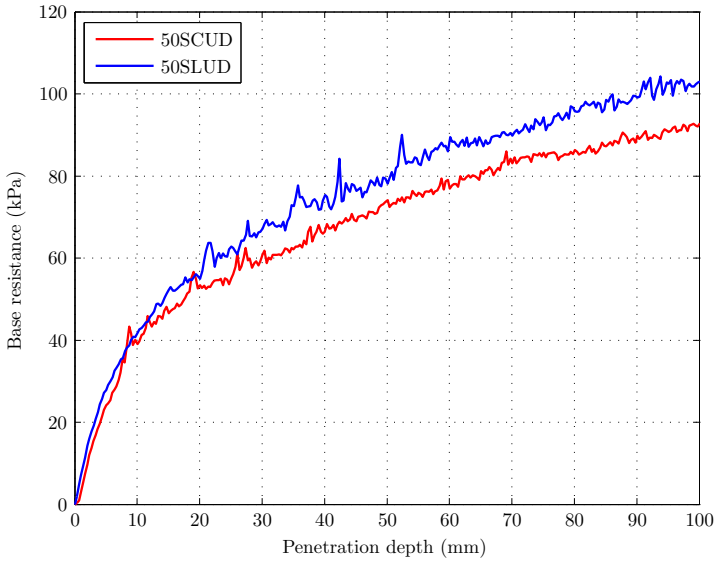

(a) $50mm$

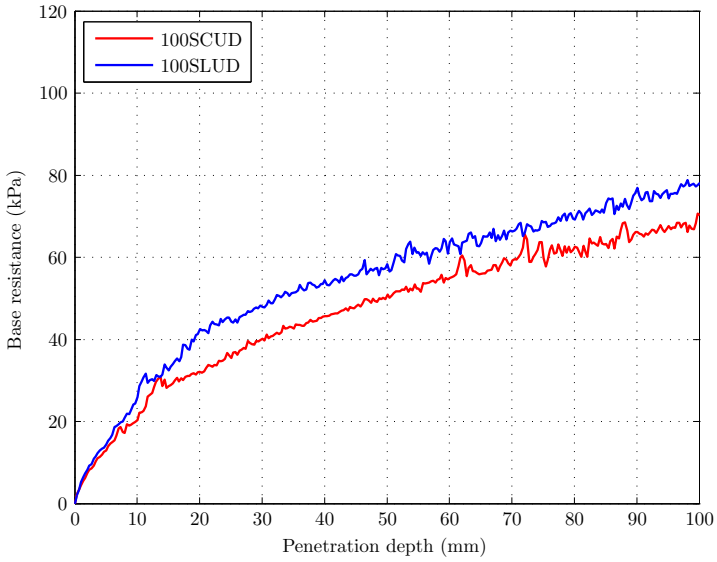

(b) $100mm$

Figure 5.37: Loading response for sand: influence of filling method

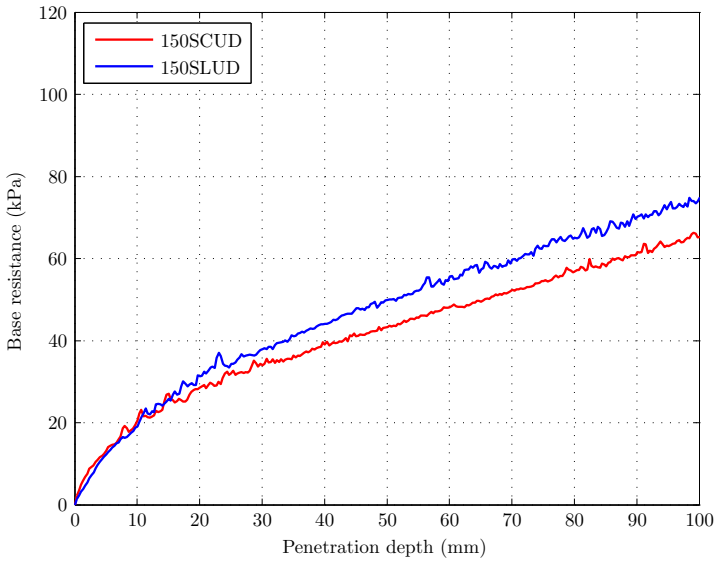

(c) 150mm

Figure 5.37: (*continued*) Loading response for sand: influence of filling method

5.5.2.2 Barley

For the tests using barley, as the 50mm footing may have insufficient particle contacts at its base, only footings with size of 100mm and 150mm were selected in order to obtain relatively smooth loading curves. A new packing structure BLDD was introduced here to further explore the differences between a general loose sample and a dense one. Expectedly, this densely compact sample produced a considerably higher penetration resistance than the other two loose samples (Figure 5.39). Comparing the loading responses between BCUD and BLUD, the concentrically filled samples posed higher packing density and thus gave rise to a greater bearing capacity during footing installation. Noticeably, this is a reversal of the behaviour observed in the Leighton Buzzard sand, where the layered samples presented a higher penetration resistance. It leads to the assumption that the particle orientation may play a role in the macroscopic behaviour (recalling

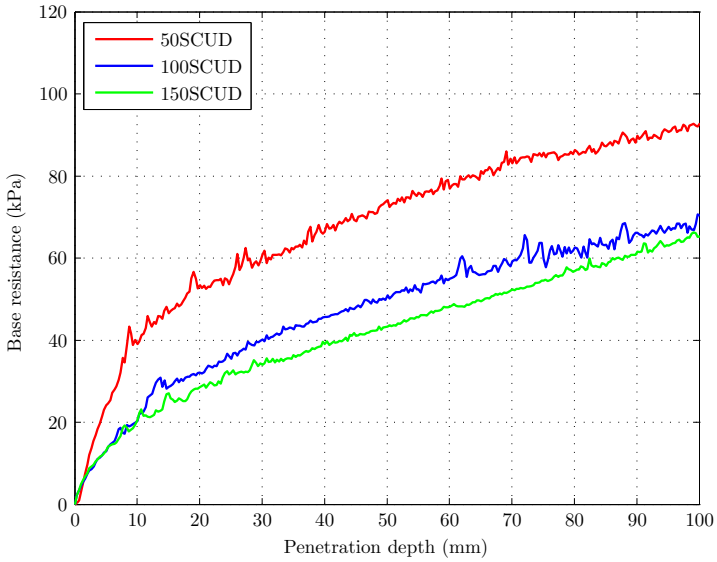

(a) SCUD

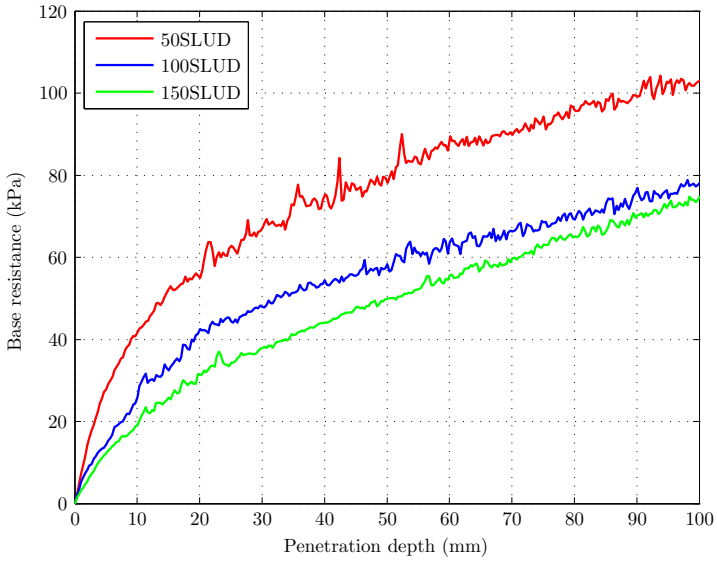

(b) SLUD

Figure 5.38: Loading response for sand: influence of footing size

Figure 5.30). For barley, the well organised packing arrangement exhibited in the concentric samples can be a source to the increase of bearing capacity, where the ease of particle rotation was minimised by the predominantly horizontal grain orientation. The layered samples did not present such a neat interlocking configuration, thus particles became easier to rotate and rearrange under the footing penetration.

Similar to Leighton Buzzard sand samples, Figure 5.40 shows that smaller footing generated a greater footing resistance, which is apparent for all filling methods and packing densities in the barley samples. Regarding the loading gradient in each test for barley, the transition from the initial loading phase to the hardening phase took place smoothly over a relatively small footing settlement.

5.5.2.3 Ultimate bearing capacity

To summarise the main feature of the loading-displacement curves as shown for both sand and barley, there is a general trend of linear increasing base resistance during the first $10mm$ settlement, during which the footing behaviour can be related to shallow foundation process. However, throughout all the test carried out, a constant value of base resistance were not reached. Instead, a steady increase with a lower gradient comparing to the initial loading stiffness was observed. Here, the bearing capacity in each test is evaluated based on the these loading responses. Terzaghi (1943) proposed a formula to calculate the ultimate bearing capacity of shallow foundation, which is normally referred as "$3N$ bearing capacity theory". This well known theory can be expressed as:

$$q_{ult} = cN_c + qN_q + \frac{1}{2}\gamma BN_\gamma \tag{5.3}$$

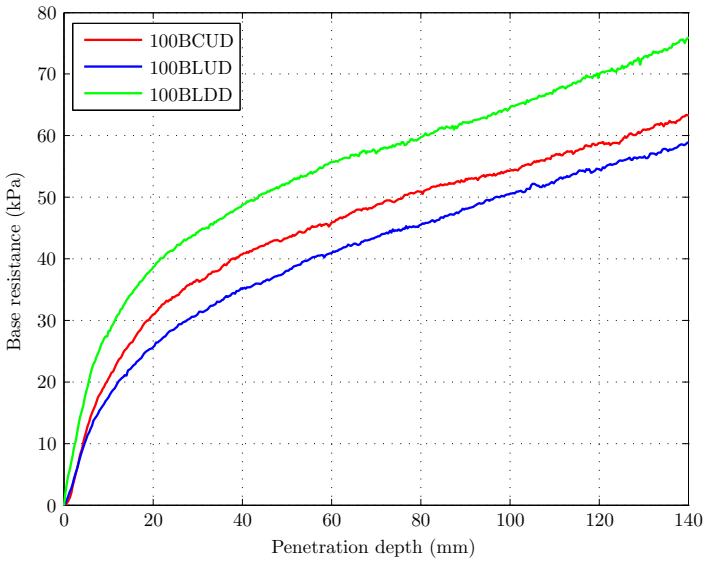

(a) footing breath: $100mm$

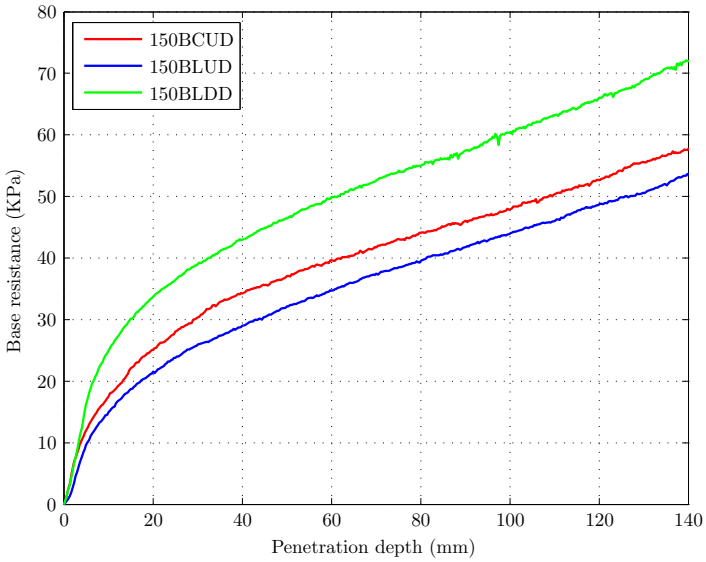

(b) footing breath: $150mm$

Figure 5.39: Loading response for barley: influence of filling method and packing density

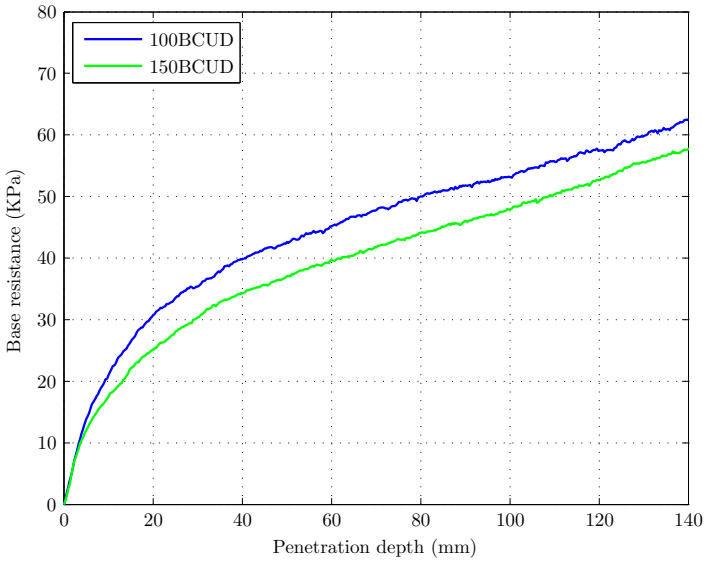

(a) BCUD

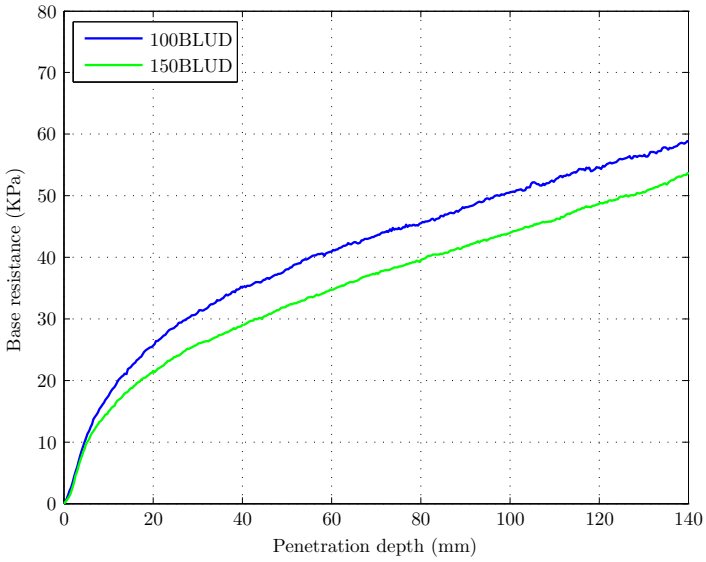

(b) BLUD

Figure 5.40: Loading response for barley: influence of footing size

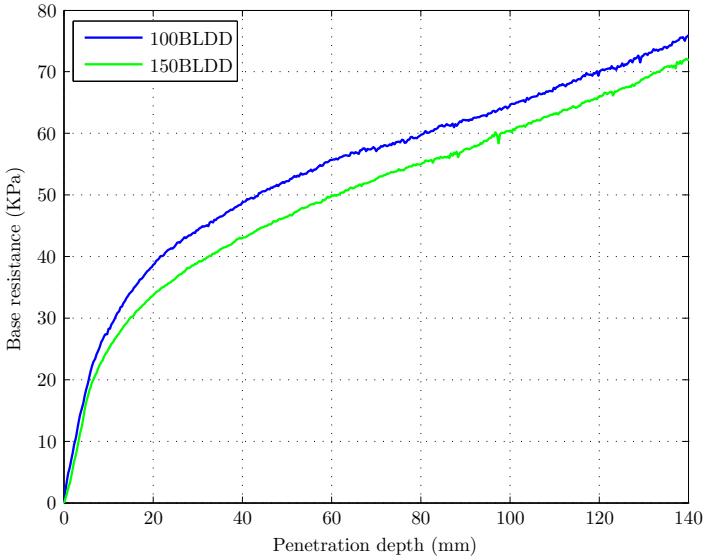

(c) BLDD

Figure 5.40: (*continued*) Loading response for barley: influence of footing size

where

q_{ult}	ultimate bearing capacity of the footing;
c	cohesion parameter;
q	surcharge around foundation, which equals to γD_f;
γ	unit weight of soil;
B	foundation breadth;
D_f	depth of foundation below soil level;
N_c, N_q, N_γ	dimensionless bearing capacity factors.

It is difficult to specify a failure point in the loading-displacement curve, as in the current tests the transition between initial loading and hardening phases was more ongoing that did not occur at a single point. In order to consistently and equally compare each loading response, an unbiased approach must be applied to determine the ultimate bearing capacity. Lutenegger and Adams (1998) compared

four ways in the literature to define the value of ultimate bearing capacity from loading curves, as illustrated in Figure 5.41:

- Tangent intersection method: two linear curve fittings are carried out in the initial loading and hardening phases. The intersection point of the two lines thus corresponds to the q_{ult};
- Log-log method: this is quite similar to the tangent intersection method, apart from that it returns the natural logarithm values for both footing stress and settlement;
- Hyperbolic method: the settlement is first divided by the stress and q_{ult} is determined by extrapolating to the asymptotic value corresponding to an upper limit of stress;
- $0.1B$ method: the penetration depth is normalised by the footing breadth and the ultimate capacity is chosen at a settlement of 10% of the footing breadth as suggested by Briaud and Jeanjean (1994).

Each of these methods will produce a different value of q_{ult} since they are empirical in nature. It thus becomes important to choose one method in the current study to maintain consistency. Lutenegger and Adams (1998) carried out a large number of footing tests on sand samples and found that generally the value of predicted q_{ult} increases according to: log-log method $<$ tangent intersection method $<$ $0.1B$ method $<$ hyperbolic method.

The loading curves in the current footing tests exhibit a bilinear pattern, in which a initial loading phase and a hardening phase can be observed similar to the presentation of tangent intersection method. Accordingly, Figure 5.42a shows the the two idealised line segments fitting the experimental results. Overall, the loading-displacement curve can be adequately described by the proposed bilinear fitting plot in tangent intersection method. By having a close look at the two

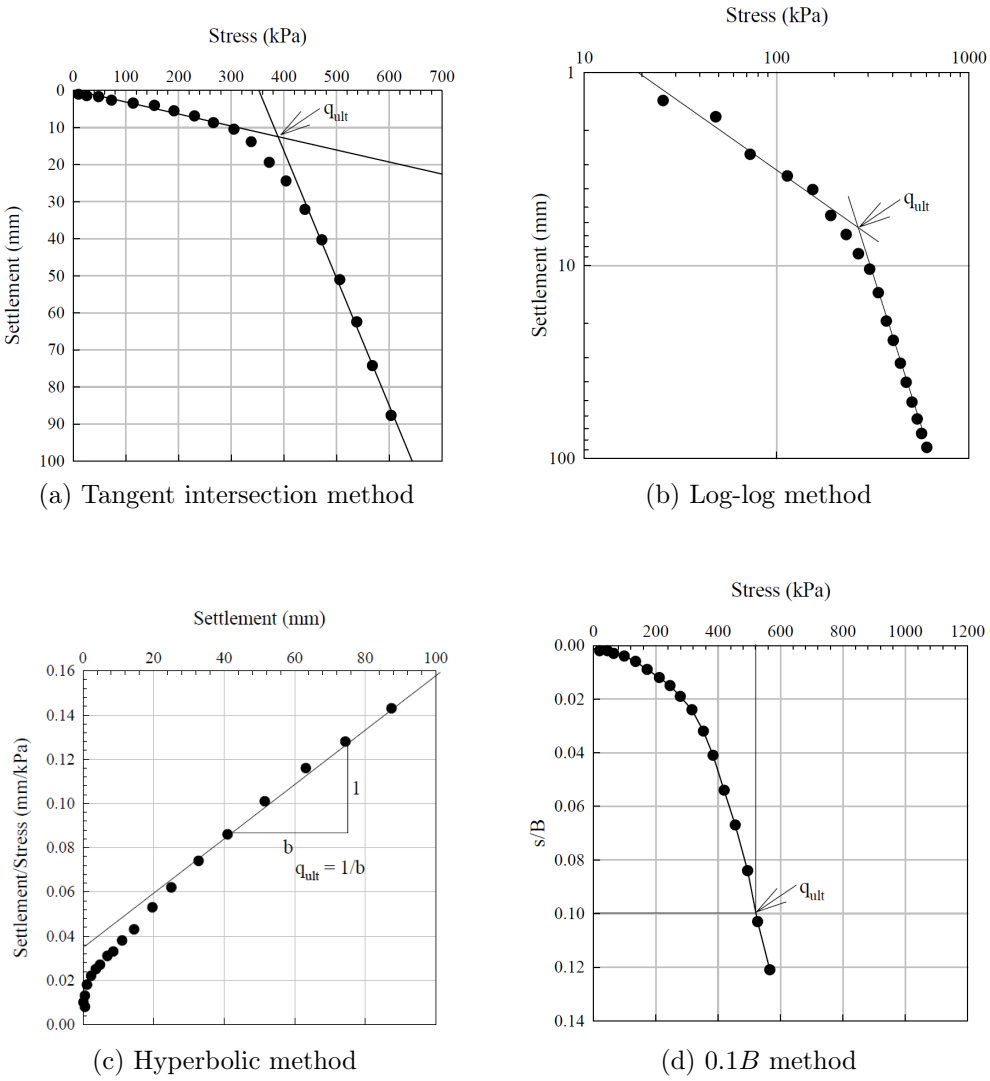

(a) Tangent intersection method

(b) Log-log method

(c) Hyperbolic method

(d) $0.1B$ method

Figure 5.41: Defining ultimate bearing capacity from loading tests (Lutenegger and Adams, 1998)

loading phases separately, the hardening phase well matched the linear fitting (Figure 5.42c), whereas the definition of the initial linear loading region (Figure 5.42b) is rather subjective, completely depending on the data points selected. Noticeably, all the loading-displacement curves in this study display a very short initial loading phase. Therefore, similar to tangent intersection method, the curve fitting used in log-log method and hyperbolic method will indeed produce significant numerical uncertainty in the determination of q_{ult}.

Among these methods, $0.1B$ method achieves a fixed value of q_{ult} at a settlement of 10% of the footing width, which is easily implemented and does not require the data belonging to the intial loading phase to be spicified. Although this method being arbitrary, it is capable of equally treating the loading response with different footing sizes. Furthermore, its obtained value of ultimate bearing capacity is comparable to the ones from other methods. Therefore this method is adopted in the current study to calculate q_{ult} from the loading-displacement curves.

Figure 5.43 and 5.44 show the loading responses in which the settlement was normalised by the footing breadth. For all the cases, the curves from samples with the same material and packing density collapse into a narrow band, which indicates that the normalised curves are independent of footing breadth. Similar results have been reported as shown in Figure 5.45, in which Briaud and Gibbens (1999) carried out five footing tests in a silty sand sample and Consoli et al. (1998) performed the footing experiments in sandy clays. In both cases, the normalised curves were independent of footing size and fell essentially into one representative curve with a small amount of scatter.

Based on these normalised curves, the values of ultimate bearing capacity can be determined according to the $0.1B$ method and reported in Figure 5.46. Generally, the ultimate bearing capacity in sand sample is greater than the one achieved in the sample composed of barley. Considering the Leighton Buzzard

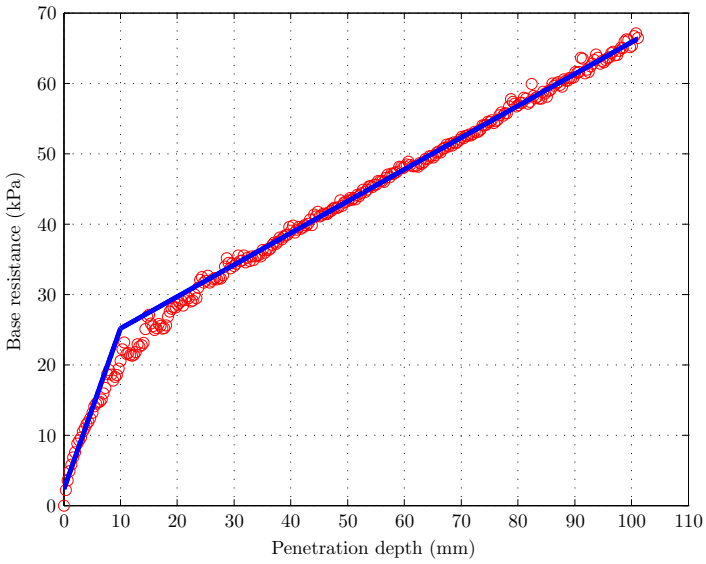

(a) BCUD

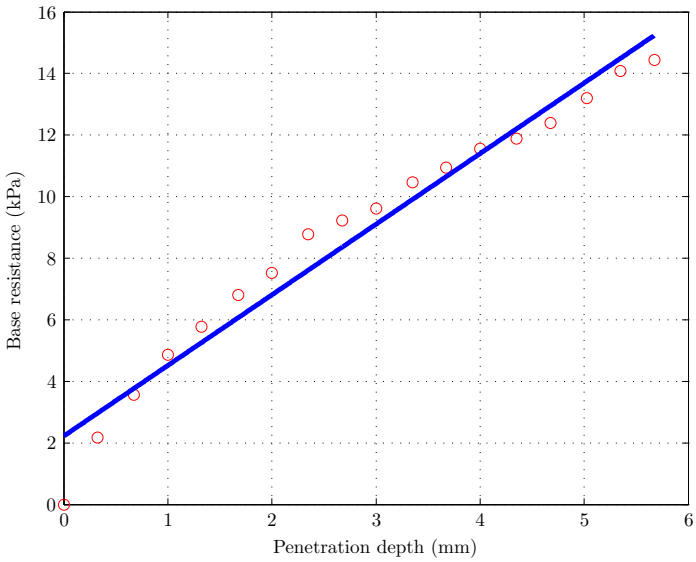

(b) Initial loading region

Figure 5.42: Example of bilinear curve fitting in tangent intersection method

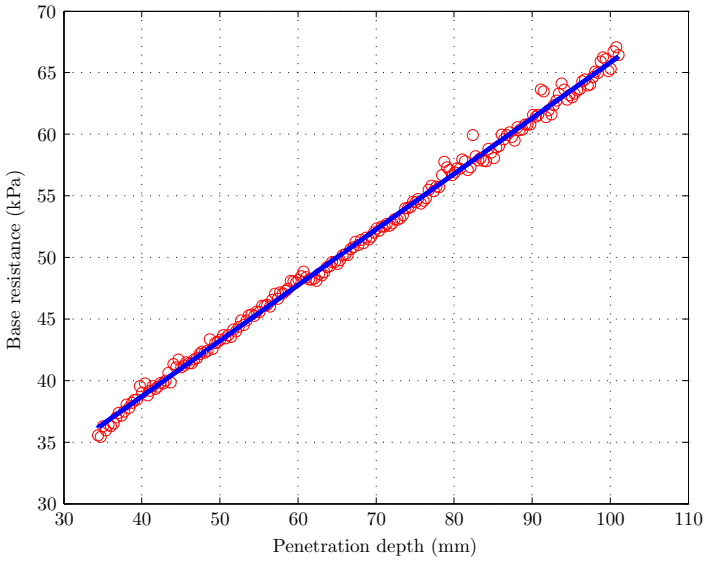

(c) Hardening phase

Figure 5.42: (*continued*) Example of bilinear curve fitting in tangent intersection method

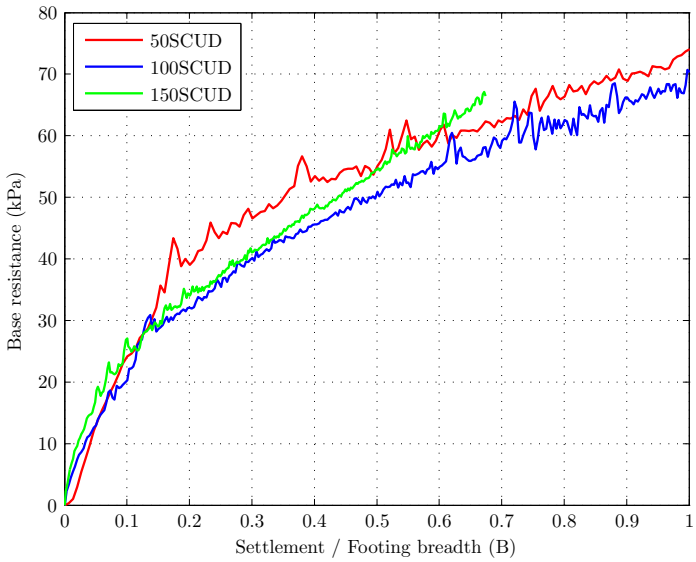

(a) SCUD

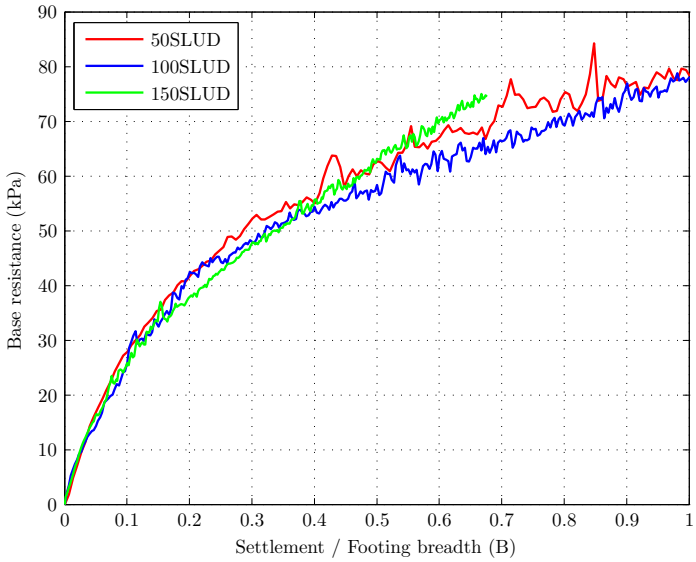

(b) SLUD

Figure 5.43: Loading results of sand with the settlement normalised by footing breadth

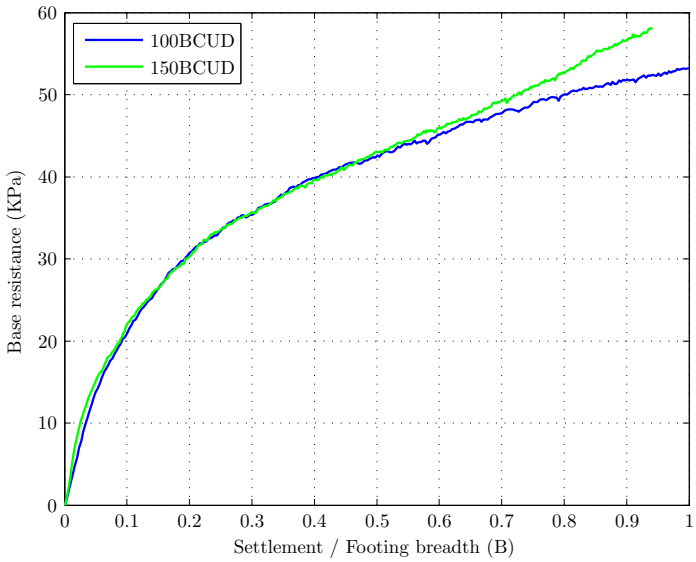

(a) BCUD

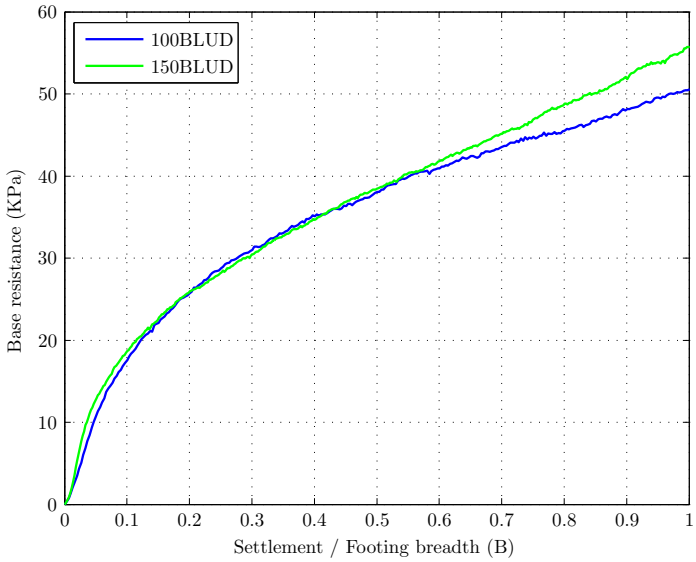

(b) BLUD

Figure 5.44: Loading results of barley with the settlement normalised by footing breadth

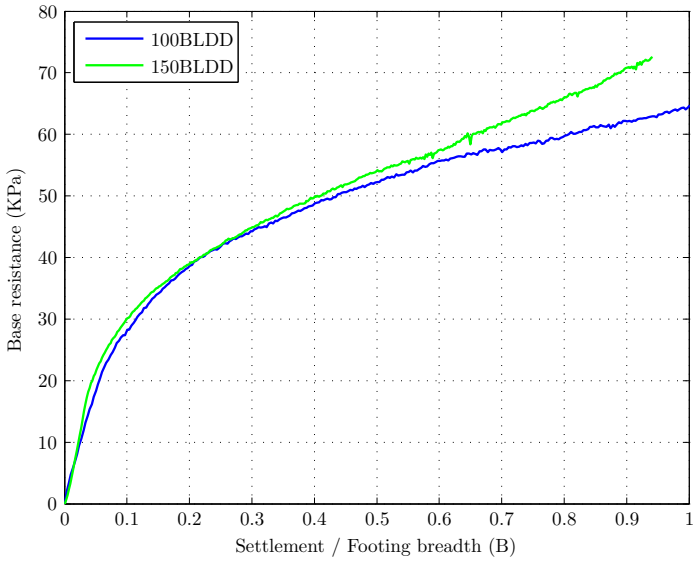

(c) BLDD

Figure 5.44: (*continued*) Loading results of barley with the settlement normalised by footing breadth

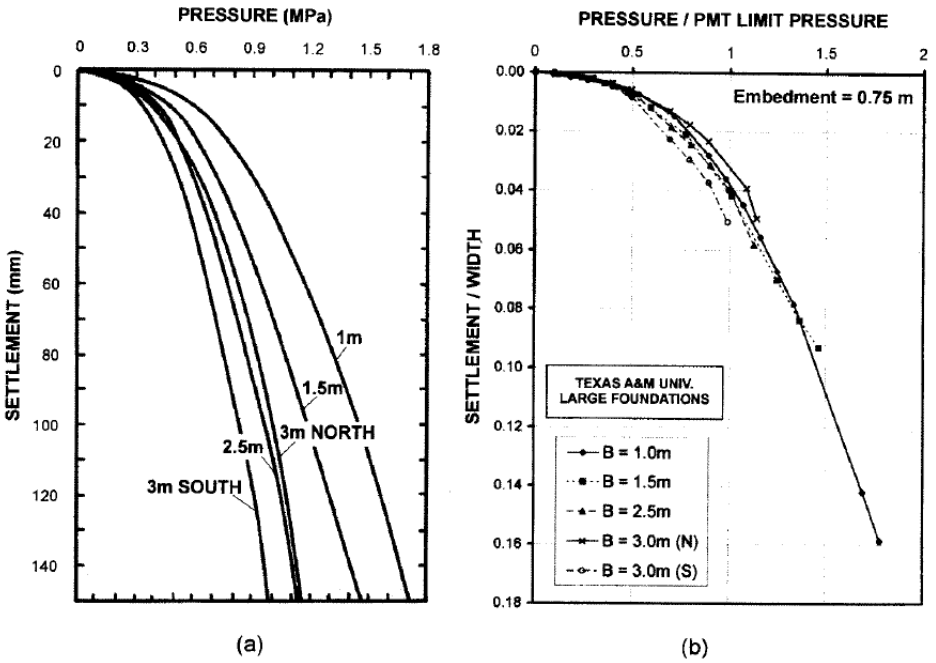

(a) Spread footing tests in sand (Briaud and Gibbens, 1999)

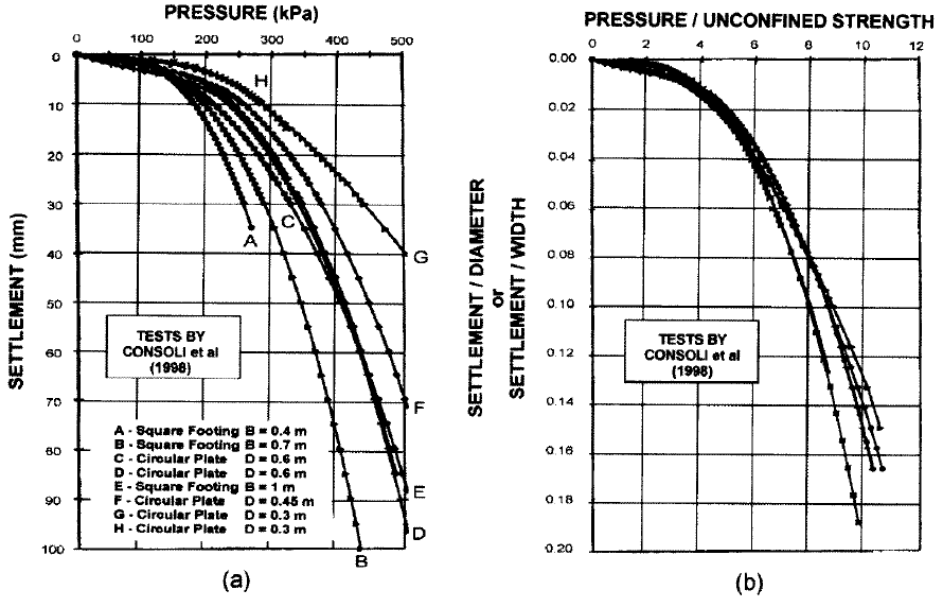

(b) Footing (circular and square) tests in clay (Consoli et al., 1998)

Figure 5.45: Normalising the settlement by footing breadth in loading-displacement curves

sand, the sample prepared by central filling exhibited a 12.5% lowerer bearing capacity than the one prepared by layered filling. Conversely, the barley presented a higher strength in the concentrically poured state, with a 22.2% increase than the one achieved in the layered sample. The highest bearing capacity was achived in the vibrated barley sample, with an increase of around 61% compared to the one in the loose layered sample. Note that the value of q_{ult} reported here is helpful in quantifying the influence of filling method and packing density, and there is no intention to directly relate these experimental results to field tests.

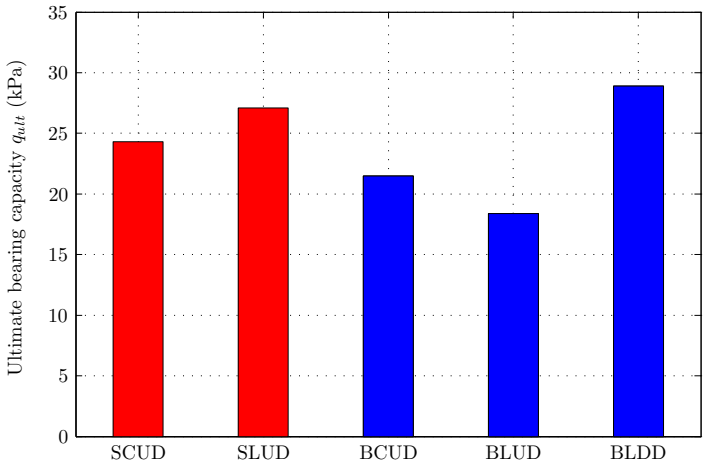

Figure 5.46: Comparison of ultimate bearing capacities q_{ult}

5.5.3 Results from PIV analysis

Prior to performing systematic PIV analysis to correlate the footing images, the choice of interrogation window size was considered to investigate the length scale effect. It is generally agreed that smaller interrogation windows can tolerate much higher displacement gradient. Raffel et al. (1998) pointed out that for the same displacement gradient, the dynamic range of the displacement scaled linearly with

the dimension of the interrogation window, leading to a proportional increase of the correlation peak value. However, there is a limit to the size of the interrogation window. Obviously, a too small interrogation window may not contain sufficient pixel information for image correlation. Figure 5.47 compares the displacement fields by using two different sizes (32×32 and 64×64), where each interrogation window has a 50% overlapping area with its neighbours in order to produce a continuous displacement field.

As shown in Figure 5.47, fairly good results were achieved with interrogation subsets sized 64×64 pixel, although decreasing the window size down to 32 pixel square yielded more vivid information. The displacement data measured by PIV from images (pixel) were converted into physical length (mm) at a scale of 0.25-0.3mm/pixel. Thus the interrogation window size of 32 pixels corresponds to physical length of about $8.0 \sim 9.6mm$, which is only slightly larger than the mean particle diameter of barely and can sometimes be smaller than the maximum displacement occurred between two testing images. Therefore, throughout the following PIV operations, interrogation scheme with window size 64×64 pixel was chosen to evaluate the displacement field. A nonlinear colour map was adopted for vector plotting which well suits the current penetration problems. By allocating more colours to regions of interest (i.e. around footing base) and fewer colours to all other areas, more features in the primary deformation zone can be revealed.

5.5.3.1 Displacement fields and streamline

The primary results from PIV analysis are displacement data of the interrogation window. Here, the displacement field observed at the planar boundary of the model setup will be presented with arrows denoting directions and colour scales for magnitudes of displacement. To perform systematic analysis and capture the key variations during loading, PIV evaluation was performed at three reference

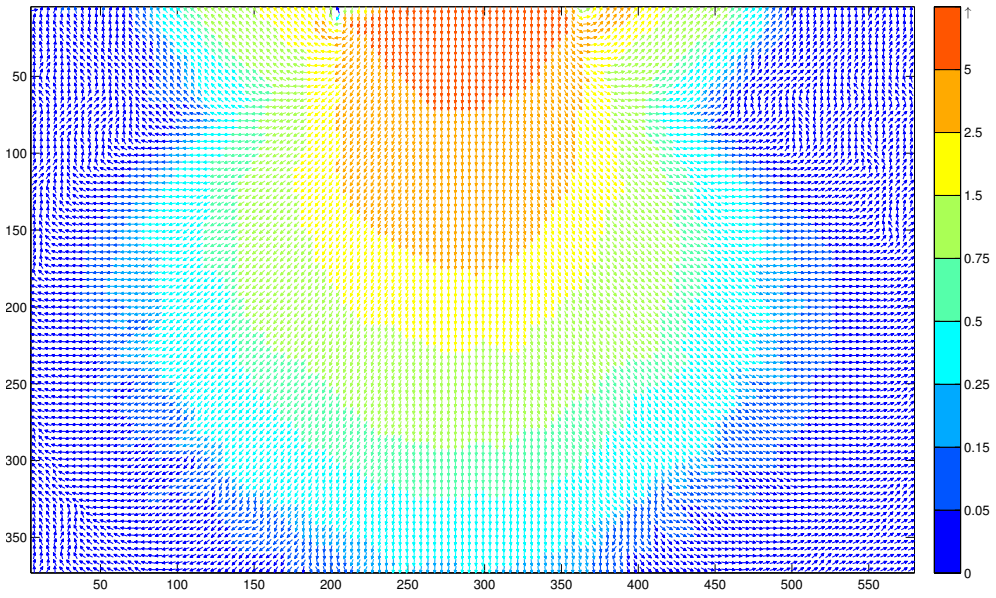

(a) 32×32

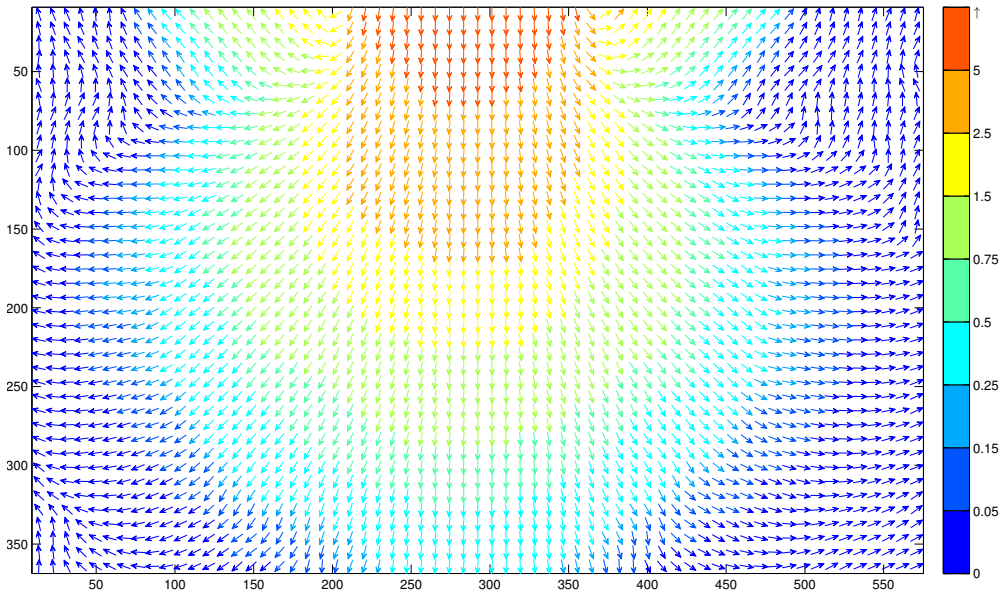

(b) 64×64

Figure 5.47: Comparison of displacement field from PIV using two different sizes of interrogation window

stages along the loading-displacement curve, namely (1) the initial loading phase, (2) the transition point, and (3) the hardening phase. For all the footing tests, the first images at each reference stage selected for PIV correlation were obtained at the same footing settlement as illustrated diagrammatically in Figure 5.48. The time interval between the two images was different for Leighton Buzzard sand and barley, which was 10 seconds and 20 seconds, respectively. The larger time lapse used in the barley sample allows the maximum displacement occurred to be greater than the mean particle diameter. Apart from the displacement fields, streamlines tracing the flow path were also presented to provide an overview of the global flow information, which will direct the research attention to areas of special interest.

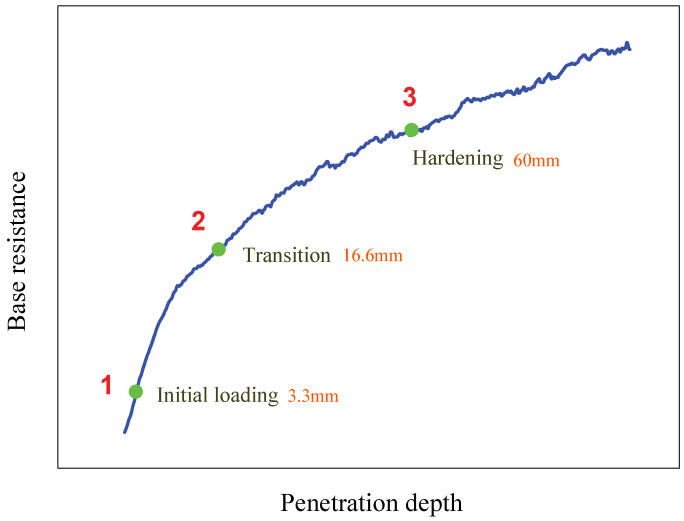

Figure 5.48: Three reference stages for PIV analysis

In total, there were 12 footing test carried out as listed in Table 5.4, but the results from PIV analysis are not presented for all these samples. In sand specimen, 50SCUD and 50SLUD were selected to study the effect of filling method, while the influence of footing size can be investigated by comparing the results of

50/100/150SLUD. For the samples composed of barley, 100BLDD and 100BLUD were compared to explore the influence of packing density; footing size effect can be examined by observing 100/150BLUD; results from 150BLUD and 150BCUD will reveal the effect of filling method. Table 5.5 lists the figure index for these 8 demonstrations of PIV evaluation for sand and barley.

Table 5.5: Figure index of the PIV results

Test name	Initial	Transition	Hardening
50SCUD	Figure 5.49	Figure 5.50	Figure 5.51
50SLUD	Figure 5.52	Figure 5.53	Figure 5.54
100SLUD	Figure 5.55	Figure 5.56	Figure 5.57
150SLUD	Figure 5.58	Figure 5.59	Figure 5.60
100BLDD	Figure 5.61	Figure 5.62	Figure 5.63
100BLUD	Figure 5.64	Figure 5.65	Figure 5.66
150BLUD	Figure 5.67	Figure 5.68	Figure 5.69
150BCUD	Figure 5.70	Figure 5.71	Figure 5.72

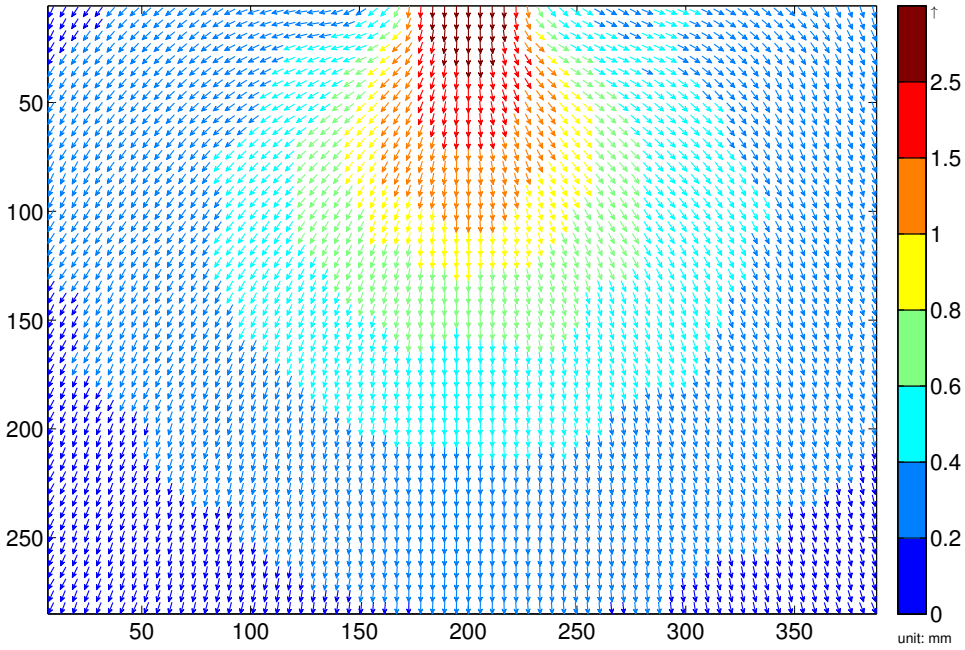

(a) Displacement field

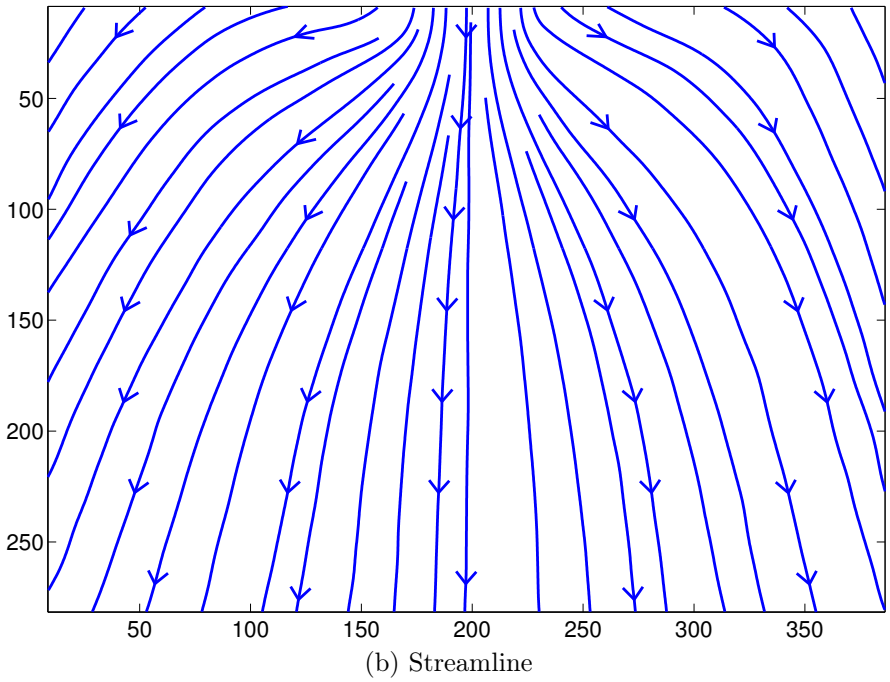

(b) Streamline

Figure 5.49: 50SCUD: initial

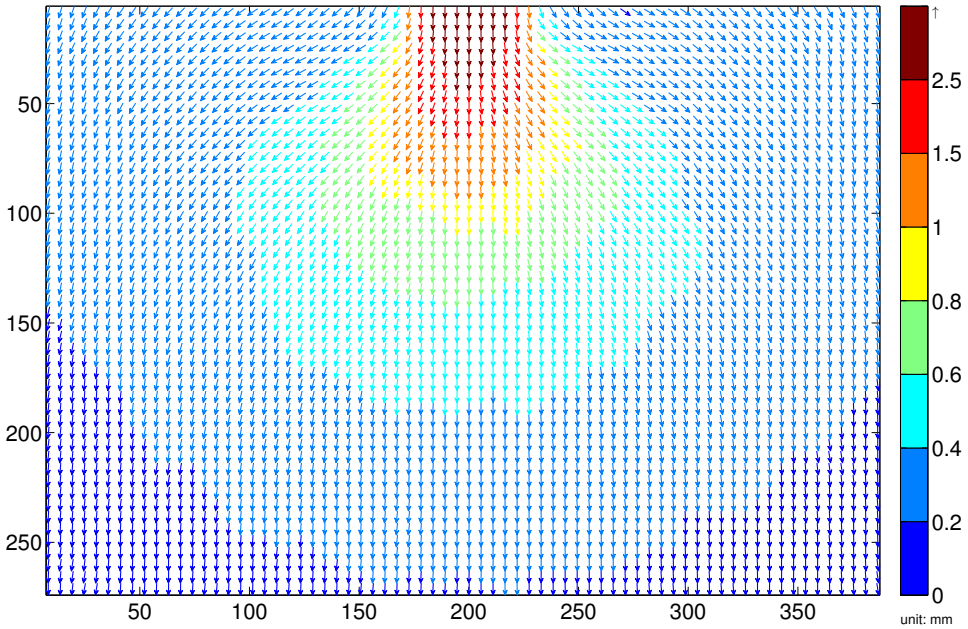

(a) Displacement field

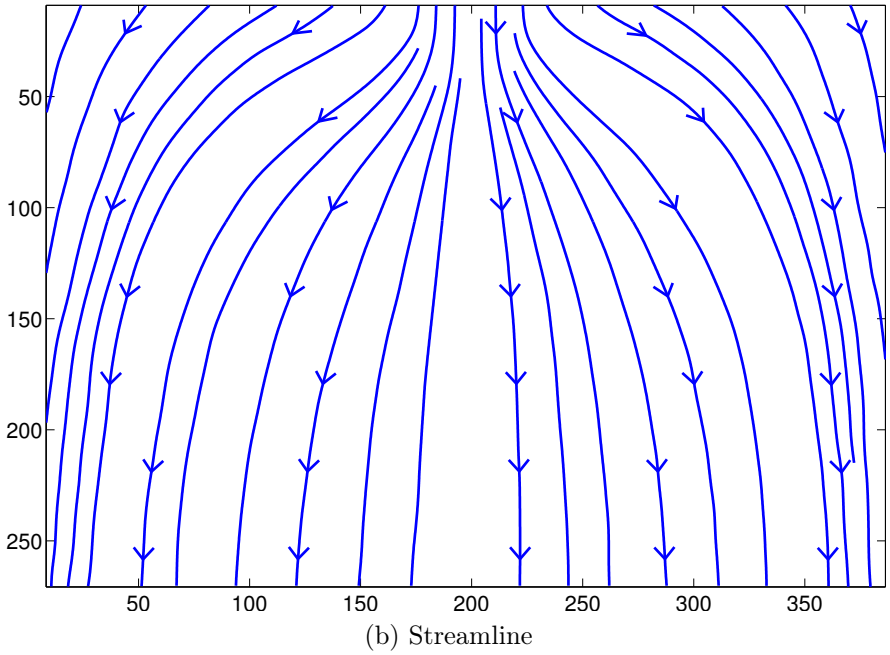

(b) Streamline

Figure 5.50: 50SCUD: transition

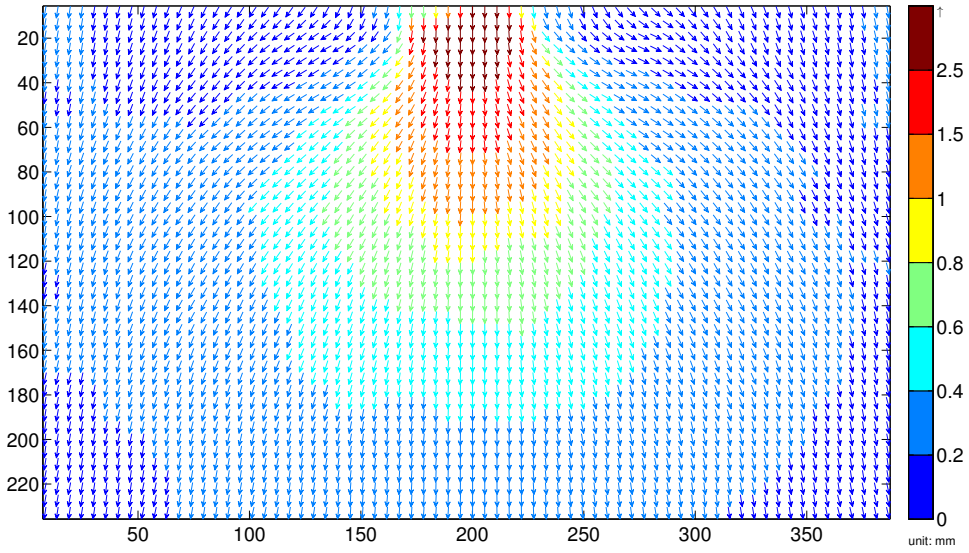

(a) Displacement field

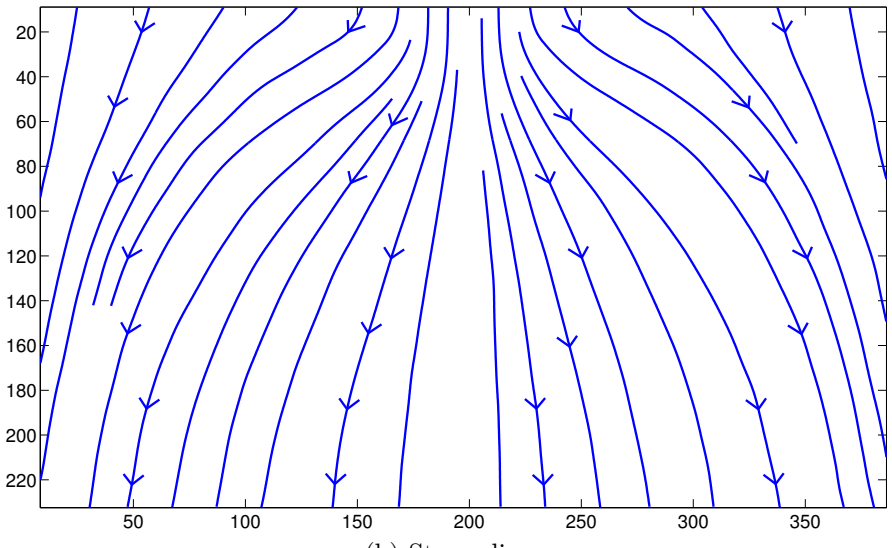

(b) Streamline

Figure 5.51: 50SCUD: hardening

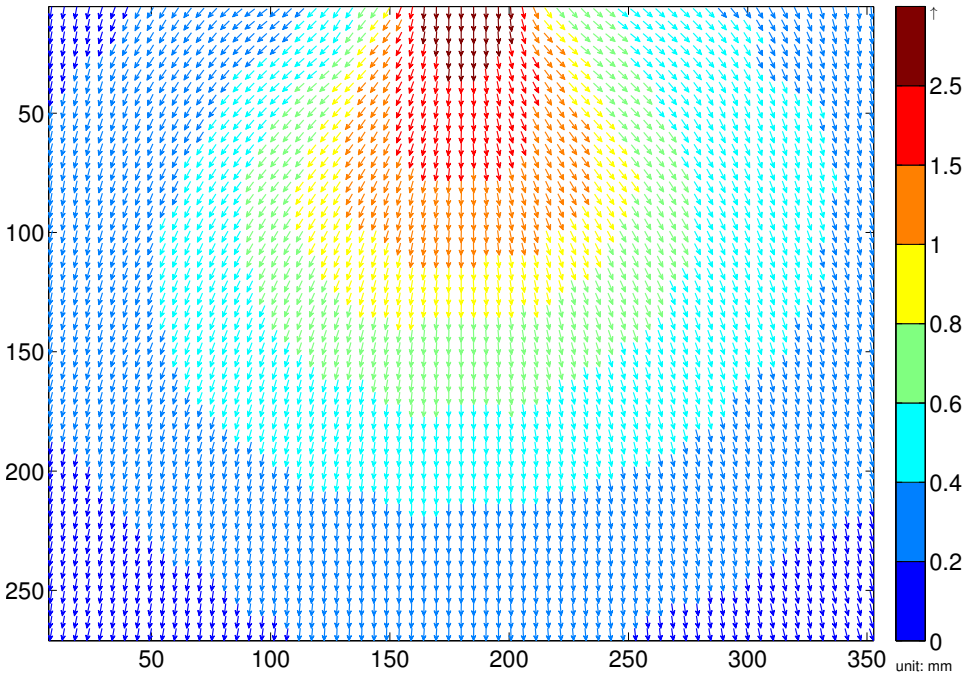

(a) Displacement field

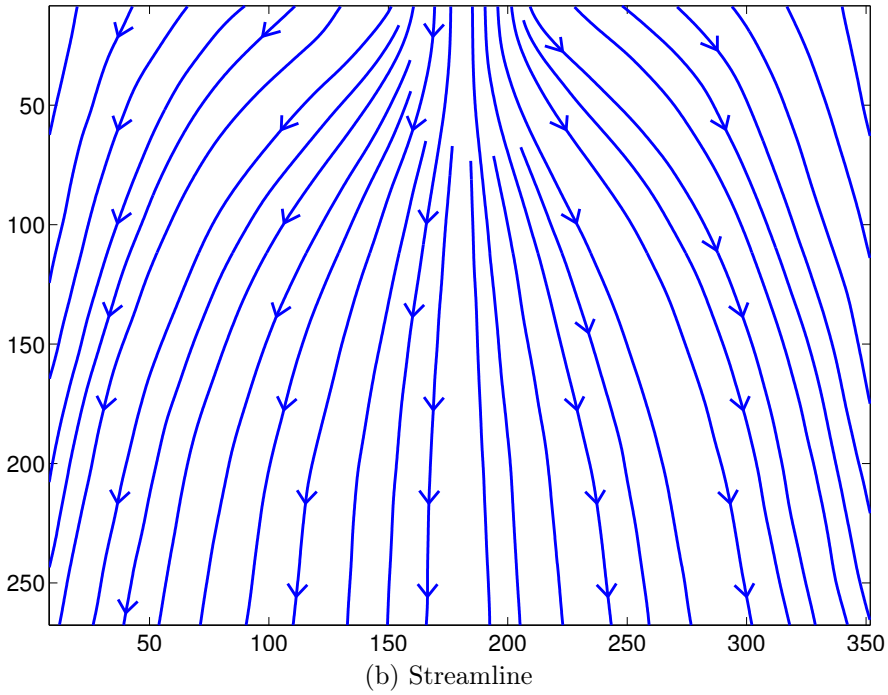

(b) Streamline

Figure 5.52: 50SLUD: initial

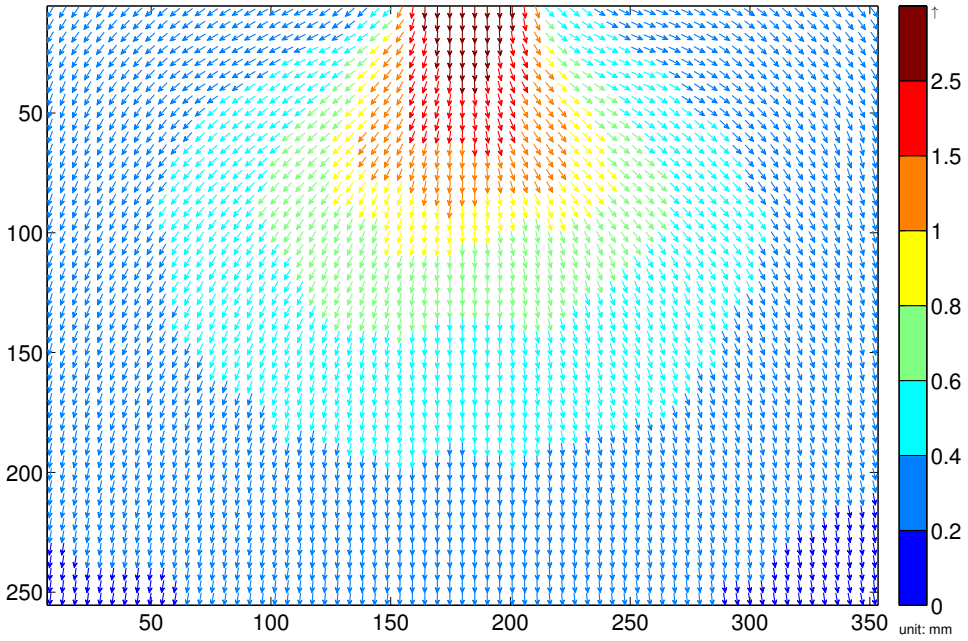

(a) Displacement field

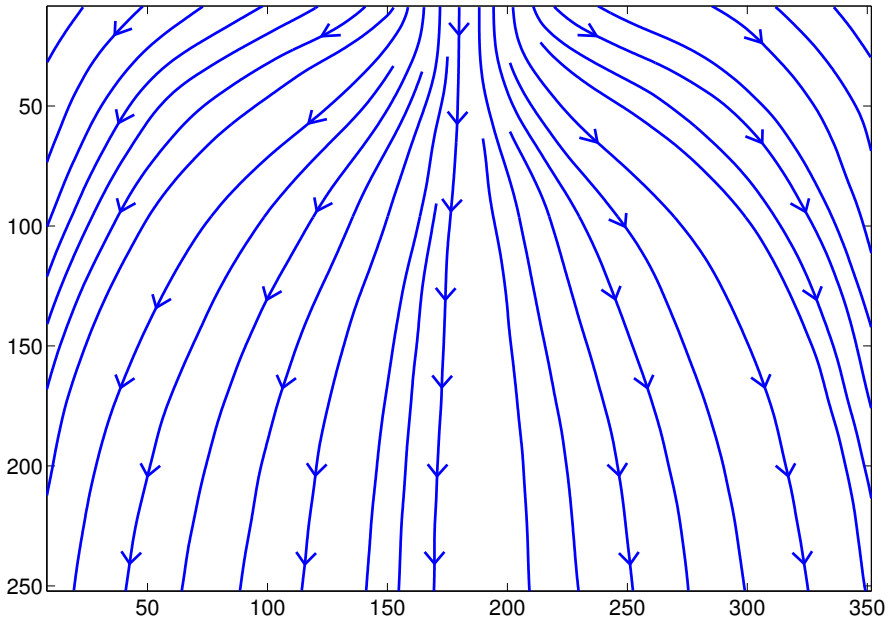

(b) Streamline

Figure 5.53: 50SLUD: transition

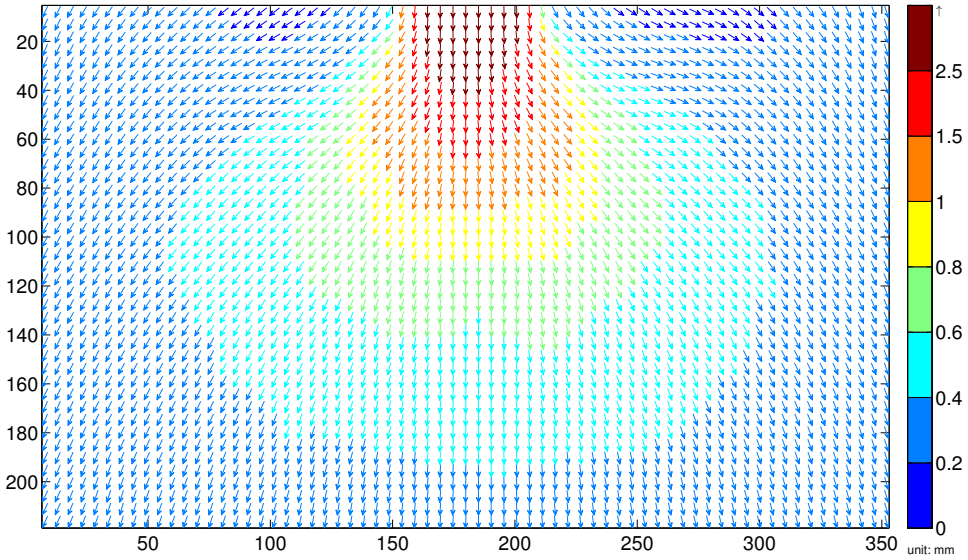

(a) Displacement field

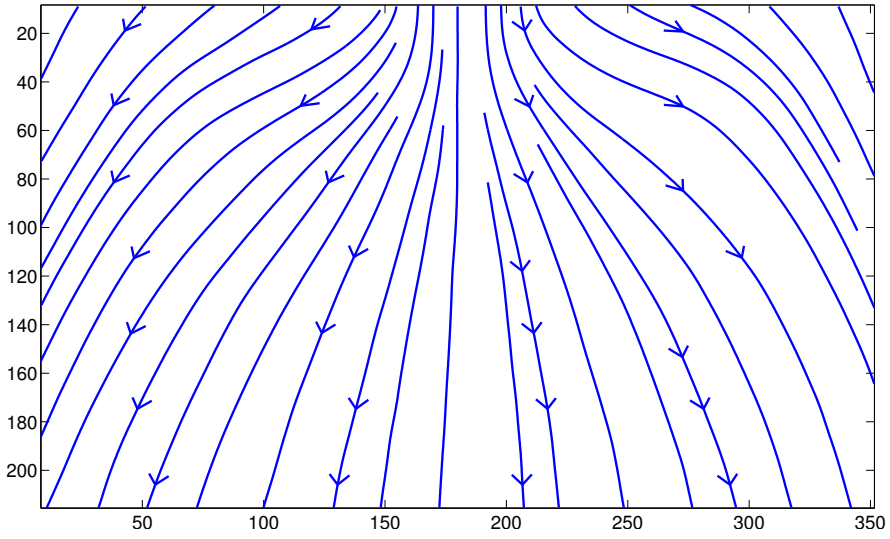

(b) Streamline

Figure 5.54: 50SLUD: hardening

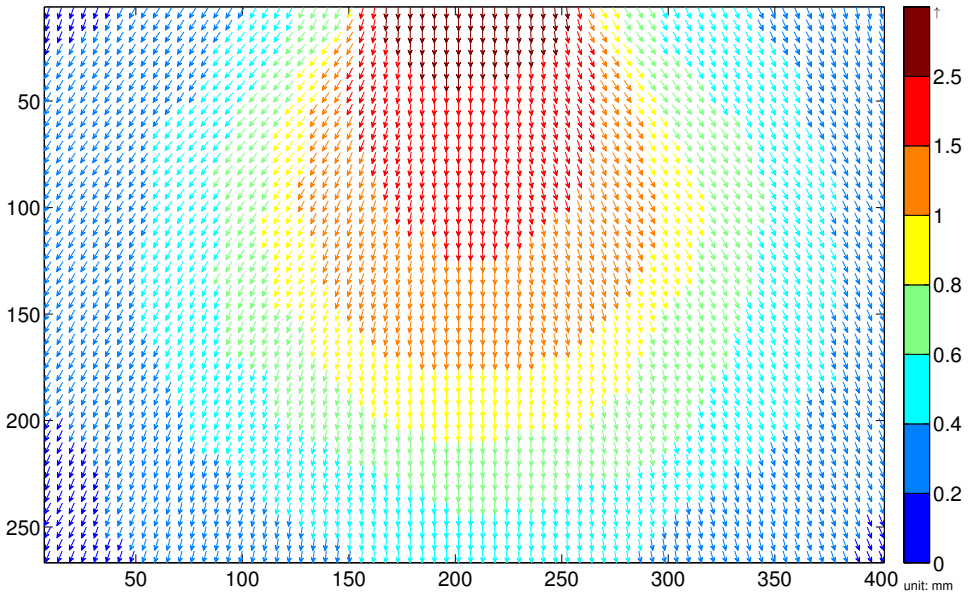

(a) Displacement field

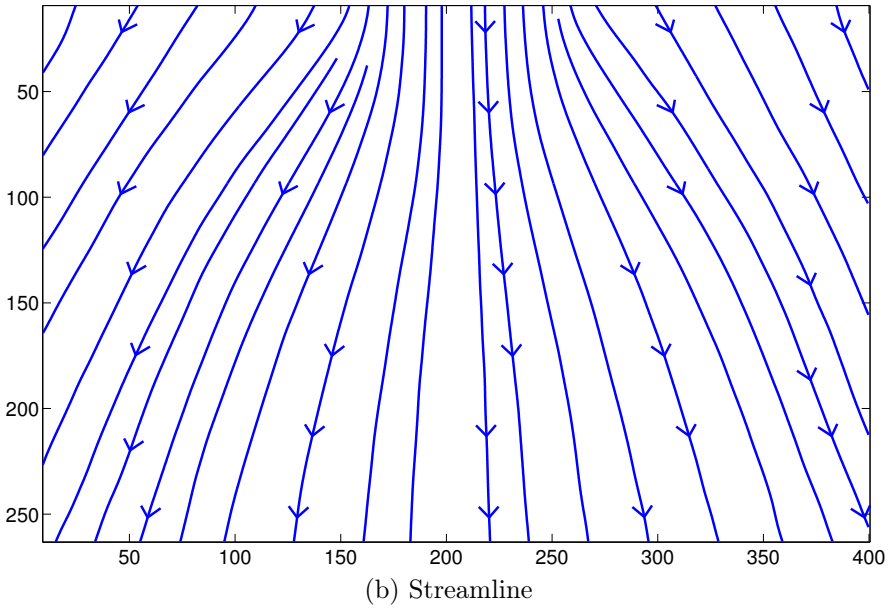

(b) Streamline

Figure 5.55: 100SLUD: initial

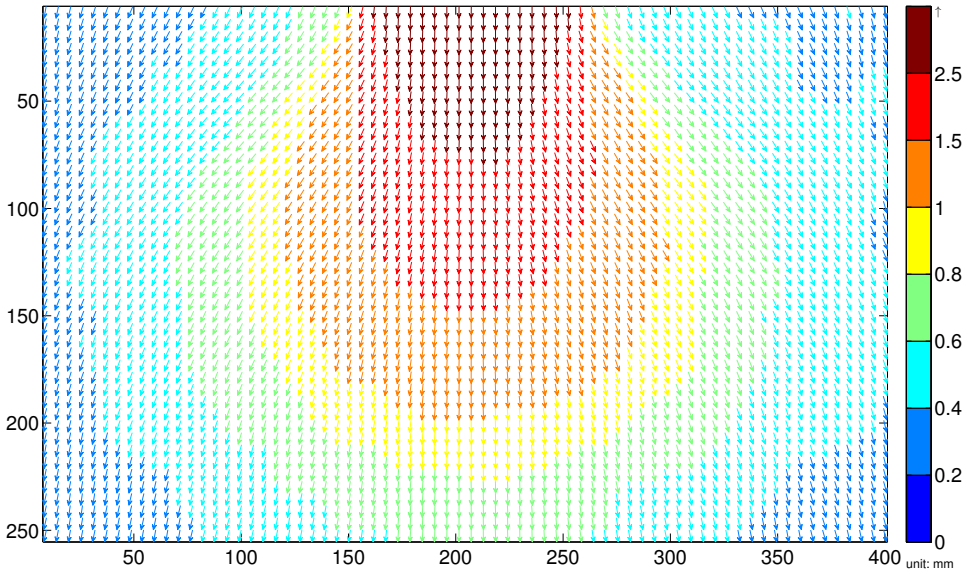

(a) Displacement field

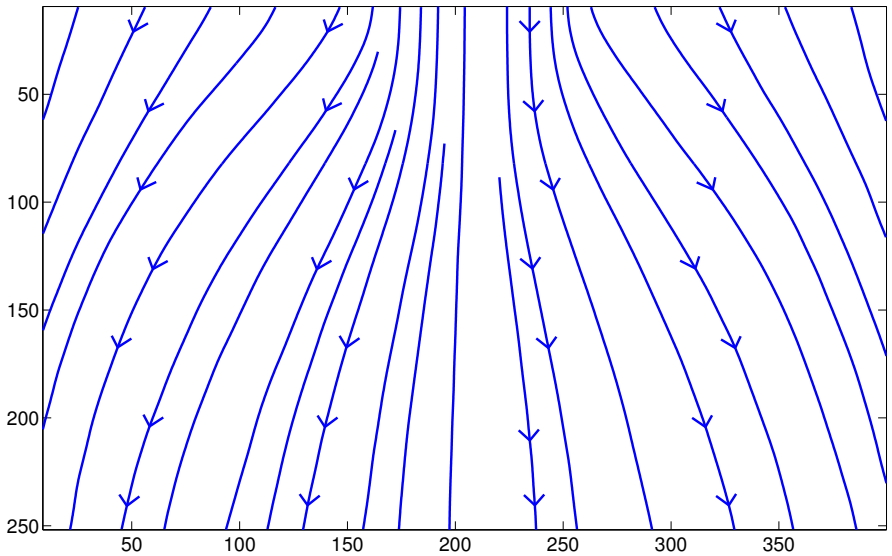

(b) Streamline

Figure 5.56: 100SLUD: transition

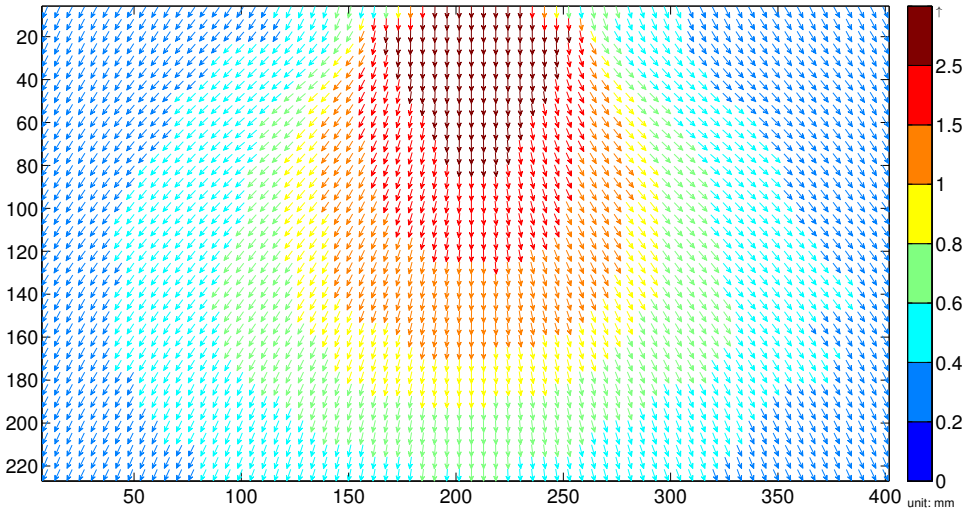

(a) Displacement field

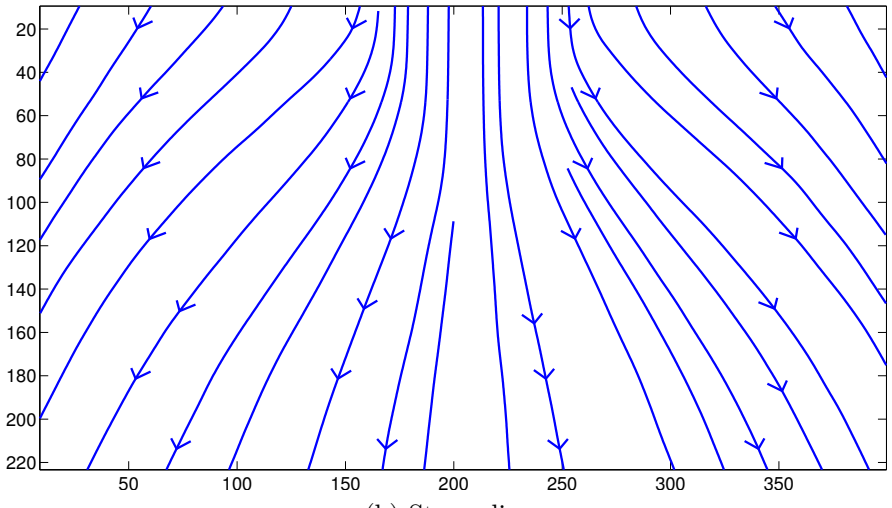

(b) Streamline

Figure 5.57: 100SLUD: hardening

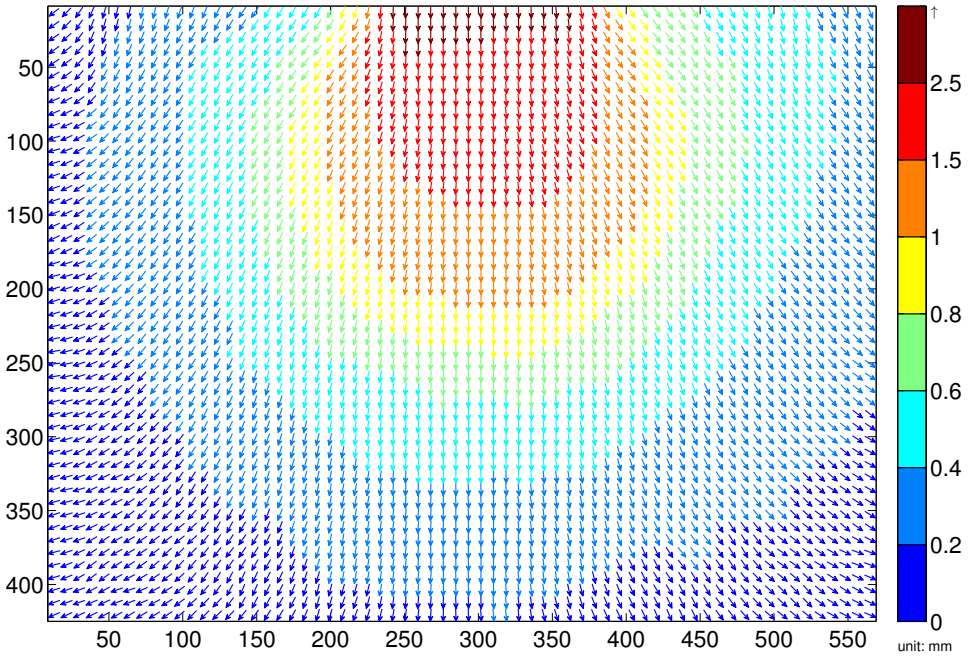

(a) Displacement field

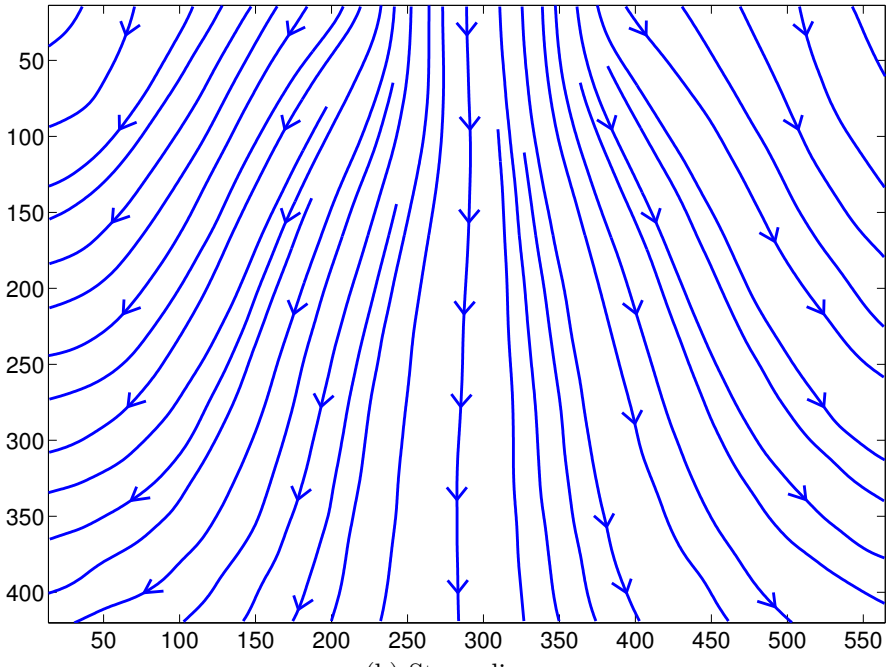

(b) Streamline

Figure 5.58: 150SLUD: initial

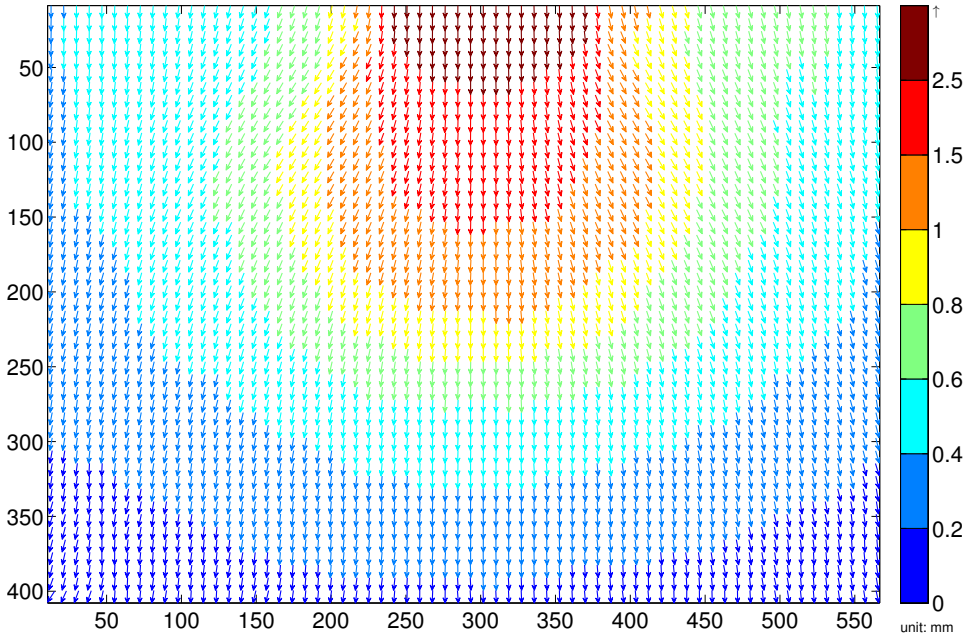

(a) Displacement field

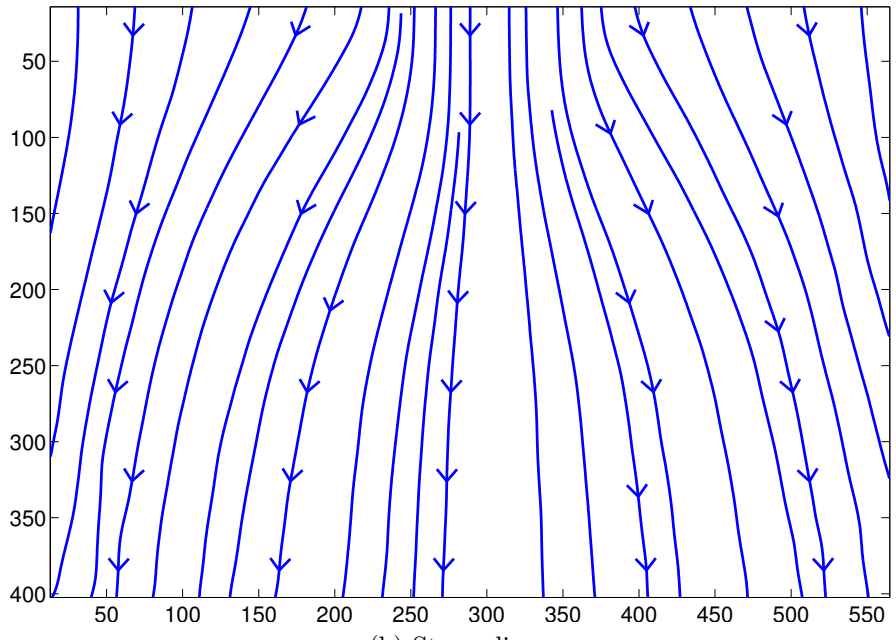

(b) Streamline

Figure 5.59: 150SLUD: transition

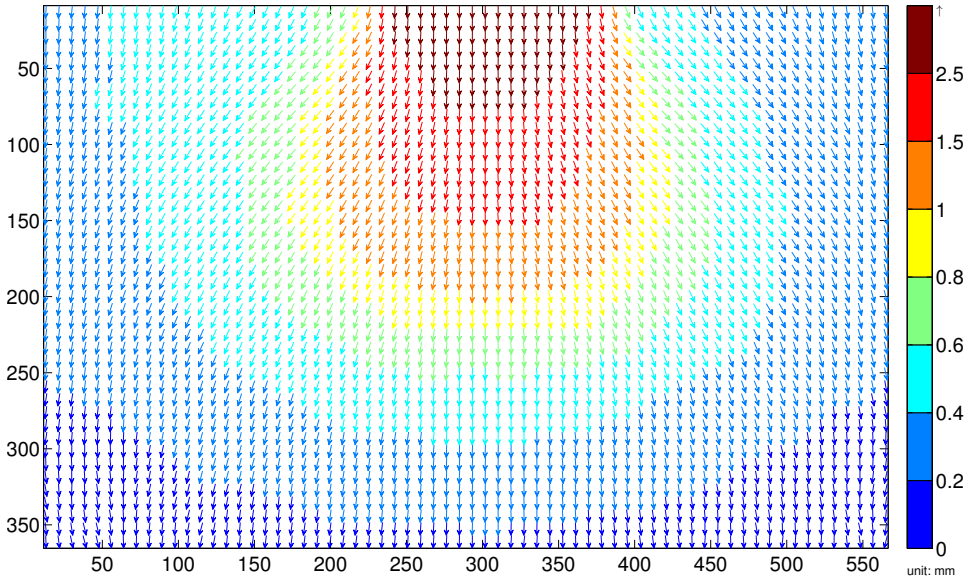

(a) Displacement field

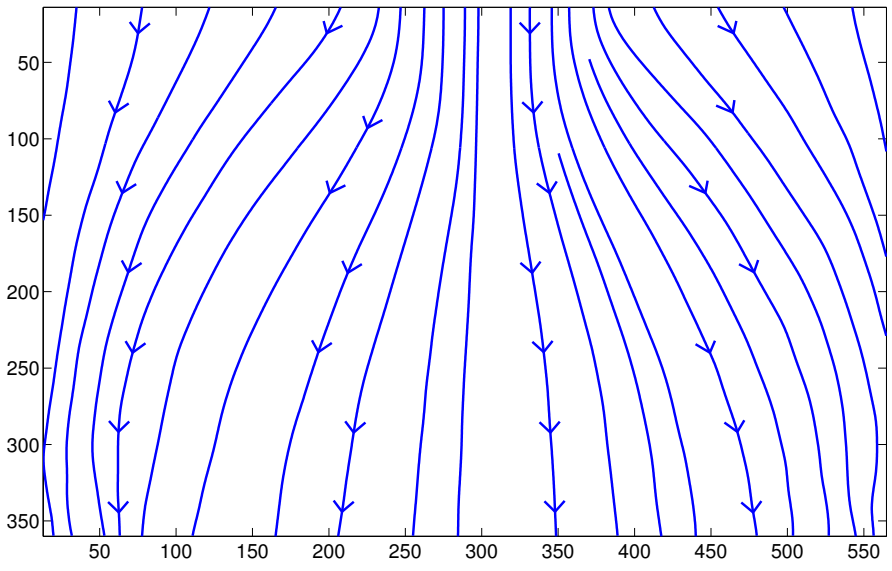

(b) Streamline

Figure 5.60: 150SLUD: hardening

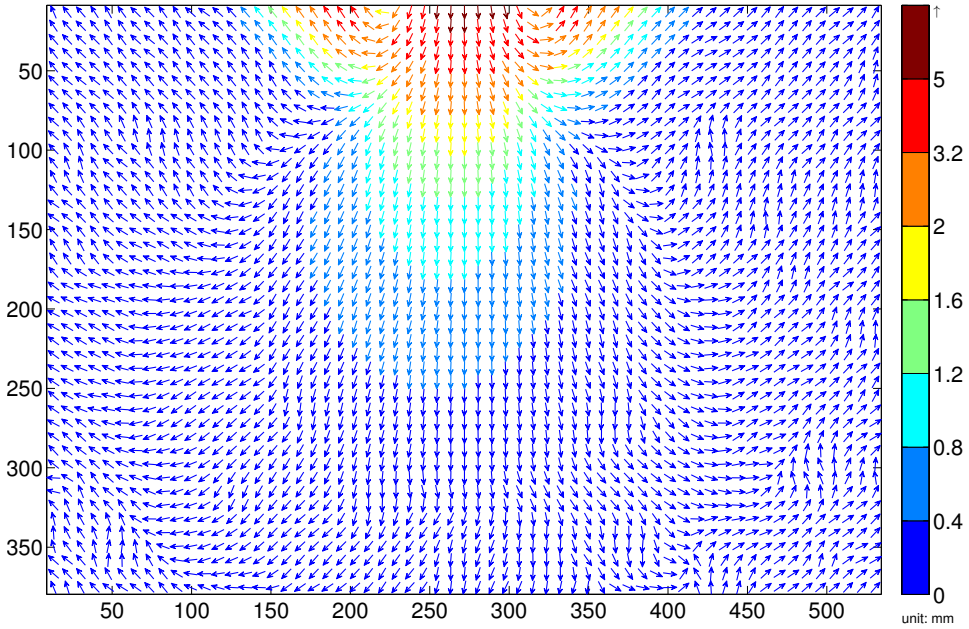

(a) Displacement field

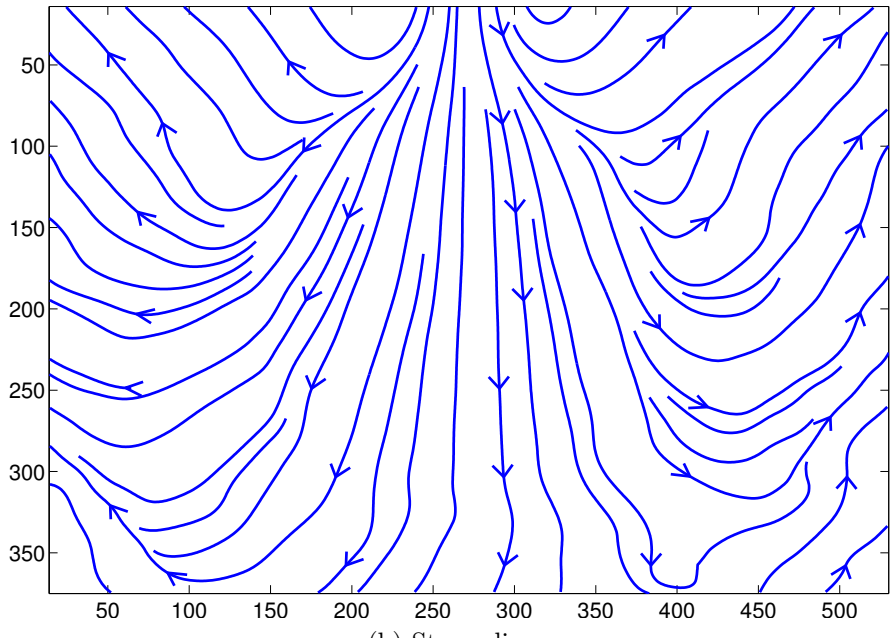

(b) Streamline

Figure 5.61: 100BLDD: initial

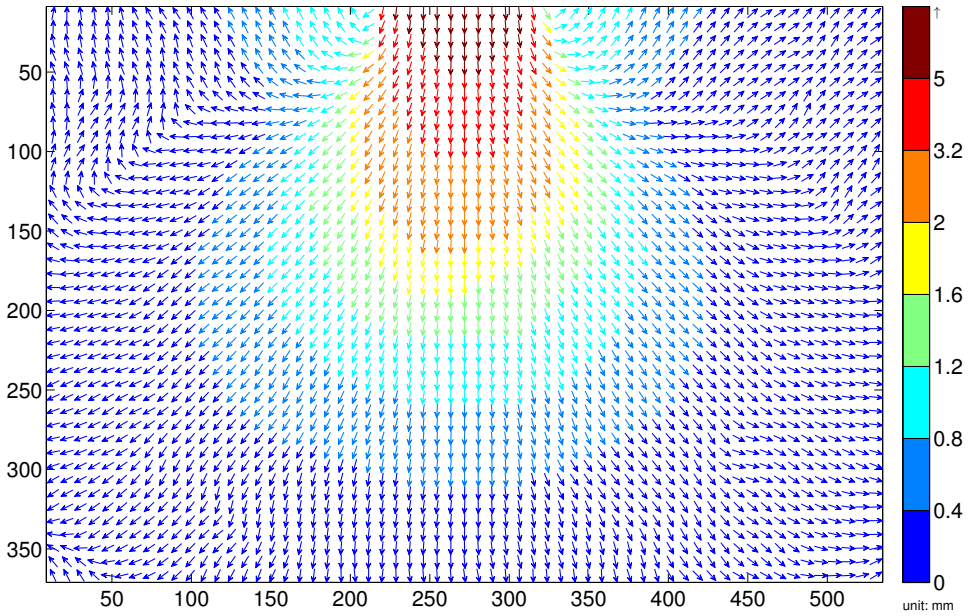

(a) Displacement field

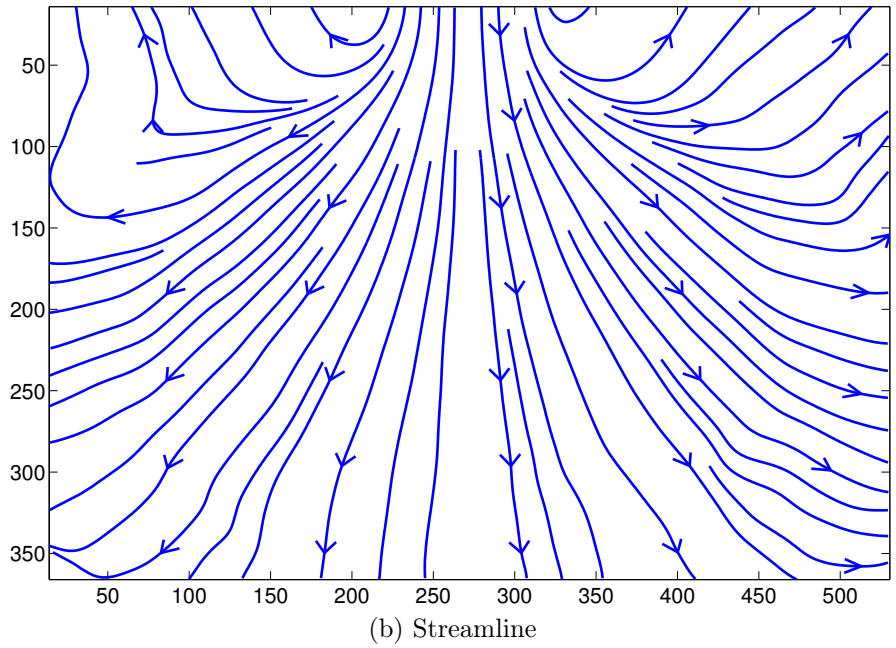

(b) Streamline

Figure 5.62: 100BLDD: transition

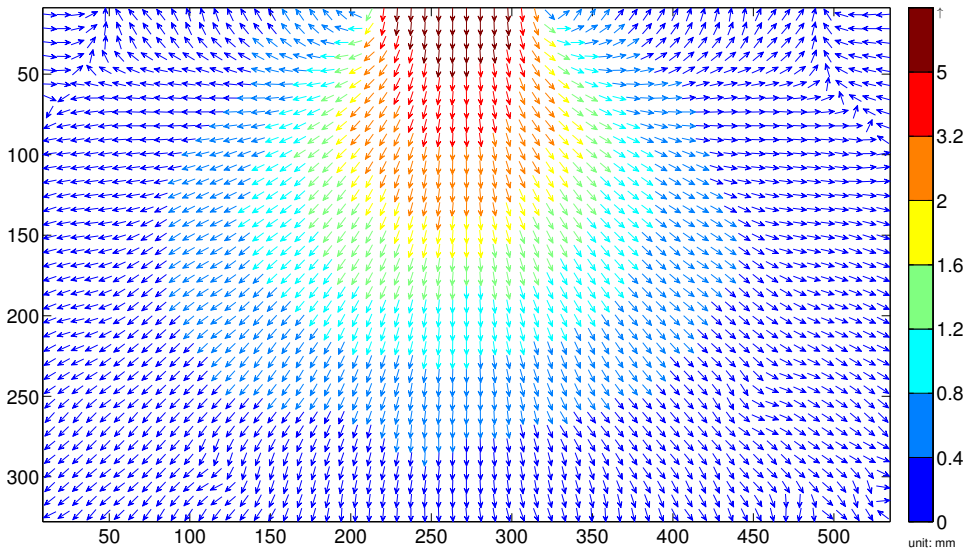

(a) Displacement field

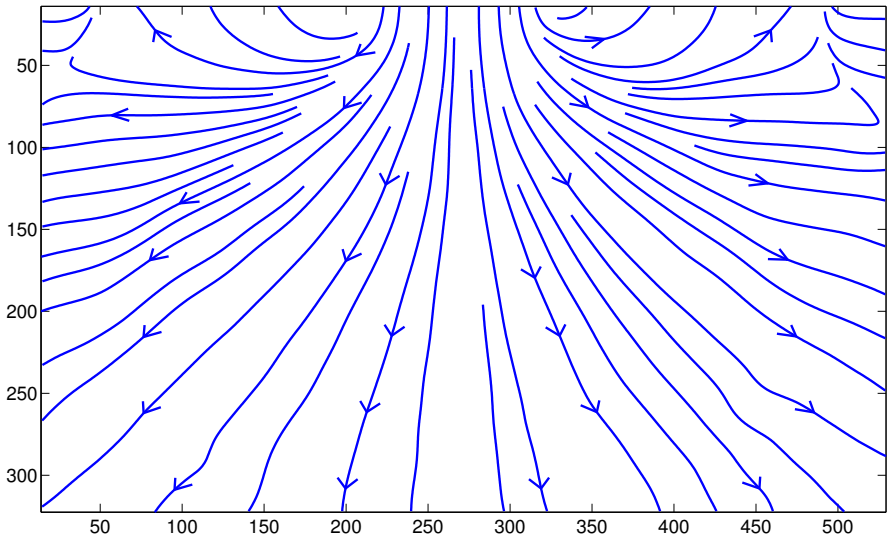

(b) Streamline

Figure 5.63: 100BLDD: hardening

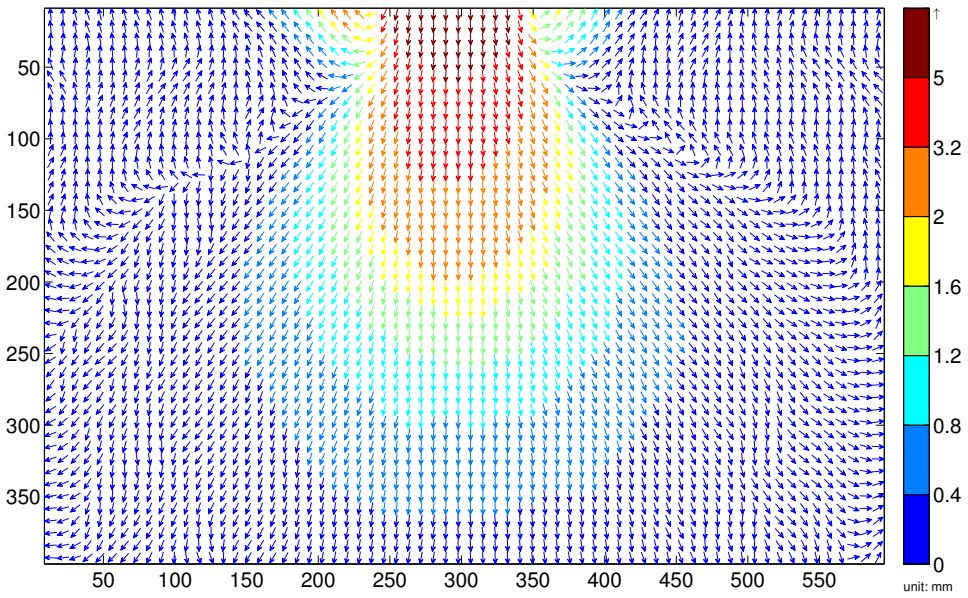

(a) Displacement field

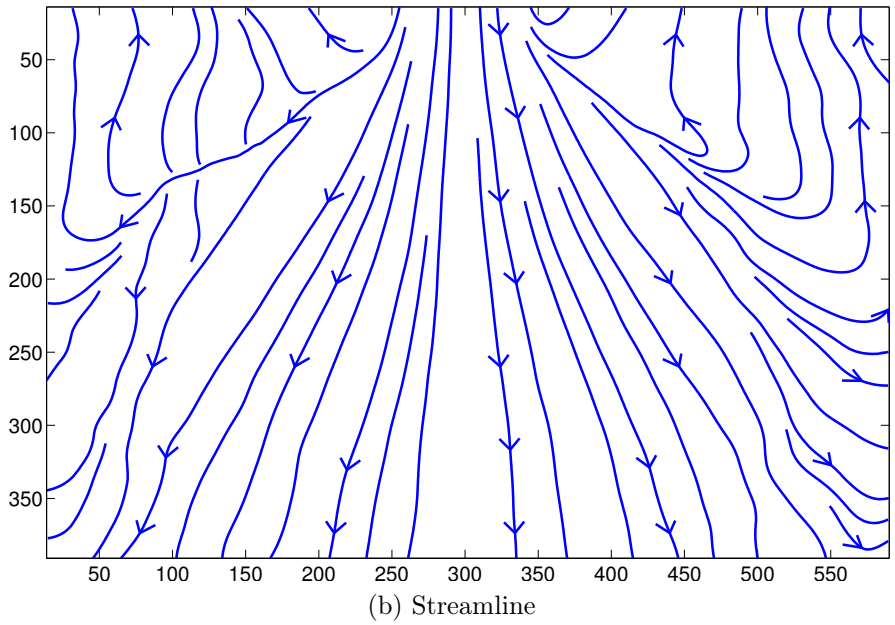

(b) Streamline

Figure 5.64: 100BLUD: initial

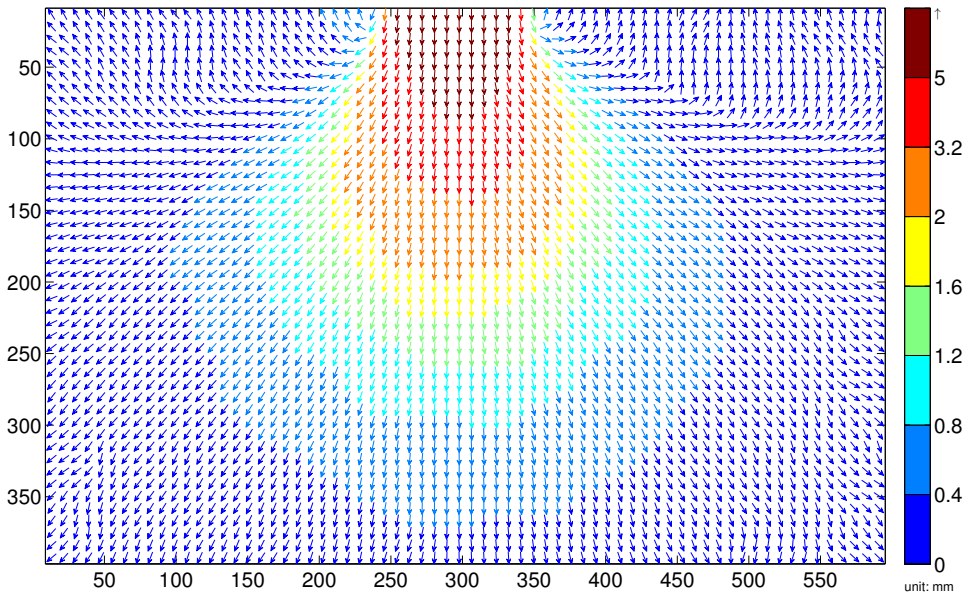

(a) Displacement field

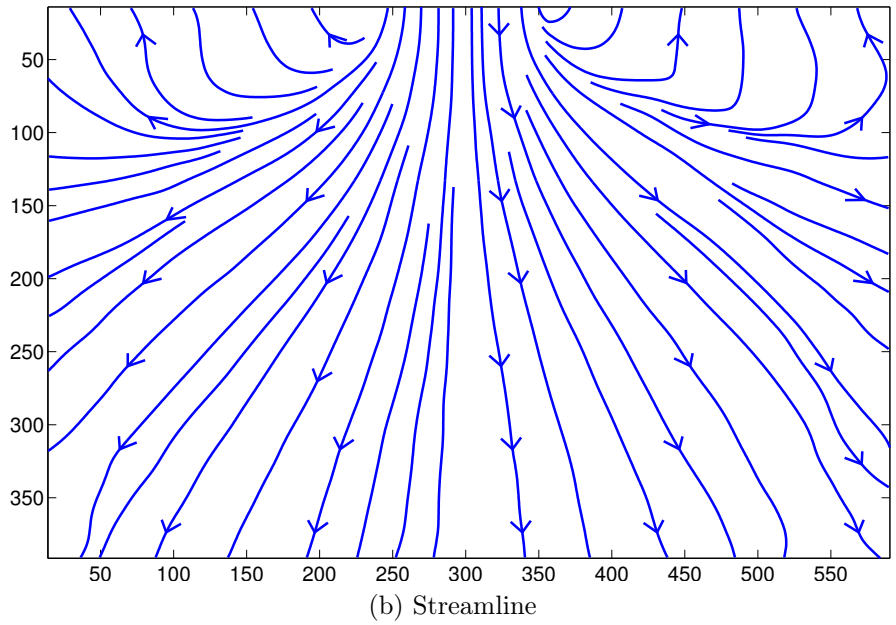

(b) Streamline

Figure 5.65: 100BLUD: transition

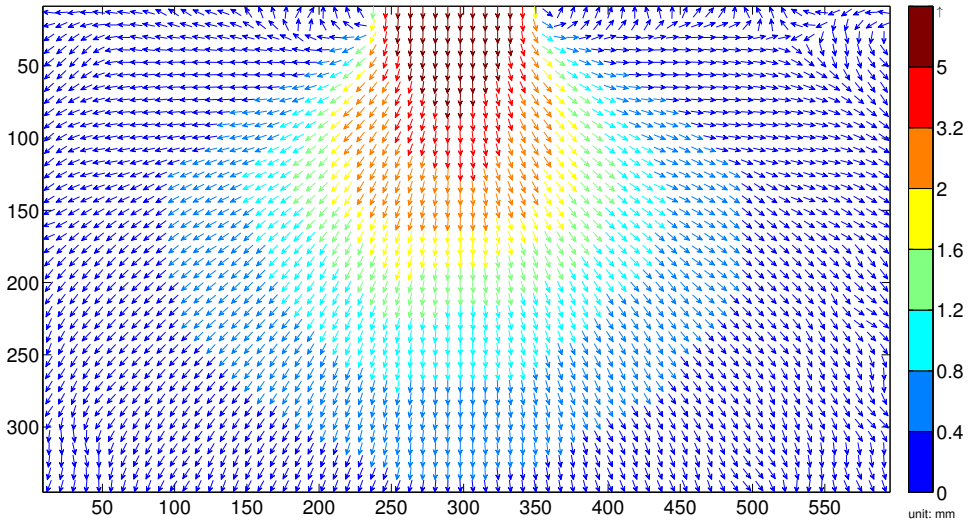

(a) Displacement field

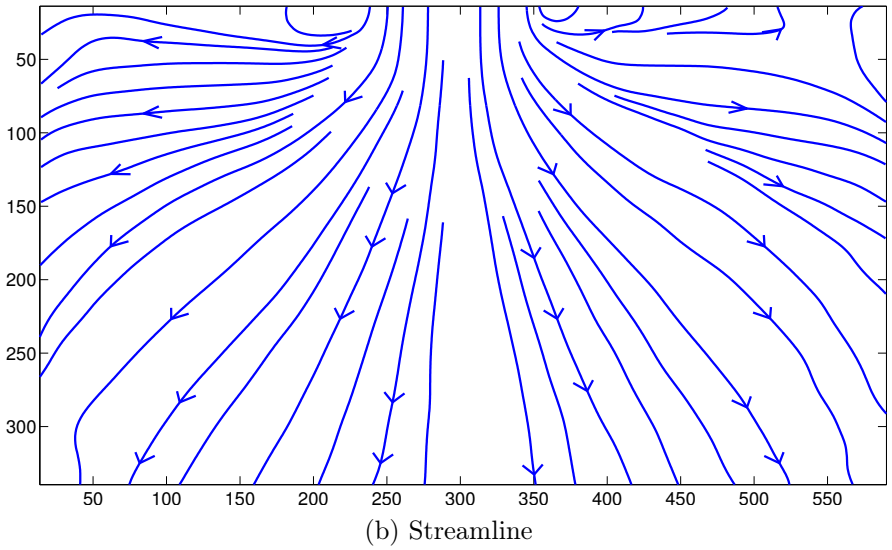

(b) Streamline

Figure 5.66: 100BLUD: hardening

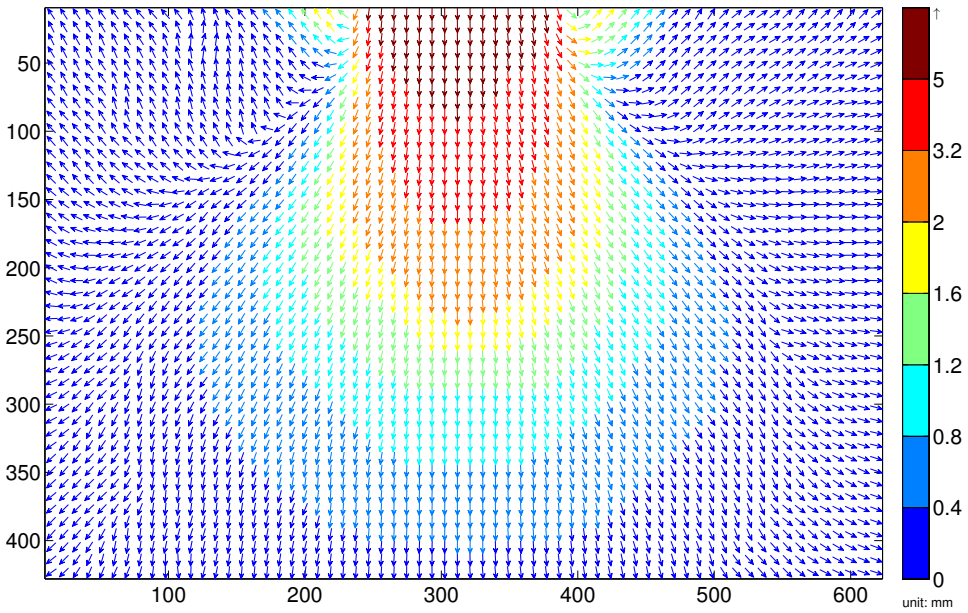

(a) Displacement field

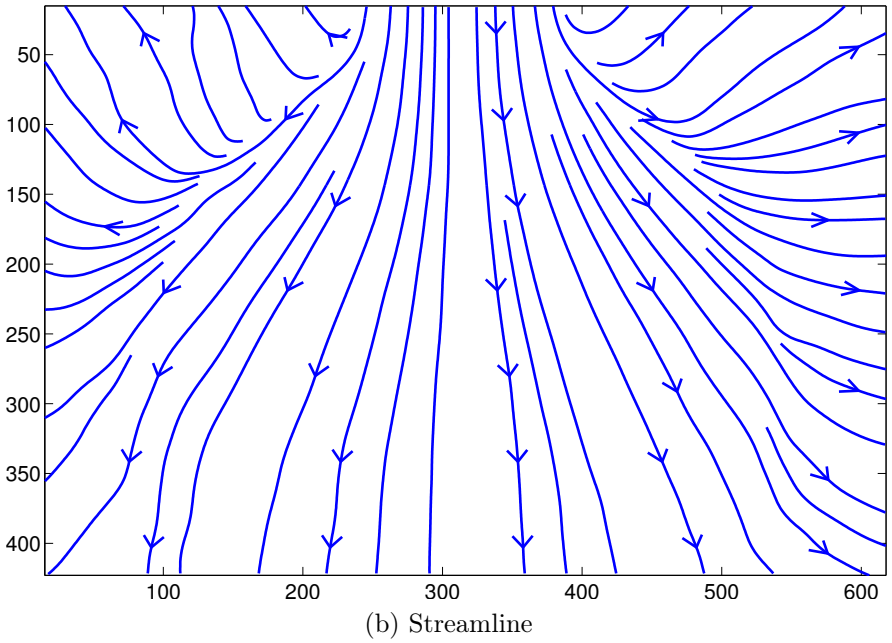

(b) Streamline

Figure 5.67: 150BLUD: initial

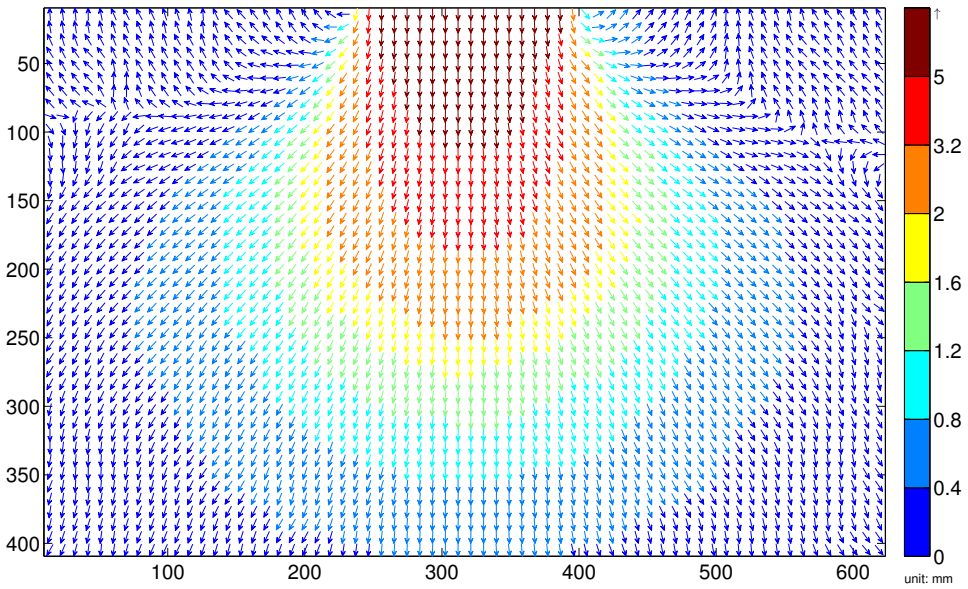

(a) Displacement field

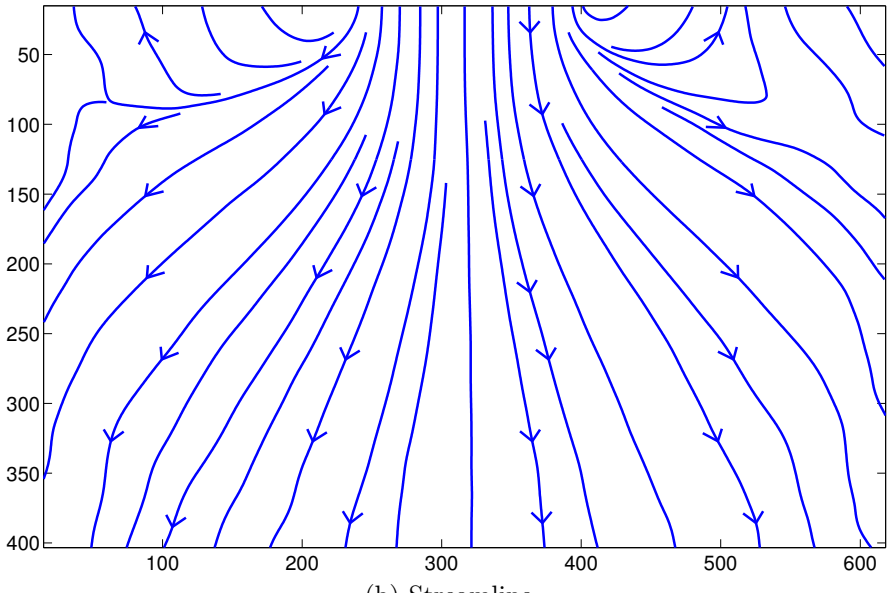

(b) Streamline

Figure 5.68: 150BLUD: transition

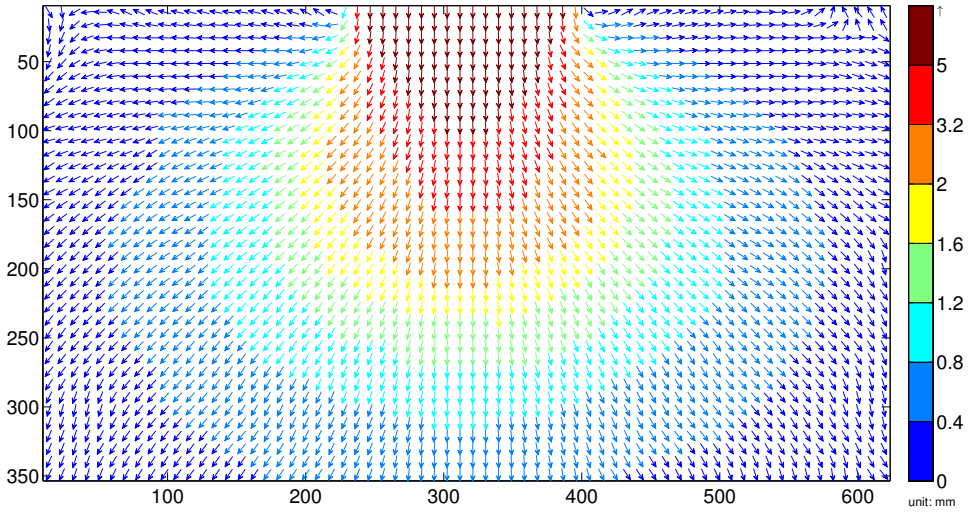

(a) Displacement field

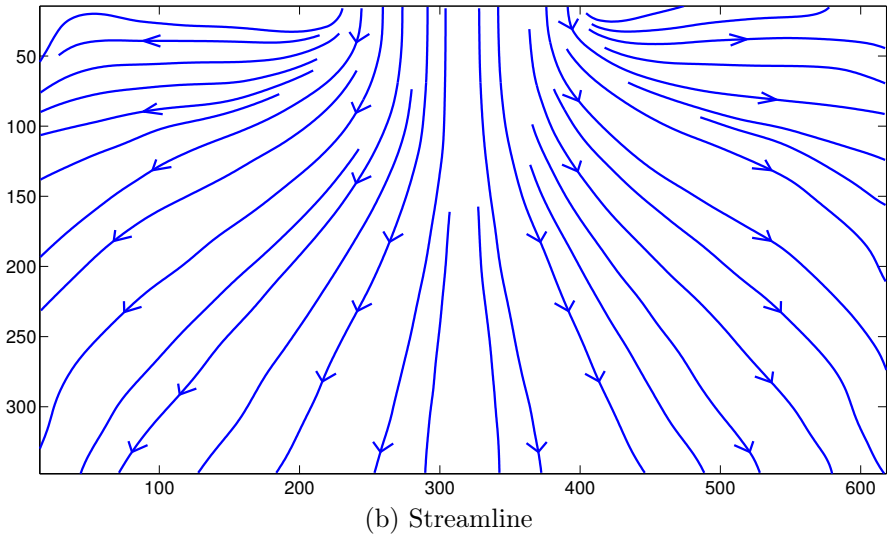

(b) Streamline

Figure 5.69: 150BLUD: hardening

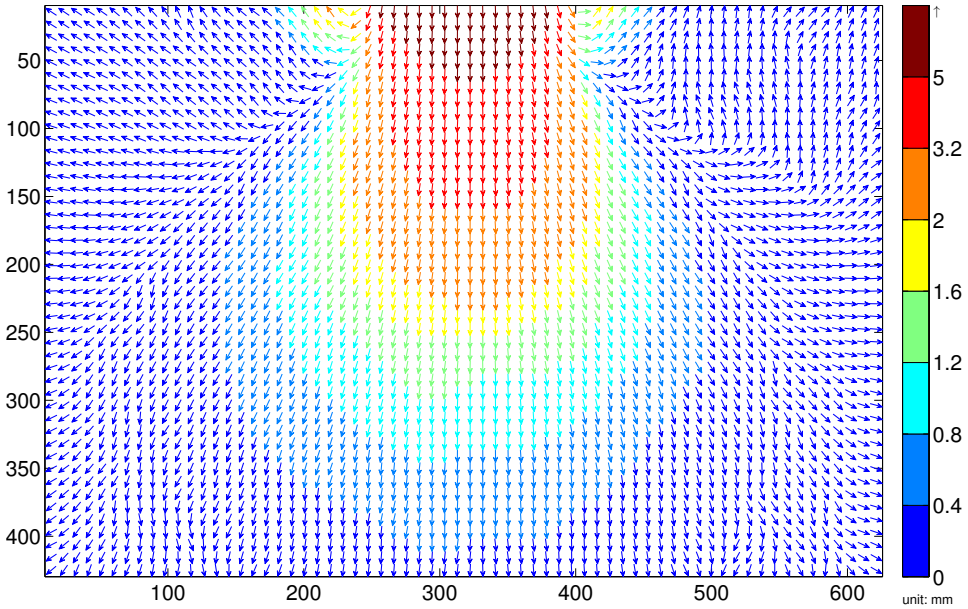

(a) Displacement field

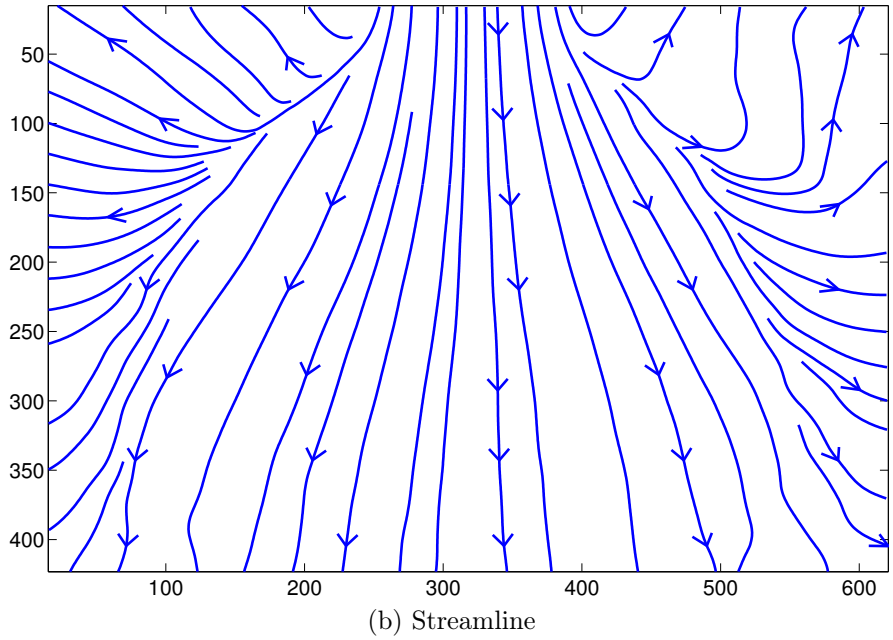

(b) Streamline

Figure 5.70: 150BCUD: initial

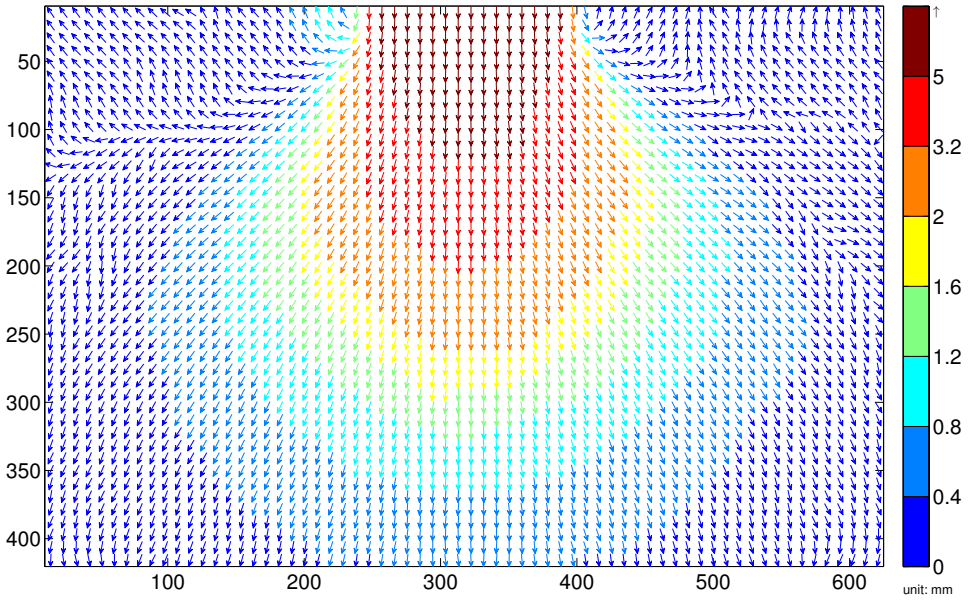

(a) Displacement field

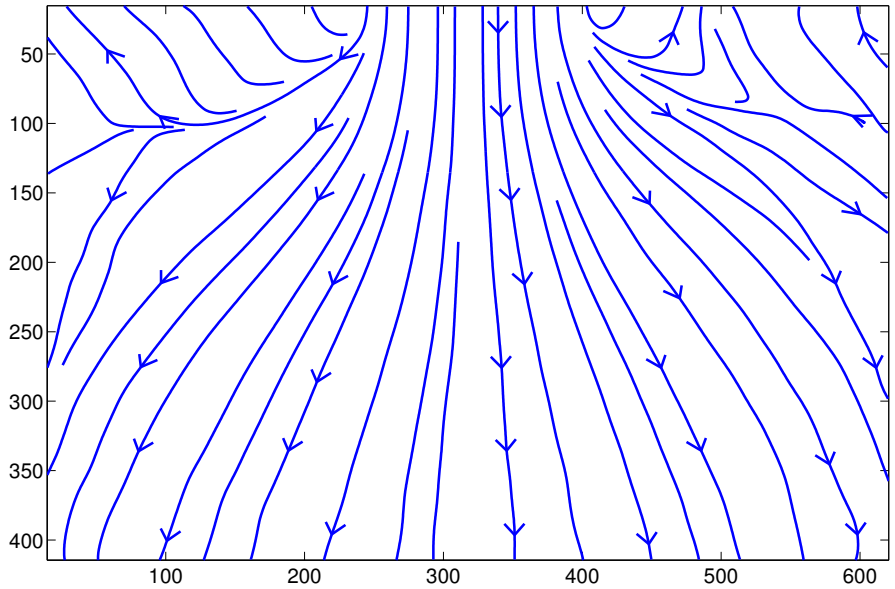

(b) Streamline

Figure 5.71: 150BCUD: transition

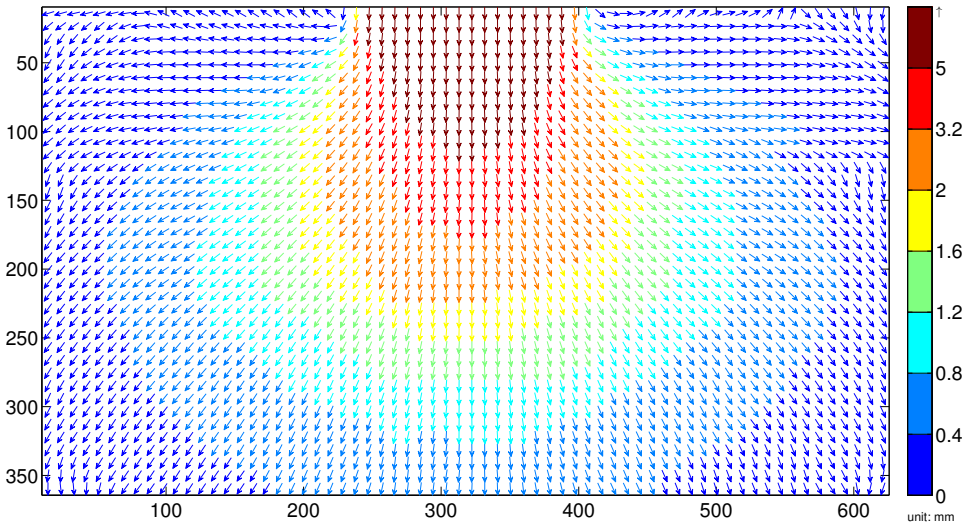

(a) Displacement field

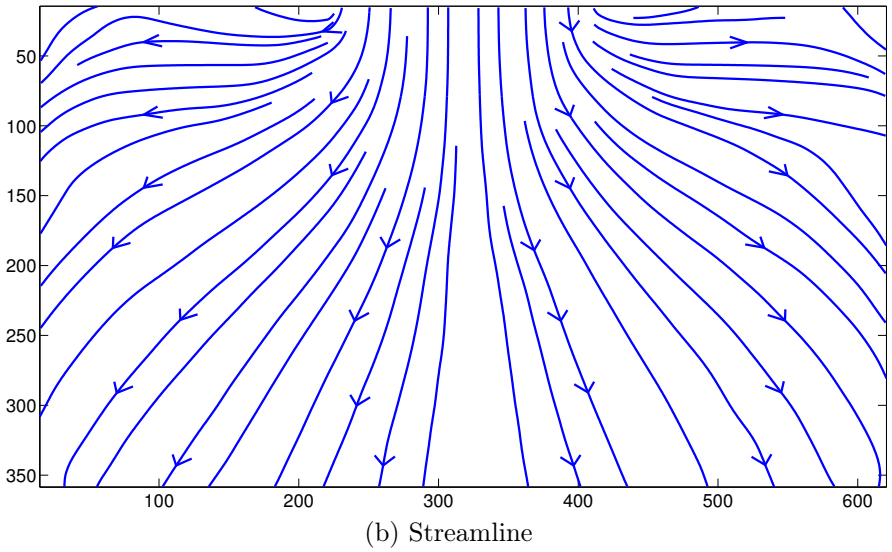

(b) Streamline

Figure 5.72: 150BCUD: hardening

Comparing the displacement fields from 50SCUD (Figure 5.51) and 50SLUD (Figure 5.54), the influential zone (defined as magnitude greater than $0.4mm$ and coloured in light blue) was larger in the sample prepared by layered filling. As more sand particles were mobilised, it allowed the shear plane to propagate outwards which eventually provided a higher footing resistance as observed in the earlier loading-displacement curves (Figure 5.38). The footing size effect can be clearly observed from the displacement fields of 50/100/150SLUD. As the footing breadth gets larger, the primary deformation zone immediately beneath the footing base becomes wider accordingly from $50mm$ to $150mm$. In each case reported, there was a cone-shaped active zone (coloured in dark red) with maximum pure vertical displacement below the footing base, where high stress concentration and volumetric compression were encountered. The size and shape of this active zone can be well compared with the experimental work of White and Bolton (2004), where a flat pile was driven into Leighton Buzzard sands (Figure 5.73). Noticeably, outside this zone the displacement paths changed and the particles tended to move downwards and sidewards symmetrically underneath either side of the footing. However, upon further penetration the flow path did not rise back near the surface as predicted in typical bearing capacity mechanism, but continued to flow downwards instead.

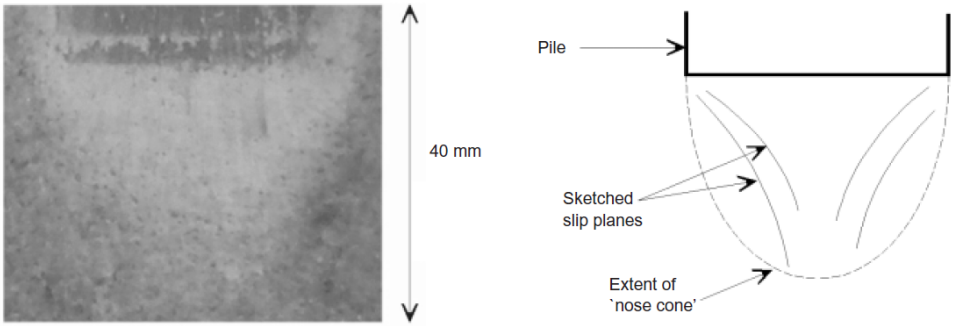

Figure 5.73: High resolution photograph of the pile tip (White and Bolton, 2004)

Observing the PIV results throughout the three loading stages in Leighton Buzzard sand, both the streamline progression and the displacement arrows pointed primarily downwards, indicating that particles even those not directly beneath the footing were undergoing vertical movement. In general, a granular assembly subject to footing penetration will exhibit downward vertical displacement under the footing base, whereas particles immediately adjacent to the footing will experience horizontal displacements and perhaps upward vertical displacements in the form of heaving, while particles at a certain distance away at ground level will be less affected and experience rather limited movement. However, in the current sand tests, particles that lie well away from the footing edge and meanwhile at the top surface were clearly moving downwards although no vertical load was being applied at that location. This behaviour is likely to be caused by the out-of-plane deflection (bulging) of the slice model, which allowed the small sand particles to pass through the newly formed volume. Figure 5.74 illustrates this phenomenon by showing the sample surface level dropped with increasing footing settlement. Although the slice model has been carefully clamped at several positions, the combined forces generated from the self weight of sands and the loading stresses have caused small deflections on the Perspex sidewalls, thus violating the initial assumption of plane strain deformation. The effect was exaggerated in the $150mm$ footing test, where larger reaction forces led to a more pronounced out-of-plane deflection, which eventually produced the primarily downward flow pattern as reflected in PIV.

Figure 5.74: Decrease of sand surface during footing test

For the barley samples, the particle movement evaluated from PIV is entirely different from that of the sand. In addition to the well defined active zone where the displacements were pure vertically downward, there was a distinct exhibition of the passive zone in the barley sample. A portion of particles adjacent to the footing edge heaved up towards the sample surface at early loading stages, however the particles mostly underwent sideway movements at deeper penetrations due to the higher confining pressures. Comparing the results between BLDD and BLUD, the shapes of the primary deformation zone were completely different. In the general loose sample (Figure 5.64), the most excessive particle (red arrows) displacements largely happened below the footing, with only a small portion took place next to the footing edge. On the other hand, as shown in the densely packed sample (Figure 5.61), the significant particle displacement mainly spread in lateral direction and did not propagate much deeper into the granular mass. Also, a much higher heaving rate is observed in the densified BLDD sample in terms of the streamline progression, which suggests that the internal friction angle varies notably with the stress state and the packing density. Increasing the footing size (100/150BLUD) has minimal influence on the deformation pattern, where the only noticeable effect is the increase of the area of primary deformation zone. Concerning the effort of the filling method, the difference between BLUD (Figure 5.67) and BCUD (Figure 5.70) is not immediately apparent. Upon closer inspection, only in the hardening the concentrically filled sample produced a slightly larger active zone (Figure 5.72), despite the fact that the ultimate bearing capacity in BCUD sample is 22% higher than BLUD as reported earlier in Figure 5.46. The reason that the differences in the bearing capacity of barley samples cannot be reflected through the displacement field determined from PIV correlation may be attributed to the multi-scale nature of granular media (micro-, meso- and macro-scale). Recalling the size of the interrogation window (D_w) is approximately $16\times16mm$, while the mean particle diameter (D_{50}) of barley is $5.1mm$.

The dimension ratio of D_w/D_{50} (≈ 3) is able to capture the particle motion within such a subregion, as illustrated by the smooth contour lines in the displacement field. However, the bearing capacity in the bulk sample is closely related to the variation in both packing density and internal friction angle, whose influence can only be characterised over a representitive avaeraging area where the particulate nature is not prominent. It thus suggests that meso-scale investigation of collective behaviour in granular solids should be approached at a sufficiently large length scale. Another interesting finding is that the primary deformation zone can be covered by a dimension of $4B \times 4B$, and outside this area the particle movement was rather limit. This information provides an important guidance for the dimension choice in future DEM footing simulation using a reduced-scale model.

Based on experimental observations of the mechanical behaviour of shallow foundations, it has been well accepted that bearing capacity failure mostly occurs in the form of shear failure. Three types of failure modes have been identified during the installation of shallow foundation, with the profiles shown in Figure 5.75.

- General failure occurs in soils that are relatively incompressible and reasonably strong. As load increases, the failure surface initiates around the edges of the footing, then gradually extend downwards and outwards. A clearly formed bulge appears on the ground surface around the foundation. This is the most common mode of failure.

- Local shear occurs in sands of moderate density with relatively large settlements. The development of failure surface starts from the edges of the footing but end within the soil mass, i.e. becomes vague near the ground surface.

- Punching shear occurs in very loose sands, or weak soils and clays. The

high compressibility of these soil profiles cause large settlements with shear failure directly under the edges of footing, where the failure surface cannot further propagate.

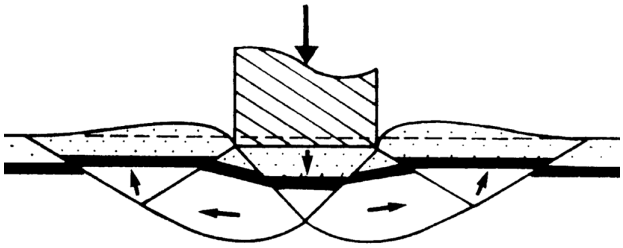

(a) General failure

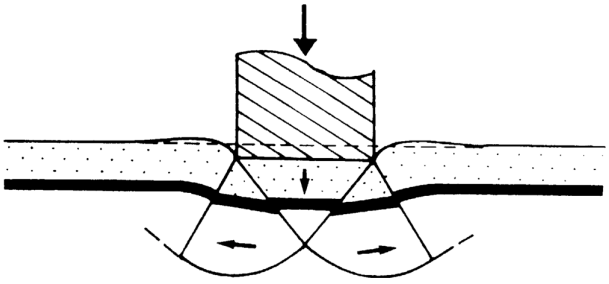

(b) Local shear

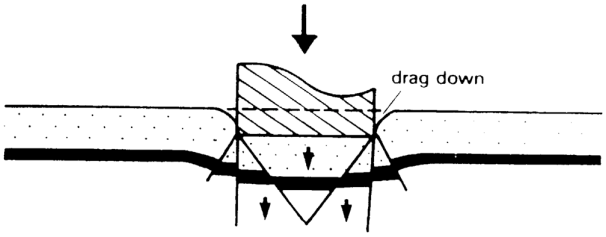

(c) Punching shear

Figure 5.75: Three modes of bearing capacity failures (Handy and Spangler, 2007)

In general, the compressibility of the soil plays an important role in the mode of failure. According to the observation of the displacement fields as shown in this section, the most densely packed barley sample (BLDD) exhibited a distinct

general shear failure, where a continuous rupture surfaces developed from below the footing to the ground surface. However, the failure modes in the rest samples were less well defined, which can be further investigated based on some improvements of testing facilities.

5.5.3.2 Velocity profile

The displacement fields have provided much insight into the the full deformation pattern. Here, analysis focuses on the local interaction between particles and footing base was performed by examining the velocity profile (horizontal v_x and vertical v_y components) in the first horizontal layer of the interrogation windows that immediately beneath the footing base.

Figure 5.76 and 5.77 compare the local velocity fields of 50/150SLUD. For vertical velocity, the particles directly beneath the footing moved predominantly vertically at a similar rate to the the footing penetration rate ($0.33mm$/second), which provides the evidence of satisfactory accuracy in the current PIV evaluation. The width of each plateau can be directly related to the footing breadth, where the sudden drop of vertical displacement occurred near the edges of the footing, suggesting the particles adjacent to either side of the footing were not influenced much by the indentation and experiencing considerably less vertical movement. In terms of the horizontal velocity, there was a neutral point right beneath the centre of the footing base with zero horizontal movement due to the symmetry constraint, from where the value increased to its maximum at the location of $0.5B$, and then followed by a gradual decrease to zero velocity near the edge of the planar chamber.

For barley, velocity profiles were presented for three packing structures with the $100mm$ footing, namely BLDD (Figure 5.78), BLUD (Figure 5.79) and BCUD (Figure 5.80). For all these cases, the profiles of vertical velocity during initial

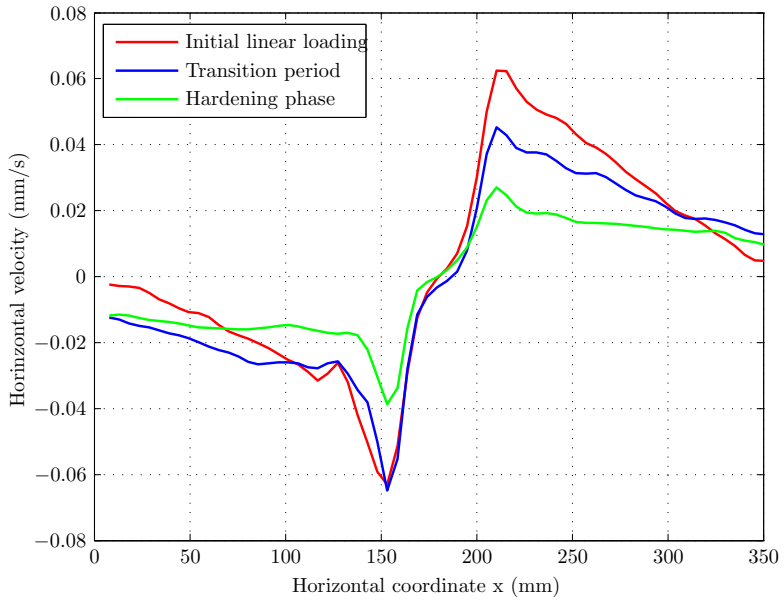

(a) v_x

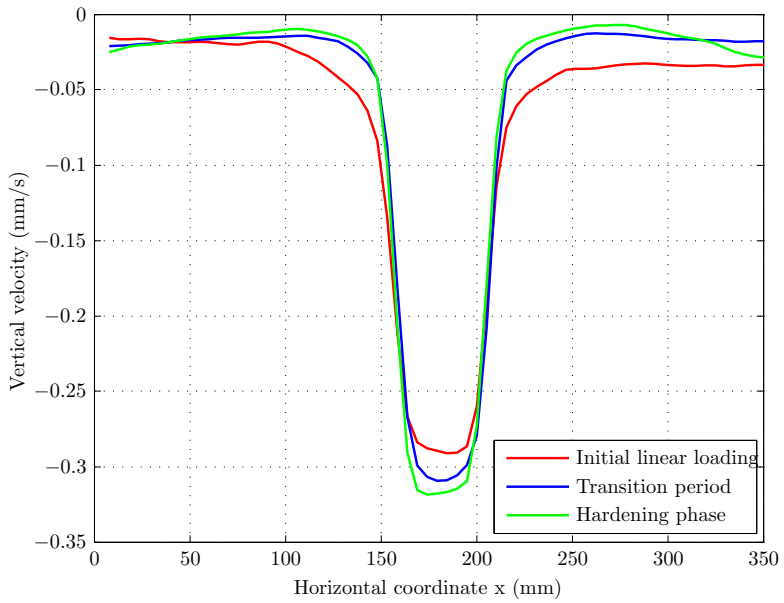

(b) v_y

Figure 5.76: Velocity field immediately below the footing: 50SLUD

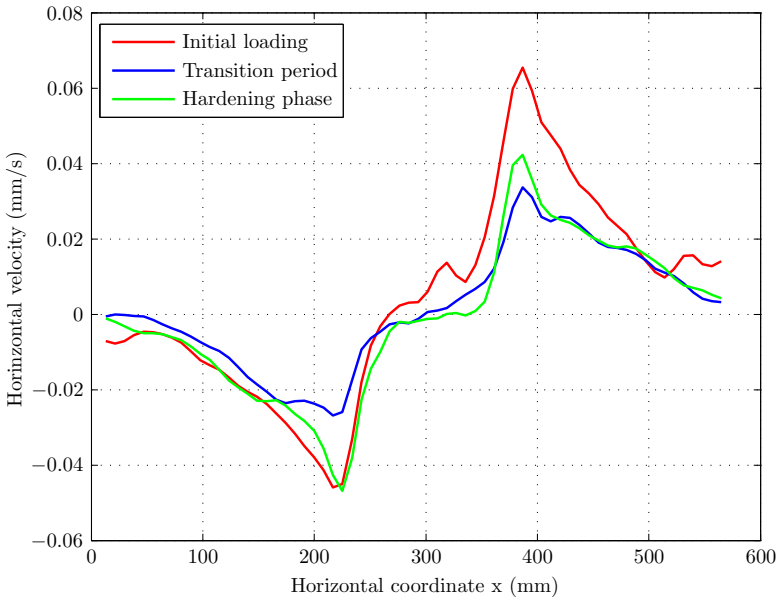

(a) v_x

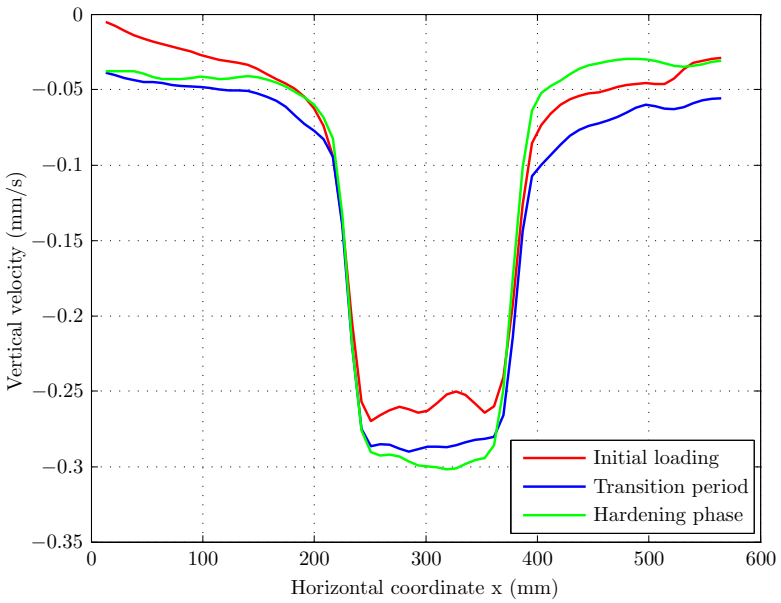

(b) v_y

Figure 5.77: Velocity field immediately below the footing: 150SLUD

penetration show that particle flow extended upwards to the surface leading to the heaving adjacent to the edges of the footing. The densely packed sample (BLDD) displays larger particle movements in both vertical and horizontal direction, compared to the loose concentric (BCUD) and layered sample (BLUD). This behaviour can be explained as that particles in a more densely packed specimen are more interlocked, thus the induced perturbation can cause significant particle rearrangements in terms of translation and rotation. Consequently, the degree of particle interlocking becomes less prominent in general loose samples due to the large interstitial voids.

5.5.3.3 Shear strain

Here, shear strain is investigated to understand the kinematic mechanism associated with the shear failure during loading. As the footing moved into the granular mass, significant shear resistance developed at the footing edges and consequently the shear strain became concentrated at that location. Figure 5.81 shows the shear strain at different loading stages for 50SCUD. The three contours presented are quite similar to each other, in which a pair of vertical stripes of shear strain concentration are observed. The shear strain was most localised at the corner of the footing at initial loading stage, and thereafter developed downwards along the interface between the footing edges and particles.

Figure 5.82 compares the strain profiles in the SLUD tests with three footing sizes at transition point. In the three plots, the vertical lengths of strain concentration zone (with magnitude above 3%) are quite similar, around $90mm$ irrespective of the footing size. However, the zones of the most localised strain (larger than 7%) are quite different, in which the smallest footing gave rise to the most intense concentration of shear strain. This can be explained as that with the same packing density and penetration depth, the smaller footing experi-

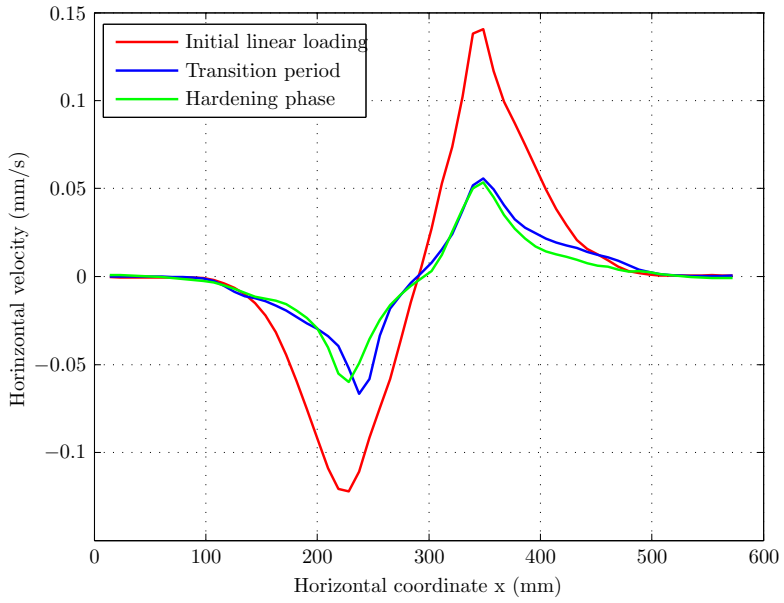

(a) v_x

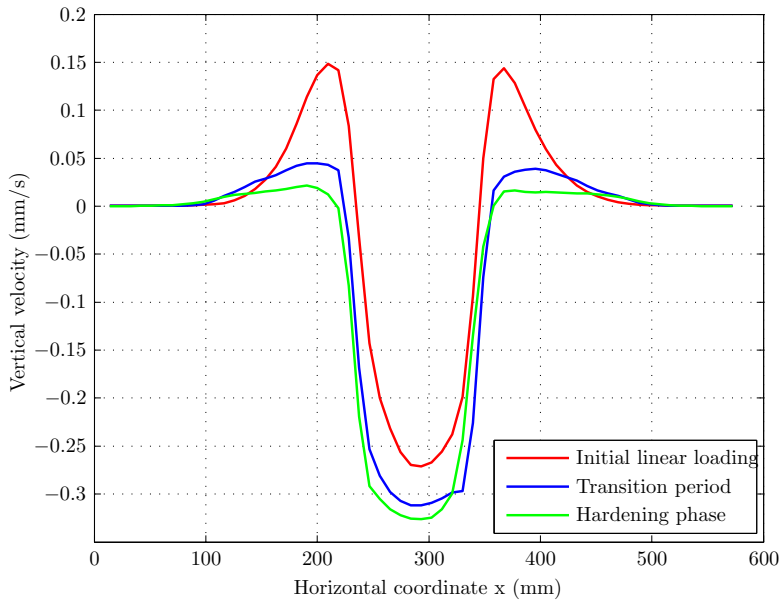

(b) v_y

Figure 5.78: Velocity field immediately below the footing: 100BLDD

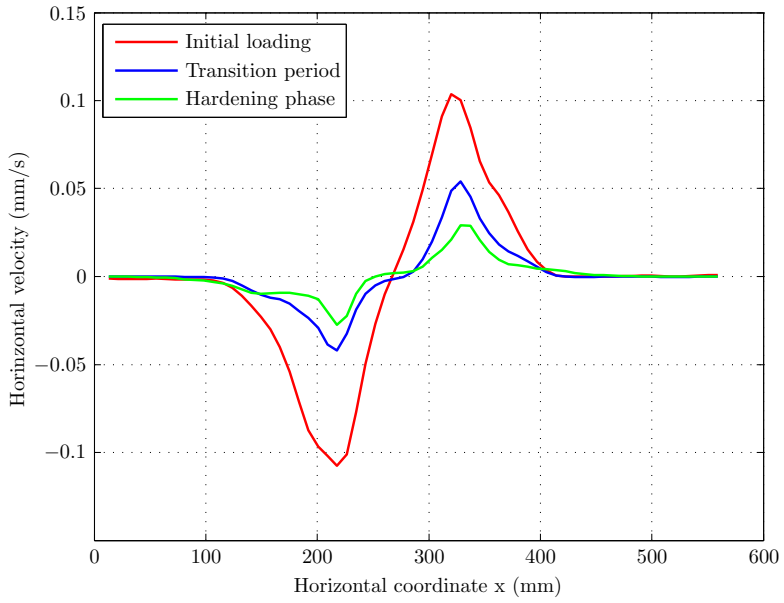

(a) v_x

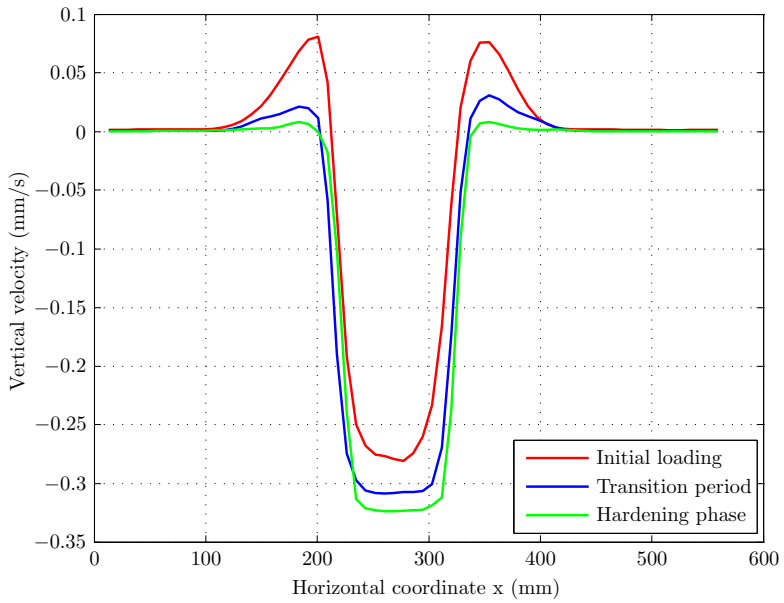

(b) v_y

Figure 5.79: Velocity field immediately below the footing: 100BLUD

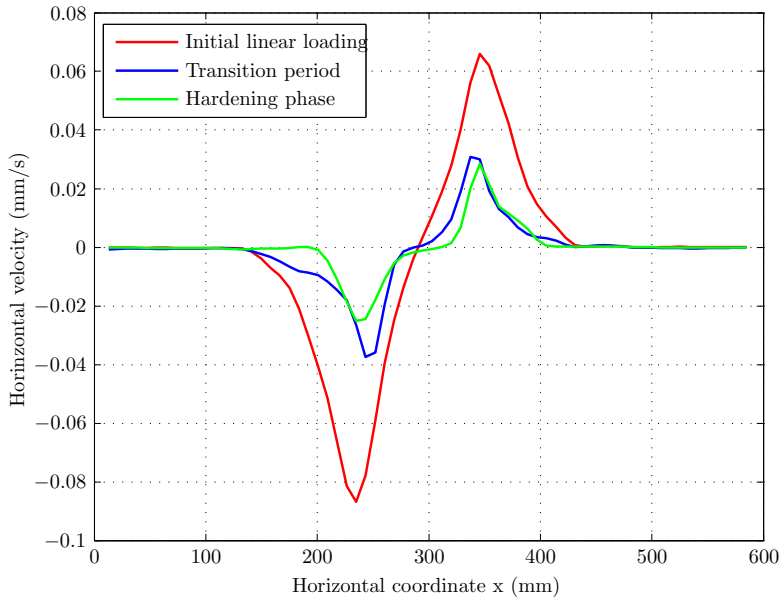

(a) v_x

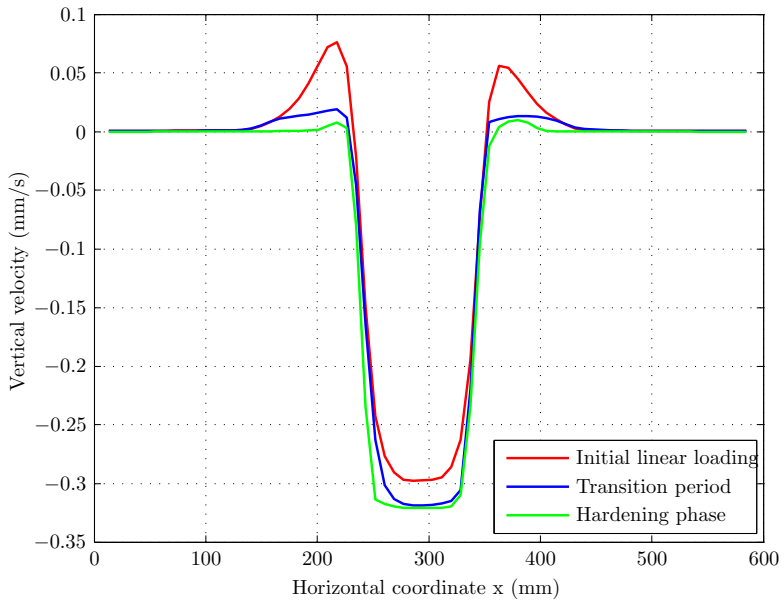

(b) v_y

Figure 5.80: Velocity field immediately below the footing: 100BCUD

enced less reaction forces on its base, which in turn increased relative interparticle movement close to the footing edge.

The shear strain in the barley samples with different packing densities was shown in Figure 5.83 and 5.84 for 100BLDD/BLUD, respectively. Similar to the observation in sand, clear vertical shearing developed adjacent to the footing edges. Under the same footing size, the far more compacted sample (BLDD) produced less strain concentration compared to the general loose sample (BLUD). This can be attributed to the fact that after the vibratory compaction, the densely packed sample possessed a significantly low local compressibility. During the footing penetration, due to the much higher internal friction angle, only a small number of particles were mobilised. The occurrence of these large non-uniform strain around the footing reiterates the importance of large deformation analysis and adaptive meshing technique in future FEM study.

Recalling the knowledge gained from the sensitivity test performed in Chapter 3, there is a potential loss of more localised information at a scale smaller than the interrogation window size (Figure 3.54, 3.55, 3.56 and 3.57). A more comprehensive evaluation of the averaging length scale used in the PIV analysis will shed light on the underlying micromechanism.

5.5.4 Limitations of the current experiments

Reviewing the current footing experiments on a granular mass composed of Leighton Buzzard sand and barley, it is apparent that these test specimens were not representative of natural soil samples. Even the densely packed barley samples achieved by vibratory compaction did not achieve the density level encountered in geotechnical field. Due to the way that the sample was prepared, it contained a certain amount of voids and exhibited a relatively high compressibility, which produced less well defined failure mode in the current small scale test. A sur-

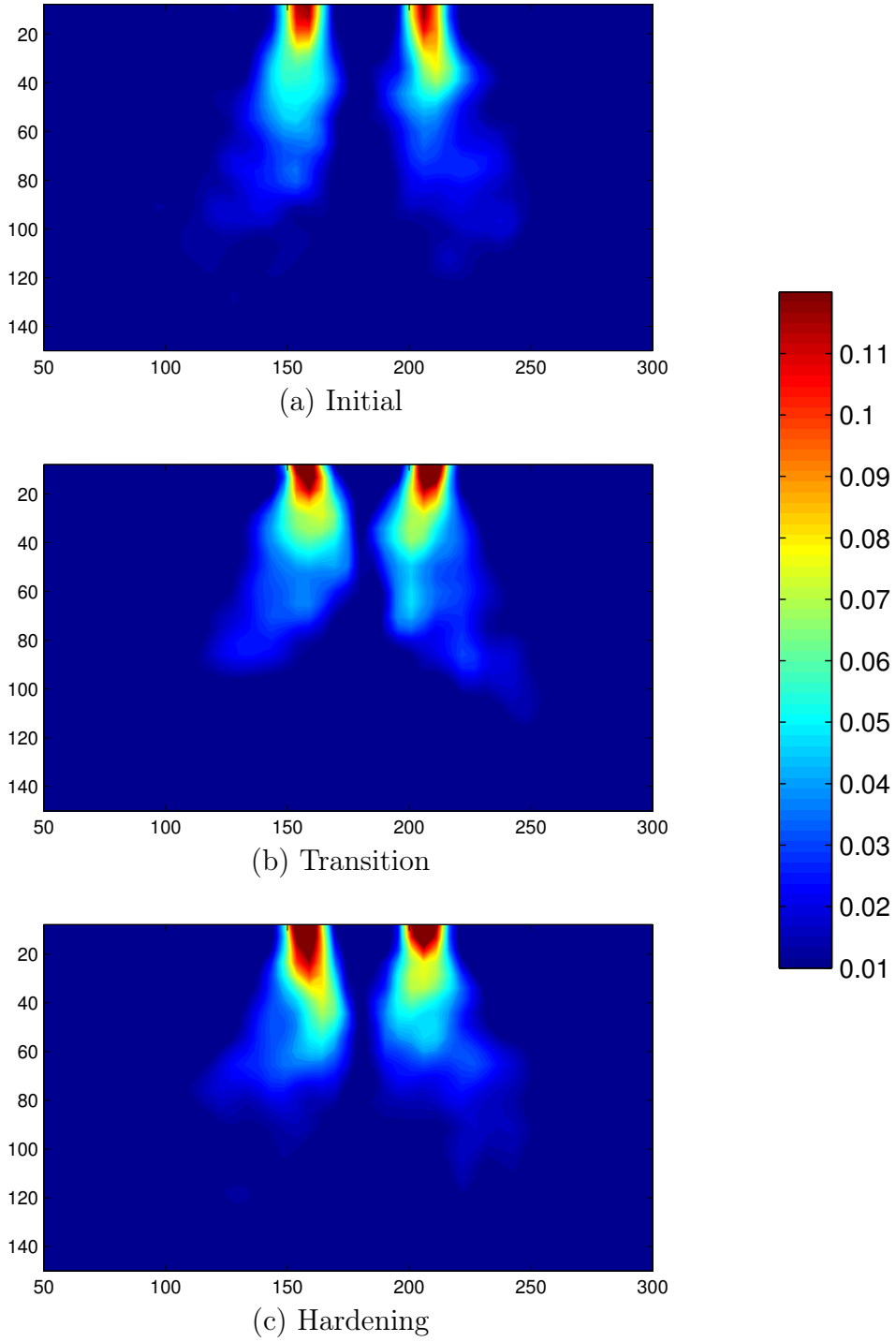

(a) Initial

(b) Transition

(c) Hardening

Figure 5.81: Shear strain field at different loading stages: 50SCUD

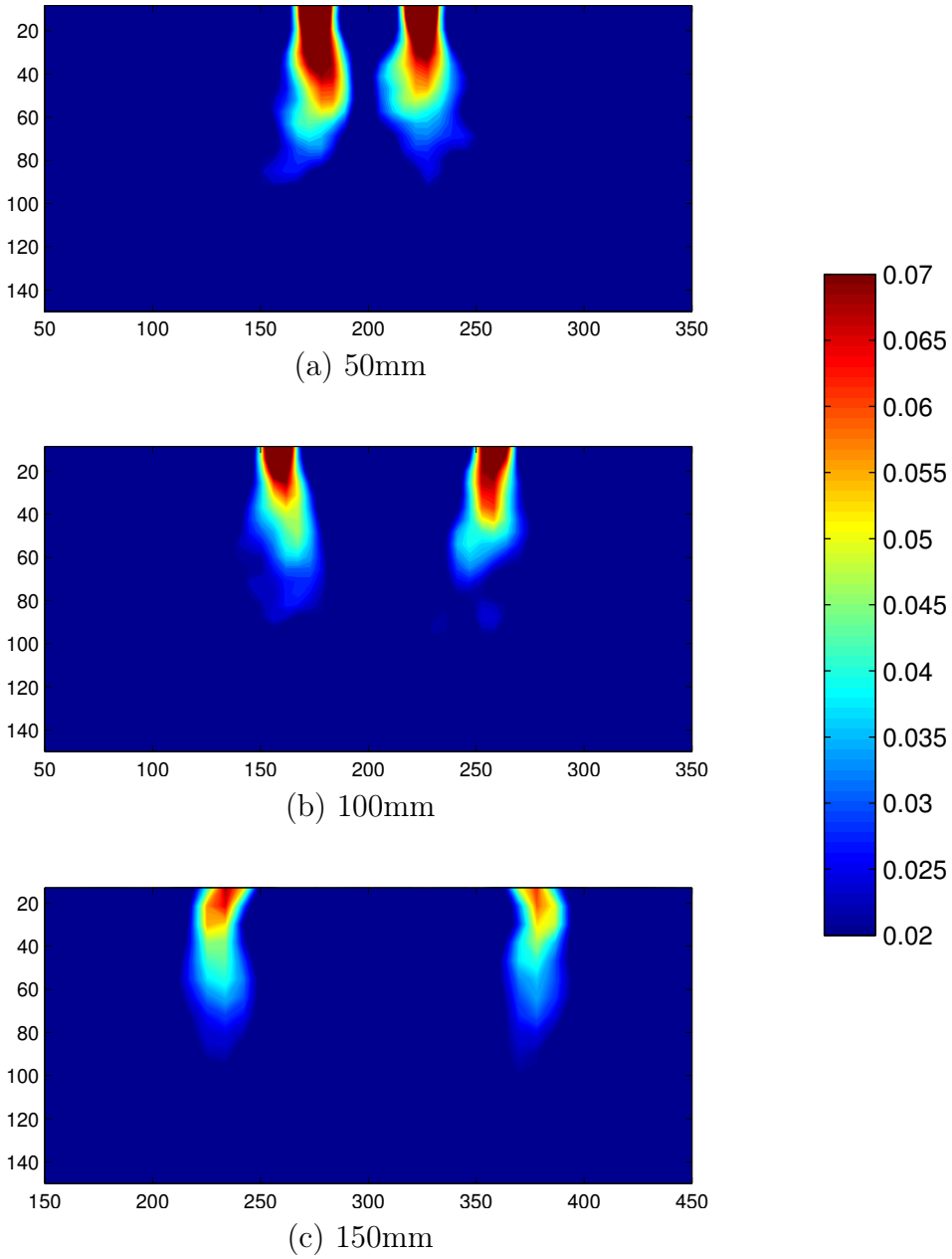

(a) 50mm

(b) 100mm

(c) 150mm

Figure 5.82: Shear strain at transition point for SLUD with different footing sizes

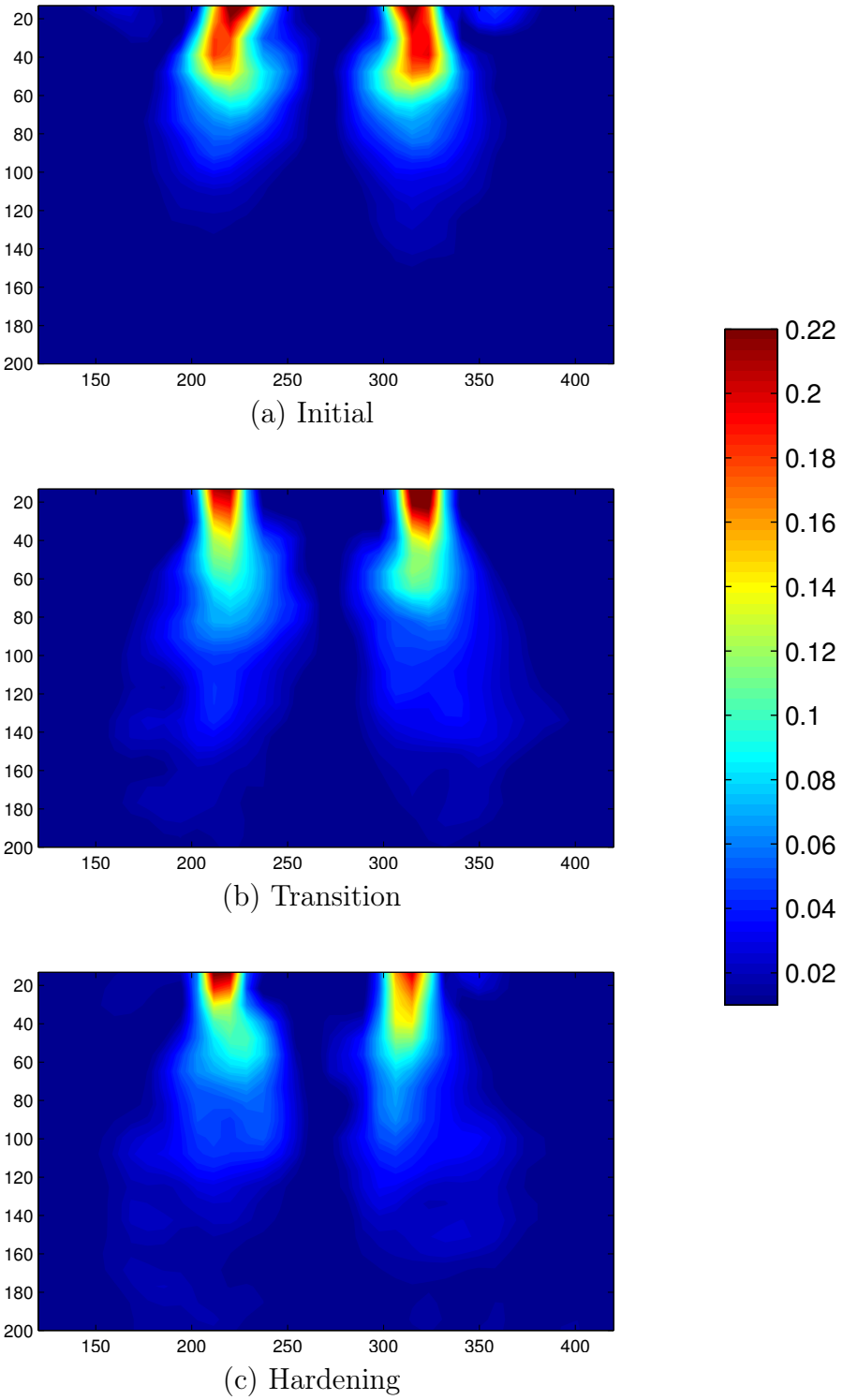

(a) Initial

(b) Transition

(c) Hardening

Figure 5.83: Shear strain field at different loading stages: 100BLDD

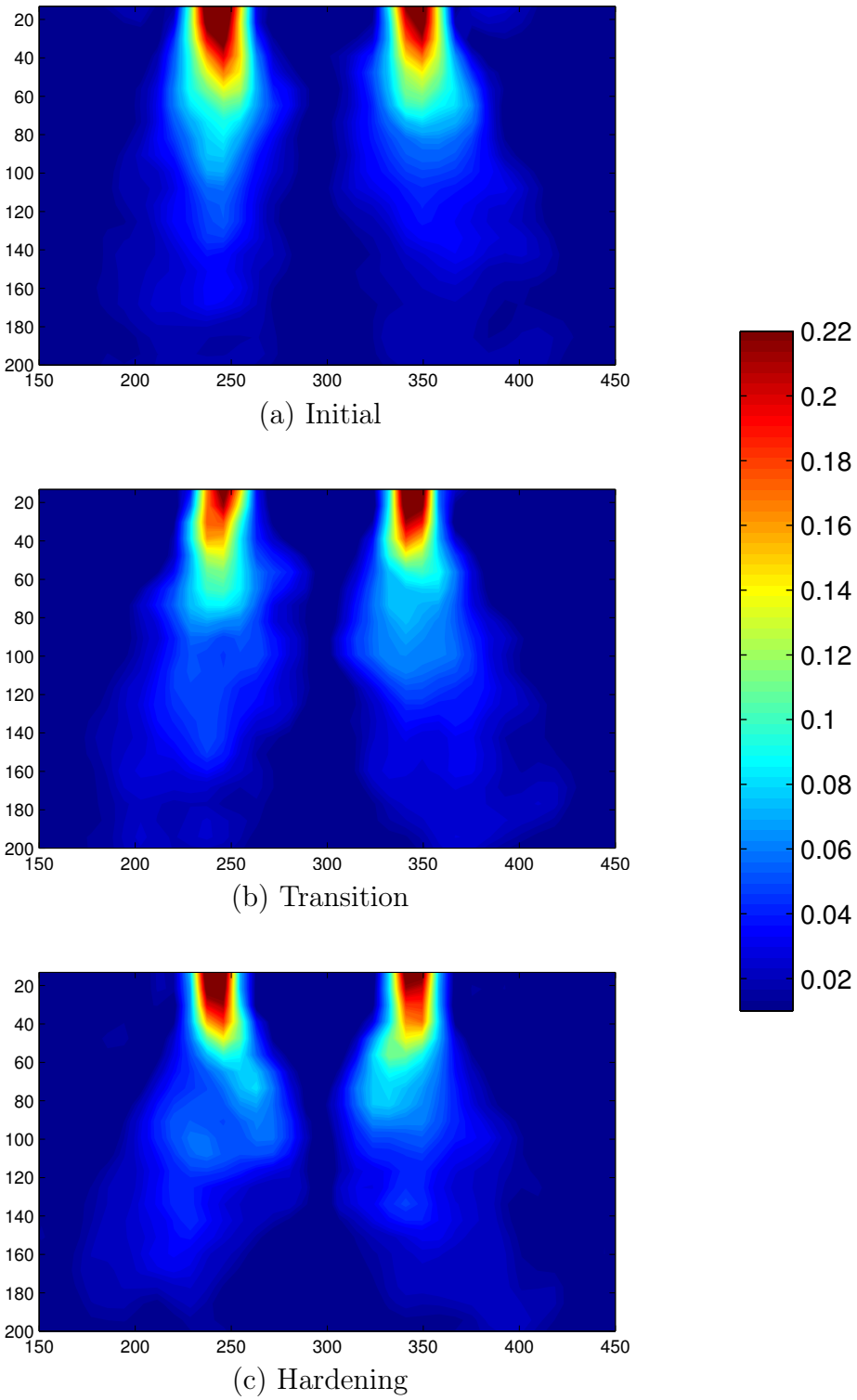

(a) Initial

(b) Transition

(c) Hardening

Figure 5.84: Shear strain field at different loading stages: 100BLUD

charge load applied on the sample surface can increase the confining pressure, which will generate more variations of the internal friction angle and allow more well defined failure modes to develop. Also, centrifuge tests are commonly carried out to simulate the full scale stress field. However, these approaches are not an option given the available laboratory facilities.

In addition, the slice model did not perform as required particularly in the test of Leighton Buzzard sand. The major problem was the out-of-plane deflection of the slice model under the footing load eradicated the assumption of an ideal plane strain deformation. Several conclusions cannot be drawn based on the PIV results in sand, in which the displacement field was characterised by the predominantly vertical movement. Therefore, for future investigation the slice model should be either rebuilt, perhaps with toughened glass as the translucent face material, or braced sufficiently to further minimise the out-of-plane deflection which will become more pronounced if the surcharge loads are applied during testing.

5.5.5 DEM verification simulation of footing test

Although DEM has been shown to be a promising numerical tool to simulate granular solids, careful validations of the simulation outcomes are still rare in the literature and there is a question as to whether DEM is capable of producing quantitative predictions rather than only qualitative representation of the particulate assembly. In addition, the input parameters used in DEM simulations are often simply given without any explanation as to where they came from, and seldom measured in laboratory tests, so influence of the input parameters on the prediction outcomes is rather obscure. For completeness, this section performs preliminary validations of DEM simulation against the results from the current footing experiments. By way of illustration, only the $100mm$ footing on barley grains was studied in detail here.

The original dimension of the granular sample is 1000×550×30mm, which contained up to several hundred thousand barley particles (and much more for sand). It thus becomes impractical to simulate the full scale physical model within the current computational capability. According to the engineer manual published by US Army Corps of Engineers (1990), the recommended depth of analysis should be at least twice the least width of the footing or mat foundation, four times the width of infinite strips or embankments, or the depth of incompressible soil, whichever comes first. The selection of this reduced scale is also in line with the observation from the PIV results in terms of particle displacement and strain distribution, where the primary influential zone can be covered by an area of $4B \times 4B$ immediately beneath the footing base. As a result, the dimension of the DEM model with the 100mm footing was narrowed down to 400×400×30mm in order to reduce the computational time, as shown in Figure 5.85. To simulate the barley grain, non-spherical particle by clumping two spheres which gives an aspect ratio of 1.5 was adopted and Table 5.6 lists the material parameters. With the radius of constituent sphere being 4mm, there were totally 6732 particles in the DEM model after filling the volume.

Table 5.6: Values of the DEM parameters used

Name of the variable	Symbol	Value
Radius of constituent spheres (mm)	R	4
Particle density (kg/m^3)	ρ	1260
Poisson's ratio	ν	0.3
Young's modulus (MPa)	E	450
Sliding friction between particle and particle	f_p	various values
Sliding friction between particle and wall boundaries	f_w	0.1357

Based on the knowledge gained from the DEM simulations in this thesis, the

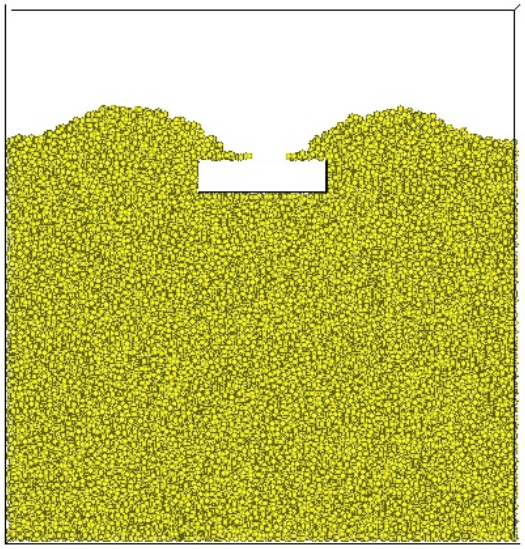

Figure 5.85: DEM setup of the footing experiment

predicted collective behaviour is largely governed by the inperparticle friction, as the externally applied forces are carried and transmitted through particle contact forces. Haertl (2008) carried out a study in an effort to determine the input value of interparticle friction in DEM simulation that can match the bulk friction measured from direct shear test, and the relationship is illustrated in Figure 5.86. The nonlinear curves as shown suggest that the bulk friction is mobilised from a combination of contact friction and geometric interaction between particles, with the need for particles to slide or roll over one another for shear failure to occur. Interestingly, only a small contact friction of 0.05 is sufficient to mobilise a bulk friction of the order of 0.3 in DEM direct shear simulation. Taking barley as an example, the input value of interparticle friction in DEM model was back calculated as $f_p = 0.0335$, based on the bulk friction measured ($f_{bulk} = 0.2730$, recalling Figure 5.34) and the particle aspect ratio of 1.5. In the current DEM verification tests, three coefficients of interparticle friction were assigned and the resulting loading responses were compared:

- $f_p = 0.0335$, determined from Figure 5.86;
- $f_p = 0.2730$, which is the bulk friction reported in Figure 5.34 ;
- $f_p = 0.1365$, half of the bulk friction;

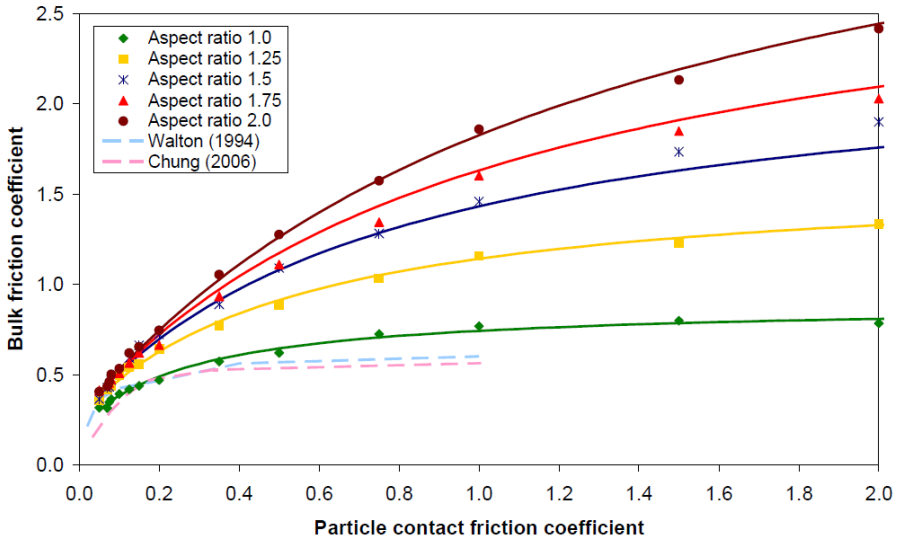

Figure 5.86: Influence of interparticle friction on bulk friction for particles with different aspect ratio (Haertl, 2008)

The predicted bulk responses using these different input values of f_p were assessed against the experimental measurement, as shown in Figure 5.87. It is particularly worthy of mention that as the experimental measurement was recorded at a frequency of 1Hz, which is much higher than the one in the DEM runs (around 10^3Hz). Therefore, moving averaging method was utilised to smooth the DEM data and to match up the output frequency in the experiments. The original raw data produced from DEM simulation will be shown in the subsequent plots. It can be observed that the DEM simulation using f_p determined from Haertl (2008) produced an extremely low resistance compared to the experimental result, which indicates that the relationship between bulk friction and interparticle friction established in direct shear test is not valid to the current footing model. In the

direct shear test, all the particles were confined in a shear ring. The situation significantly changed in the footing test, where only a small portion of particles were influenced by the footing while most of the particles were rather unconfined. Although there are a large number of methodologies and apparatuses available to measure the particle properties, this finding clearly emphasises the importance in choosing a proper calibration test to derive DEM input parameters. The other two simulations using the bulk friction as interparticle friction led to an significant overestimation of system strength, while reducing f_p to half of the bulk friction gave a better match to the experiments. Further investigation is required to clarify this underlying discrepancy.

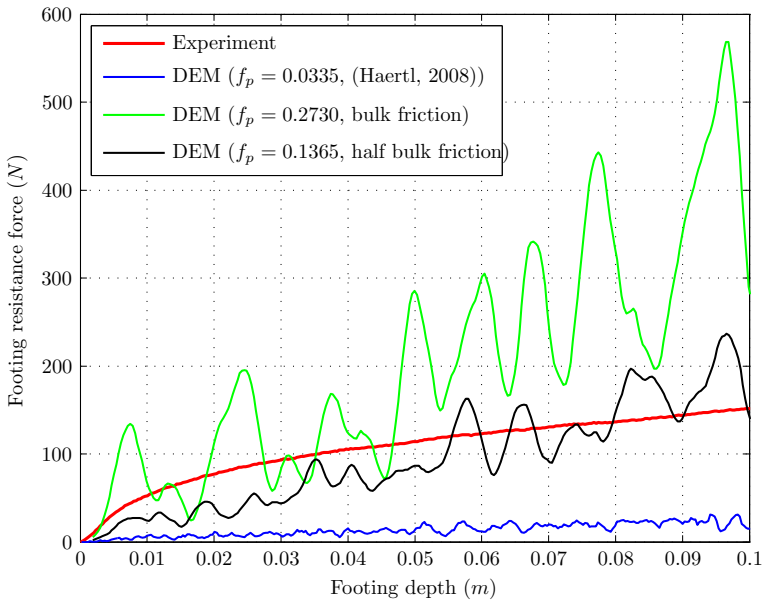

Figure 5.87: Comparison of the bulk footing response between DEM predictions and experimental measurement

To better understand the mismatch between experimental measurement and DEM predictions, the manner that the force transmitted within the bulk sample is analysed. In the current footing apparatus, two components played major roles

in carrying the forces imposed by the footing indentation. The first one came from the bearing capacity of the granular solids, and the other one originated from the frictional force acting on the side walls (referring to the front and rear walls) of the slice model. An attempt was therefore made to separate the contribution to the predicted DEM bulk response by the side and base wall. Three reaction forces are plotted in Figure 5.88, i.e. the net vertical force on the footing base, vertical shear force on the side walls, and vertical force on the base wall. Naturally, it is assumed that the majority of the externally applied force will be eventually transmitted to the base wall under vertical equilibrium. However, the current results suggest that most of the footing load reached the front and rear walls in the manner of vertical shear stress, whereas the base wall only carried a small portion of the load. This transmission mechanism can be related to the particle arching, which is commonly encountered in soils. Terzaghi (1943) interpreted the stress redistribution caused by arching effect as that the shearing resistance tends to keep the yielding mass in its original position resulting in a change of the pressure on both of the yielding part's support and the adjoining part of soil. Therefore, if the yielding part moves downwards, the shear resistance will act upwards and reduce the stress at the base of the yielding mass (Tien, 1996). Additionally, the intermittent fluctuations in the loading response appear to be caused by the particle interaction with the side walls.

Since the model has a constant volume, the number of larger particles contained is significantly smaller than the number of smaller particles. Consequently when the same load is applied, particle arching effect between the front and rear walls is less prone to develop in the system composed of smaller particles, with the increase of the average number of particles in the out-of-plane direction. To confirm this hypothesis, another simulation was conducted by using constituent spheres with a smaller radius of $3mm$. In this DEM model, the total number of particles was 15139, which was more than twice as the particle number in

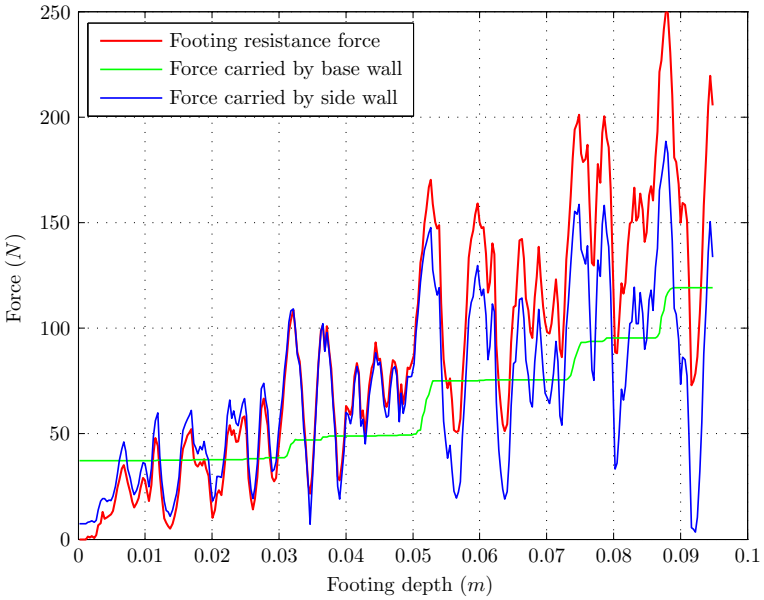

(a) $f_p = 0.1365$

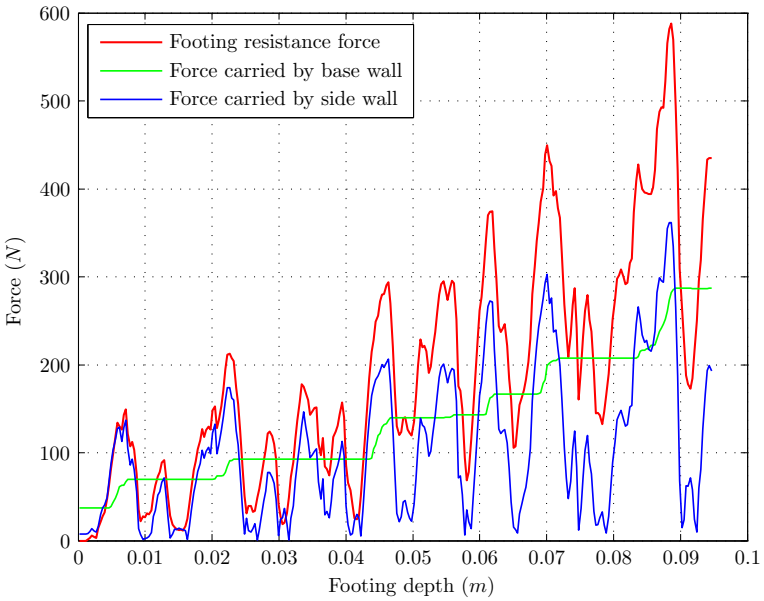

(b) $f_p = 0.2730$

Figure 5.88: Force transmission in the DEM sample of barley (particle number: 6732; radius of constituent spheres: $4mm$)

the case reported in Figure 5.88. The predicted load transmission in this DEM model employing a larger number of particles with smaller radius is illustrated in Figure 5.89. As a result of the increased average number of particles across the out-of-plane direction of the slice model, the arching structure became less easier to develop. Therefore, the portion of indentation force that carried by the container base significantly increased during the footing installation process. This information confirmed the earlier assumption that particle arching promotes the development of frictional forces between particles and side walls.

The predicted collective loading responses from simulations using two different particle sizes are shown in Figure 5.90. As can be observed, the magnitudes of the two footing resistances are almost the same. However, one cannot draw the conclusion that the footing resistance is independent of grain size simply based on these two DEM runs, as the particle numbers involved is considerably small compared to a real granular sample. That said, even reducing the sphere radius down to $2mm$ will give a DEM model up to 90000 particles. To overcome the limitation of computational recourse, a number of algorithms can be utilised to reduce the simulation time. For example, periodic boundary conditions has been widely used to simulate a large system by modelling a small part that is far from its edge. This topic is beyond the scope of the current work and is worthy of further investigation.

To summarise, the objective of the DEM verification tests is twofold. On one hand, the capability of DEM simulation to produce quantitative bulk measurement is examined. Interparticle friction was identified as a critical input parameter that governs the bulk behaviour. On the other hand, the force transmission mechanism in the footing test was revealed, where a large portion of the load induced from footing indentation was carried by the side walls of container.

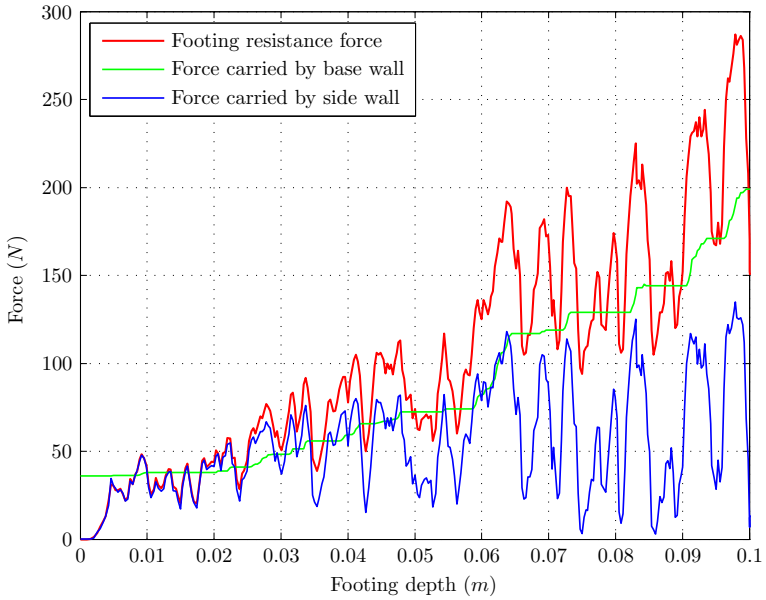

(a) $f_p = 0.1365$

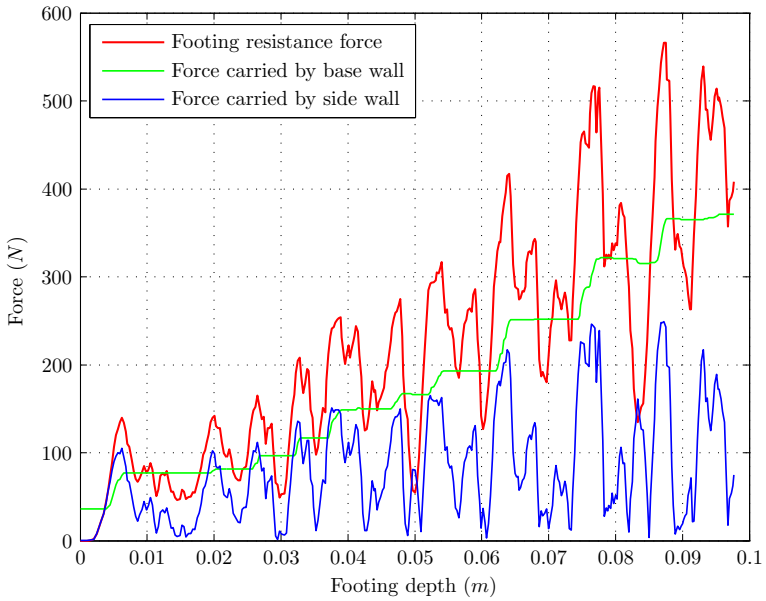

(b) $f_p = 0.2730$

Figure 5.89: Force transmission in the DEM sample of barley (particle number: 15139; radius of constituent spheres: $3mm$)

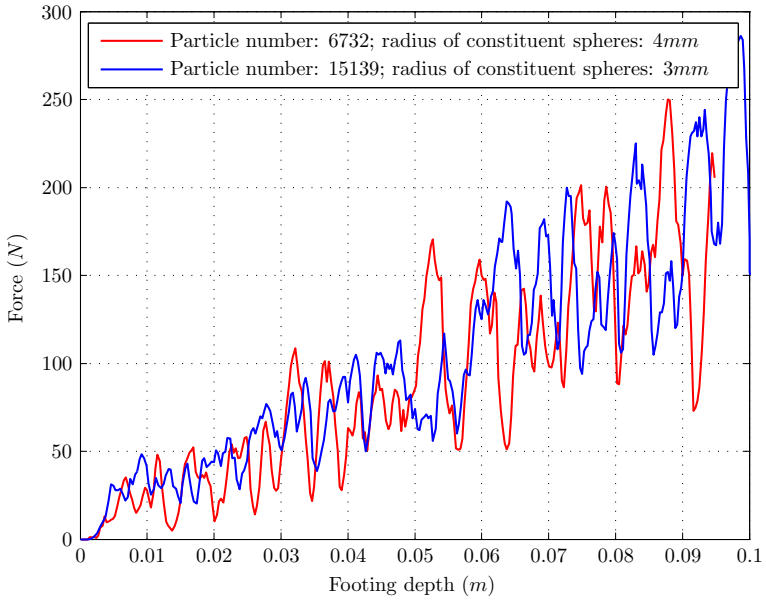

(a) $f_p = 0.1365$

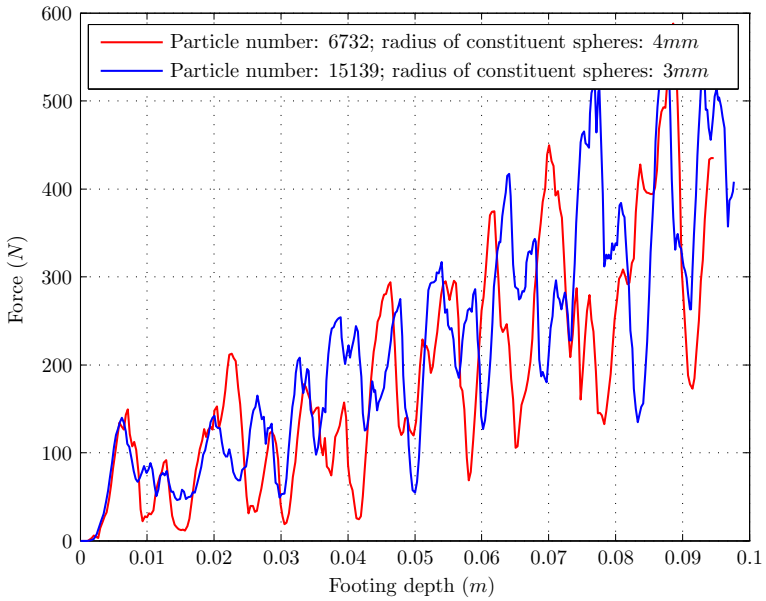

(b) $f_p = 0.2730$

Figure 5.90: Comparison of the predicted bulk footing response between DEM simulations using two different particle sizes

5.6 Summary

This study presents a series of DEM simulated penetration tests with a flat base punch forced into spherical and non-spherical grain assemblies. The primary objective is to improve the understanding of penetration mechanisms at different length scales, including microstructural analysis at the grain level and stress homogenisation from a macroscopic perspective.

The predicted penetration resistance increased with the indentation depth, and a much higher bulk strength was achieved from non-spherical particles where the interlocking effect played a major role. The influence of gravitational acceleration ($1g$ and $100g$) on the system responses was found as that the vertical reaction forces experienced by the punch scaled linearly with gravity. These findings are in agreement with existing scientific evidence and thus lends credence to the idea of using DEM to conduct numerical extraterrestrial experiments. Meanwhile, the significant fluctuation observed in the penetration response was explored by examining the force network. The spatial arrangement of these interparticle contacts revealed the origin of the temporal inhomogeneity, primarily caused by the successive collapse and reformation of force chains.

Homogenisation method via measurement sphere in PFC^{3D} was utilised to calculate the stress distribution within the granular assembly. The results showed that the stress propagated along different directions and strong stress concentration developed around the punch. The stress gradient quantified from the pressure bulb varied for different stress components, with the largest occurred in the vertical stress. It was found that when the punch was pushed into the particulate assembly, two distinct penetration mechanisms were revealed from particle displacement fields, which are qualitatively similar to several analytical solutions of soil slip line. In the shallow penetration, the excessive particle movement can be adequately described by the Terzaghi (1943) theory, including the active, ra-

dial shear and passive zones. Observations at deep penetration phase suggest that the kinematic displacement field can be properly considered by the solution proposed by Meyerhof (1951). Although the displacement fields provide an easy approach to evaluate the rupture surface, a more rigorous analysis to study the failure mode needs further investigation.

The evolution of force transmission and propagation were monitored as a function of penetration depth. New insights into the progressive penetration mechanism was gained at the grain scale, whereas most of the previous interpretation theories are based on macroscopic observations and continuum concepts. With the knowledge of strong load-bearing contact network, the force structures inside the current dense granular assemblies were found to be highly heterogeneous. At shallow penetration stage, most force chains carrying large interparticle forces aligned vertically to provide the bulk resistance. As the penetration further proceeded, where the vertical stress became considerably high, it was revealed that there was a significant growth of force chains in the horizontal direction within the strong network, to laterally support the previously formed vertical chains and thus prevent them from buckling. The ramified contact network provided more pathways for force transmission and was necessary to maintain the structural stability. The magnitudes of the normal contact forces within the granular assembly followed an exponentially decaying function. Current study also highlights the need for mathematical formulations to quantify the force chains (e.g. length, curvature and the degree of branch), which will shed further light on how these factors affect the bulk strength particularly the force transmission mechanism. Such studies would provide an opportunity to connect the recent advances in DEM simulation with the accumulated practical understanding in soil disturbances.

Another focus of this chapter lies in the experimental investigation of model footing experiment on a granular mass contained in a transparent chamber, al-

lowing the particle flow to be captured continually using a digital camera. Correlation of pairs of testing images was performed using the open source code MPIV, an implementation of the PIV technique as a toolbox in Matlab. Three footing sizes were tested in the samples composed of Leighton Buzzard sand and barley. Special attention was given to the influence of packing structure on the bulk strength and deformation pattern. Therefore, the samples were prepared manually by using different filling and compaction methods. With the two materials tested, in which the barley is far more elongated and larger than the sand, the possible variation in the achieved packing arrangement is considerably high. It can be observed that the barley particles in the samples prepared from concentric filling are mainly oriented horizontally, being the optimally most stable position under gravity. The ultimate bearing capacity was determined by using the $0.1B$ method. After normalising the settlement depth with the footing breadth, the loading curves with different footing sizes collapsed into a narrow band in the current small scale model. The measured footing loads include both the resistance force experienced by the footing base, as well as the frictional force acting between footing and chamber walls (front and rear). Therefore, improvements on the experimental facility are necessary to separate these two components in the future.

The PIV measurement is able to capture not only the high displacement gradient close to the footing tip, but also the very small movements in the far field. In the sand specimens, the particle movement exhibited primarily downward displacement, partially caused by the out-of-plane deflection of the slice model. For barley, the general shear failure was identified in the most densely packed sample achieved by vibratory compaction, where the grains flowed along streamlines curving from the footing base to the ground surface on either side of the footing. The failure modes in the rest samples were less well defined, which can be further investigated based on some improvements of the testing facilities. Additionally,

local velocity and shear strain were investigated to further explore the interaction between the footing and particles. The influence of footing size and packing density on the velocity profile immediately beneath the footing was quantitatively addressed. Regarding the shear strain approximated from displacement field, the strain concentration developed downwards into the particulate sample along the footing edges with little propagation. To summary, PIV is able to yield a significant increase in the accuracy and spatial resolution of deformation measurement in granular solids. Although relatively new in geomechanics, this method is a useful investigative tool for the study of two dimensional granular flow and can also provide insight into surface dominated three dimensional flow.

Finally, DEM simulations corresponding to the model footing test were conducted and assessed against the experiments results. In a series of preliminary DEM runs, the coefficient of interparticle friction was identified as a critical input parameter that governs the predicted bulk loading response, in which a significant discrepancy between numerical simulation and experiment measurement existed. The findings from the DEM verification highlight the importance and complexity of well designed physical calibration test to derive mechanical properties of granular solids. The information gained from simulations using different particle sizes and numbers shed some light on the numerical scaling effect on the DEM outcomes. In the relatively small scale DEM runs presented in this chapter, particle arching developed across the side walls was revealed as a key element in the force transmission mechanism. In addition to the above conclusions, it should be noted that there are still other useful results can be derived from further analyses based on this large set of experiments and DEM simulations. Some further investigations have already begun and will be presented elsewhere at a later stage.

Chapter 6

Conclusions

6.1 General conclusion

The principal objective of the current research is to bridge the link between the micro- and macroscopic understanding of mechanical behaviour of densely packed granular solids. In this study, DEM simulations have been extensively performed to model particulate systems under a variety of loading actions, in particular those pertain to multiple interacting bodies undergoing large deformation and strain localisation. The loading scenarios under investigation include biaxial compression, formation of granular piles and rigid body penetration. As an alternative approach to the conventional continuum theory, DEM proved to be a promising method in the numerical modelling of discontinua, where feasible results were yielded from both a micro- and macroscopic perspective. Special attention was paid to the influence of particle shape by employing both spherical and non-spherical grains. Numerical results revealed the significant differences between these two resulting packing structures in terms of bulk response and micromechanics. The findings present critical implications for the numerous DEM simulations conducted to date where circular or spherical particles

were used. Furthermore, many new insights were gained regarding bifurcation instability, stress-strain-dilation relationship, granular dynamics and progressive failure mechanism, which cannot be obtained from laboratory experiments and classical continuum theory. In this section, the main achievements related to the simulation results is briefly summarised.

- **Biaxial compression test**: DEM simulations were performed on specimens composed of spherical and non-spherical particles, with special focus on the micromechanical behaviour associated with strain localisation. In general, depending on the particle shape, contact friction and boundary condition, various loading responses and localisation patterns were observed, such as single and conjugate shear bands. Particle scale analysis suggests that during a biaxial compression, there were considerable amount of changes in magnitude and spatial distributions of some micromechanical quantities regarding the packing structure and contact network. Comparing to the unsheared specimens, the void ratio in sheared specimens showed both higher mean values and higher standard deviations, which became more pronounced with the increase of particle non-sphericity. Distributions of local void ratio indicated that the voidage growth mainly took place within the region of shear band. The variation in the contact orientation implied that an initial isotropic packing was gradually replaced by a pronounced anisotropic structure. The strong contact network carrying above-average contact forces was visualised by plotting the force chains at increasing strain levels, where the process of force chain bucking was observed and linked with the formation of shear band. Meanwhile, the constitutive response in terms of stress and strain was also investigated, in order to link particle analyses with continuum interpretation. The average stress tensor was calculated based on the algorithm of measurement sphere while

the incremental strain components were evaluated through the application of PIV correlation. The strain measurement at high spatial resolution revealed that multiple shear bands formed initially prior to reaching peak strength, while the persistent pattern of strain localisation became more definitive in the softening phase.

- **Base pressure distribution underneath a granular pile**: Simulations were performed using both spherical and non-spherical particles in several numerical models of granular piles. A pressure profile with a significant pressure dip under the apex was predicted for all three models under certain conditions. The spherical assembly appeared to produce a more erratic pressure profile with a less significant pressure dip than the non-spherical particles. It is suggested that spherical particles with its perfect symmetry has the propensity for excessive rotation that can obscure the phenomena pertaining to real granular solids. The history of the pile preparation was shown to be important whilst the base deflection did not appear to be a requirement for the dip to form. The results are in good agreement with some published experimental observations. The granular fabric in terms of the magnitude of contact force, the contact orientation and the particle orientation within a granular pile have also been described to understand the underlying force transmission mechanism.

- **Rigid body penetration test**: A series of simulated penetration tests were conducted with a rigid punch forced into a granular deposit, in which the influence of particle shape and gravitational acceleration on the micro- and macroscopic behaviour were examined. With regard to the bulk response, the predicted penetration resistance increased with the indentation depth, with its initial gradient larger than the one in deep penetration. The influence of gravitational acceleration was found as that the contact

forces acting on the punch base linearly scaled with gravity. One notable feature in DEM predicted penetration resistance is the presence of intermittent numerical fluctuations of significant magnitude. Current research highlights the requirement of appropriate averaging schemes, and preliminary explanation to the temporal and spatial inhomogeneities was given in terms of force chain collapse and reformation, supported by the careful examination of the force network. Homogenisation method was performed in order to relate the kinematic interparticle forces in DEM to macroscopic stresses. The results showed that as the penetrator passed through the granular solids, strong stress concentration developed around the punch. Stress gradient varied for different stress components, with the highest occurring in the vertical stress. Successive analysis of the contact orientation in the strong contact network illustrated that during the penetration, there was a significant growth in the horizontal contact to laterally support the vertical chains carrying the largest contact forces and thus prevent them from buckling. Also, a set of experimental footing tests using sand and barley were conducted in a transparent chamber, allowing the particle flow to be captured continually using a digital camera and subsequently correlated through PIV analysis. The image correlation algorithm was operated on images containing particle samples, and the local displacement vectors were determined. The PIV technique produced a far greater level of detail and accuracy than conventional measurements. Apart from displacement fields, special focus was paid to the evolution of induced shear strain, instantaneous velocity and particle flow pattern at different footing depths. The way in which all these aspects of the phenomena are influenced by variables such as particle shape, filling method, packing density and footing size, was discussed. Based on the displacement vectors in the primary deformation zone and the distribution of the non-uniform strain around the footing, the

failure mode was explored which largely depends on the sample compressibility. The most densely packed barley sample exhibited the general shear failure while the failure modes in the rest samples were less well defined, which can be further investigated based on some improvements of testing facilities. Additionally, DEM simulations corresponding to the footing tests were also performed to evaluate its capability in quantitative prediction. The critical role of interparticle friction as part of DEM input parameters was addressed. Although there was a significant discrepancy between the numerical results and experiment measurement, the key mechanism in force transmission was identified as the arching effect between front and rear walls of the slice model.

6.2 Recommendations for further research

This research has produced a body of novel scientific data that can be exploited for more in-depth analysis. The need for future research in key potential areas is briefly outlined below:

1. The particle rotation may be excessive in the DEM modelling of spheres which do not reflect real particles that are rarely perfectly spherical. This excessive rolling can lead to reduced aggregate frictional behaviour and less resistance to shear. Formulation of contact law considering the rolling resistance needs to be incorporated if spherical particle is used.

2. Discrete element method requires intensive computational power, which limits either the length of simulation time and the number of particles. Therefore, DEM applications to large-scale problems are currently difficult or impossible. As the relatively inexpensive high performance hardware and smart computational strategies are becoming available, it is possible

to consider implementing parallel algorithm into the current DEM codes to scale up its processing capability (Maknickas et al., 2006). Systems of discontinua comprising billions of particles can be simulated.

3. The combined finite-discrete element method is gaining increasing importance in engineering programmes and is at the forefront of the current effort in computational modelling of the failure of solids (Munjiza, 2004). Full two-way coupling of these two methodologies can extend the application of DEM to a wider range of engineering applications.

4. In most DEM simulations, it is assumed that each particle is rigid and no crushing occurs during the loading and deformation. However, particle crushing has been found to be a key principle underlying soil plasticity (Cheng et al., 2004). The current deep penetration simulation confirmed that particles around the punch base experienced a sharp increase of stress gradient which could cause the crushing of the particles. There have been various DEM simulations that include particle crushing, which will require further development of numerical algorithms to capture the particle crushing micromechanics.

5. The accuracy of the PIV algorithm needs to be further quantified in the detection of particle movement. Possible error sources (e.g. image distortion and peak locking) should be minimised through better designed experimental apparatus. Alternatively, more robust numerical algorithms in determining the correlation peak and post-processing error vectors need to be developed.

6. The study of the influence of a subset of DEM input parameters was briefly presented in Chapter 5. The relative importance of these parameters and the complexity involved in quantitative prediction were highlighted. Further

studies are clearly warranted to achieve quantitative bulk predictions. It is important that the significance of each DEM input parameter is explored to understand its effect in different loading actions, accompanied by well designed physical calibration methods.

7. Natural particle size variation exists in the physical collection of granular solids. The influence of particle size variation and model scale should be further investigated, especially to understand if it is one of the reasons for the discrepancy reported in the DEM verification of the footing installation.

References

Adrian, R. J., 1991. Particle-imaging techniques for experimental fluid mechanics. Annual Review of Fluid Mechanics 23 (1), 261–304. 17

Ai, J., Chen, J. F., Ooi, Y. J., Rotter, J. M., 2008. Assessment of rolling resistance models in discrete element simulation. Internal research report, the University of Edinburgh. 36, 175

Allersma, H. G. B., 1995. Simulation of subsidence in soil layers in a geotechnical centrifuge. Land subsidence. Proc. international symposium, the Hague, 1995, 117–126. 196

Alshibli, K. A., Sture, S., 2000. Shear band formation in plane strain experiments of sand. Journal of Geotechnical and Geoenvironmental Engineering 126 (6), 495–503. 64, 71, 72, 75

Anand, L., Gu, C., 2000. Granular materials: constitutive equations and strain localization. Journal of the Mechanics and Physics of Solids 48 (8), 1701–1733. 59

Antony, S. J., Kuhn, M. R., 2004. Influence of particle shape on granular contact signatures and shear strength: new insights from simulations. International Journal of Solids and Structures 41 (21), 5863–5870. 60

Azéma, E., Radjai, F., Saussine, G., 2009. Quasistatic rheology, force transmission and fabric properties of a packing of irregular polyhedral particles. Mechanics of Materials 41 (6), 729 – 741. 38

Bagi, K., Bojtar, I., 2001. Different microstructural strain tensors for granular materials. Proceedings of the Fourth International Conference on Analysis of Discontinuous Deformation, 111–133. 14

Bagi, K., Kuhn, M. R., 2004. A definition of particle rolling in a granular assembly in terms of particle translations and rotations. Journal of Applied Mechanics 71 (4), 493–501. 36

Baligh, M., 1985. Strain path method. Journal of Geotechnical Engineering 111 (9), 1108–1136. 194

Bardet, J. P., 1994. Observations on the effects of particle rotations on the failure of idealized granular materials. Mechanics of Materials 18 (2), 159 – 182. 36

Bardet, J. P., 1998. Introduction to computational granular mechanics. Behaviour of Granular Materials, 99–169. 13

Bardet, J. P., Proubet, J., 1992. Shear-band analysis in idealized granular material. Journal of Engineering Mechanics 118 (2), 397–415. 77, 78

Bishop, A. W., Green, G. E., 1965. The influence of end restraint on the compression strength of a cohesionless soil. Geotechnique 15 (3), 243–266. 66

Bishop, R., Hill, R., Mott, N., 1945. The theory of indentation and hardness tests. Proceedings of the Physical Society 57 (3), 147–159. 193

Bouchaud, J.-P., Cates, M. E., Claudin, P., 1995. Stress distribution in granular media and nonlinear wave equation. Journal de Physique I 5 (6), 639–656. 169

Briaud, J.-L., Gibbens, R., 1999. Behavior of five large spread footings in sand. Journal of Geotechnical and Geoenvironmental Engineering 125 (9), 787–796. 261, 267

Briaud, J. L., Jeanjean, P., 1994. Load settlement curve method for spread footings on sand. Geotechnical Special Publication 2, 1774–1804. 259

Calvetti, F., Combe, G., Lanier, J., 1997. Experimental micromechanical analysis of a 2d granular material: relation between structure evolution and loading path. Mechanics of Cohesive-frictional Materials 2 (2), 121–163. 36

Cambou, B., Chaze, M., Dedecker, F., 2000. Change of scale in granular materials. European Journal of Mechanics - A/Solids 19 (6), 999–1014. 14

Cates, M. E., Wittmer, J. P., Bouchaud, J.-P., Claudin, P., Aug 1998. Jamming, force chains, and fragile matter. Phys. Rev. Lett. 81 (9), 1841–1844. 167

Cheng, Y., Bolton, M., Nakata, Y., 2004. Crushing and plastic deformation of soils simulated using dem. Geotechnique 54 (2), 131–141. 333

Cheng, Y. P., Nakata, Y., Bolton, M. D., 2003. Discrete element simulation of crushable soil. Geotechnique 53 (7), 633–641. 1

Chung, Y., 2006. Discrete element modelling and experimental validation of a granular solid subject to different loading conditions. Ph.D. thesis, The University of Edinburgh. 37

Cleary, P., Sawley, M., 2002. Dem modelling of industrial granular flows: 3d case studies and the effect of particle shape on hopper discharge. Applied Mathematical Modelling 26 (2), 89–111. 37

Colliat-Dangus, J. L., Desrues, J., Foray, P., 1988. Triaxial testing of granular soil under elevated cell pressure. Advanced Triaxial Testing of Soil and Rock 977, 290–310. 68

Consoli, N. C., Schnaid, F., Milititsky, J., 1998. Interpretation of plate load tests on residual soil site. Journal of Geotechnical and Geoenvironmental Engineering 124 (9), 857–867. 261, 267

Coppersmith, S. N., 1997. Force fluctuations in granular media. Physica D: Nonlinear Phenomena 107 (2-4), 183–185. 188

Cui, L., O'Sullivan, C., O'Neill, S., 2007. An analysis of the triaxial apparatus using a mixed boundary three-dimensional discrete element model. Geotechnique 57 (10), 831–844. 71

Cundall, P. A., 1989. Numerical experiments on localization in frictional materials. Ingenieur-Archiv 59 (2), 148–159. 63

Dedecker, F., Chaze, M., Dubujet, P., Cambou, B., 2000. Specific features of strain in granular materials. Mechanics of Cohesive-frictional Materials 5 (3), 173–193. 14

Desrues, J., Chambon, R., Mokni, M., Mazerolle, F., 1996. Void ratio evolution inside shear bands in triaxial sand specimens studied by computed tomography. Geotechnique 46 (3), 529–546. 81

Desrues, J., Viggiani, G., 2004. Strain localization in sand: an overview of the experimental results obtained in grenoble using stereophotogrammetry. International Journal for Numerical and Analytical Methods in Geomechanics 28 (4), 279–321. 57, 80

Durgunoglu, H., Mitchell, J., 1975. Static penetration resistance of soils: I. analysis. Proc. ASCE, Specialty Conference on In Situ Measurements of Soil Properties 1, 151–171. 24, 232

Evans, T. M., 2005. Microscale physical and numerical investigations of shear banding in granular soils. Ph.D. thesis, Georgia Institute of Technology. 64

Finno, R. J., Harris, W. W., Mooney, M. A., Viggiani, G., 1997. Shear bands in plane strain compression of loose sand. Geotechnique 47 (1), 149–165. 78

Frost, J. D., Yang, C. T., 2003. Effect of end platens on microstructure evolution in dilatant specimens. Soils and Foundations 43 (4), 1–11. 68

Galindo Torres, S. A., Muñoz Castaño, J. D., Jun 2007. Simulation of the hydraulic fracture process in two dimensions using a discrete element method. Physical Review E 75 (6), 066109. 1

Gao, D., Herbst, J. A., 2009. Alternative ways of coupling particle behaviour with fluid dynamics in mineral processing. International Journal of Computational Fluid Dynamics 23 (2), 109 – 118. 1

Geng, J., Behringer, R. P., 2005. Slow drag in two-dimensional granular media. Phys. Rev. E 71 (1), 011302. 204

Geng, J., Longhi, E., Behringer, R. P., Howell, D. W., 2001. Memory in two-dimensional heap experiments. Physical Review E - Statistical, Nonlinear, and Soft Matter Physics 64 (6 I). 179, 188

Gui, L., Merzkirch, W., 2000. A comparative study of the mqd method and several correlation-based piv evaluation algorithms. Experiments in Fluids 28 (1), 36–44. 20

Guo, Y., Morgan, J. K., 2004. Influence of normal stress and grain shape on granular friction: Results of discrete element simulations. Journal of Geophysical Research 109 (B12), B12305. 38

Haertl, J., 2008. A study of granular solids in silos with and without an insert. Ph.D. thesis, University of Edinburgh. 17, 26, 45, 47, 48, 50, 207, 316, 317

Haertl, J., Ooi, J., 2008. Experiments and simulations of direct shear tests: porosity, contact friction and bulk friction. Granular Matter 10 (4), 263–271. 241

Hall, S. A., Muir Wood, D., Ibraim, E., Viggiani, G., 2010. Localised deformation patterning in 2d granular materials revealed by digital image correlation. Granular Matter 12 (1), 1–14. 21, 23, 138, 144, 155, 156

Handy, R. L., Spangler, M. G., 2007. Geotechnical engineering: soil and foundations principles and practice. McGraw-Hill Professional. 26, 301

Harris, W. W., Viggiani, G., Mooney, M. A., Finno, R. J., 1995a. Use of stereophotogrammetry to analyze the development of shear bands in sand. Geotechnical Testing Journal 18 (4), 405–420. 17, 58

Harris, W. W., Viggiani, G., Mooney, M. A., Finno, R. J., 1995b. Use of stereophotogrammetry to analyze the development of shear bands in sand. Geotechnical Testing Journal 18 (4), 405–420. 78

Holst, J. M. F. G., Rotter, J. M., Ooi, J. Y., Rong, G. H., 1999. Numerical modeling of silo filling. ii: Discrete element analyses. Journal of Engineering Mechanics 125 (1), 104–110. 49

Howell, D., Behringer, R. P., Veje, C., 1999. Stress fluctuations in a 2d granular couette experiment: A continuous transition. Physical Review Letters 82 (26), 5241–5244. 12

Hu, N., Molinari, J. F., 2004. Shear bands in dense metallic granular materials. Journal of the Mechanics and Physics of Solids 52 (3), 499–531. 78

Huang, W., Sheng, D., Sloan, S. W., Yu, H. S., 2004. Finite element analysis of cone penetration in cohesionless soil. Computers and Geotechnics 31 (7), 517–528. 197

Itasca Consulting Group Inc, ., 2003. User manual, pfc3d - particle flow code in 3 dimensions, version 3.0. 16, 31, 33, 35

Iwashita, K., Oda, M., 1998. Rolling resistance at contacts in simulation of shear band development by dem. Journal of Engineering Mechanics 124 (3), 285–292. 36, 60, 78

Jiang, M., Zhu, H., Harris, D., 2008. Classical and non-classical kinematic fields of two-dimensional penetration tests on granular ground by discrete element method analyses. Granular Matter 10 (6), 439–455. 198

Johnson, K. L., 1985. Contact mechanics. Cambridge University Press, Cambridge, U.K. 34

Jotaki, T., Moriyama, R., 1979. On the bottom pressure distribution of the bulk materials piled with the angle of repose. J. Soc. Powder Technol. Japan. 60, 184–191. 164, 165

Kheiripour Langroudi, M., Sun, J., Sundaresan, S., Tardos, G. I., 2010. Transmission of stresses in static and sheared granular beds: The influence of particle size, shearing rate, layer thickness and sensor size. Powder Technology Article in Press. 203, 204

Kuhn, M. R., 1999. Structured deformation in granular materials. Mechanics of Materials 31 (6), 407–429. 14, 81, 100

Lade, P. V., Wang, Q., 2001. Analysis of shear banding in true triaxial tests on sand. Journal of Engineering Mechanics 127 (8), 762–768. 75

Lebert, M., Burger, N., Horn, R., 1988. Effects of soil structures and stress duration on pressure transmission in tilled soil. Proceedings of the 11th ISTRO Conference 1, 281–287. 23, 215, 218

Lee, K. L., 1978. End restraint effects on undrained static triaxial strength of sand. Journal of the Geotechnical Engineering Division, ASCE 104 (6), 687–704. 66

Lee, K. L., Seed, H. B., 1964. Discussion of importance of free ends in triaxial testing. J. Soil Mech. and Found. Div., ASCE 90 (6), 173–175. 66

Lesniewska, D., Muir Wood, D., 2010. Observations of stresses and strains in a granular material. Journal of Engineering Mechanics 135, 1038–1054. 138, 139

Lin, X., Ng, T.-T., 1997. A three-dimensional discrete element model using arrays of ellipsoids. Geotechnique 47 (2), 319–329. 36, 42

Liu, C., Nagel, S. R., Schecter, D. A., Coppersmith, S. N., Majumdar, S., Narayan, O., Witten, T. A., 1995. Force fluctuations in bead packs. Science 269 (5223), 513–515. 188, 201

Liyanapathirana, D. S., 2009. Arbitrary lagrangian eulerian based finite element analysis of cone penetration in soft clay. Computers and Geotechnics 36 (5), 851–860. 23, 216

Lobo-Guerrero, S., Vallejo, L., 2007. Influence of pile shape and pile interaction on the crushable behavior of granular materials around driven piles: Dem analyses. Granular Matter 9 (3), 241–250. 197, 203, 204

Lueptow, R. M., Akonur, A., Shinbrot, T., 2000. Piv for granular flows. Experiments in Fluids 28 (2), 183–186. 22

Lutenegger, A. J., Adams, M. T., 1998. Bearing capacity of footings on compacted sand. In: Proceedings of the 4th International Conference on Case Histories in Geotechnical Engineering. pp. 1216–1224. 24, 258, 259, 260

Maknickas, A., Kaceniauskas, A., Kacianauskas, R., Balevicius, R., Dziugys, A., 2006. Parallel dem software for simulation of granular media. Informatica 17 (2), 207–224. 333

Matuttis, H. G., Luding, S., Herrmann, H. J., 2000. Discrete element simulations of dense packings and heaps made of spherical and non-spherical particles. Powder Technology 109 (1-3), 278–292. 170

McBride, W., 2006. Base pressure measurements under a scale model stockpile. Particulate Science and Technology 24 (1), 59–70. 189

Meyerhof, G., 1951. The ultimate bearing capacity of foundations. Ge?otechnique 2 (4), 301–332. 229, 232, 325

Morgan, J. K., 2004. Particle dynamics simulations of rate- and state-dependent frictional sliding of granular fault gouge. Pure and Applied Geophysics 161 (9), 1877–1891. 36

Mori, N., Chang, K.-A., 2003. Introduction to mpiv. Website, http://www.oceanwave.jp/softwares/mpiv/. 18

Muir Wood, D., 2004. Geotechnical modelling. Taylor & Francis. 14, 45, 118, 196

Muir Wood, D., 2008. Modelling granular materials: discontinuum - continuum. Structures and Granular Solids: From Scientific Principles to Engineering Application, 21–40. 84

Muir Wood, D., 2010. Personal communication. University of Dundee, UK. 144

Munjiza, A., 2004. The combined finite-discrete element method. Wiley-Blackwell, Heidelberg, Germany. 333

Muthuswamy, M., Tordesillas, A., 2006a. How do interparticle contact friction, packing density and degree of polydispersity affect force propagation in particulate assemblies? Journal of Statistical Mechanics: Theory and Experiment 2006, P09003. 13, 111, 114, 197, 201

Muthuswamy, M., Tordesillas, A., 2006b. Multiscale analysis of the effects of changing gravity on stress propagation in a material subject to an indenting rigid flat punch. Vol. 188. ASCE, pp. 33–33. 204

Nedderman, R. M., 1992. Statics and Kinematics of Granular Materials. Cambridge University Press, Cambridge, U.K. 1

Ng, T. T., 2004. Shear strength of assemblies of ellipsoidal particles. Geotechnique 54 (10), 659–669. 38

Nguyen, N.-S., Magoariec, H., Cambou, B., Danescu, A., 2009. Analysis of structure and strain at the meso-scale in 2d granular materials. International Journal of Solids and Structures 46 (17), 3257–3271. 61

Nouguier-Lehon, C., Vincens, E., Cambou, B., 2005. Structural changes in granular materials: The case of irregular polygonal particles. International Journal of Solids and Structures 42 (24-25), 6356 – 6375. 16, 10, 38, 177

Oda, M., Kazama, H., 1998. Microstructure of shear bands and its relation to the mechanisms of dilatancy and failure of dense granular soils. Geotechnique 48 (4), 465–481. 57, 75

Oda, M., Konishi, J., Nemat-Nasser, S., 1982. Experimental micromechanical evaluation of strength of granular materials: Effects of particle rolling. Mechanics of Materials 1 (4), 269–283. 36, 81, 100

Oda, M., Takemura, T., Takahashi, M., 2004. Microstructure in shear band observed by microfocus x-ray computed tomography. Geotechnique 54 (8), 539–542. 78

Ooi, J., Ai, J., Zhong, Z., Chen, J., Rotter, J., 2008. Progressive pressure measurement beneath a granular pile with and without base deflection. Structures and granular solids - from scientific principles to engineering application, 87–92. 22, 168, 182, 184

O'Sullivan, C., Bray, J. D., Li, S., 2003. A new approach for calculating strain for particulate media. International Journal for Numerical and Analytical Methods in Geomechanics 27 (10), 859–877. 16, 15

O'Sullivan, C., Bray, J. D., Riemer, M. F., 2002. Influence of particle shape and surface friction variability on response of rod-shaped particulate media. Journal of Engineering Mechanics 128 (11), 1182–1192. 9

Ottino, J. M., Khakhar, D. V., 2000. Mixing and segregation of granular materials. Annual Review of Fluid Mechanics 32, 55–91. 1

Park, L. K., Suneel, M., Chul, I. J., 2008. Shear strength of jumunjin sand according to relative density. Marine Georesources and Geotechnology 26 (2), 101–110. 61

Pena, A. A., Lizcano, A., Alonso-Marroquin, F., Herrmann, H. J., 2008. Biaxial test simulations using a packing of polygonal particles. International Journal for Numerical and Analytical Methods in Geomechanics 32 (2), 143–160. 60, 61

Peters, J. F., Muthuswamy, M., Wibowo, J., Tordesillas, A., 2005. Characterization of force chains in granular material. Physical Review E 72 (4), 041307. 13

Powrie, W., 1996. Soil Mechanics: Concepts and Applications. Spon Press. 195

Powrie, W., Ni, Q., Harkness, R., Zhang, X., 2005. Numerical modelling of plane strain tests on sands using a particulate approach. Geotechnique 55 (4), 297–306. 61, 68

Radjai, F., Wolf, D. E., Jean, M., Moreau, J.-J., 1998. Bimodal character of stress transmission in granular packings. Physical Review Letters 80 (1), 61–64. 12, 188

Raffel, M., Willert, C., Kompenhans, J., 1998. Particle image velocimetry: A practical guide. Springer-Verlag, Heidelberg, Germany. 268

Rechenmacher, A. L., 2006. Grain-scale processes governing shear band initiation and evolution in sands. Journal of the Mechanics and Physics of Solids 54 (1), 22–45. 23

Rice, J. R., 1975. On the stability of dilatant hardening for saturated rock masses. Journal of Geophysical Research 80 (11), 1531–1536. 59

Roberts, A., 2007. "ncquiverref" code submitted at matlab central. Website, http://www.mathworks.co.uk/matlabcentral/fileexchange/17582-ncquiverref. 16, 22

Rotter, J. M., Holst, J. M. F. G., Ooi, J. Y., Sanad, A. M., 1998. Silo pressure predictions using discrete-element and finite-element analyses. Philosophical Transactions of the Royal Society A: Mathematical, Physical and Engineering Sciences 356 (1747), 2685–2712. 1

Rowe, P. W., Barden, L., 1964. Importance of free ends in triaxial testing. Journal of the Soil Mechanics and Foundations Division, ASCE 90 (SM1), 1–27. 66, 68

Shahinpoor, M., 1980. Statistical mechanical considerations on the random packing of granular materials. Powder Technology 25 (2), 163–176. 88

Shinneeb, A.-M., Bugg, J., Balachandar, R., 2004. Variable threshold outlier identification in piv data. Measurement Science and Technology 15 (9), 1722–1732. 20

Sielamowicz, I., Blonski, S., Kowalewski, T. A., 2005. Optical technique dpiv in measurements of granular material flows, part 1 of 3–plane hoppers. Chemical Engineering Science 60 (2), 589–598. 23

Singer, T., 2003. Dense-phase pneumatic conveying: Applications, system design, and troubleshooting. Powder and Bulk Engineering 17 (3), 27–33. 1

Smid, J., Novosad, J., 1981. Pressure distribution under heaped bulk solids. Ind. Chem. Eng. Symp. 63, 1–12. 164, 165

Smid, J., Van Xuan, P., Thyn, J., 1993. Effect of filling method on the packing distribution of a catalyst bed. Chemical Engineering and Technology 16 (2), 114–118. 237

Smith, L., Baxter, J., Tuzun, U., Heyes, D. M., 2001. Granular dynamics simulations of heap formation: Effects of feed rate on segregation patterns in binary granular heap. Journal of Engineering Mechanics 127 (10), 1000–1006. 48

Tang, J., Sagdiphour, S., Behringer, R. P., 2009. Jamming and flow in 2d hoppers. Powders and grains 2009: Proceedings of the 6th international conference on micromechanics of granular media 1145 (1), 515–518. 12

Taylor, R., 1995. Geotechnical centrifuge technology. Taylor & Francis. 196

Tejchman, J., Wu, W., 2008. Fe-calculations of stress distribution under prismatic and conical sandpiles within hypoplasticity. Granular Matter 10 (5), 399–405. 169

Terzaghi, K., 1943. Theoretical soil mechanics. John Wiley and Sons, New York. 229, 232, 255, 319, 324

Thomas, P., Bray, J., 1999. Capturing nonspherical shape of granular media with disk clusters. Journal of Geotechnical and Geoenvironmental Engineering 125 (2-3), 169–178. 38

Thornton, C., Zhang, L., 2006. A numerical examination of shear banding and simple shear non-coaxial flow rules. Philosophical Magazine 86, 3425–3452. 63

Tien, H.-J., 1996. A literature study of the arching effects. Master's thesis, Massachusetts Institute of Technology. 319

Tordesillas, A., 2007. Force chain buckling, unjamming transitions and shear banding in dense granular assemblies. Philosophical Magazine 87 (32), 4987 – 5016. 80

Tsuji, Y., Tanaka, T., Ishida, T., 1992. Lagrangian numerical simulation of plug flow of cohesionless particles in a horizontal pipe. Powder Technology 71 (3), 239–250. 31

Tuzun, U., Baxter, J., Heyes, D. M., 2004. Analysis of the evolution of granular stress-strain and voidage states based on DEM simulations. Philosophical Transactions of the Royal Society of London. Series A: Mathematical, Physical and Engineering Sciences 362 (1822), 1931–1951. 48

Ueng, T., Tzou, Y., Lee, C., 1988. The effect of end restraint on volume change and particle breakage of sands in triaxial tests. Advanced Triaxial Testing of Soil and Rock 977, 679–691. 66

US Army Corps of Engineers, ., 1990. Engineering and design - settlement analysis, engineer manual 1110-1-1904. 315

Van Den Berg, P., De Borst, R., Huétink, H., 1996. An eulerean finite element model for penetration in layered soil. International Journal for Numerical and Analytical Methods in Geomechanics 20 (12), 865–886. 197

Vanel, L., Howell, D., Clark, D., Behringer, R. P., Clément, E., 1999. Memories in sand: Experimental tests of construction history on stress distributions under sandpiles. Physical Review E - Statistical Physics, Plasmas, Fluids, and Related Interdisciplinary Topics 60 (5 A), R5040–R5043. 22, 165, 166, 169, 179

Vardoulakis, I., Sulem, J., 1995. Bifurcation analysis in geomechanics. Taylor & Francis. 59

Wang, X. S., Rahman, F., Rhodes, M. J., 2007. Nanoparticle fluidization and geldart's classification. Chemical Engineering Science 62 (13), 3455–3461. 1

Westerweel, J., 1994. Efficient detection of spurious vectors in particle image velocimetry data. Experiments in Fluids 16 (3), 236–247. 20

White, D. J., Bolton, M. D., 2004. Displacement and strain paths during plane-strain model pile installation in sand. Geotechnique 54 (6), 375–397. 26, 297

White, D. J., Take, W. A., Bolton, M. D., 2003. Soil deformation measurement using particle image velocimetry (piv) and photogrammetry. Geotechnique 53 (7), 619–631. 22

Williams, J. R., Rege, N., 1997. The development of circulation cell structures in granular materials undergoing compression. Powder Technology 90, 187–194. 68

Wittmer, J. P., Claudin, P., Cates, M. E., Bouchaud, J.-P., 1996. An explanation for the central stress minimum in sand piles. Nature 382 (6589), 336–338. 169

Yan, G., Yu, H.-s., McDowell, G., 2009. Simulation of granular material behaviour using dem. Procedia Earth and Planetary Science 1 (1), 598–605. 61

Yu, H.-S., 2000. Cavity expansion methods in geomechanics. Springer. 194

Yu, H. S., Mitchell, J. K., 1998. Analysis of cone resistance: Review of methods. Journal of Geotechnical and Geoenvironmental Engineering 124 (2), 140–149. 193

Zhong, Z., Ooi, J. Y., Rotter, J. M., 2001. The sensitivity of silo flow and wall stresses to filling method. Engineering Structures 23 (7), 756–767. 48, 49, 237

Zhou, J., Long, S., Wang, Q., Dinsmore, A. D., 2006. Measurement of forces inside a three-dimensional pile of frictionless droplets. Science 312 (5780), 1631–1633. 13

Zhou, Y. C., Wright, B. D., Yang, R. Y., Xu, B. H., Yu, A. B., 1999. Rolling friction in the dynamic simulation of sandpile formation. Physica A: Statistical Mechanics and its Applications 269 (2), 536–553. 170, 171, 175

Zhou, Y. C., Xu, B. H., Zou, R. P., Yu, A. B., Zulli, P., 2003. Stress distribution in a sandpile formed on a deflected base. Advanced Powder Technology 14 (4), 401–410. 170, 179

Zuriguel, I., Mullin, T., 2008. The role of particle shape on the stress distribution in a sandpile. Proceedings of the Royal Society A: Mathematical, Physical and Engineering Sciences 464 (2089), 99–116. 165, 177, 178

Zuriguel, I., Mullin, T., Rotter, J. M., 2007. Effect of particle shape on the stress dip under a sandpile. Physical Review Letters 98 (2), 028001. 165